

12-26-2013

MEMS Cantilever Sensor for THz Photoacoustic Chemical Sensing and Spectroscopy

Nathan E. Glauvitz

Follow this and additional works at: <https://scholar.afit.edu/etd>

Part of the [Electrical and Electronics Commons](#)

Recommended Citation

Glauvitz, Nathan E., "MEMS Cantilever Sensor for THz Photoacoustic Chemical Sensing and Spectroscopy" (2013). *Theses and Dissertations*. 509.

<https://scholar.afit.edu/etd/509>

This Dissertation is brought to you for free and open access by the Student Graduate Works at AFIT Scholar. It has been accepted for inclusion in Theses and Dissertations by an authorized administrator of AFIT Scholar. For more information, please contact richard.mansfield@afit.edu.



**MEMS CANTILEVER SENSOR FOR THZ PHOTOACOUSTIC CHEMICAL
SENSING AND SPECTROSCOPY**

DISSERTATION

Nathan E. Glauvitz, Major, USAF

AFIT-ENG-DS-13-D-03

**DEPARTMENT OF THE AIR FORCE
AIR UNIVERSITY**

AIR FORCE INSTITUTE OF TECHNOLOGY

Wright-Patterson Air Force Base, Ohio

APPROVED FOR PUBLIC RELEASE; DISTRIBUTION UNLIMITED

The views expressed in this dissertation are those of the author and do not reflect the official policy or position of the United States Air Force, Department of Defense, or the United States Government. This material is declared a work of the U.S. Government and is not subject to copyright protection in the United States.

AFIT-ENG-DS-13-D-03

**MEMS CANTILEVER SENSOR FOR THZ PHOTOACOUSTIC CHEMICAL
SENSING AND SPECTROSCOPY**

DISSERTATION

Presented to the Faculty

Graduate School of Engineering and Management

Air Force Institute of Technology

Air University

Air Education and Training Command

In Partial Fulfillment of the Requirements for the

Degree of Doctor of Philosophy

Nathan E. Glauvitz, BSEE, MSEE

Major, USAF

December 2013


APPROVED FOR PUBLIC RELEASE; DISTRIBUTION UNLIMITED

MEMS CANTILEVER SENSOR FOR THZ PHOTOACOUSTIC CHEMICAL SENSING AND SPECTROSCOPY

(Nathan E. Glauvitz, BSEE, MSEE

Major, USAF

Approved:



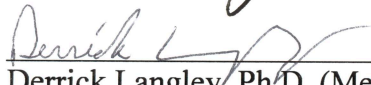
Ronald A. Coutu, Jr., Ph.D. (Chairman)

4 Dec 13
Date




William F. Bailey, Ph.D. (Member)

25 Nov 2013
Date



Derrick Langley, Ph.D. (Member)

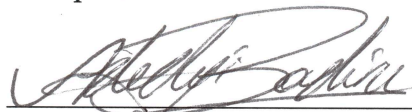
25 Nov 2013
Date



Douglas T. Petkie, Ph.D. (Member)

25 Nov 2013
Date

Accepted:



Adedeji B. Badiru, Ph.D.
Dean, Graduate School of Engineering
and Management

10 Dec 2013
Date

Abstract

Sensitive Microelectromechanical System (MEMS) cantilever designs were modeled, fabricated, and tested to measure the photoacoustic (PA) response of gasses to terahertz (THz) radiation. Surface and bulk micromachining technologies were employed to create the extremely sensitive devices that could detect very small changes in pressure. Fabricated devices were then tested in a custom made THz PA vacuum test chamber where the cantilever deflections caused by the photoacoustic effect were measured with a laser interferometer and iris beam clipped methods. The sensitive cantilever designs achieved a normalized noise equivalent absorption coefficient of $2.83 \times 10^{-10} \text{ cm}^{-1} \text{ W Hz}^{-\frac{1}{2}}$ using a $25 \text{ } \mu\text{W}$ radiation source power and a 1 s sampling time. Traditional gas phase molecular spectroscopy absorption cells are large and bulky. The outcome of this research resulted was a photoacoustic detection method that was virtually independent of the absorption path-length, which allowed the chamber dimensions to be greatly reduced, leading to the possibility of a compact, portable chemical detection and spectroscopy system.

To my loving Family, Spouse, and wonderful Children...

Thank you for all your love and support, you make everyday brighter.

Acknowledgements

I would like to express my sincere appreciation to my research advisor, Dr. Ronald Coutu Jr., for his guidance and support through the course of this dissertation research effort. I would also like to thank the Air Force Office of Scientific Research for their support and funding this research topic area.

I am also very appreciative of the technical support, discussions, and the use of their resources at the Air Force Research Laboratory (AFRL) Sensors and Air Vehicles Directorates. The cooperation and professionalism of the AFIT and AFRL staff was greatly appreciated over the course of this research endeavor.

Nathan E. Glauvitz

Table of Contents

	Page
Abstract	iv
Acknowledgements	vi
List of Figures	ix
List of Tables	xvii
List of Abbreviations	xviii
I. Introduction	1
1.1. Challenges for Terahertz Photoacoustic Chemical Sensing and Spectroscopy.....	1
1.2. Potential Applications	2
1.3. Summary.....	4
II. Background	5
2.1. Chemical Sensing and Spectroscopy.....	5
2.2. Photoacoustic Sensing.....	14
2.3. MEMS Fabrication Technology.....	17
2.3.1. Etching.....	20
2.3.1.1. Wet etching.....	21
2.3.1.2. Dry Etching.....	22
2.3.2. Deposition of Films.....	25
2.3.3. MEMS Electrical Sensor Methods.....	29
2.4. PA Sensor Systems.....	35
2.5. Other Sensing Applications.....	43
2.6. Summary.....	48
III. Photoacoustic and Cantilever Modeling	50
3.1. Chamber Photoacoustics	50
3.2. Cantilever Model.....	55
3.2.1. Cantilever Under Static Load Conditions.....	55
3.2.2. Cantilever Dynamic Behavior.....	58
3.3. Finite Element Modeling of Cantilever Designs.....	66
3.4. Summary.....	82
IV. Fabrication	84
4.1. Photolithography Mask Fabrication	84
4.2. Cantilever Device Fabrication.....	87
4.2.1. Metal Deposition.....	89
4.2.2. Device Layer Etch.....	92
4.2.3. Backside Etch.....	95
4.3. Summary.....	102
V. Experimental Results	104

5.1. Experimental Setup	104
5.2. Cantilever Dynamics	112
5.3. THz Photoacoustic Spectra.....	124
5.4. Performance Analysis and Limitations	144
5.5. Summary.....	155
VI. Conclusions	157
6.1. Contributions	157
6.1.1. Fabrication	158
6.1.2. PA Spectroscopy and Sensitivity Results	158
6.2. Future Research.....	160
Appendix A. Additional Cantilever Design Models.....	164
Appendix B. PA Chamber Design.....	170
Appendix C. Additional PA Spectral Data.....	174
Appendix D. MATLAB[®] Code for PA Data Analysis	177
Appendix E. Visual Bibliography.....	183
Vita	185
Bibliography	186

List of Figures

	Page
Figure 1. Traditional absorption spectrometer systems can be large; with typical path-lengths of 3 ft or more for increased sensitivity.....	6
Figure 2. Terahertz photomixing used three fiber-coupled lasers in (a) to generate THz radiation and collect absorption spectra of CH ₃ CN at 60 mTorr chamber pressure, © IEEE 2000 [19].....	11
Figure 3. A.G. Bell’s ‘spectrophone’ developed to investigate PA effect on samples of interest [7].	14
Figure 4. Isotropic etch in (a) removes the desired material uniformly in all directions, while (b) and (c) are examples of anisotropic etches which exhibited preferential etch directions.	21
Figure 5. Illustration of DRIE process sequence of etch, deposit polymer, and etch, where sidewall passivation leads to an overall vertical, anisotropic etch profile [37].	23
Figure 6. Cantilever tip displacement in the -z direction causes the PZT material to elongate a small amount Δx in the +x direction, generating a net potential difference on the opposite surfaces of the PZT material in the z direction.	31
Figure 7. Cantilever and paddle style pizeoresistive airflow sensors with different tip widths; from left to right, 0.4, 1.2, and 2 mm wide respectively [94].	45
Figure 8. Notional diagram of the chemical absorption cell illustrates the characteristic dimensions and other parameters used for the chamber design.....	51
Figure 9. Absorption spectra plot of CH ₃ CN from JPL database.....	53
Figure 10. Small portion of simulated absorption coefficient spectra of methyl cyanide at 18 mTorr after appropriate pressure broadening conditions are applied.	54
Figure 11. Rectangular, single fixed end cantilever beam design of length L , width w , and thickness h	55
Figure 12. Deflections for three different cantilever designs under a 10 mPa uniform static pressure load.	58

Figure 13.	Mass and spring oscillator motion described through Hooke's Law and Newton's second law of motion.....	59
Figure 14.	Equivalent mass-spring-damper model for cantilever displacement which describes the forces, mass, spring, and damping conditions for the system.	61
Figure 15.	Amplitude of the frequency response curve for $5 \times 2 \times 0.01 \text{ mm}^3$ cantilever design with a 0.2 mPa harmonic excitation and a damping condition of $5.76 \times 10^{-7} \text{ kg/s}$	63
Figure 16.	Envelope of the tip displacement in (a) of a $5 \times 2 \times 0.01 \text{ mm}^3$ cantilever design when a harmonic pressure of 0.2 mPa was initiated at time $t=0$ under damping condition of $b = 5.76 \times 10^{-7} \text{ kg/s}$. A zoomed in view of the tip displacement due to the excitation load is shown in (b).	65
Figure 17.	Tip displacement in (a) of $5 \times 2 \times 0.01 \text{ mm}^3$ cantilever design after PA pressure of 0.2 mPa was removed at time $t=0$ under damping condition of $b = 5.76 \times 10^{-7} \text{ kg/s}$ and a zoomed in view in (b) of the tip displacement decay due to damping.....	66
Figure 18.	CoventorWare [®] mesh model of $3 \times 1 \times 0.01 \text{ mm}^3$ cantilever using $25 \times 25 \mu\text{m}^2$ square elements, extruded $10 \mu\text{m}$ in the Z-direction.	68
Figure 19.	Tip displacement results of mesh study for the $5 \times 2 \times 0.01 \text{ mm}^3$ cantilever design using a z-extruded parabolic brick mesh under 1 mPa static load.....	70
Figure 20.	The finer mesh dimensions for the $5 \times 2 \times 0.01 \text{ mm}^3$ cantilever shows the polynomial fit function predicted a displacement of 5.5636 nm for a 1 mPa load.....	70
Figure 21.	Comprehensive CoventorWare [®] model created from L-Edit mask layouts and fabrication process file to define the handle wafer, device, and BOX layers. The $10 \mu\text{m}$ thick device layer was subjected to a 1 Pa pressure load which caused a $4 \mu\text{m}$ tip displacement.....	71
Figure 22.	CoventorWare [®] finite element model of a $5 \times 2 \times 0.01 \text{ mm}^3$ cantilever under a 1_mPa static load had a resultant beam deflection of 5.5 nm.	73
Figure 23.	Resultant mises stress generated in the $5 \times 2 \times 0.01 \text{ mm}^3$ cantilever beam under the same 1 mPa static load.	73
Figure 24.	Cantilever resonant mode shapes and frequencies for a $5 \times 2 \times 0.01 \text{ mm}^3$ cantilever due to a sinusoidal load.	75

Figure 25.	Amplitude displacement frequency response generated in FEM software of a $5 \times 2 \times 0.01 \text{ mm}^3$ cantilever under a 0.1 mPa harmonic load for different damping conditions.	77
Figure 26.	Amplitude displacement response shown for the first four lowest resonant modes of the $7 \times 2 \times 0.01 \text{ mm}^3$ cantilever under a 0.1 mPa harmonic load and 10% of the critical damping coefficient.	78
Figure 27.	Three cantilever designs, using a $10 \text{ }\mu\text{m}$ thick device layer, under a 0.1 mPa harmonic load with 0.5% damping illustrated by the dashed lines while a 10% damping factor results in significantly less deflection shown by the solid lines.	79
Figure 28.	Tip displacement results for four different cantilever designs under 0.1 mPa harmonic load, 0.5% of the critical damping coefficient, the more flexible $7 \times 2 \times 0.005 \text{ mm}^3$ design showed significantly more deflection.	80
Figure 29.	Resultant tip deflections from modal harmonic analysis of a plain silicon $5 \times 2 \times 0.01 \text{ mm}^3$ cantilever design under four periodic load conditions using 0.1% of the critical damping coefficient.	81
Figure 30.	Verniers from the power exposure series result shown in (a) were under exposed, a good exposure level in (b), and over exposure dose in (c) where the narrow line of resist was removed during the develop process.	86
Figure 31.	Cantilever fabrication process began with the (A) deposit Ti/Au for reflective surface, (B) etch device layer to define cantilever, (C) backside etch through handle wafer, and (D) the removal of the exposed BOX with HF vapor. An optical image (E) of a fabricated $5 \times 2 \times 0.01 \text{ mm}^3$ silicon cantilever with a $6 \text{ }\mu\text{m}$ gap etched through the device layer to define the cantilever beam.	89
Figure 32.	(a) Layout of cantilever design and in (b) an optical image of the $3 \text{ }\mu\text{m}$ gap etched through the device layer with the Plasma-Therm DRIE system.	93
Figure 33.	Larger $8.4 \text{ }\mu\text{m}$ gap shown with photoresist mask still in place after additional isotropic etch.	95
Figure 34.	Device surface in (a) with cracks in protective SF-11 photoresist after backside DRIE. Another sample viewed from the backside in (b) after DRIE and RIE, stress between the cracks in the SF-11, BOX, and device layer caused the cantilever to crack near the anchor.	98

Figure 35.	Darker areas on cantilever are due curvature in device layer and BOX, viewed from backside, of 5 μm device layer in (a) and a 10 μm device layer in (b) with 1818 PR used as protective/support layer on device surface.	99
Figure 36.	Residual PR in the highlighted areas remained around gap after acetone clean of released cantilever shown in (a) and same cantilever shown in (b) after 15 min O_2 plasma ash at 125 W had no remaining PR.	101
Figure 37.	Zygo 3D model of a $5 \times 2 \times 0.01 \text{ mm}^3$ cantilever design showed a 15 μm out of plane tip displacement.....	102
Figure 38.	Schematic diagram of photoacoustic cell shown with the front portion of the chamber removed; highlights the chamber dimensions and cantilever position in relation to the absorption cell volume.	105
Figure 39.	Diagram (not to scale) shows both the PA optical measurement techniques used; beam clipped by the iris when the reference mirror is blocked and a Michelson interferometer displacement measurement when the reference arm was used.....	107
Figure 40.	Assumed Gaussian profile of the HeNe laser beam, passed through a 0.8 mm diameter iris, with normalized intensity color bar on right.	109
Figure 41.	Signal intensity strengths for five different attenuation levels of the HeNe laser beam centered on one axis and swept across the aperture along the other axis. The strongly attenuated signal is the bottom curve and the above curves are due to decreasing the amounts of beam attenuation.	110
Figure 42.	Photograph of experimental setup highlights the PA chamber, optics, iris, detector for HeNe PA signal, THz radiation source, and THz detector.	111
Figure 43.	PA response of the $5 \times 2 \times 0.01 \text{ mm}^3$ cantilever as a function of modulation frequency for four different pressures tested revealed the maximum PA signal was achieved at slightly higher modulation frequencies with increased chamber pressure.	113
Figure 44.	Resonant frequency of the $5 \times 2 \times 0.01 \text{ mm}^3$ cantilever taken over a range of pressures shown with a second degree polynomial curve fit.	114
Figure 45.	Resonant frequency response for the $5 \times 2 \times 0.005 \text{ mm}^3$ cantilever was taken over a smaller pressure range and had a linear increase with chamber pressure.	115

Figure 46.	Based on Equation (5.2), the quality factor for the $5 \times 2 \times 0.01 \text{ mm}^3$ and $5 \times 2 \times 0.005 \text{ mm}^3$ cantilever designs were evaluated over a segment of low chamber pressures.	116
Figure 47.	PA data recorded at 3 mTorr in plot (a) shows the slow response of the lock-in amplifier and raw PA signals at the low chamber pressure and a quality factor of 4,085. Plot (b) is a zoomed in view of the raw PA signal from the diode and modulated THz signal as the radiation turned off.	117
Figure 48.	PA data in plot (a), taken at 80 mTorr had a quality factor of 1,091 illustrates the quicker response time of the lock-in PA signal and raw PA signal from the THz excitation radiation at higher chamber pressure. Plot (b) is a zoomed in view of the raw PA signal from the diode and modulated THz signal.	118
Figure 49.	Time constants found through exponential curve fit to the decay of PA signals over the range of pressures shown for $5 \times 2 \times 0.01 \text{ mm}^3$ cantilever.	119
Figure 50.	Measured THz diode signal and corresponding PA signals for four different THz source powers P0-P3 inserted into the PA chamber.	120
Figure 51.	PA Lock-in Signals generated due to the P0-P3 power levels of the THz radiation source.	121
Figure 52.	Linear response of the PA Signal and PA Lock-in Signals produced versus the absolute value of the THz detector voltage.	122
Figure 53.	Graph of measurements taken on $5 \times 2 \times 0.01 \text{ mm}^3$ cantilever at different chamber pressures show PA peak-to-peak signals represented by a diamond shape corresponded to the scale on left while the interferometrically measured cantilever amplitude deflections, shown with a circle and error bars correspond to the deflection scale on the right.	124
Figure 54.	Spectral PA signals taken at 59 mTorr with 2, 0.5, and 0.1 s excitation times using a 0.05 MHz step size, moving from low to high frequency; the PA peak response shifted to higher frequencies and reduced amplitudes as the excitation time was decreased.	126
Figure 55.	PA spectral data plots of CH_3CN collected with the $5 \times 2 \times 0.01 \text{ mm}^3$ cantilever at three pressures utilized a 0.05 MHz step size and recorded the 0.5 s average PA signal for each frequency step.	128

Figure 56.	PA spectra with the $5 \times 2 \times 0.005 \text{ mm}^3$ cantilever recorded at 4 mTorr with the THz radiation source not-attenuated and attenuated by plexiglass.	129
Figure 57.	Photoacoustic data and the simultaneously recorded THz diode signal are compared to the simulated absorption spectra of methyl cyanide recorded at 13 mTorr with the $5 \times 2 \times 0.01 \text{ mm}^3$ cantilever.	130
Figure 58.	CH_3CN spectra collected at 15 mTorr; THz diode measured transmittance shown in (a) and simultaneous recorded PA signal in (b) from the $5 \times 2 \times 0.005 \text{ mm}^3$ cantilever sensor.	131
Figure 59.	CH_3CN spectra collected at 38 mTorr used the $5 \times 2 \times 0.005 \text{ mm}^3$ cantilever sensor; THz diode transmittance shown in (a) had a large power increase between 460-461 GHz and the simultaneously recorded PA signal shown in plot (b).	132
Figure 60.	Simulated spectrum of CH_3CN matched very well to the PA spectral data of the first excited state rotational absorption lines in the 459.79-461.6 GHz range.	133
Figure 61.	Stronger excited state absorption lines masked the weaker ground state absorption lines of the simulated spectrum at 457.186 GHz, 457.471 GHz, and 457.992 GHz.	134
Figure 62.	PA spectra of higher excited state absorption lines not accounted for in the simulated spectrum are shown from 461.6-462.6 GHz.	135
Figure 63.	CH_3CN THz diode transmittance spectra collected at 268 mTorr showed a $2 \times 10^{-4} \text{ V}$ mean fluctuation in the signal magnitude between frequency steps.	136
Figure 64.	PA spectra of CH_3CN collected at 268 mTorr with the $5 \times 2 \times 0.005 \text{ mm}^3$ cantilever sensor showed significant line broadening due to the high chamber pressure.	137
Figure 65.	Zoomed in view of the same PA spectra shown in Figure 64 has a large number of weak spectral absorption lines below 586 GHz that are visible due to the high chamber pressure.	137
Figure 66.	3-D view of PA modulation frequency scan data collected over a 15 min period every hour for a 23 hr period showed a 66.9% reduction in PA signal amplitude over the test period.	139

Figure 67.	2-D view of data scan showed a 0.1 Hz increase in the modulation frequency required to achieve maximum PA signal as the chamber pressure rose from 10 mTorr to 22 mTorr over the 23 hour period.	139
Figure 68.	Calculated SNR using $n=100$ for the PA spectral data collections shown over the lower portion of the pressure range tested.	142
Figure 69.	Fourier analysis of a 1 s photoacoustic signal, collected at 200 mTorr taken at Freq 1, showed very low noise in the system with no single dominant noise frequency in the iris clipped PA measurement method with the $5 \times 2 \times 0.01 \text{ mm}^3$ cantilever.	145
Figure 70.	Lower portion of the frequency spectrum for the $5 \times 2 \times 0.005 \text{ mm}^3$ cantilever in the larger PA cell at 268 mTorr, showed significant signal at the resonant frequency of the cantilever and at 60 Hz internals from electrical noise.	146
Figure 71.	Complete frequency spectrum from data in Figure 70 out to 30 kHz, highlights the high frequency noise attributed to the HeNe laser source for the PA measurements.	147
Figure 72.	Example of PA signal spikes, which occurred due to acceleration noise coupled into the cantilever through the PA chamber and experimental setup.	155
Figure 73.	Dual anchored cantilever design had total over all dimensions of $5 \times 3 \times 0.01 \text{ mm}^3$; the two anchor segments were 1 mm long and 0.5 mm wide. Deflection was due to a 10 mPa static load condition.	164
Figure 74.	Mises stress map showed a high concentration of stress in the corner where the anchor arm attachment to the plate.	165
Figure 75.	Corners filleted using a 300 μm radius reduced the peak level of stress in the corners, and the stress is now at a maximum at the surface of the device at the anchor points.	166
Figure 76.	Amplitude displacement comparison between traditional and dual anchored cantilever designs under 0.1 mPa harmonic load using 0.5% of the critical damping factor.	167
Figure 77.	Mises stress distribution on a $5 \times 2 \times 0.005 \text{ mm}^3$ cantilever design with Pt electrodes and a piezoelectric layer of PZT covering $1/16^{\text{th}}$ the length of the cantilever under a 1 Pa static load.	168
Figure 78.	Simulation results of the voltage generated for different fractional coverage lengths of PZT along the length of the cantilever.	169

Figure 79.	Assembled CAD model of the PA chamber with labels of primary components.....	171
Figure 80.	Exploded view of chamber shows the individual pieces prior to assembly.	171
Figure 81.	Back half of the PA chamber which contains the absorption cell shows the area for the SOI device placement and location of o-rings to seal the chamber.	172
Figure 82.	Side view in (a) and frontal view in (b) of PA chamber shown in semi-transparency to highlight internal construction of the system.....	173
Figure 83.	Full display of PA spectral snippet shown in Figure 59 (38 mTorr) with addition of scaled PA signal data due to the chamber pressure changes due to the vacuum leak rate.	174
Figure 84.	Zoomed in view of Figure 83 ground state absorption lines scaled PA signal matched up to the simulated spectrum.....	175
Figure 85.	Zoomed in view of ground state absorption scaled PA signal matched up to the simulated spectrum.....	176
Figure 86.	Visual bibliography connects related works, arranged by direct references.....	184

List of Tables

	Page
Table 1. Recent PA detection system performance limits.	42
Table 2. Tip displacement results, listed in nanometers of deflection, for 10 mPa static applied pressure load on the different cantilever designs with a 10 μm device layer thickness.	72
Table 3. Mode 1 and 2 resonant frequencies for each beam design length and width tested, utilizing a 10 μm thick device layer.	76
Table 4. Analytical and FEM resonant frequency calculations for two cantilever designs.	81
Table 5. Relative change in PA signals as power inserted into the chamber is reduced.	122
Table 6. SNR results for multiple sample size intervals for data set in Figure 58 (b).	141
Table 7. Best sensitivity results for the two cantilever sensors.	142
Table 8. Best NNEA's achieved by the system for each sensor design.	143
Table 9. Pressure changes due to thermal fluctuations of the gas in a 3.99 cm^3 PA chamber.	149
Table 10. Estimated cantilever deflections due to fluctuations in PA chamber pressure.	150
Table 11. Minimum absorption coefficient at the gas thermal fluctuation limit for the 3.99 cm^3 PA cell.	151
Table 12. Minimum detectable cantilever displacement due to thermal fluctuations when $\omega \ll \omega_0$	153
Table 13. Minimum detectable cantilever displacement due to thermal fluctuations for the case when $\omega = \omega_0$	153

List of Abbreviations

AFM	Atomic Force Microscopy
AR	Anti-Reflective
BWO	Backward Wave Oscillator
DRIE	Deep Reactive Ion Etch
DUV	Deep Ultra Violet
FASSST	Fast Scan Submillimeter Spectroscopy Technique
FEA	Finite Element Analysis
FEM	Finite Element Method
LED	Light Emitting Diode
LPCVD	Low-Pressure Chemical Vapor Deposition
MEMS	Microelectromechanical Systems
NEMS	Nanoelectromechanical Systems
NNEA	Normalized Noise Equivalent Absorption
PA	Photoacoustic
PAS	Photoacoustic Spectroscopy
PSD	Position Sensitive Detector
PZT	Lead Zirconate Titanate
RIE	Reactive Ion Etch
SOI	Silicon-On-Insulator
SEM	Scanning Electron Microscope
SNR	Signal-to-Noise Ratio

THz Terahertz

XRD X-Ray Diffraction

MEMS CANTILEVER SENSOR FOR THZ PHOTOACOUSTIC CHEMICAL SENSING AND SPECTROSCOPY

I. Introduction

1.1. Challenges for Terahertz Photoacoustic Chemical Sensing and Spectroscopy

Advancements in Microelectromechanical System (MEMS) fabrication technology over the last several decades has been a driving force behind the miniaturization and increased reliability of sensor designs. MEMS devices are an enabling technology and through modification of engineering design parameters, extremely sensitive sensors can be created. The primary objective of this research was to design, model, and fabricate a compact photoacoustic spectroscopy gas sensor system responsive to sub-millimeter/terahertz (THz) radiation. Micro-fabrication of these sensitive MEMS devices presents challenges because as the cantilever sensitivity improves, the difficulty in the manufacturability also increases. The challenge here was to create the cantilever sensor to be as sensitive as possible and yet robust enough to withstand the required fabrication processes, handling, transportation, and experimental photoacoustic (PA) measurement conditions.

Spectroscopy is the study of the interaction between physical matter and electromagnetic radiation [1, 2]. Atoms and molecules absorb and dissipate energy through various pathways such as radiative, vibrational, rotational, translational, or electronic means [3]. Many sensing techniques over the years have been employed for molecular spectroscopy and detection of trace gases [4]. One very compact spectral

detection method can take advantage of the photoacoustic (PA) effect on gas phase sample species. The photoacoustic effect is the result of molecules absorbing energy from an electromagnetic wave; where the absorbed energy is then released through collisions and other non-radiative pathways into translational energy, resulting in an increased pressure. This pressure wave can then be detected by a cantilever or other pressure sensing device. Photoacoustic detection of radiation is an experimental technique widely used for spectral detection in solids, liquids, and gasses [4-7].

Traditional gas phase molecular spectroscopy absorption cells can range from 2-10 feet long, making them only practical in a dedicated laboratory setting. The novelty of this work was realized through the combination of a sensitive fabricated MEMS cantilever transducer, the miniature size of the custom designed photoacoustic chamber, the high spectral resolution, and broad frequency range capabilities of the THz radiation source. The outcome of this research was a virtually baseline free photoacoustic spectral detection method, independent of the absorption cell path-length which allowed the chamber size to be greatly reduced. The compact MEMS cantilever-based PA cell developed during this research was a significant reduction in size when compared to traditional THz spectroscopy methods. This work was also a critical step in the development of a technology that may lead to portable or hand held THz chemical sensing systems.

1.2. Potential Applications

There are numerous applications for PA chemical sensing technology in scientific and industrial communities, as well as, in the Air Force and across the Department of

Defense. An obvious scientific application of PA spectroscopy is analyzing gaseous samples. With the compact PA method developed here, this system could be paired with an existing spectroscopy cell to enhance measurements or ultimately replace the larger traditional THz spectroscopy absorption cell systems. This technology could also be applied in an industrial setting to perform chemical leak or contamination detection for multiple hazardous chemicals in the workplace due to the specificity enabled by the high spectral resolution and broad frequency range of the THz radiation source.

Additional applications of MEMS and THz radiation technologies have also been investigated for imaging purposes. The incorporation of superconductor [8] and metamaterial [9] layers on MEMS devices has enabled the direct absorption and sensing of THz radiation. As an acoustic sensor, arrays of piezoelectric cantilever and spiral-beam-supported diaphragm transducers have shown increased sensitivity by about 30 times when many transducers were connected in parallel [10].

A mobile chemical detection system would be a valuable tool for troops; giving them the ability to monitor environmental conditions as they moved through the battlefield. In the event a chemical weapons attack, multiple detection units deployed around an air base could monitor the toxicity levels of the chemical agents. The ability to identify chemical agents and also their concentration is a powerful tool; providing critical information about chemical threats. A compact chemical sensing system, like the one designed here, could be used on board a vehicle or medium sized unmanned aerial vehicle (UAV) if noise mitigation techniques were employed. The vehicle or UAV could map and track airborne contamination from a hazardous waste or chemical attack incident

in real time. The broad frequency range capability of the radiation source should allow for the excitation and thereby identification of a wide range of chemical compounds.

1.3. Summary

MEMS cantilever pressure sensors are designed, modeled, fabricated and tested in a unique THz PA chamber designed to measure molecular absorption spectra at low chamber pressures. Based on the modeling results, improved sensor designs were created and fabrication process improvement techniques were developed to create very sensitive cantilever designs. The MEMS sensor and PA measurement techniques developed in this work allowed for the overall dimensions of the system to be reduced in size; an order of magnitude smaller when compared to traditional spectroscopy absorption cell designs. The compact analyzer system offers a virtually baseline free measurement of molecular absorption since the PA signal is a direct measure of the power absorbed by the gas under investigation. The remaining five sections of this dissertation document are: II. Background, III. Photoacoustic and Cantilever Modeling, IV. Fabrication, V. Experimental Results, and VI. Conclusions.

II. Background

The background for this research effort is broken down into two main areas, chemical sensing/spectroscopy and MEMS sensor technologies for PA detection. In the first portion of this section, current techniques used for chemical sensing and spectroscopy are discussed. The various detection methods, sensors used, and performance factors of each scenario are also evaluated. Then sensor technologies for PA detection are discussed which includes MEMS sensor technologies, fabrication methods, piezoelectric thin films and thin film conditioning techniques are discussed.

Gas phase chemical sensing and photoacoustic spectroscopy has an advantage over traditional transmittance spectroscopy measurements in that the absorption chamber dimensions can be made much more compact and still achieve high sensitivity. The significantly more compact size of the PA chamber is made possible through the use of MEMS sensor technologies to create sensitive miniature microphones.

2.1. Chemical Sensing and Spectroscopy

Chemical sensing and spectroscopy measurements of gas phase species can be made through different means. “A chemical sensor is a device that transforms chemical information, ranging from the concentration of a specific sample component to total composition analysis, into an analytically useful signal” [11]. The sensor is a critical part of the analyzer, which is typically an automated system that can sample, process, and record data about the analyte or chemical sample under investigation. Chemical sensors can be classified according to the principle of operation of the transducer, be it: optical,

absorbance, reflectance, luminescence, fluorescence, refractive index, photothermal effect, or light scattering [11]. Many chemical sensor systems have two functional segments, a receptor and a transducer portion. The receptor portion of a sensor often transforms information from a chemical sample into energy. The transducer part of the sensor then converts the energy into a usable signal for analysis. Chemical sensing methods can occur based on many principles, but they are predominantly divided into categories of either physical or chemical reactions. Sensors based on physical phenomenon where no chemical reaction takes place use measurements of absorbance, changes in refractive index, conductivity, pressure, or mass to analyze samples. While in the second method, chemical sensors rely on a chemical reaction to occur or sense changes at the molecular level in a sample of interest [11]. In some cases like absorption based sensors, they can't always be classically divided into two separate categories because they operate based on the chemical makeup of a material which in turn can cause or rely on a physical phenomenon to occur.

Absorbance is a physical property of an analyte and widely used method for a chemical analysis, which typically utilizes an absorption measurement technique using a radiation source, detector, and an absorption cell. A notional layout of a traditional absorption spectrometer is shown in Figure 1.

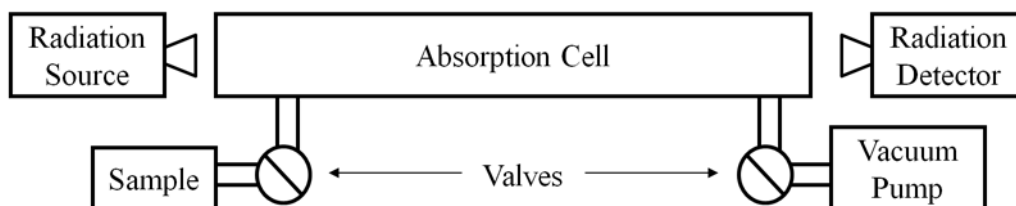


Figure 1. Traditional absorption spectrometer systems can be large; with typical path-lengths of 3 ft or more for increased sensitivity.

In the configuration shown in Figure 1, radiation emitted by the source passes through an absorption cell, the gas in the cell absorbs a portion of the energy, and the remaining transmitted energy is detected by the receiver. Attached to the absorption cell is a port to allow in a sample species for investigation and a vacuum pump on another port to control the pressure in the cell which allows for flexibility of testing gas species over a range of pressures. Gas species in the cell can absorb a portion of the radiation and when the right conditions are satisfied, the absorbance of the gas in the system will follow the Beer-Lambert law. The absorption coefficient for a sample species is a function of frequency and the units are typically given in units of reciprocal length, cm^{-1} or m^{-1} . The absorption coefficient, α , in the Beer-Lambert law is defined as

$$I(l) = I(0)e^{-\alpha l} \quad (2.1)$$

where l is the path-length the radiation traveled through the cell, $I(0)$ is the intensity of the radiation entering the sample, $I(l)$ is the transmitted light intensity that exits the cell [12]. This law is valid when a small fraction of the radiation is absorbed by the gas and when light losses due to scattering are negligible [13]. In this absorption cell configuration, the intensity of the radiation that exits the cell is typically an exponential function of the product of the absorption coefficient and the cell path-length. For weakly absorbing species, $\Delta I \sim \alpha l$, and the sensitivity scales linearly with the cell length. For either case, the sensitivity of the measurement is enhanced by making the cell path-length longer for traditional spectroscopy techniques.

This change in energy is an essential aspect of spectroscopy, therefore relevant equations and some basic terminology are discussed next. A photon in an electromagnetic wave has energy E , represented as

$$E = h\nu \quad (2.2)$$

where the photon energy is the product of Planck's constant $h=6.626\times 10^{-34}$ J s and the frequency ν , of the radiation [14]. The absorbed energy required to excite a molecule from energy level E_1 to a higher allowed energy level E_2 is also related to the exposed radiation frequency through

$$E_2 - E_1 = h\nu. \quad (2.3)$$

Spectral absorbance plots are often represented in terms of the radiation frequency, wavelength, or wavenumber. The wavelength λ of the radiation is defined as

$$\lambda = \frac{c}{\nu} \quad (2.4)$$

where c is the speed of light. The other common way to relate spectral absorbance plots is through the wavenumber $\tilde{\nu}$, defined as

$$\tilde{\nu} = \frac{1}{\lambda}. \quad (2.5)$$

Units for the wavenumber are also often given in cm^{-1} , depending on the wavelength of the radiation.

The energy absorbed by the molecules can be absorbed into rotational or vibrational motion, or into electrical states depending on the excitation frequency/wavelength. The change in radiation power observed at the detector at specific frequencies is due to the molecules absorbing a portion of the radiation energy into specific allowable energy states. The allowed energy states are unique to each molecular structure, which enables the specificity of the absorption measurement technique. At longer wavelengths of the microwave, THz, and far infrared spectral region, absorption

lines are due primarily to energy absorbed into quantized rotational transitions. As the wavelength of the radiation decreases in the infrared, visible, and ultra violet, excitable vibrational states also have specific absorption lines. Finally at shorter x-ray wavelengths, electronic transitions in the molecules occur when the electrons of the atoms are excited to higher energy states [15].

For absorption spectroscopy applications, some typical radiation sources include blackbody, arc lamps, microwaves, lasers, or tunable lasers. White *et al.* developed several absorption cell designs that could achieve very long path-lengths to collect gas phase absorption spectra with the use of mirrors inside the cell, which caused the radiation to make multiple passes through the gas under investigation. An infrared grating spectrometer presented in reference [16] where the absorption cell had an overall physical length of 1 m; but through adjustments to the internal cavity, path-lengths of 4-32 m path-lengths could be achieved. The spectra collected of N₂O (nitrous oxide) was a direct measurement of the radiation transmittance and radiation source wavelength. The radiation used was generated from a carbon arc source. The final wavelength of the radiation that was passed into the cell was achieved through the use of prisms, gratings, and specific slit configurations. Due to the complicated optical setup, cell size, and radiation source filtering, the spectrometer system had a large physical footprint of approximately 4×8 ft² [16].

Other developed absorption cells were more compact; which had an overall length of ~45 cm, an internal volume of 6 liters, and weighed 29 lbs. This smaller cell could be operated at elevated pressures of up to 10 atmospheres, and could utilize path-lengths of 10 cm, 1 m, or 10 m [17]. An absorption cell developed by Pilston *et al.* was slightly

more compact measuring in at ~31 cm long. The effective cell length could be set to 1.25 m, and increased in length at increments of 1.25 m, all the way up to 10 m. The developed long-path cell was connected to a commercial Perkin-Elmer Model 12 or Model 112 spectrometer [18]. For all of these “compact”, long path-length absorption designs, the efficiency of the transmitted energy decreased with effective cell length. Efficiency losses of up to 40% were observed between the 1.25 m and 10 m path-lengths due to reflections, scattering, variations of mirror reflectivity for different wavelengths, and atmospheric absorption [18].

Matsuura *et al.* created a highly tunable THz source through difference frequency mixing of three fiber-coupled lasers [19]. They used low-temperature-grown ultra-fast GaAs photoconductors and the THz radiation was amplified through a master-oscillator power amplifier. To demonstrate the frequency control of the THz generation, absorption spectroscopy analysis of methyl cyanide (CH_3CN) was performed through a small absorption cell, 8 cm long and 1 inch in diameter. Experimental setup of the THz generation scheme is shown in Figure 2 (a) and the resultant spectral signature of the CH_3CN taken at 60 mTorr around 312 GHz region is shown in Figure 2 (b). The second derivative of the absorption spectra collected illustrates the $J_K = 16_K \rightarrow 17_K$ rotational transitions. The second derivative of recorded spectra enhances the identification of absorption peak frequencies for partially overlapping absorption lines. The $K=0-11$ numbered rotational transitions are labeled the graph in Figure 2 (b), as well as some isotopic absorption features in the inset image between $K=5$ and $K=6$. The spectra was collected at a 2 MHz/s sweep rate and had an estimated minimum detectable absorption of $\sim 10^{-5}$, limited by the detector noise [19]. The THz system demonstrated by Matsuura

et al. exhibited very good frequency generation control and the sensitivity of their spectroscopy measurements would have likely improved had they used a longer absorption cell.

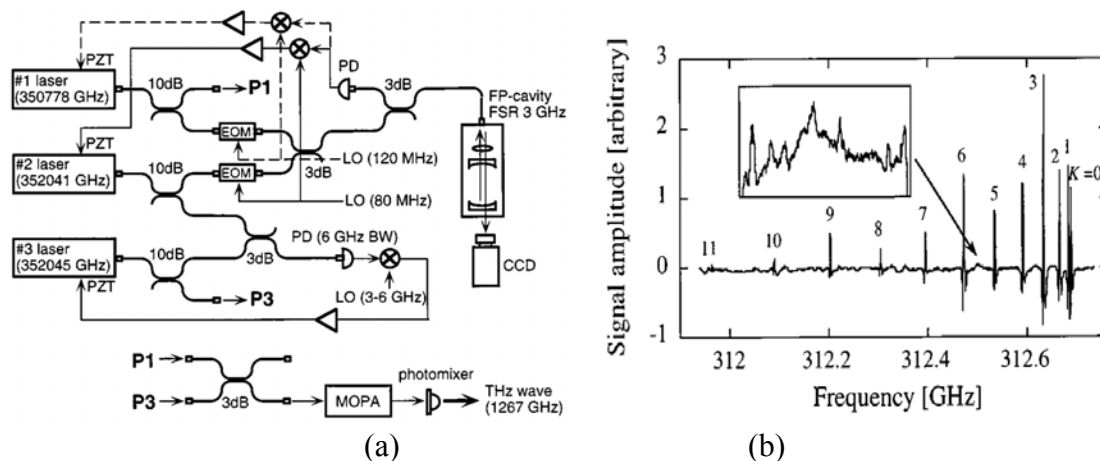


Figure 2. Terahertz photomixing used three fiber-coupled lasers in (a) to generate THz radiation and collect absorption spectra of CH_3CN at 60 mTorr chamber pressure, © IEEE 2000 [19].

THz spectral signatures enable chemical sensor designs capable of near ‘absolute’ selectivity in complex gas phase chemical mixtures due to the intrinsic narrowness of spectral signatures [20, 21]. Spectral line widths are typically less than 1 MHz; this near ‘absolute’ selectivity, good sensitivity, and low amounts of sample necessary for detection make THz spectral range very attractive for detection of polar molecular species. An additional benefit of THz is that normal atmospheric constituents at low pressures do not cause significant spectral interference. Inexpensive technology is commercially available up to 100 GHz courtesy of the wireless communications industry [21].

As mentioned previously, traditional absorption cells are often made to create very long path-lengths to increase sensitivity. Options like folded cells [21] or multi-pass

enhancement techniques [4, 16-18] were used to reduce the overall physical dimensions of the absorption cell designs, but they are still rather large. For radiation sources in the THz range, the absorption spectra are primarily due to the rotational degrees of freedom of molecules. Complex absorption spectra of a mixture of 20 gaseous species were recorded at the Doppler-limited rotational spectrum with a backward-wave-oscillator-based fast scan submillimeter spectroscopy technique (FASSST) system [21]. The gas mixture was simultaneously tested in the 2.5 cm diameter, 1.2 m long folded absorption cell.

Because rotational energy level spacings are small in comparison to thermal energy, a spectrum with a complex redundancy and specific molecular fingerprint resulted. The density of these spectra is a strong function of molecular size and symmetry. Spectra in the ~320–380 GHz region, with the exception of a few relatively light species, any comparable bandwidth can access suitable fingerprints for the large majority of molecules. A small segment of spectra from the mixture spanned a 200 MHz frequency range and took about 10 ms to acquire [21]. An advantage to the FASSST spectral data collection technique was that it has a very rapid spectral data collection rate, and slightly more compact configuration due to the folded cell geometry.

Traditional absorption spectroscopy measurements over the years have used a variety of radiation sources and absorption cell designs to achieve very good sensitivity. The primary detractor for the absorbance based spectroscopy technique is that the detection limits improve with cell length, which can make the overall system size large. Another small detractor to the traditional absorption measurement technique is that a baseline measurement, with an evacuated absorption cell is required. The baseline

accounts for losses inherent to the cell design and generated standing waves which can causes fluctuations in the detector signal at different wavelengths. Baseline variations caused by the standing waves can obscure absorption lines and therefore must be accounted for in order to get a more accurate record of the absorption signature for the gasses to be investigated.

A more compact technique to make spectroscopic measurements on gaseous samples takes advantage of the photoacoustic effect. The PA effect is a direct result of the energy absorbed by the gaseous sample and the generated pressure wave is then detected by a pressure sensitive device. This shorter absorption path-length photoacoustic sensing and spectroscopy technique is discussed in greater detail in the next section.

2.2. Photoacoustic Sensing

The photoacoustic effect was published by Alexander Graham Bell in 1880-1881 when he found that modulated sun light incident on a thin disk generated sound waves [7]. A drawing of one of Bell's many devices to study the PA effect was a 'spectrophone', shown in Figure 3. When the light radiation was modulated, regions of generated sound and silence were observed for given radiation spectra, and "that the sounds are in every case due to those rays of the spectrum that are absorbed by the body" [7].

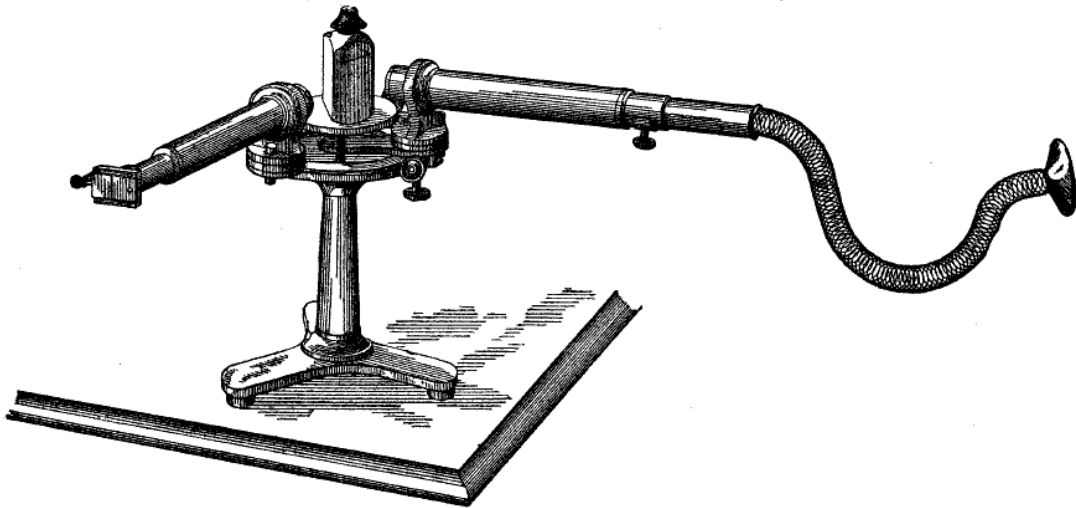


Figure 3. A.G. Bell's 'spectrophone' developed to investigate PA effect on samples of interest [7].

Since the initial discovery, photoacoustic detection methods have found many applications to include trace gas analysis and spectroscopy. The photoacoustic effect when used on solid, liquid, or gas specimens is used to investigate the electromagnetic absorption properties of those materials. Most chemical detection methods take advantage of the fact that different chemicals have their own unique absorption coefficients. For PA gas sensing systems, the pressure operating conditions have

classically been divided into intrinsic, molecular, or viscous regimes [22]. Each pressure regime was named after the dominant damping mechanisms. Chamber pressures higher than 750 mTorr, operate in the pressure spectrum dominated by viscous damping effects. The molecular regime has been defined as the range of 7.5-750 mTorr (1-100 Pa) and the intrinsic regime is defined as pressure environments less than 7.5 mTorr [22]. As mentioned earlier, this background work will primarily focus on photoacoustic analysis of gaseous species.

Before delving into specific examples of recent PA detection systems, figures of merit and other terms traditionally used to evaluate system performance must be discussed. For PA trace chemical detection and spectroscopy systems, figures of merit that are most frequently used are a detection limit, signal-to-noise ratio (SNR), sensitivity, and normalized noise equivalent absorption (NNEA). When PA systems perform trace chemical detection, the chemical species of interest is then diluted with nitrogen, argon, ambient air, or other a non-absorbing buffer gas. The detection limit, describes what minimum detectable concentration of the species of interest the system can achieve. Normally the detection limit is given in parts per million (ppm) or parts per billion (ppb), for a SNR equal to one.

Many parameters affect the detection sensitivity of a PA system. One of the key parameters that affects the sensitivity are the noise in the source and detector measurements. Typical sources of noise in a PA system are electrical, Brownian, and vibrational noise. The SNR for the PA system is defined as

$$\text{SNR} = \frac{PA_{\text{Signal}}}{PA_{\text{Noise}}} \quad (2.6)$$

where PA_{Signal} is the measure of the PA signal strength on an absorption line center and PA_{Noise} is the PA signal strength when the radiation is tuned to an off absorption line frequency. To determine the noise floor of the PA signal, the root-mean-squared (RMS) value of the PA signal is calculated over some sample interval measured away from an absorption line. In some cases, the radiation frequency cannot be shifted away from an absorption line, so the PA_{Noise} is determined when the radiation source is either blocked or turned completely off.

The sensitivity α_{min} , of a system describes what minimum absorption strength the system can detect, and it is defined as

$$\alpha_{min} = \frac{\alpha_{peak}}{SNR} \quad (2.7)$$

where α_{peak} is the strength of the absorption coefficient measured divided by the SNR of the measurement. To achieve the best sensitivity, signals can be averaged over a period of several minutes. Since PA systems can be configured differently, another useful figure of merit is the normalized noise equivalent absorption (NNEA) coefficient and it is expressed as

$$NNEA = \alpha_{min} P_o \sqrt{T} . \quad (2.8)$$

NNEA calculations allow for a better performance comparison between different PA systems by taking into account the system sensitivity, P_o the radiation source power, and T , the PA signal averaging time.

For comparison purposes, the maximum achievable SNR of a traditional THz absorption spectrometer is determined by the noise arising from the mixing of the background thermal fluctuations with the power generated by the radiation source [23].

Equation (2.9) gives the expression for the maximum signal-to-noise in terms of source power P_o , receiver noise temperature T_r , and electrical post detection bandwidth, $\Delta\nu$.

$$\left(\frac{P}{\delta P}\right)_{\max} = \frac{P_o}{\sqrt{kT_r P_o \Delta\nu}} \quad (2.9)$$

For example, $P_o=10$ mW, and $T_r=1500$ K, the maximum signal-to-noise approximately equals 6×10^8 Hz^{-1/2}. Given a 1 cm absorption path-length, the minimum detectable absorption coefficient is $\sim 10^{-9}$ cm⁻¹Hz^{-1/2}. If the incoming power is too high, it can saturate the molecular transition, resulting in a lower sensitivity. To avoid saturation, the radiation source power can be attenuated, and is usually kept below 100 μ W, which corresponds to 10^{-8} cm⁻¹ sensitivity for 1 cm of absorption path-length.

2.3. MEMS Fabrication Technology

MEMS and Nanoelectromechanical systems (NEMS) are a tremendously diverse field, where devices from the sub-nanometer to millimeter scale can be created via numerous means. Techniques to create these miniature devices are accomplished through many fabrication methods; including surface micromachining, bulk micromachining, micromolding, and wafer bonding technologies. MEMS structures can be fabricated using crystalline semiconductors, metals, polycrystalline, amorphous, and polymer materials. Surface micromachining techniques are the processing steps performed above the surface of the substrate, through the deposition and removal of layers [24]. Bulk micromachining includes processing techniques that remove large portions of the substrate to form large pits or holes through a wafer [24].

Crystalline semiconductors, in particular Silicon, have been the focus of bulk micromachining efforts due to its availability, low cost, mature processing techniques, crystal plane structure, and potential for integration with microelectronic circuits [24]. The atoms in crystalline silicon form four covalent bonds in a diamond-cubic structure, which can be represented two face-centered cubic lattices interpenetrating one another by $(\frac{1}{4}, \frac{1}{4}, \frac{1}{4})$ [25]. The atoms in the lattice form crystal planes and the $\{111\}$ family of planes represent the highest packing density. The difference in packing density of the atomic planes can cause differences in the achieved etch rates, which is discussed further in section on 2.3.1 Etching. Wafers can be formed in different crystal plane orientations. When the $\{100\}$ set of planes is parallel to wafer surface, they are referred to as (100) wafers. Likewise, when one of the other major crystal planes are normal to the surface, they are called (110) or (111) wafers [26].

Material properties play an important role in MEMS, Young's modulus E_Y , of a material describes the deformation of a material in the elastic region, which is represented by a form of Hooke's law as

$$E_Y = \frac{\sigma}{\varepsilon} \quad (2.10)$$

where σ is the stress applied in force per area and ε is the resulting strain to the material. Young's modulus for silicon is generally reported to be 130-190 GPa, depending on the crystal orientation of the wafer [25, 27].

To create patterned structures on a wafer substrate, virtually all MEMS and semiconductor integrated circuits are created through the use of photoresist and photolithography systems. Photoresists are photosensitive films that come in two distinct

varieties, positive or negative tone resists. When a region of a positive resist is exposed to an appropriate dosage of ultraviolet (UV) light, the exposed region can then be selectively removed; dissolved away by a developer solution. Negative tone resists function in the opposite manner, areas exposed to UV light will remain on the wafer surface after the develop process. Optical lithography systems, used to expose the samples, can be grouped into contact and non-contact methods. Contact photolithography is performed with a typical mask aligner system where the sample to be patterned can be touching the surface of the metalized photomask. Mask aligner systems can typically specify proximity, soft, low vacuum, high vacuum, or hard contact exposure modes. Resolution of the contact exposure mask aligner systems is limited by several factors, the resist thickness r_t , the separation distance between the mask and the resist surface s , and the wavelength λ of the exposure radiation. Based on those parameters, the diffraction limited minimum transferable feature size, $\min_{feature}$ can be defined as [25]

$$\min_{feature} = \frac{3}{2} \sqrt{\lambda \left(s + \frac{r_t}{2} \right)}. \quad (2.11)$$

The achievable minimum feature size is reduced by minimizing the separation distance, utilizing a thinner resist layer, and a shorter wavelength for the exposure radiation.

Non-contact exposure systems include optical projection steppers, electron and ion beam lithography, and laser direct write systems. Non-contact systems offer an advantage in that contaminants or other debris cannot be transferred to the sample through coming into contact with the mask surface. Smaller feature sizes are achievable when using optical projection techniques; features projected onto the wafer are factor of 5 to 10 times smaller than the features on the mask depending on the system configuration.

For example, a 1 μm feature on the mask results in a 0.1 μm feature size in the resist for a 10 \times reduction system. Stepper projection systems can replicate an area of approximately 1-1.5 cm^2 onto a wafer, the wafer is then moved to the next location and the same pattern can be exposed at the new position. Stepper systems can produce high resolution at relatively high production rates. Single electron and ion beam lithography systems can achieve extremely small resolutions of 3-100 nm, but single beam systems are limited in their production rates [25, 28-30]. Arrays of electron beam writing systems have been developed to increase the production rates [31].

2.3.1. Etching

Etching thin films and bulk micromachining of materials is classically grouped into two categories, liquid and dry etch technologies. The type of etch used to remove the unwanted material depends on material properties, the desired etch profile, mask material used, and etchant selectivity. Etch profiles produced are also grouped into two categories, isotropic and anisotropic, where the etch profile results can vary depending on the etch conditions. A completely isotropic etch, shown in Figure 4 (a), ideally removes the target material uniformly in all directions below the opening in the mask layer. Anisotropic etch, shown in Figure 4 (b) had a preferential etch in the vertical direction and in Figure 4 (c) can be created due to the slower etching of the $\{111\}$ crystal planes, creating a 54.7° angle to the surface.

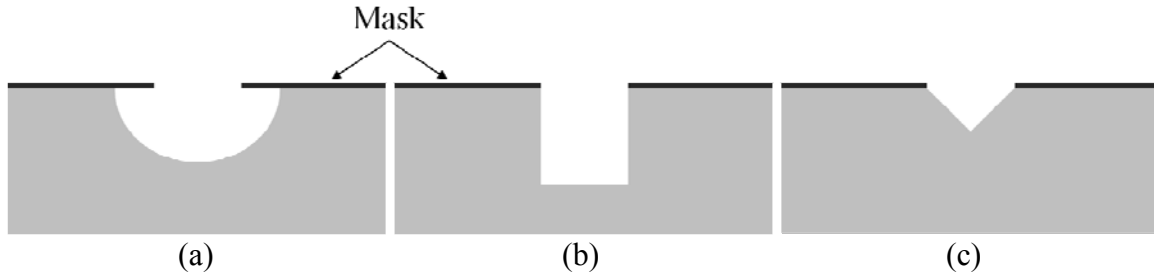


Figure 4. Isotropic etch in (a) removes the desired material uniformly in all directions, while (b) and (c) are examples of anisotropic etches which exhibited preferential etch directions.

2.3.1.1. Wet etching

Wet etching methods can produce isotropic or anisotropic results depending on the material being etched and the etch chemistry. Wet etching is one of the simplest ways to remove thin films and bulk material. The etch rate of the material is function of the temperature at which the etch is performed and the concentration of the etchant used. The enthalpy of a chemical reaction is “the difference between the enthalpies of the products and the enthalpies of the reactants” which represents the energy given off or absorbed in the reaction [32]. Elevated temperatures provide more energy for the reaction, making the etch process occur more rapidly as a function of temperature. The concentration strength of the etchant also affects the etch rate; solutions are typically diluted to a level that creates the desirable uniform, repeatable etch profile. Uniformity of wet etch chemistry can be limited by mass transport. Agitation of the liquid etchant allows fresh reactant and removal of the reaction byproducts below the mask opening to increase the etch uniformity [24].

Mask material selection is typically chosen for a high etch selectivity ratio. Most bulk silicon etch processes use LPCVD Si_3N_4 , SiO_2 , or a few different metallic films for the mask layer. The mask layer needs to be robust and defect free, since pin hole defects

through the mask layer allow unwanted etching. Photoresist masks are not typically used during bulk silicon wet etching because they do not hold up well to etchants with oxidizing agents. Common liquid etchants for silicon are KOH, TMAH, HF/HNO₃/CH₃COOH, and HNO₃/BOE/water solutions [25, 33].

2.3.1.2. Dry Etching

Dry etching techniques are typically performed through vapor or plasma systems. A plasma is considered to be the fourth state of matter, it is a quasi-neutral collection of charged particles that exhibit collective effects [34]. In plasma etch systems, the ions and free radicals in the low pressure gas mixture can be generated through different sources. Reactive ion etch (RIE) systems utilize a parallel plate configuration, biasing the cathode chuck with a radio frequency (RF) power source, typically at 13.56 MHz, to generate the plasma. Another reactor configuration is an inductively coupled plasma (ICP) system, where a liquid cooled helical coil around the outer circumference of the chamber is connected to a RF source to generate the plasma. ICP sources can create a high density, low energy plasma due to the electron confinement generated by the RF source. Microwave electron cyclotron resonance (ECR) systems are another means of creating high density plasmas. ECR systems have reported etch rates 10 times faster than traditional RIE systems while operating at lower chamber pressures [35].

Deep reactive ion etch (DRIE), often referred to as the “Bosch process”, was developed and patented by Robert Bosch GmbH, in 1996 [36]. Since then, many companies have claimed patent rights to modified version of deep silicon etch technologies. DRIE systems utilize RIE and ICP power sources, etch chemistry that

utilizes a mixture of gasses, and pressure changes to achieve an overall anisotropic etch of silicon. There are three general sequences to the DRIE process which are illustrated in Figure 5, where the first step is the etch of the Si material with SF₆ rich plasma. Next a conformal passivation polymer layer is deposited over the entire surface using a C₄F₈ gas. In the next step, the polymer layer on the horizontal surfaces is removed with increased ion energy. The sidewalls maintain the passivation layer and the SF₆ gas is again used to etch a small thickness of the exposed silicon material. The etch profile through each step is controlled through achieving the desired chamber conditions of pressure, gas chemistry, and RF power. The sequence of passivation and etch steps are repeated until the desired etch depth is achieved.

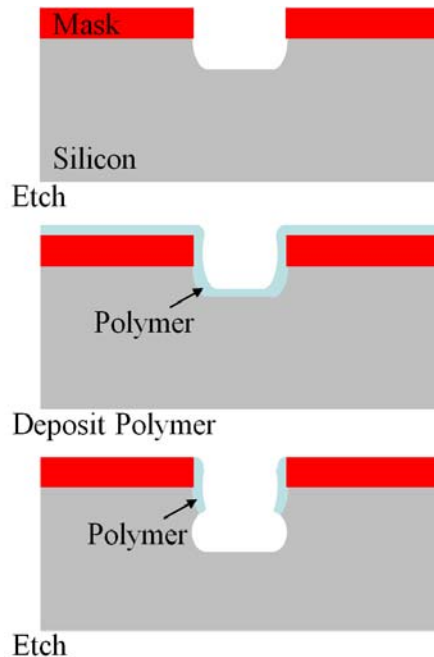


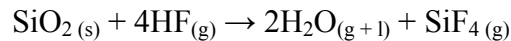
Figure 5. Illustration of DRIE process sequence of etch, deposit polymer, and etch, where sidewall passivation leads to an overall vertical, anisotropic etch profile [37].

Hooda *et al.* performed a systematic evaluation on DRIE performance characteristics; studying the effects of etchant gas flow, pressure, platen power, ICP

power, platen temperature, etch, and passivation cycle times [38]. They provided a detailed analysis on the effect that each etch parameter had on the etch rates and sidewall profile angles. Shorter passivation cycles and higher flow rates of SF₆ lead to negative sloped sidewalls. A phenomenon occurred, as the platen temperature increased, the etch rate decreased due to the lower residence time of the free radicals near the surface [38]. Parasuraman *et al.* created ultra high aspect ratios of 160:1 with 250 nm wide trenches using DRIE and 120:1 ratio with 35 nm wide trenches using a cryogenic DRIE process [39].

Plasma etch system reactions can be complex but more versatile in the achievable etch profiles than wet etch chemistries. Plasma etch rates and profiles are a function of several variables. In a parallel plate RF RIE system, a negative DC bias builds up at the cathode due to the significantly higher electron velocities in the plasma. Chamber pressure plays an important role in the etch process because the pressure affects the mean free path of the ions. Ion impact velocities increase at the cathode due to an increase in DC bias and when the chamber pressure is reduced.

Two examples of vapor etching methods include etching SiO₂ with HF vapor and Si etching using XeF₂. The chemical reaction of SiO₂ with HF vapor is described as



where this thermodynamically favorable reaction at room temperature creates gas phase SiF₄ and H₂O in the gas and liquid phases. If the desorption rate of the H₂O from the surface is slower than the reaction rate, liquid H₂O can accumulate on the surface, inhibiting the etch process.

Etching Si with XeF₂ can be performed through vapor etching. When XeF₂ in solid form is exposed to low pressures in the 4 Torr range, it vaporizes and will react with silicon. Samples are exposed to cycles for XeF₂ vapor followed by low vacuum; etch rates for wafer level processing of 0.2-0.5 μm cycle were reported, while rates were higher for small sample sizes [40]. To demonstrate the silicon vapor etching process, thermal isolation of thermocouples was performed by removing the Si substrate material under the MEMS device.

2.3.2. Deposition of Films

The majority of additive surface micromachining is performed through the deposition of additional films through physical or chemical vapor deposition (CVD) techniques. Physical vapor deposition (PVD) is performed through evaporation, pulsed laser deposition (PLD) [41, 42], sputtering, molecular beam epitaxy (MBE), and atomic layer deposition (ALD). The characteristic attribute of PVD is that the material arrives at the substrate based on the line-of-sight from the deposition source. Evaporation is typically performed under high vacuum conditions, and can utilize different heating methods: resistive, e-beam, RF induction, or lasers [25]. The heated target material vaporizes due to the elevated temperature, high vacuum, and the plume of material is deposited on the substrate suspended over the source. Electron beam evaporation can produce extremely pure films, while resistive and RF heaters can introduce contamination. Due to the highly directional deposition from a small source, evaporated films exhibit poor step coverage. PLD is a physical deposition method performed under high vacuum or with a backfill of a reactive gas. A high energy laser is focused on the

target material; localized heating at the surface of the target creates a vapor plume of the target material that is then deposited on the substrate.

Sputtering offers a larger selection of deposition materials and can create a more conformal coating with better step coverage than evaporation. Sputtering is typically performed with inert gasses such as Ar or Xe, resulting in films composed of the target material. The elevated chamber pressure utilized for sputtering means the particles dislocated from the target have a shorter mean free path, going through multiple collisions causing a random arrival angle before particles reach the substrate. Sputter cathodes for conductive targets can utilize DC plasma, for nonconductive ceramic targets, RF magnetron cathodes must be used. Reactive sputtering can be performed where a gas such as oxygen is added to the chamber during the sputter deposition resulting in oxidized films. Several factors affect the resulting sputtered film quality, chamber pressure, sputter power, bias voltage, substrate temperature, and electrode distance [25].

Deposition through CVD consists of a vapor phase of precursors and reactants that adsorb to a heated substrate surface to form the deposited film. CVD processes require an energy source for the favorable reactions to occur at the wafer surface, and can create uniform conformal step coverage on complex surface geometries. Resultant CVD films are not limited by line-of-sight deposition, but are a function of the reactant gas flow, mean free path, and surface migration of the reactant molecules. Energy sources commonly used are RF-induced plasmas, microwave plasmas, or resistive thermal heaters. Low-pressure CVD (LPCVD) systems can deposit polysilicon films, SiO₂, and phosphosilicate glass (PSG) which are used to create surface micromachines. LPVCD allows a large batch wafer processes with uniform film growth, with low deposition rates,

at relatively high operating temperatures [25]. Thermal CVD processes have also been widely utilized for the growth and synthesis of carbon nanotubes [43-49].

Plasma enhance (PECVD) growth techniques supply the necessary energy to the reactants which allows the substrate to be maintained at a lower temperature. Low temperature processes are good for devices that cannot be exposed to the high temperatures of thermal CVD systems which could affect dopant profiles or metal contact quality. PECVD systems are commonly used to deposit SiO₂ films, which can be used as dielectric insulator or passivation layers on devices [50]. Growth of SiO₂ in PECVD reactors is also affected by RF-power, gas flow rates, gas ratios, and post deposition anneals which affect the film's stress and etch rate [51]. Higher chamber pressure deposition results in films having a tensile stress, as the pressure is lowered, the deposited films tend to become denser producing a compressive stress in the films [25].

To create thick, high aspect ratio MEMS devices, electroplating can be performed through a patterned photoresist. The LIGA process is a specific way to create thick MEMS structures through patterned electroplating which then can be used to transfer the pattern into molds [52]. Named after the three primary steps in the fabrication process, "LIGA is the German acronym for x-ray lithography (x-ray lithographie), electrodeposition (galvanoformung), and molding (abformtechnik)" [25]. The LIGA process uses a several hundred micron thick layer of polymethyl methacrylate (PMMA), which is photosensitive to x-ray radiation, to create the pattern for the devices. One of the key technologies was the use of a synchrotron radiation source to expose the resist, which produced collimated x-rays at wavelengths of ~0.5 nm. The exposure and develop steps took several hours for each step [52].

In the next step, the Ni seed layer exposed below the PMMA pattern is electroplated in a nickel sulfamate bath. Due to non-uniformity of the nickel plating, the Ni surface was then ground flat while still in the PMMA mold. The PMMA mold was then dissolved in a solvent solution, leaving only the thick grown Ni structures. Injection molding was performed in the next phase where a plastic or resin was injected around the Ni structures and cured. Once the Ni and mold are separated, the molds could be used again to re-created the Ni structures almost identical to the original; recreating features less than 0.1 μm , once again through electroplating. Original, 300 μm thick Ni separation nozzle structures were created from the PMMA cast, and additional Ni nozzles were created from the secondary plastic templates. The plastic templates were used 100 times with no visible damage to the mold, leading to the potential that the molds could be used for mass-production [52].

LIGA like processes have been used to create thick structures of micro manipulators with sub micron features [53], accelerometers [54, 55], and have extended the fabrication techniques to alloys and ceramic materials [56]. Processes have also been developed to utilize SU-8 resist to create the mold for electroplating, creating Ni electrostatic micromotors 160 μm thick in a 300 μm deep mold [57]. The primary advantage to LIGA processes is the ability to create devices with large thicknesses, high aspect ratios, with smooth surfaces, out of metal or polymer components through replication techniques [58].

2.3.3. MEMS Electrical Sensor Methods

In MEMS sensor technologies, there are three primary means to detect displacement of a MEMS device through an electrical readout: piezoelectric, piezoresistance, or capacitive. Capacitive sensing methods rely on the relative movement of the MEMS structure to another, typically a fixed surface where the change in the capacitance is determined by the separation gap distance. While the piezoelectric and piezoresistive effects rely on the changes in material stresses induced through the motion of the device.

The piezoelectric effect was first discovered by Pierre and Paul-Jacques Curie in 1880 when they found that when an external force was applied to a single crystal of quartz, the surface of the quartz developed a charge [24]. They also found that an applied voltage across a piezoelectric material would cause the material to deform. Due to the proportional conversion of mechanical stress to electrical charge, many different piezoelectric materials have been used to make sensor devices. The converse effect, used to make actuators where an applied electric potential causes mechanical displacement in a device. The piezoelectric effect is known to occur in many materials such as crystals, ceramics, bones, dentin, ivory, silk, wood, nucleic acid, and many more [25].

Some of the commonly used piezoelectric materials include quartz, barium titanate (BaTiO_3), zinc oxide (Zn_2O_3), lead zirconate titanate ($\text{Pb}[\text{Zr}_x\text{Ti}_{1-x}]\text{O}_3$), lead titanate (PbTiO_3), lithium niobate (LiNbO_3), sodium potassium niobate ($(\text{K,Na})\text{NbO}_3$), and polyvinylidene fluoride (PVDF). Lead zirconate titanate, commonly referred to as PZT is one of the more widespread piezoceramics in use today. Thin piezoelectric films

can be deposited via sputtering [59-66], the sol-gel process [61, 67, 68], metal organic chemical vapor deposition (MOCVD) [69], or pulsed laser deposition (PLD) [41, 42, 70-72]. The sol-gel method requires many iterative steps which consist of spinning on a suspension solution, followed by an anneal step to remove the liquid and other undesired compounds from the film. Multiple layers can be applied in this sequence to make a thicker film. MOCVD uses precursor gases that are flowed into a chamber over a heated substrate. A chemical reaction occurs on the heated surface and a thin film is grown mono-layers at a time while the by-products of the chemical reaction are flowed out of the chamber.

Piezoelectricity in most cases is described by anions (-) and cations (+) bonded in a lattice structure of the material that displace in opposite directions when put under the influence of a mechanical or electrical force. The opposite displacement of the anions and cations causes dipoles and a net potential difference across the material. Piezoelectric materials can have an amorphous or a crystal structure. Most often the crystal forms can be described by seven crystal structure groups, which are triclinic, monoclinic, orthorhombic, tetragonal, trigonal, hexagonal, or cubic. Several ceramic piezoelectric materials have the perovskite structure of type ABX_3 with the oxygen atom at the face center. The oxygen anion bonds the different sized (A & B) cations in the crystal structure. Perovskite materials can take on cubic, orthorhombic, tetragonal, or disordered structures.

Different crystal lattice configurations and orientations are possible for piezoelectric materials, the piezoelectric coefficients are best described in an orthogonal Cartesian coordinate system (x, y, z) and are specified for each direction. This is due to

the difference is atomic spacing and composition along each crystal plane. Frequently a tensor notation is used to describe the piezoelectric coefficients along specific directions in the coordinate system. For example, when two parallel surfaces on a cantilever form a bottom electrode and top electrode with PZT material in between them as illustrated in Figure 6, the transverse piezoelectric constant is given as d_{31} . An induced strain in the x axis causes a charge separation in the perpendicular z axis, generating a potential. The d coefficient is the same for both sensing and actuating applications.

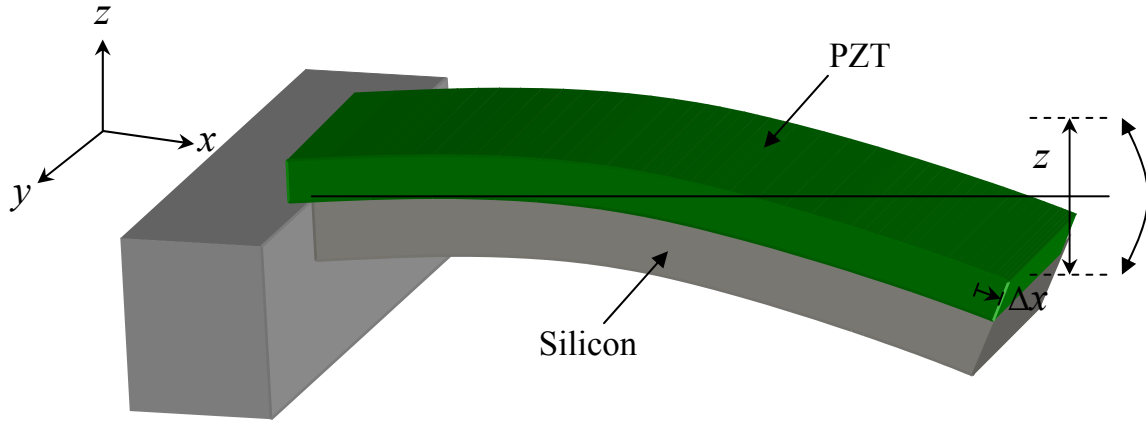


Figure 6. Cantilever tip displacement in the $-z$ direction causes the PZT material to elongate a small amount Δx in the $+x$ direction, generating a net potential difference on the opposite surfaces of the PZT material in the z direction.

Performance characteristics of several different types of cantilever piezoelectric benders was presented by Wang *et al.* [73]. For a uniform pressure p , applied a piezoelectric cantilever bender, the anticipated voltage generated was defined as

$$V = p \frac{d_{31} L^2}{\epsilon_{33} h_p} \frac{AB(B+1)}{1 + 4AB + 6AB^2 + 4AB^3 + A^2 B^4 - k_{31}^2 AB(1 + AB^3)} \quad (2.12)$$

where h_p is the thickness of the piezoelectric layer, ϵ_{33} dielectric coefficient of the piezoelectric material, L is the length of the cantilever, and k_{31} is the transverse

piezoelectric coupling coefficient. The A term in Equation (2.12) is the ratio of the Young's modulus of the cantilever material E_m over the Young's modulus of the piezoelectric material E_p ,

$$A = \frac{E_m}{E_p}. \quad (2.13)$$

The B term is the ratio of the cantilever material thickness h_m over the piezoelectric material layer thickness,

$$B = \frac{h_m}{h_p}. \quad (2.14)$$

To make the cantilever sensor as sensitive as possible, the piezoelectric material should have a high d_{31} / ϵ_{33} ratio and a high k_{31} .

To optimize performance, most ceramic piezoelectric thin films have to go through a poling process to align the randomly oriented dipoles after deposition. To align the dipoles in the material, samples are exposed to a large electric field at an elevated temperature. Required electric field strengths are normally on the order of 10 kV/cm. While the sample is subjected to the electric field, they are heated to just above the Curie point. The Curie point is the temperature at which the dipoles in the material can take on a random orientation. With the electric field still applied, samples are then cooled back down to room temperature. The molecules cannot re-order in the cooled state due to the accumulated mechanical stress and are 'frozen' in the crystal orientation created during the poling process [25].

PZT films sputter deposited on prepared Ti cantilevers, by Kanda *et al.*, in an RF magnetron system utilized a 600 °C substrate temperature and 200 W of RF power on a Zr:Ti target ratio of 53:47 with PbO excess [74]. The gas composition in the sputter chamber was Ar+O₂ (19.5 sccm + 0.5 sccm) and the operating pressure was 0.33 Pa (2.5 mTorr). The deposited PZT films were 3.8 μm thick. Samples were further annealed at 650 °C for one hour to enhance the crystal structure of the film. The hysteresis loop taken using the Sawyer-Tower circuit showed the remnant polarization to be 20 μC/cm² and coercive electric field to be -50 and 70 kV/cm. Before cantilevers were tested, they were poled with -30 V (-79 kV/cm), a field strength greater than coercive field on the top electrode. Then in tip displacement tests, the roughly 1 mm long cantilevers exhibited good linear tip displacement versus applied voltage from 0 to -19 V, reaching 1 μm deflection at -19 V [74].

Direct patterning sol-gel method of PZT films has been performed by Hwang *et al.* where they added photo-reactive ortho-nitrobenzaldehyde compound to the PZT precursor solution. After the combined solution was spin-deposited and dried on a hotplate at 60 °C, the samples were exposed to UV light under a negative tone mask. The then patterned samples were then annealed at 400 °C to remove the carbon ligands from the film; one group in ambient air the other in an O₂ atmosphere. Then a sequential anneal step was then performed at 650 °C for 45 minutes in O₂. Samples from the intermediate anneal in O₂ resulted in films that had better piezoelectric and ferroelectric properties. The surface structure of the PZT films did contain some micro-voids due to the organics burning out of the films in an oxygen rich environment, but a direct-patternable PZT film was successfully demonstrated [75].

The transverse piezoelectric coefficient, d_{31} of PZT films, was studied in detail by Shepard Jr. *et al.* with the use of a wafer flexure apparatus which used air pressure to cause mechanical stress on the films. Two poling tests were conducted and then tested in the apparatus. One test applied different electric field strengths (50-250 kV/cm) for less than 1 min and then took measurements to obtain d_{31} value. This quick poling field application yielded d_{31} coefficients of 5-16 pC/N. The second series of tests poled the samples at a constant 150 kV/cm for durations of 1 min up to ~21 hours and resulted in d_{31} coefficients of ~25-58 pC/N.

The d_{31} coefficient increased rapidly for poling times up to 20 mins; after which time the gain began to taper off. A maximum of -59 pC/N for d_{31} was achieved after poling the sample for ~21 hours, which is very similar value to the value Lee *et al.* reported -58 pC/N when they poled the sample at a lower field and elevated temperature.

A PZT microcantilever, built by Lee *et al.* for a scanning force microscopy application, was an excellent demonstration of the sensing and actuating capabilities of a piezoelectric cantilever. Fabricated cantilevers were relatively small, only 125 μm long and 50 μm wide. The bottom electrode material was Ti/Pt on SiO_2 similar to what many others have used previously [77]. A sol-gel deposited PZT layer was 1.25 μm thick and in a previous work, they baked the spun on PZT film layer at 600 $^\circ\text{C}$ for 20 min [78]. After the 0.25 μm Au/Cr top metal contact material, PZT films were poled with an applied electric field of 30 kV/cm at 110 $^\circ\text{C}$ [78]. The low poling temperature allowed Au to be used as the upper contact metal. At resonance operation, the vibrational amplitude of the 125 μm cantilever was approximately 24 nm/mV. The d_{31} piezoelectric coefficient of the PZT film was calculated to be -58 pC/N [77].

Properties of piezoelectric materials, deposition methods, fabrication techniques, and some basic applications of piezoelectric sensors were discussed. Platinum electrodes have been the favored by most research groups due to high temperatures samples can experience during deposition, anneal, or poling processes. The fabrication methods and techniques used to create piezoelectric devices varied greatly depending on the materials used.

2.4. PA Sensor Systems

Several research groups have tackled the photoacoustic analysis of gasses and other materials using fabricated cantilever, bridges, and membrane microphones. Cantilever designs can be used in a wide range of sensor applications. Cantilever feature dimensions can be on the millimeter scale all the way down to the nanometer scale depending on the application. For sensor applications, there are many ways to extract information based on the cantilever behavior. Changes in the cantilever resonant frequency, tip amplitude displacement, piezoelectric signal, or combinations of these signal behaviors can be used to infer information about changes to the environment.

De Paula *et al.* reported an early optical microphone for PA spectroscopy of solids where they optically measured the deflection of a pellicle placed over a duct outside a PA chamber [79]. The sensor used was a mirrored 25 μm thick Mylar droplet shaped pellicle cantilever which was 13 mm long, 2.5 mm wide at the tip, with a narrower anchor segment of 1.5 mm wide. A 1,000 W Xeon lamp was used at the radiation source which was then filtered using 10 nm band pass slits. PA spectra of a blackened Teflon surface was collected over the approximately 300-900 nm wavelength range at a sweep rate of 50

nm/min, a time constant of 3 s, and a modulation frequency of 17 Hz [79]. Modulation frequency scans of the radiation source showed the maximum PA signal was achieved at 17 Hz due to the long, flexible design of the Mylar pellicle sensor.

Ledermann *et al.* fabricated piezoelectric acoustic sensors out of bridge and cantilever structures for CO₂ detection [80]. Samples were fabricated out of a solid silicon wafer that was backside etched to determine the device layer thicknesses, which ranged from 5-20 μm. One of the 2×2×0.017 mm³ (length × width × thickness) fabricated cantilever designs used a 5 μm gap around the edge of the beam. A pulsed incandescent lamp was used in the test chamber as the radiation source. The photoacoustic results produced 200-1,300 μV for the measured voltage generated by the PZT material on the cantilever design depending on the CO₂ concentration. The cantilever design by far outperformed the bridge sensor by almost a factor of two; with the cantilever producing 170 mV/Pa and the bridge sensor producing 93 mV/Pa.

For the fabrication process, Ledermann *et al.* used a 1 μm thick thermal oxide under the bottom electrode to compensate for stress in the cantilever that built up as the additional layers were added [80]. The TiO₂/Ti and Pt bottom electrode materials along with a {100}-oriented PbTiO₃ seed layer was used to improve the crystal formation of the deposited lead zirconate titanate (PZT) films. The seed layer established the desired orientation and texture for the preferential crystal formation of the PZT. Deposited by chemical solution deposition (sol-gel), a 1 μm thick PZT film was used as the piezoelectric material layer. During the PZT spin on deposition process, samples went through multiple bakes at 350 °C and a final anneal at 650 °C under a flow of oxygen. X-ray diffraction (XRD) analysis was performed on the annealed PZT films which

showed good film crystallinity. After the top Cr/Au contact layer was in place, the PZT film was hot poled at 150 °C for 10 minutes with a 200 kV/cm applied electric field, which is about a 20 V applied potential [80].

Kuusela *et al.* has made recent progress in making a small photoacoustic trace gas detection chamber with cantilever sensor and laser interferometer measurements [5, 6]. In 2009, they tested six different gases in their chamber with a 10 μm thick silicon cantilever that was 3×1.5×0.01 mm³ with 5 μm gap around edge of the cantilever. In the tests, three different LED sources centered at 3.4, 4.2, and 7.0 μm wavelengths were used to excite the gaseous species that had absorption lines within those wavelengths. The lowest detection limit achieved was 6 ppm for propane with a 1 s sample integration time. Experiments were performed at atmospheric pressure (760 Torr) and the gas species were diluted with nitrogen to control the concentration [6]. LED's offered a compact, low cost option for the for PA excitation source. The broad emitted power spectrum of the LED sources, spanned multiple absorption lines of the gasses under investigation. Dips in the spectral output power of the 7 μm wavelength LED was due to the absorption lines of water. Due to the broad spectral output of the LED's, this system design could only perform chemical detection for a limited number of gases.

Work done by McNaghten *et al.*, published in 2012, reported on interferometer based photoacoustic cantilever detection method that used multiplexed tunable diode lasers as the radiation sources for trace gas detection in a PA chamber manufactured by Gasera Ltd [81]. The cylindrical PA absorption cell region was 11.5 cm long and a diameter of 3 mm. Normal data collection times to analyze a gaseous sample was approximately 2.62 s. To achieve the best sensitivity, signals were averaged over several

minutes. Over a 12 hour data collection run, they found that the Michelson interferometer setup showed some instability and fluctuations in signal intensity. They attributed the shifts in signal intensity to acoustic noise in the room and phase shifts in the interferometer setup seen at the photodiode. The Michelson interferometer setup remained stable for up to one hour before realignment was needed. PA measurements were taken on gas samples over a range of pressures from very low up to atmosphere. They found that the optimal photoacoustic signal for their system configuration was at 93.7 Torr (125 mbar) [81].

In an earlier work by Kauppinen *et al.* they performed trace detection of methane (CH₄) in a diluted nitrogen environment [82]. The chamber pressure was set at 465 Torr (0.6 atm) and a sensitive 4×2×0.005 mm³ cantilever with a 30 μm gap around the device was used to detect CH₄ down to an estimated detection limit of 0.2-0.8 ppb. They used an optically chopped black body source and a band pass filter that allowed 2.94-3.85 μm wavelength radiation to excite the methane gas which has an absorption line at 3.33 μm [82].

In another work by Koskinen *et al.* they devised a photoacoustic sensor system, operated at atmospheric pressure, for trace chemical detection of CO₂ in an argon dilution [83]. They used a 30 mW tunable laser diode source centered around 1,572 nm wavelength, which spanned one absorption line of CO₂. They achieved a normalized noise equivalent sensitivity of $1.7 \times 10^{-10} \text{ cm}^{-1} \text{ W/Hz}^{1/2}$, which was 10 times better than previously reported results. The increased sensitivity of the system over previous designs was achieved by reducing the PA chamber diameter from 10 mm down to 3 mm and by using an improved cantilever design. The exact dimensions of the cantilever and gap

used in the work were not discussed. The photoacoustic test chamber provided by Gasera Ltd, used a compact integrated Michelson type interferometer for displacement measurements [83]. PA results with the laser on and in the off state was used to compare the signal to noise ratio in the system. The achieved detection limit with the system was 0.3 ppm and required a 100 s measurement time [83].

Adamson *et al.* used an atomic force microscopy (AFM) cantilever with some post processing, and a position sensitive detector (PSD) to perform photoacoustic spectral detection on a 2% acetylene (C₂H₂) mixture in a helium dilution [84]. The cantilever used was 1 μm thick, 500 μm long, and 100 μm wide, which was positioned over a 1.5 mm diameter hole in the acoustic chamber. PA data was collected at a chamber pressure of 37.5 Torr (50 mbar) with a 14 mW modulated laser diode radiation source. Using a 1 s acquisition time, the NNEA for the system was $1.2 \times 10^{-7} \text{ cm}^{-1} \text{ W Hz}^{-1/2}$. The PA spectra took ~30 min to collect and spanned the 6,520–6,550 cm⁻¹ wavenumber ($\lambda=1,533\text{-}1,525 \text{ nm}$) range [84]. The absorption path-length in the chamber was only 3 mm, the cantilever size and the large hole around the cantilever contributed to the lower sensitivity of the system.

Peltola *et al.* did recent work on gas phase species that utilized an interferometer based analyzer system, which included the cantilever sensor, PA chamber, and software, manufactured by Gasera Ltd. in Turku, Finland [85]. They investigated the detection limits of hydrogen cyanide (HCN) and methane. The cantilever sensor was $5 \times 1.5 \times 0.01 \text{ mm}^3$ and they used a continuous-wave optical parametric oscillator (OPO) centered at ~3 μm wavelength as the radiation source. The detection limit for HCN was calculated to be 190 ppt (parts per trillion) in nitrogen and the NNEA was $1.8 \times 10^{-9} \text{ cm}^{-1} \text{ W Hz}^{-1/2}$ with an

OPO power of 0.5 W, and a 1 s signal averaging time. PA measurements were conducted at 300 Torr (~ 0.4 atm) while the HCN and nitrogen mixture was flowed through the chamber at ~ 1 L/min [85].

Sievilä *et al.* fabricated and tested several different cantilever sensor designs [86, 87]. They recently performed PA spectral measurements on solid sample species where they compared the performance of three different cantilever lengths (3, 4, & 5 mm) and two different cantilever thicknesses (5 & 10 μm). The fabrication process to make their cantilever devices started with an SOI wafer which then through two iterations of SiO_2 depositions and 30 minute anneals at 1,000 $^\circ\text{C}$. The added SiO_2 layer was used to mitigate residual stress issues later in the release process. The deposited oxide layer was then patterned using optical lithography and etched via RIE to define the cantilever shape in the surface oxide layer. The backside of the handle wafer material was removed through DRIE. Then the device layer was etched in a hot TMAH solution to define the cantilever shape. After removing the oxide layers with a buffered hydrofluoric acid solution, the final step in the fabrication process was to coat both sides of the devices with a reflective Ti/Au evaporated coating. The completed cantilever devices had gaps at the corners of the cantilever, as a result of the TMAH etch of the device layer. The cantilevers fabricated by Sievilä *et al.* were then tested in a PA301 photoacoustic accessory from Gasera Ltd [87]. The performance comparison of the different cantilever designs was accomplished by collecting a small PA spectra of polyethene that contained ~ 4 strong absorption lines. The PA signal strength for the thinner 5 μm thick cantilever devices was markedly stronger than the 10 μm thick beams. For all three cases, SNR

improved for the thinner cantilever designs, and had the largest SNR improvement of 25% was seen for the $5 \times 1.2 \times 0.005 \text{ mm}^3$ device [87].

In the mid 1970's, Krupnov *et al.* constructed a sub-millimeter PA spectrometer which utilized a membrane sensor to measure the PA effect on gases [88]. The sensor was a Mylar membrane capacitive microphone, 3 μm thick and 5 cm in diameter. Their cylindrical absorption cell was 13 cm long and 2 cm in diameter. A smaller diameter tube lead away from the center of the absorption tube into the membrane sensor area. The active electrode area on the membrane microphone was 2 cm in diameter and placed a distance of 40 μm above the bottom electrode of the capacitive sensor setup. The radiation source used was a broadband submillimeter backward wave oscillator (BWO) that could produce wavelengths of 1.5-0.28 mm. Due to the wavelengths produced by the radiation source, transmissive Teflon windows were used as end caps on the cylindrical chamber. The radiation source could be used on one absorption cell or on multiple absorption cells aligned end to end. Recorded microphone PA data presented in the work was the first derivative of the absorption profile. They tested chemicals such as HCOOH (formic acid), SO₂ (sulfur dioxide), and N₂O in the chambers to examine the rotational energy transitions of the molecules. Chamber pressures tested ranged from 0.05-10 Torr and were able to achieve sensitivities of $6 \times 10^{-9} \text{ cm}^{-1}$ with a radiation source power of 10 mW [88].

Hippler *et al.* created a sensitive microphone based PA detection system that utilized a cavity-enhanced resonance [89]. The absorption lines of water vapor in an ambient air background were measured at 0.2 bar. Due to the multiple reflections of the laser source in the cavity, they achieved a NNEA of $2.6 \times 10^{-11} \text{ cm}^{-1} \text{ W Hz}^{-1/2}$, and has the

lowest reported PA sensitivity. This cavity-enhanced technique utilizes a continuous wave laser and the PA signal is generated through the resonant acoustic modes of the chamber cavity.

Many factors contribute to the performance of a photoacoustic detection and chemical sensing system. The PA chamber, sensor design, radiation source power, and absorption strength of the chemical under investigation can greatly affect the achievable detection limits and sensitivity of the system. Table 1 presents a performance summary of the recent trace gas phase PA detection and spectroscopy systems. Factors from each previous work highlight the gas investigated, sensor type used, radiation source power, NNEA, and the detection limit of the PA system if available.

Table 1. Recent PA detection system performance limits.

Gas	Sensor	Source Power (mW)	NNEA ($\text{cm}^{-1}\text{W Hz}^{-1/2}$)	Detection Limit (ppb)	Reference
CH ₄	Tuning Fork	2	1.2×10^{-7}		[90]
CH ₃ OH	Tuning Fork	0.04	2.0×10^{-10}	7,000	[91]
N ₂ O	Membrane	10	6.0×10^{-11}		[88]
C ₂ H ₂	Membrane			1.5	[92]
HCl	Microphone	2		3,000	[93]
CH ₄	Microphone	10		500	[93]
H ₂ O	Microphone	3	2.6×10^{-11}		[89]
C ₃ H ₈	Cantilever	0.15		6,000	[6]
CO	Cantilever	2.93	3.4×10^{-9}	249,600	[81]
C ₂ H ₂	Cantilever	1.71	3.6×10^{-9}	1,500	[81]
CH ₄	Cantilever	0.81	1.4×10^{-9}	293,700	[81]
CH ₄	Cantilever			0.8	[82]
CO ₂	Cantilever	30	1.7×10^{-10}	300	[83]
C ₂ H ₂	Cantilever	14	1.2×10^{-7}		[84]
HCN	Cantilever	500	1.8×10^{-9}	0.19	[85]

2.5. Other Sensing Applications

Cantilever sensors have been used for many other applications besides PA chemical detection such as imaging, wind speed, mass detection, or anomaly detection in harsh environments. THz radiation sources also have been used in other sensing applications. Microelectronics and THz radiation technologies have been utilized to demonstrate advanced imaging capabilities. Ariyoshi *et al.* built microelectronics detector arrays using a niobium based superconductor material to detect THz radiation for astronomy and industrial applications [8]. The superconducting detector array was operated in a cryostat, which was cooled to temperatures around 0.3-4.2 K. THz radiation can propagate through some materials that are optically opaque in the visible light spectrum while absorbed or reflected by other materials. Their experiments examined the signal that was transmitted through thin materials that were transparent to the THz radiation wavelengths. Raster scans were performed on a piece of paper with metallic patterns on it and a plastic card that contained integrated circuits. The THz radiation propagated through the plain paper and plastic areas, while the regions that contained metal blocked the radiation from getting to the detector [8].

A MEMS THz detector array was developed by Tao *et al.* that enabled the direct absorption of THz radiation at room temperature using metamaterials [9]. A thin silicon nitride layer was used create the physical structure of the plate suspended by two cantilever arms. On the nitride layer, a split ring resonator (SSR) made of Cr/Au was deposited and used as the energy absorbing structure. At THz resonance frequencies of the SSR, the device experiences ohmic heating due to the induced current. The generated

heat was primarily dissipated through the cantilever legs that were comprised of a bi-layer material of silicon nitride and Cr/Au. The difference in the coefficients of thermal expansion between the bi-layer materials resulted in the deflection of the cantilever arms. The resulting deflection of a single plate was measured optically with a laser and position sensitive photodetector (PSD) [9]. An advantage to this sensing technique was that the experiments were conducted at room temperature and pressure; meaning the detector didn't have to be cryogenically cooled.

Piezoresistive cantilever style sensor designs have been fabricated for wind and airflow detectors. Wang *et al.* utilized rectangular cantilever and paddle designs using a 1 μm thick silicon nitride layer that comprised the cantilever structure and platinum traces as the piezoresistive layer to create airflow sensors [94]. Residual stress in the deposited nitride layer caused the cantilever structures to curve up out of plane. The paddle designs had narrow anchor widths to reduce the spring constant and large tip surface area to capture the pressure from the airflow across the surface of the sensor. Tests were performed at ambient temperature with airflow rates of 0-45 m/s. The three sensor designs tested are shown in Figure 7. The connecting anchor width was held constant at 0.4 mm wide. The other two designs, the top half of the cantilever tip was widened to 1.2 mm (center) and 2 mm wide at the tip (on right) in Figure 7. The widest cantilever tip design had the highest sensitivity during the wind tunnel measurements, producing a change in resistance of 0.0284 $\Omega/(\text{m/s})$.

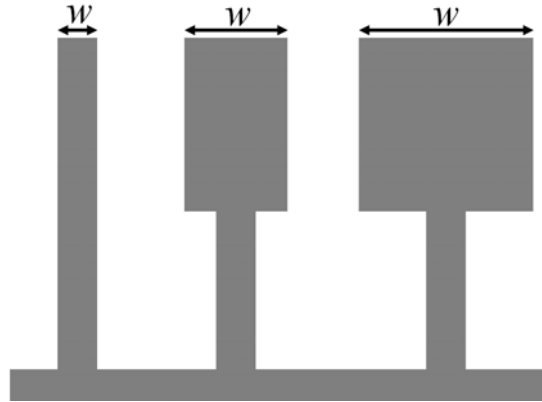


Figure 7. Cantilever and paddle style piezoresistive airflow sensors with different tip widths; from left to right, 0.4, 1.2, and 2 mm wide respectively [94].

Du *et al.* made a two cantilever piezoresistive wind speed sensor that utilized a Wheatstone bridge configuration. The designed cantilevers, etched out of silicon wafer, were $1.53 \times 0.5 \times 0.012 \text{ mm}^3$ with deposited platinum traces covering the anchor half of the beams. The wind tunnel tests were conducted at wind speed velocities from 0-8 m/s. The input of the Wheatstone bridge was set to a constant potential of 5 V and the output voltage of the bridge sensor dropped with increasing velocity from ~ 25 -22 mV. Sensitivity of this configuration was found to be $0.49 \text{ mV}/(\text{m/s})$.

Chen *et al.* created piezoelectric cantilever and spiral-beam-supported diaphragm transducers to generate and sense acoustic pressure [10]. The physical support layer for the cantilever designs was a $0.8 \text{ }\mu\text{m}$ thick layer of low-pressure chemical vapor deposition (LPCVD) silicon nitride. Sputtered ZnO was used as the piezoelectric material and evaporated aluminum was used for the electrode material. The cantilever devices were somewhat warped due to stresses between the layers of the deposited films. Individual $250 \text{ }\mu\text{m}$ long by $250 \text{ }\mu\text{m}$ wide cantilever designs with 5 - $25 \text{ }\mu\text{m}$ gap widths around the cantilever edge were tested to examine the effect on the generated acoustic pressure. Using a calibrated microphone 3 mm away from the sample; the generated

acoustic pressure from the cantilever was measured for the different cantilever gap dimensions. The device was operated at the resonant excitation frequency of 21 kHz and a 75 V peak-to-peak sinusoidal driving voltage. The generated output pressures dropped by about 50% of the maximum value achieved when the larger 25 μm gap was used [10].

Chen *et al.* also evaluated arrays of the devices connected in parallel. An 8×8 array connected 64 transducers in parallel. When four of the 64 transducer arrays were connected in series, the output pressure generated increased to 10 Pa. The sensitivity as a arrayed sensor increased to 2.9 mV/Pa compared to 0.1 mV/Pa for an individual transducer. In the sensor mode, the arrayed configuration increased the sensitivity by about 30 times when the four, 64 transducer parallel device arrays were connected in series [10]. With some modifications to Chen's design, similar arrays of piezoelectric cantilever designs have the potential to be used for PA detection or imaging applications.

Another application of cantilever sensors has been mass detection. Minute changes in mass on the cantilever cause a detectable shift in the resonant frequency. Kim *et al.* used alkane chain molecules with thiol groups as a cross-link receptor to detect prostate specific antigen-antibodies in liquid [96]. They achieved a mass detection resolution of 1.56 ng/cm²/Hz on 1.1 mm long cantilevers. PZT films 20-40 μm thick were made on the silicon substrates via multiple screen-printing and drying steps. Lee *et al.* used smaller PZT cantilevers, 100 μm long, to detect insulin binding protein and poly T-sequence DNA that had masses on the order of 10^{-15} g [97]. The smaller cantilever designs had much higher resonant frequencies of ~ 1.25 MHz and could detect smaller changes in mass based on the shift in resonant frequency of the beam.

Kim *et al.* made improvements to a parallel operation AFM system through the uses of thin film PZT to actuate the cantilever instead of a conventional piezotube scanner configuration [98]. Signals read from a piezoresistor in the cantilever allowed the improved design to have a scan rate of 1 mm/s, much better than the 180 $\mu\text{m/s}$ conventional piezotube scan speed. Cantilever tip displacements of 0.55 μm per applied volt were observed along with non-linear behavior for large tip displacements [98].

Murakami *et al.* in Japan fabricated diaphragm and cantilever PZT microphone sensors for anomaly detection in machines such as turbines or engines in the presence of large background noise [99]. Through the sol-gel process, a 1 μm PZT film required 12 layers of spin coated film and was annealed at 600 $^{\circ}\text{C}$ for ten minutes in an oxygen environment every three layers. Studying the generated output voltage signals from the cantilevers; typical transient signals lasted for $\sim 2\text{-}3$ ms in the ambient pressure environment from a sound pulse caused from electrical discharge. A sample cantilever with rough dimensions of 1 mm long by 0.5 mm wide had a sensitivity of 7.1 mV/Pa at the resonant frequency of 21.4 kHz [99].

Surface adhesion can play a large role in the frequency shift of a resonating cantilever. Sharma *et al.* used piezoelectric-excited millimeter-sized cantilever sensors to investigate adhesion effects at the second-order excitation mode, which was operated at resonant frequencies of 57-78 KHz [100]. When a dry 300 μg quartz sample was placed on the end of an oscillating cantilever, surprisingly no appreciable frequency shift was observed. When 400 μg of water was added to the tip of the cantilever, the additional mass caused a 1,495 Hz reduction in the oscillation frequency. When a quartz sample with a residual water film was placed on the cantilever the additional mass caused an

instant shift in the resonant frequency lowering it 1,527 Hz. In comparison, when ethanol was used instead of water on the quartz sample as the interfacial layer, the observed shift in resonant frequency was not as great, roughly 40% less than that of water. Thusly, adhesion to the cantilever did play a significant role in the observed frequency shift and water, the stronger adhesive layer, caused a larger frequency decrease for the same applied mass [100].

2.6. Summary

Traditional spectroscopy measurements using the long path-length absorption techniques have been shown to be very accurate and fast at acquiring molecular spectra due to improvements in broadband radiation sources and detector sensitivities [20, 21, 101]. In order to significantly reduce the overall dimensions of a traditional spectroscopy system, another method to measure the absorption must be used. Photoacoustic detection of trace amounts of gaseous compounds in nitrogen or argon dilution have shown to be both a compact and sensitive chemical detection method [6, 80-85, 102, 103]. The increased sensitivity of PA detection is largely attributed to the improved MEMS cantilever fabrication and PA chamber designs.

Several of the PA detection systems discussed used broad-spectrum radiation sources that spanned many absorption lines of the chemical species under investigation. PA molecular spectroscopy on gas phase samples requires a controllable, extremely narrow frequency line-width radiation source, capable of covering a wide spectral range. Several groups have performed PA spectral analysis using tunable lasers, primarily at short wavelengths in the infrared.

Cantilever sensor designs have been used for a wide range of applications. Many of the applications utilize the unique properties of the cantilever behavior to interpret changes to environmental conditions such as pressure, mass, or temperature. The environmental changes can cause the cantilever motion to shift in resonant frequency, amplitude of deflection, or both. Techniques employed to measure the induced cantilevers deflections have been predominantly optical, piezoelectric, or piezoresistive; while the optical measurement techniques have shown to be more sensitive due to differences in cantilever designs [80, 83].

In the next chapter, the photoacoustic chamber design and anticipated pressure conditions are discussed. The MEMS cantilever sensor designs are analyzed and finite element model simulations are developed to evaluate the cantilever performance in the PA chamber.

III. Photoacoustic and Cantilever Modeling

The performance of the THz photoacoustic molecular sensing and spectroscopy system developed in this work relies on the configuration of the PA chamber and sensitive MEMS cantilever designs. Pressure generated in the small absorption cell depends upon the dimensions of the cell, absorption strength of the gas, and radiation power. In this next section, the generated PA chamber pressure will be analyzed. The anticipated pressure is then used to investigate different cantilever designs in order to make them as sensitive as possible. Estimations for the anticipated cantilever deflections and resonant frequency are calculated analytically and through finite element modeling to predict the sensor performance.

3.1. Chamber Photoacoustics

The THz photoacoustic chamber design and resulting analyzer performance is based on several factors. In order to develop an adequate model to predict cantilever behavior in the photoacoustic chamber, the range of anticipated pressures must be evaluated. Expected pressures generated in a PA cell are anticipated through the use of the ideal gas law and kinetic theory of gasses. The absorption cell portion of the PA chamber shown in Figure 8 is assumed to have a cylindrical shape with characteristic length, l and radius, r . For this analysis, it is assumed that the THz radiation energy from the source is uniformly distributed and that the radius of the beam closely matches that of the absorption cell radius. The radiation source power inserted into the chamber is defined as P_o , while P is the amount of power that exits the chamber.

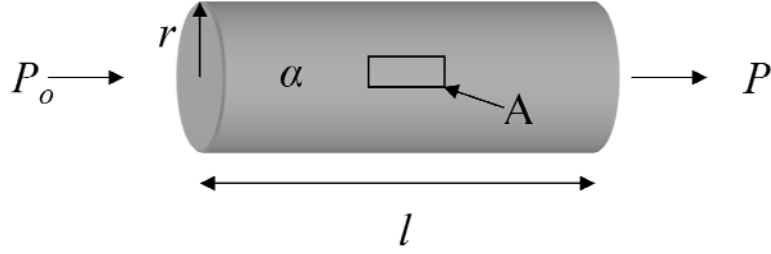


Figure 8. Notional diagram of the chemical absorption cell illustrates the characteristic dimensions and other parameters used for the chamber design.

Over long distances, molecular absorption of radiation is best described by the Beer-Lambert law, described in Equation (2.1). For cases when the concentration of the analyte is low and the chamber length is short, the absorbance of a species can be described as a linear function of the absorption coefficient α , multiplied by the cell length, and the absorbed power ΔP follows the relationship

$$\Delta P = P_o - P = P_o - P_o \cdot e^{-\alpha l} = P_o (1 - e^{-\alpha l}) \approx P_o \alpha l. \quad (3.1)$$

Equation (3.1) therefore describes the effective power absorbed by the gas as a function of the radiation source power, absorption coefficient, and the short absorption cell length. When the THz radiation source is amplitude modulated on and off, the energy absorbed, ΔE by the gas during each pulse is described as

$$\Delta E = \frac{\Delta P}{2f_m} \quad (3.2)$$

where ΔP is the power absorbed by the gas and f_m is the radiation source amplitude modulation frequency. Therefore, $1/(2f_m)$ is the duration of time the radiation source is on per period, assuming a 50% duty cycle. The amount of energy absorbed per pulse can then be described by the kinetic theory of gasses as

$$\Delta E = \frac{3}{2} N k_B \Delta T \quad (3.3)$$

where N is the number of molecules in the enclosed system, k_b is Boltzmann's constant, and ΔT is the induced temperature change. The ideal gas law is then used to determine the change in pressure, Δp generated by a temperature increase of ΔT , in the fixed volume V of the cylindrical absorption cell. This change in pressure is described as

$$\Delta p = \frac{N}{V} k_b \Delta T . \quad (3.4)$$

Substituting Equations (3.1), (3.2), and (3.3) into Equation (3.4) yields an expression for the anticipated change in pressure, Δp as function of several variables.

$$\Delta p = \frac{P_o p_x \alpha l}{3V f_m} = \frac{P_o p_x \alpha l}{3(\pi r^2 l) f_m} = \frac{P_o \alpha}{3\pi r^2 f_m} \quad (3.5)$$

Equation (3.5) describes the anticipated change in chamber pressure per cycle as a multivariable function of radiation source power, p_x the partial pressure factor of the gas, absorption coefficient, chamber radius, and the radiation modulation frequency. Here, the partial pressure factor describes the volumetric fractional abundance of the species and can be set equal to one since no backfill of gas is used to dilute the gas species under investigation. Although, for long spectral data collections, the partial pressure factor will play a role in the PA response based on the chamber leak rate. For the derived change in pressure shown in Equation (3.5), there is no dependence on the length of the absorption cell. Therefore, this PA spectroscopy technique becomes “virtually” independent of absorption path-length, and allows the cell dimensions to be very small compared to traditional absorption molecular spectroscopy techniques.

Absorption line strengths for different chemicals are available through several online databases. The NASA Jet Propulsion Laboratory (JPL) is one database that

provides detailed molecular spectroscopy information on many compounds [104]. Shown in Figure 9 is the complete listing of absorption line strengths for methyl cyanide (CH_3CN) from the JPL catalog. This stem plot shows all 1,728 listed absorption lines for CH_3CN in the JPL catalog, which provides the distinct absorption “finger print” for the molecule. Molecular absorption spectra are also available from another database called HITRAN, which stands for High Resolution Transmission [105].

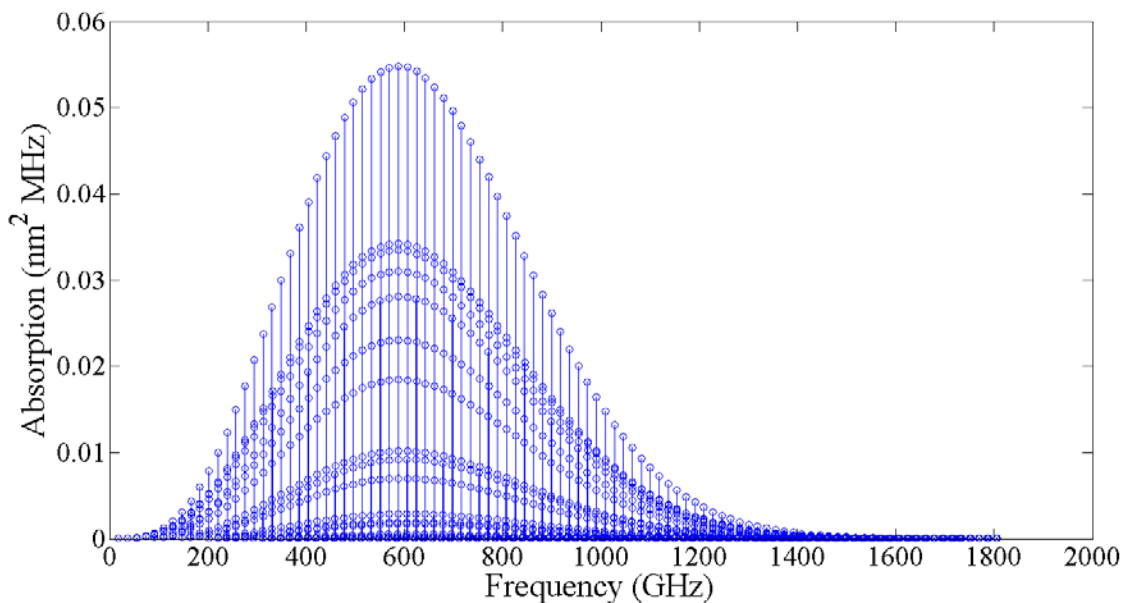


Figure 9. Absorption spectra plot of CH_3CN from JPL database.

Figure 9 contains a lot of information with closely spaced absorption lines and no broadening conditions applied. Shown in Figure 10 is a small segment of simulated absorption coefficient α (m^{-1}) spectra for methyl cyanide, at 18 mTorr with Doppler and pressure broadening conditions.

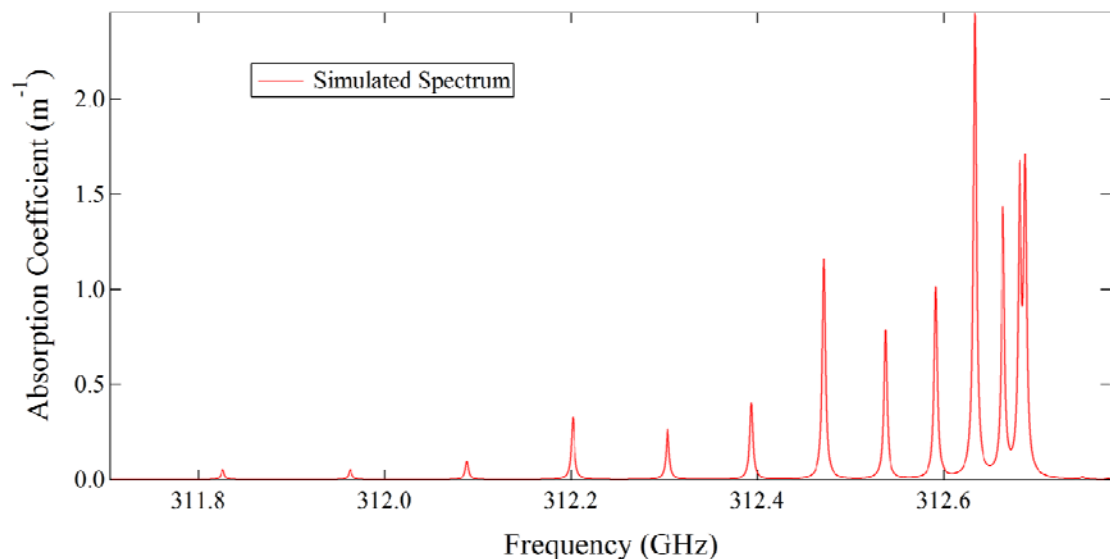


Figure 10. Small portion of simulated absorption coefficient spectra of methyl cyanide at 18 mTorr after appropriate pressure broadening conditions are applied.

Based on these design space parameters, the anticipated changes in pressures could span a very large range depending on the absorption coefficient of the gas and the radiation source power. Changes in pressure could be in the tens of Pascal down to ~ 0 Pa depending on the gas composition, radiation frequency, radiation source power, and chamber pressure. Under ideal conditions, based on Equation (3.5), the change in chamber pressure per cycle is expected to be approximately 0.77 mPa (5.79 μ Torr) when a radiation source power of 0.1 mW, $\alpha = 1 \text{ m}^{-1}$, $r = 5 \text{ mm}$, and $f_m = 550 \text{ Hz}$ are used. If the chamber radius were reduced by half, down to $r = 2.5 \text{ mm}$, and all other contributing factors remained constant, the chamber in pressure per cycle would be 3.09 mPa (23.15 μ Torr), an increase of four times the larger chamber design. With the anticipated photoacoustic conditions in mind, multiple cantilever designs were considered analytically and modeled in the CoventorWare[®] software.

3.2. Cantilever Model

To develop the model of the cantilever sensor, the material attributes of a plain silicon cantilever were used. Of particular interest are the spring constant k and the natural resonant frequency f_0 of the cantilever beam. The physical dimensions of a rectangular cantilever of length L , width w , and thickness h , shown in Figure 11, can be designed to optimally respond to the change in PA pressure generated in the chamber. The cantilever tip displacement and behavior is analyzed under static and dynamic load conditions.

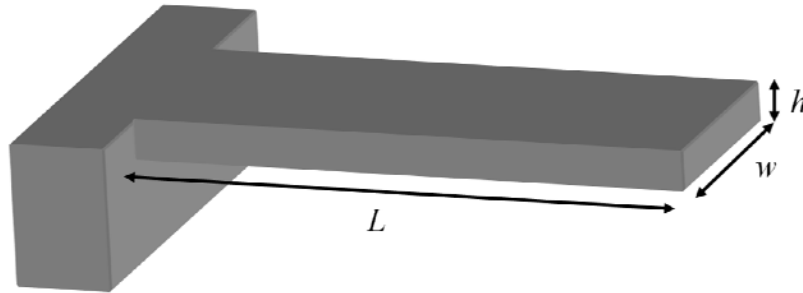


Figure 11. Rectangular, single fixed end cantilever beam design of length L , width w , and thickness h .

3.2.1. Cantilever Under Static Load Conditions

The spring constant of the cantilever determines how far the tip will deflect for an applied load. An equation for the spring constant k of a single fixed beam cantilever under a uniform applied load is written as

$$k = \frac{2}{3} E_Y \cdot w \left(\frac{h}{L} \right)^3 \quad (3.6)$$

where E_Y is Young's modulus of silicon. This equation generates two comments on potential beam designs. The stiffness of the cantilever increases linearly as a function of

width and is a cubic function of the thickness over length ratio. Through modification of the physical dimensions of the cantilever, the spring constant or stiffness of the cantilever design can easily be modified.

Hooke's law describes cantilever deflection when a small static force, F is applied to a cantilever with spring constant k . The resultant deflection distance, y away from steady state as defined by Hooke's law is

$$y = \frac{F}{k}. \quad (3.7)$$

Represented by a one-dimensional cantilever shape function, cantilever deflection caused by a uniformly distributed static pressure load p_L can be written as

$$y(x) = \frac{x^2(6L^2 - 4Lx + x^2)p_L}{24E_y I}. \quad (3.8)$$

For the uniform pressure load $p_L = (\text{force} / \text{length})$ applied in the y direction, the vertical displacement in the y direction for any point x along the length of the beam, and I is the bending moment of inertia for a rectangular beam, given as

$$I = \frac{wh^3}{12}. \quad (3.9)$$

Substituting Equation (3.9) into Equation (3.8), the total tip deflection, $y(L)$ at the free end of the cantilever due to p_L can then be written as

$$y(L) = \frac{3L^4 p}{24E_y I} = \frac{3L^4 p_L}{2E_y wh^3}. \quad (3.10)$$

Notice that the tip displacement function $y(L)$ is now also linear function of the cantilever width. The dependence of the tip displacement on cantilever width can be removed from

the equation by considering the pressure load is changed to a two dimensional load pressure $p_{wL} = (\text{force} / (\text{width} \times \text{length}))$, then

$$y(L) = \frac{3L^4 p_{wL}}{2E_Y h^3}. \quad (3.11)$$

In Equation (3.11), the cantilever tip displacement is a linear function of the uniform two dimensional applied pressure. In a photoacoustic test chamber, the changes in pressure caused by the radiation can be extremely small, so a lower spring constant would allow for greater deflection of the cantilever.

To compare potential cantilever designs, Equation (3.8) can be rewritten as

$$y(x) = \frac{x^2(6L^2 - 4Lx + x^2)p_{wL}}{2E_Y h^3} \quad (3.12)$$

and the resultant cantilever curvature and displacements were investigated for a small pressure load of 10 mPa. For the calculations, the Young's modulus for a (100) silicon device layer was used such that $E_Y = 130$ GPa. Figure 12 shows the results for three initial cantilever designs considered which had lengths of 3, 5, and 7 mm, and fixed widths and device layer thicknesses of 2 mm and 10 μm respectively. As the length of the cantilever is increased, the effective spring constant decreases, therefore resulting in a corresponding increase in cantilever deflection. Under the 10 mPa load, Equation (3.11) predicts the tip displacements to be 9, 72 and 277 nm for the corresponding 3, 5, and 7 mm long cantilever designs. Moving away from the 3 mm long device to the 5 mm long device design, the anticipated deflection increased by a factor of 8 times. Once again, moving from the 5 mm to the 7 mm long design, the anticipated deflection increased by a factor of 3.8 times. The rate of increase in the tip deflection amplitude

gained diminishes as the cantilever designs become longer. The length over thickness ratios of the three designs listed above are 300, 500, and 700 respectively. It is therefore clear that devices with a higher length over thickness ratio displace more and would be more sensitive to small pressure loads.

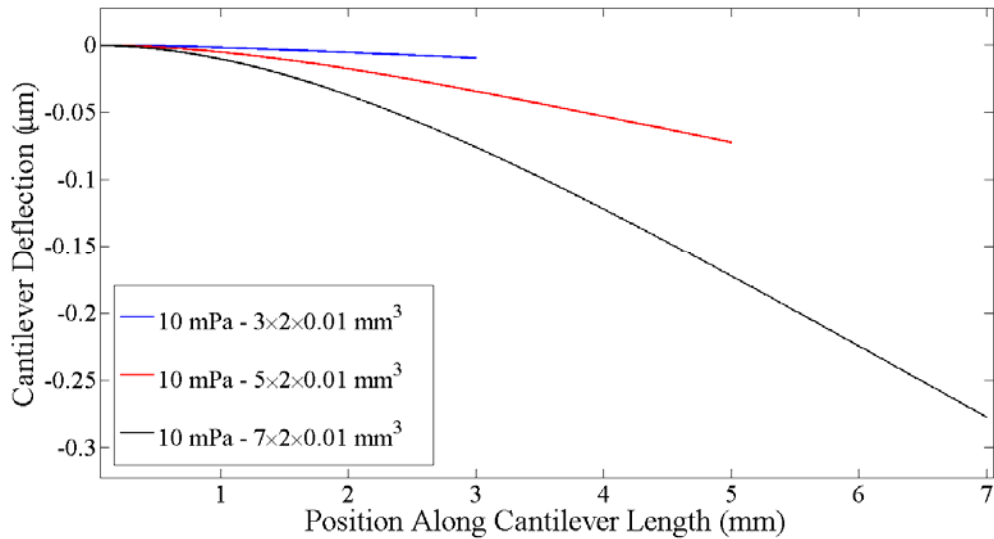


Figure 12. Deflections for three different cantilever designs under a 10 mPa uniform static pressure load.

3.2.2. Cantilever Dynamic Behavior

The other physical characteristic of interest is the natural resonant frequency, f_0 of the cantilever. The natural resonance motion of a spring and mass oscillator system shown in Figure 13 is described by Newton's 2nd Law of motion and Hooke's Law.

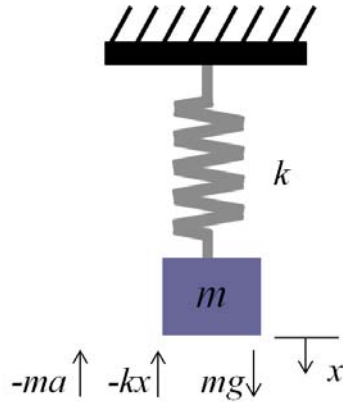


Figure 13. Mass and spring oscillator motion described through Hooke's Law and Newton's second law of motion.

Neglecting damping effects, the movement of the object is determined by the spring force kx from the spring and the weight of the object mg , where g is the acceleration due to gravity, and ma is the mass acceleration force, x is the relative displacement distance, and the acceleration $a = d^2x / dt^2$. From Newton's 2nd Law of motion, the resulting differential equation is

$$mg - kx = m \frac{d^2x}{dt^2} . \quad (3.13)$$

A solution to the differential equation has the form

$$x = A \sin(\omega t - \phi) + B . \quad (3.14)$$

Solving for the A & B coefficients results in

$$B = \frac{mg}{k} \quad (3.15)$$

$$A = \frac{g}{\omega^2 \sin(\omega t - \phi)}$$

and the solution to Equation (3.13) formulates the natural resonant frequency of motion to the spring constant and mass as

$$\omega_o = \sqrt{\frac{k}{m}} \quad \text{or} \quad f_o = \frac{1}{2\pi} \sqrt{\frac{k}{m}}. \quad (3.16)$$

For cantilever motion, an effective mass m_{eff} , is used to represent the mass of the cantilever and k is the spring constant shown earlier in Equation (3.5). This natural resonant frequency is of interest because the PA system could be operated in three distinct frequency modes; below resonance, on resonance, or above the resonant frequency of the cantilever. Operating the system at the first resonant frequency mode would cause greatest displacement of the cantilever tip for small applied PA pressures compared to operating at frequencies off resonance.

The effective mass of the cantilever can be found using Rayleigh's method through the conservation of energy. In most cases, the Rayleigh-Ritz solution provides an approximation where the stiffness is generally over predicted [106]. Applying Rayleigh's conservation of energy method, it can be shown that the effective mass of the cantilever is

$$m_{eff} = \frac{104}{405} \rho whL \approx \frac{1}{4} \rho whL \quad (3.17)$$

where ρ is the density of the material.

Under an external dynamic load condition, cantilever tip displacement again becomes a function described through a differential equation, which includes damping effects. This motion in an under damped system is again described by Newton's 2nd Law of motion, where all the internal and external forces can be setup in a detailed balance equation. Two cases of motion are of particular interest, driven oscillation and damped harmonic oscillation. Figure 14 shows the forces acting on an equivalent mass-spring-

damper configuration, which represents the cantilever tip displacement under an external driving force.

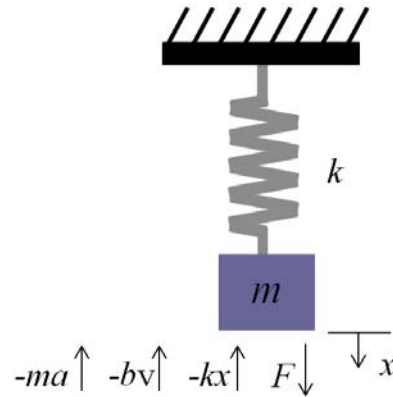


Figure 14. Equivalent mass-spring-damper model for cantilever displacement which describes the forces, mass, spring, and damping conditions for the system.

For driven oscillation, as the external force F acts on the system, movement of the object is opposed by the spring force kx and the damping force bv . Where m used here is the effective mass, x is the relative displacement distance, $v = dx/dt$ the velocity, $a = d^2x/dt^2$ the acceleration, and b is the damping coefficient. Using Newton's 2nd Law of motion, the resulting differential equation is

$$m \frac{d^2x}{dt^2} + b \frac{dx}{dt} + kx = F \cos(\omega t + \varphi) \quad (3.18)$$

where F the amplitude of the driving force, ω is the angular frequency of excitation, and φ is the phase term. The damping term b , greatly affects the response of the system. There are three regions of possible damping conditions, over damped, critically damped, or under damped. Critical damping is the case where the motion of the spring mass system returns to a steady state condition as quickly as possible, without any oscillation. The system is critically damped when the damping coefficient $b = b_o$, where b_o is the critical damping defined as

$$b_o = 2\sqrt{mk} . \quad (3.19)$$

When $b > b_o$, the system is over damped and the system returns to equilibrium more slowly, again with no oscillation. While the third case is under damped, when $b < b_o$, the system will oscillate before returning to equilibrium. The smaller the damping coefficient in the under damped regime, the longer the system will oscillate, slowly dissipating the stored energy in the spring.

The tip displacement position $x(t)$ for a periodic applied force, reaches a steady state solution after a sufficient amount of time and is described by

$$x(t) = A\cos(\omega t + \varphi) \quad (3.20)$$

where A is the amplitude of the displacement, which is also function of the angular modulation frequency ω , the angular resonant frequency ω_o of the cantilever, the time constant τ , and of the applied force, F . The amplitude of the response is a function of ω and is described as

$$A(\omega) = \frac{F}{m\sqrt{(\omega_o^2 - \omega^2)^2 + 4\left(\frac{1}{\tau}\right)^2 \omega^2}} . \quad (3.21)$$

The time constant τ , is defined as

$$\tau = \frac{2m}{b} , \quad (3.22)$$

represents how quickly the system responds to external stimuli. If the applied force and time constant of the system are held constant, and a modulation frequency scan is performed, the amplitude of deflection reaches a maximum value when the modulation frequency is equal to the resonant frequency of the cantilever, $\omega = \omega_o$. Implementing

Equation (3.21) using a $5 \times 2 \times 0.01 \text{ mm}^3$ cantilever design, a 0.2 mPa harmonic excitation pressure and a damping condition of $5.76 \times 10^{-7} \text{ kg/s}$ resulted in the frequency response curve shown in Figure 15. The damping condition used in Figure 15 was based on an under damped system where $5.76 \times 10^{-7} \text{ kg/s}$ was 0.1% of the calculated critical damping condition calculated from Equation (3.19).

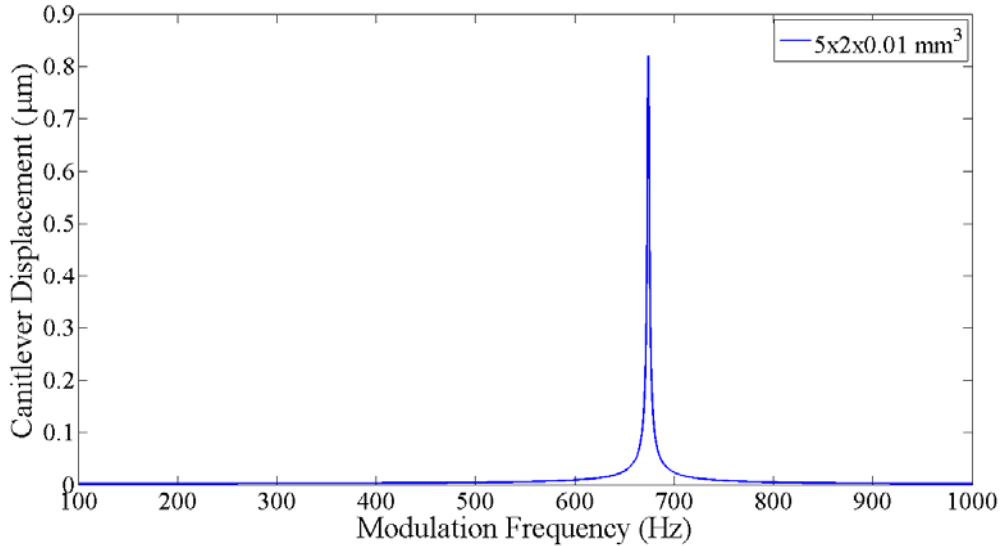


Figure 15. Amplitude of the frequency response curve for $5 \times 2 \times 0.01 \text{ mm}^3$ cantilever design with a 0.2 mPa harmonic excitation and a damping condition of $5.76 \times 10^{-7} \text{ kg/s}$.

When the system is modulated at the resonant frequency ($\omega = \omega_o$), Equation (3.21) can be simplified to

$$A(\omega) \cong \frac{F\tau}{2m\omega} \cong \frac{F}{b\omega}. \quad (3.23)$$

When operated at the resonant frequency of the cantilever, examination of Equation (3.23) reveals that greatest amplitude of deflection, for the same applied force, is achieved when the damping conditions in the system are minimized and when a cantilever with a lower natural resonant frequency is used.

Now the cantilever dynamic response to a periodic external applied force is discussed. When the cantilever is at rest, with initial position and initial velocity equal to zero; an external periodic force is applied to the system and the resulting tip displacement $x(t)$ is

$$x(t) = A \left(1 - e^{-\frac{t}{\tau}} \right) \sin(\omega t + \phi_h). \quad (3.24)$$

Applying Equations (3.22), (3.23), and (3.24) to the $5 \times 2 \times 0.01 \text{ mm}^3$ cantilever design; a 0.2 mPa harmonic excitation and a damping condition of $5.76 \times 10^{-7} \text{ kg/s}$ produced the tip displacement plots in Figure 16. In Figure 16 (a) at time $t=0$, the 0.2 mPa pressure load is applied at sinusoidal frequency of $\omega = \omega_o$; due to the high frequency, only the envelope of the amplitude tip displacement is visible and grows according to the time constant in Equation (3.22). Under the above conditions, the tip displacement clearly reaches a periodic steady state amplitude deflection of $\sim 0.82 \text{ }\mu\text{m}$ in 2 s. Shown in Figure 16 (b) is a zoomed in view of the first 42 ms of the cantilever excitation.

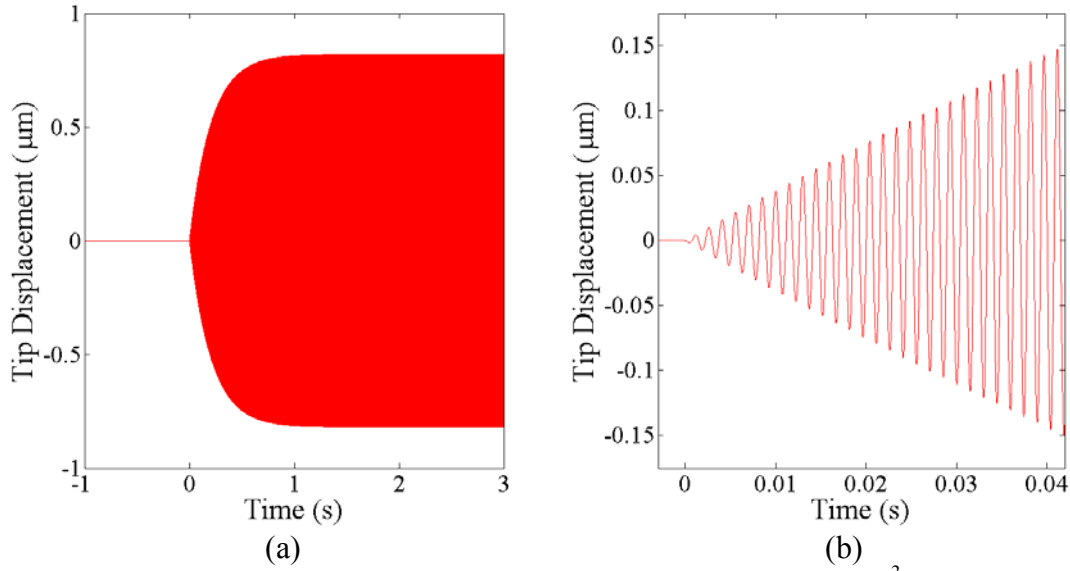


Figure 16. Envelope of the tip displacement in (a) of a $5 \times 2 \times 0.01 \text{ mm}^3$ cantilever design when a harmonic pressure of 0.2 mPa was initiated at time $t=0$ under damping condition of $b = 5.76 \times 10^{-7} \text{ kg/s}$. A zoomed in view of the tip displacement due to the excitation load is shown in (b).

The second case of interest was damped harmonic oscillation with the external excitation force removed. The cantilever tip position given an initial tip displacement amplitude decays as

$$x(t) = A e^{-\frac{t}{\tau}} \sin(\omega' t + \varphi_h) \quad (3.25)$$

where A is the initial amplitude of oscillation at $t=0$, τ is the same time constant used in Equation (3.21), ω' is the angular frequency of oscillation due to the damping conditions, and φ_h is again a phase shift term of the sine wave. For example, the same $5 \times 2 \times 0.01 \text{ mm}^3$ cantilever given an initial amplitude displacement of 0.82 μm and the same damping conditions used in the above example, the cantilever displacement dampens out as shown in Figure 17 (a) and a zoomed in time scale view of the signal in Figure 17 (b).

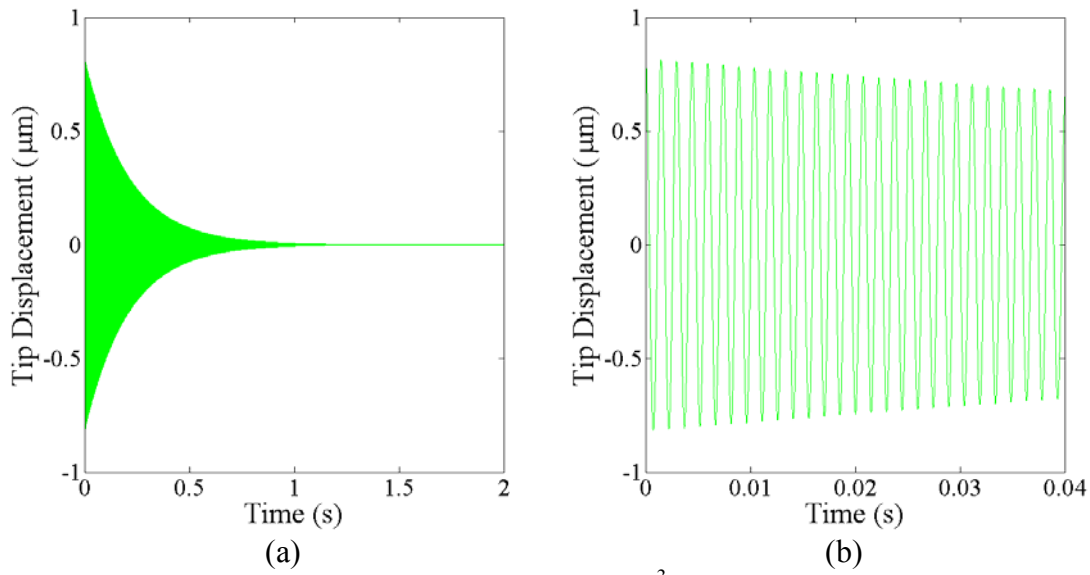


Figure 17. Tip displacement in (a) of $5 \times 2 \times 0.01 \text{ mm}^3$ cantilever design after PA pressure of 0.2 mPa was removed at time $t=0$ under damping condition of $b = 5.76 \times 10^{-7} \text{ kg/s}$ and a zoomed in view in (b) of the tip displacement decay due to damping.

The above equations described the anticipated cantilever behavior in the PA system. The overall cantilever tip displacement is a complex function of the applied pressure loads, damping conditions, and resonant frequency of the cantilever design. It could take several seconds for the cantilever to reach full amplitude tip deflection. A longer required excitation time means it will take longer to collect PA spectral data.

3.3. Finite Element Modeling of Cantilever Designs

Finite element method (FEM) or finite element analysis (FEA) involves numerical problem solving methods to find approximate solutions to a field problem [106]. Field problems, described by differential equations, seek to determine "the spatial distribution of one or more dependent variables" [106]. FEM takes a physical structure or region and divides it into finite elements; the small conjoined element pieces created represent the entire physical structure. The locations where the elements meet is called a node. The

arrangement of the elements in the structure is defined as the mesh. The finite element mesh created in the structure "is represented by a system of algebraic equations to be solved for unknowns at the nodes" [106]. Approximate solutions for the structure are performed element by element in a piecewise fashion, and the accuracy of the solution can be increased by utilizing a smaller mesh size; increasing the number of elements in the structure. The maximum number of mesh elements the software package can handle limits the smallest achievable mesh dimension. This mathematical model of the structure is created through the formation of the discrete elements which form a piecewise continuous representation of the original structure.

FEM can be used on a variety of problems to evaluate material stress, displacement, heat transfer, electromagnetic fields, and fluids. FEM simulations are used to model the behavior of a particular problem, which is constrained by material properties, boundary conditions, and the applied external stimuli.

Extensive modeling of potential cantilever sensor designs was performed with the CoventorWare[®] software package. Simulations of cantilever tip displacements under static and harmonic applied load conditions were evaluated. In addition, design aspects of resonant frequency mode shapes and material stress levels were investigated. Drawing layouts of the proposed cantilever designs, made in the Tanner L-Edit software, were imported into CoventorWare[®] for simulations. Two-dimensional (2-D) mask layouts drawn in L-Edit, used in combination with a fabrication process file in CoventorWare[®] created three-dimensional (3-D) solid models of the devices. Layer thicknesses of the silicon device, buried oxide, and metal layers were defined as part of the fabrication process file. Each mask layer used corresponded to the fabrication steps of either

depositing or etching away the desired material layers. From the constructed 3-D solid model, the devices then underwent a meshing step whereby the design was converted into a collection of smaller finite element segments. A $3 \times 1 \times 0.01 \text{ mm}^3$ cantilever mesh model, shown in Figure 18, was created using $25 \times 25 \text{ }\mu\text{m}^2$ square elements in the X-Y plane and extruded $10 \text{ }\mu\text{m}$ in the Z-direction, the same thickness as the cantilever device.

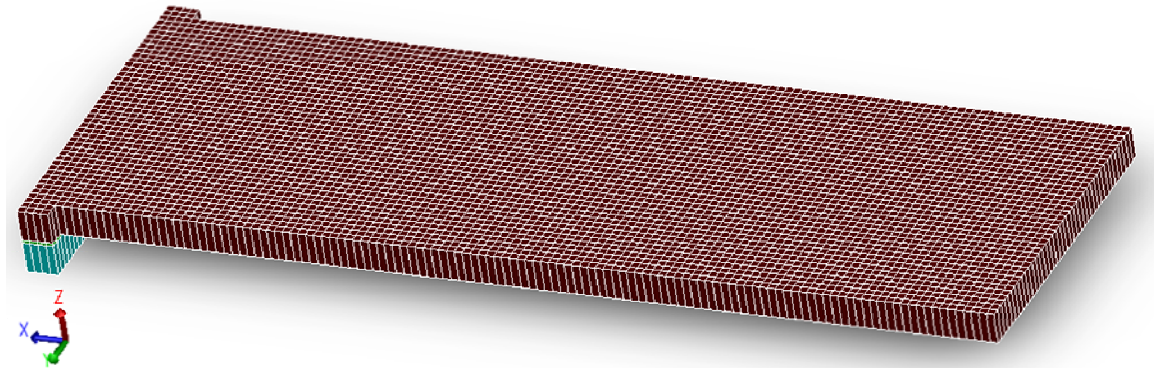


Figure 18. CoventorWare[®] mesh model of $3 \times 1 \times 0.01 \text{ mm}^3$ cantilever using $25 \times 25 \text{ }\mu\text{m}^2$ square elements, extruded $10 \text{ }\mu\text{m}$ in the Z-direction.

Available methods to create the mesh model depend on geometry of the device. When orthogonal geometries are used to create the 3-D model, and all intersecting planes meet to form a 90 degree angle; Manhattan, Extruded, or Mapped meshing can be performed. A Manhattan brick mesh type is useful when “orthogonal or nearly orthogonal geometries” are used and the Manhattan mesh supports device designs with sloped sidewall profiles [107]. The Manhattan mesh allows the user to specify the desired element sizes along the X, Y, and Z directions. While the Extruded mesh model allows for a specification of a square dimension in one plane and an extrusion length in the third direction. Modeled objects with curvatures or non-orthogonal geometries must use the Tetrahedron mesh option. The model in Figure 18 used extruded brick, partition

algorithm, and parabolic element order to create the mesh model which worked well due to the geometry of the device and dimensions.

To evaluate the performance of different mesh settings, a mesh quality study was performed to evaluate different extruded parabolic brick mesh sizes. Mesh dimensions in the X-Y plane were varied from as large as 5 mm down to 5 μm lengths per side of the bricks. The device used in the mesh study was the $5 \times 2 \times 0.01 \text{ mm}^3$ cantilever design. The cantilevers were subjected to a static pressure load of 1 mPa and the resulting tip displacements were recorded. Figure 19 contains the results of the mesh study and the tip displacement results quickly converged for the smaller mesh sizes. Based on the results, the 25 μm mesh was selected for modeling the majority of the devices. The 25 μm mesh was within 0.2% agreement of 5 μm mesh performance but generated the displacement results 18 times faster. The displacement results of the four smallest mesh sizes are shown in Figure 20, with a polynomial curve fit function displayed on the graph. As the mesh size was reduced, the predicted displacement of the $5 \times 2 \times 0.01 \text{ mm}^3$ cantilever from the polynomial fit function approached 5.5636 nm under a 1 mPa static load.

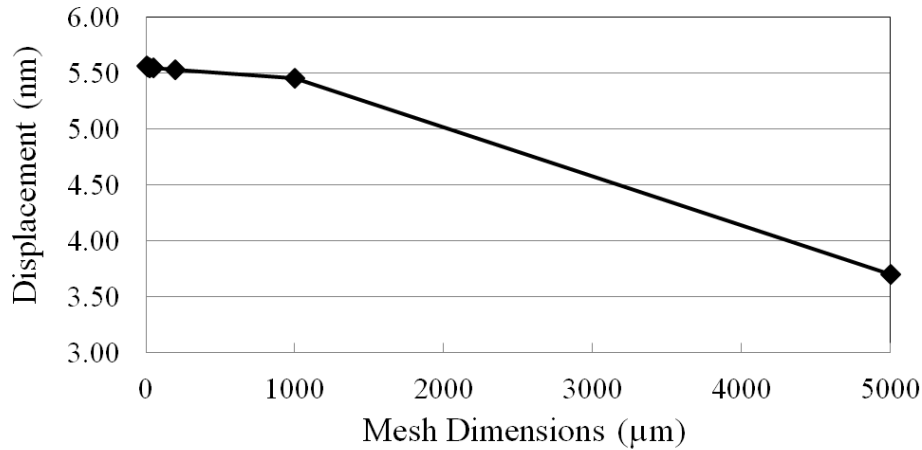


Figure 19. Tip displacement results of mesh study for the $5 \times 2 \times 0.01 \text{ mm}^3$ cantilever design using a z-extruded parabolic brick mesh under 1 mPa static load.

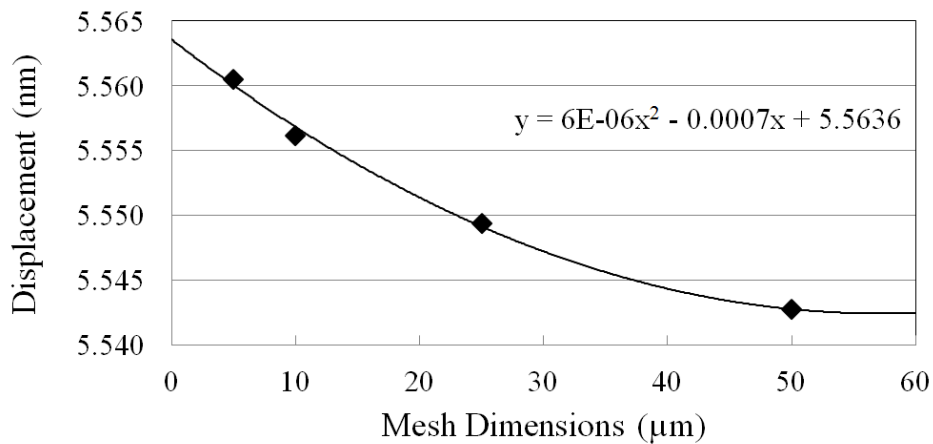


Figure 20. The finer mesh dimensions for the $5 \times 2 \times 0.01 \text{ mm}^3$ cantilever shows the polynomial fit function predicted a displacement of 5.5636 nm for a 1 mPa load.

A full design of a sample device was imported into CoventorWare[®] to show the complete view of layers and cantilever construction. Shown in Figure 21, the surface of the device was subjected to a 1 Pa load pressure and the cantilever deflection is exaggerated to make the deflection more evident. All other modeling was performed only on the cantilever portions, which included a very small anchor area of the BOX and the handle wafer which were held as fixed regions in the models.

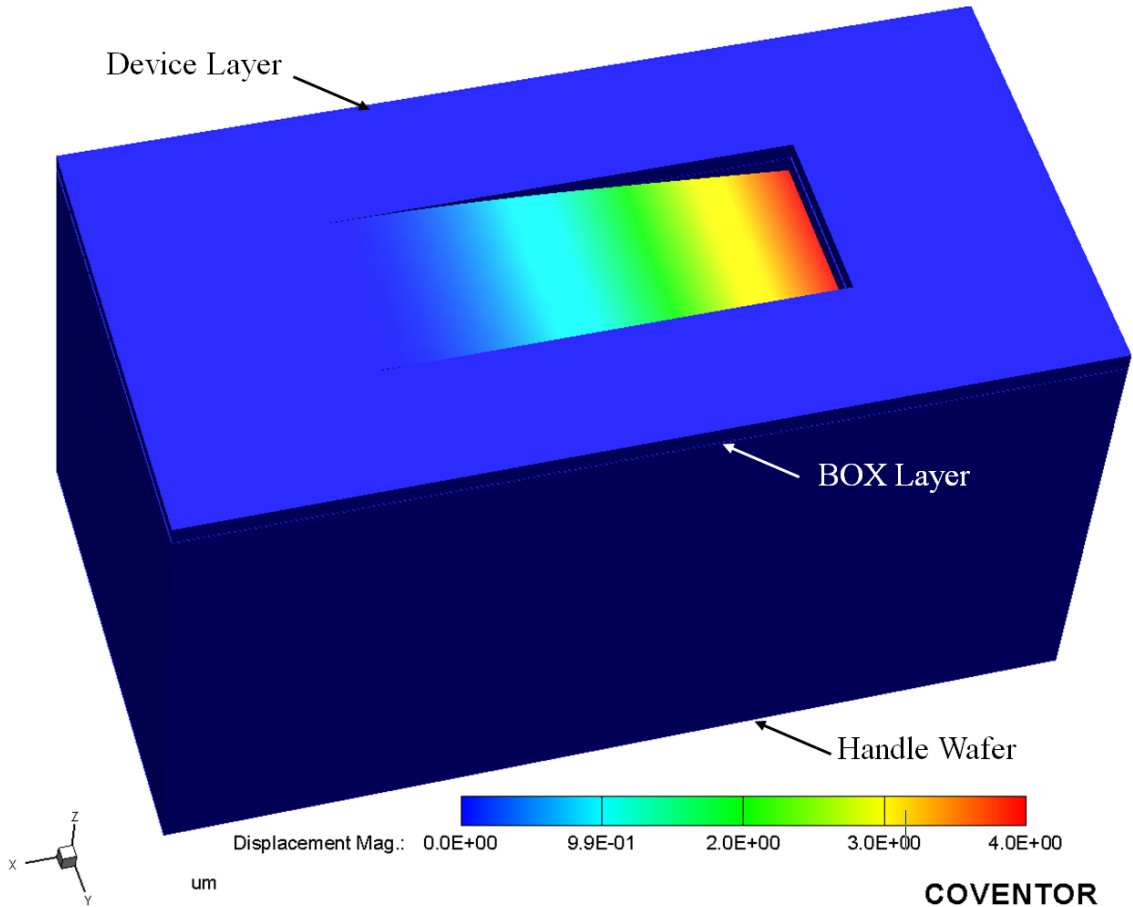


Figure 21. Comprehensive CoventorWare[®] model created from L-Edit mask layouts and fabrication process file to define the handle wafer, device, and BOX layers. The 10 μm thick device layer was subjected to a 1 Pa pressure load which caused a 4 μm tip displacement.

With a mesh setting established, multiple cantilever designs were then evaluated and compared. Traditional cantilever design parameters of length, width, and thickness were used to investigate designs sensitive to the lower end of the anticipated pressure spectrum. Beam designs must take advantage of a large length over thickness ratio to reduce stiffness of the beam and allow greater deflection under small pressure loads. Due to the large span of anticipated pressure conditions, both static and resonant modes of cantilever deflection were studied in CoventorWare[®].

Cantilever designs from 3-9 mm long and widths of 1-5 mm were drawn and then imported into CoventorWare[®]. Static load simulations were accomplished to study the resultant cantilever bending shape and tips displacements. A static load of 10 mPa was imposed on each of the design variations which all had a 10 μm thick device layer, and the displacement results are summarized in Table 2. A static load condition is somewhat representative of an operational test condition if the THz radiation was modulated at a very low frequency. The magnitude of the tip displacement increased significantly with cantilever length. As the width of the cantilevers increased, there was no change or a very slight decrease in the cantilever deflection observed in the simulations. These results predict that there is very little difference in deflection for different cantilever widths, especially between the 1 mm and 2 mm wide designs, which is in agreement with Equation (3.11).

Table 2. Tip displacement results, listed in nanometers of deflection, for 10 mPa static applied pressure load on the different cantilever designs with a 10 μm device layer thickness.

Cantilever Length (mm)	Cantilever Width (mm)			
	1	2	3	5
	Displacement (nm)	Displacement (nm)	Displacement (nm)	Displacement (nm)
3	7.3	7.2	7.2	
5	55.5	55.5	55.5	55.5
7	213.2	213.0	212.8	212.9
9	582.2	582.0	581.7	581.5

Shown in Figure 22 is the beam deflection of the $5 \times 2 \times 0.01 \text{ mm}^3$ cantilever under a 1 mPa static pressure load and the resultant mises stress in Figure 23. This beam configuration had a tip displacement of 5.5 nm and a maximum stress of 7.4×10^{-4} MPa

near the base of the beam. Beams modeled under lighter load conditions showed even less bending as the tip displacement scaled linearly with changes in load pressures.

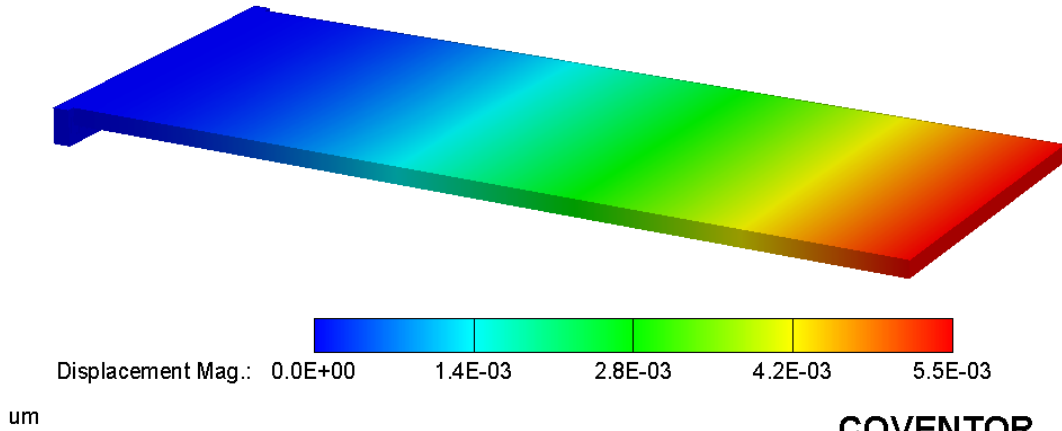


Figure 22. CoventorWare[®] finite element model of a $5 \times 2 \times 0.01$ mm³ cantilever under a 1 mPa static load had a resultant beam deflection of 5.5 nm.

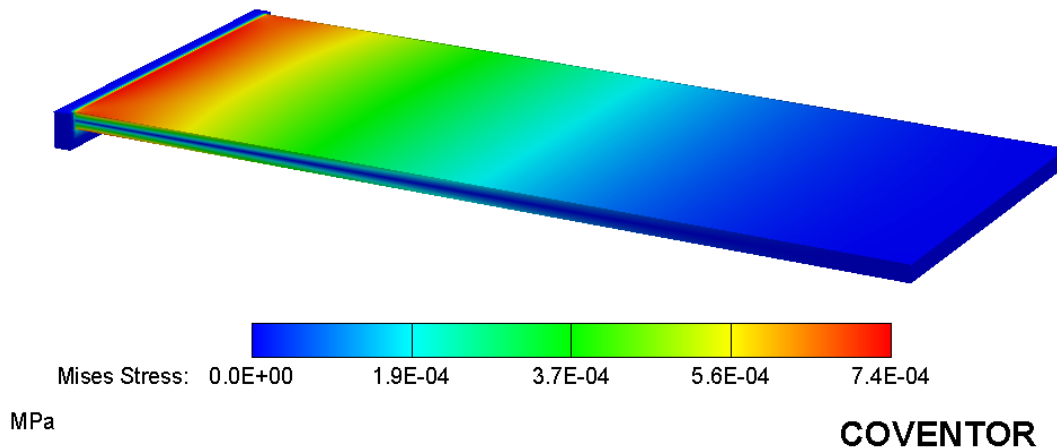


Figure 23. Resultant mises stress generated in the $5 \times 2 \times 0.01$ mm³ cantilever beam under the same 1 mPa static load.

It is important to note that the mises stress profile in the silicon device layer attains a maximum value at the surface near the anchor point of the beam. The surface stress in the silicon layer reduces along the cantilever length to near zero, just past the midpoint of the cantilever length. Stress in the material layers is of great importance if a piezoelectric or peizoresistive layer were to be incorporated into the cantilever device.

Additional simulations using piezoelectric layers and different cantilever designs are discussed in Appendix A.

A modal analysis was performed to determine the natural oscillation modes and at what frequencies they occurred for the cantilevers. The first resonant mode is desirable as it exhibits the greatest tip deflection at the lowest resonant frequency. All other higher order modes are undesirable since they experience much less tip deflection. Shown in Figure 24 are the mode shape and frequency results for a $5 \times 2 \times 0.01 \text{ mm}^3$ cantilever subjected to a 1 mPa sinusoidal load. The second resonance is a torsional mode, third resonance is a small amplitude multi-peak longitudinal mode, while the fourth resonance is a combination longitudinal and torsional modes. A desirable beam design would have a large separation between the first and second modes of resonance to minimize the potential of exciting the torsional mode during testing in the photoacoustic chamber.

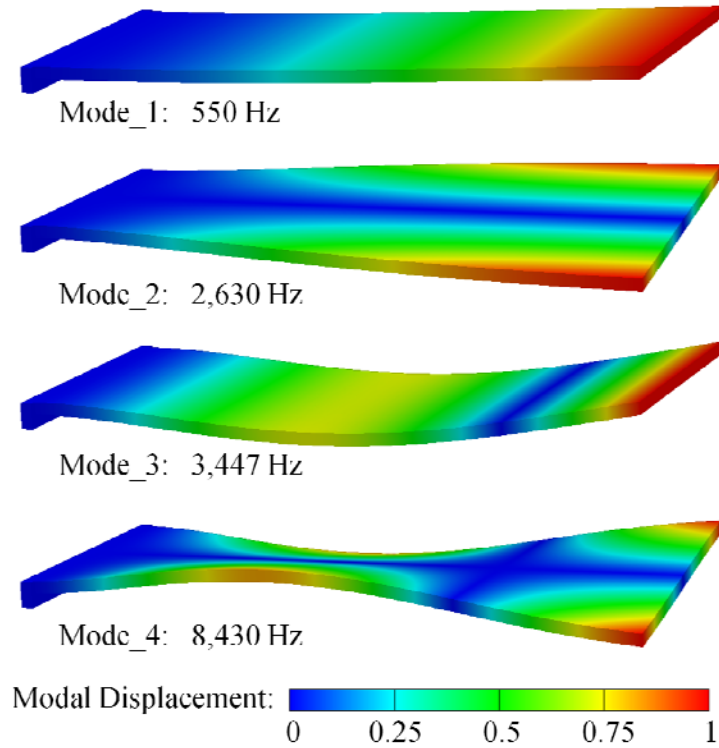


Figure 24. Cantilever resonant mode shapes and frequencies for a $5 \times 2 \times 0.01 \text{ mm}^3$ cantilever due to a sinusoidal load.

A summary of the first and second resonant frequency results is shown in Table 3 for each of the beam designs modeled. As the beam width increased, the second resonance mode moved significantly closer to the lower first resonant mode frequency. As the cantilever beam width increased, the first resonant mode increased only slightly. Cantilever designs that utilized the 5 mm beam widths produced significantly lower second mode resonant frequencies. Based on these results, it is advantageous to select beam designs that have a narrow width since increased widths cause the second harmonic mode to shift down closer toward the first resonance mode. Also, for these standard rectangular cantilever pressure sensor designs, there is no advantage to utilizing an increased width, other than to make alignment in the PA system easier.

Table 3. Mode 1 and 2 resonant frequencies for each beam design length and width tested, utilizing a 10 μm thick device layer.

Length (mm)	Width (mm)							
	1		2		3		5	
	Mode 1 (Hz)	Mode 2 (Hz)	Mode 1 (Hz)	Mode 2 (Hz)	Mode 1 (Hz)	Mode 2 (Hz)	Mode 1 (Hz)	Mode 2 (Hz)
3	1,516.63	8,542.32	1,56.28	4,765.54	1,527.36	3,500.80		
5	549.92	3,445.98	550.12	2,629.64	550.25	1,869.13	550.40	1,261.26
7	280.67	1,758.70	280.76	1,759.10	280.93	1,264.61	280.90	830.15
9	169.83	1,064.09	169.86	1,064.13	169.91	953.96	169.96	614.70

The next examination performed was a harmonic modal analysis which computed the magnitude of cantilever tip deflection caused by a harmonic load applied to the surface of the cantilever as a function of frequency. In this method, a cantilever damping parameter is used and is defined as a fraction of the critical damping coefficient b_0 . A series of percentages of the critical damping coefficient values were selected and tested to represent a range of possible pressure damping effects in the test chamber from atmospheric down to low vacuum conditions. Anticipated test conditions in the photoacoustic chamber were in the 5-600 mTorr pressure range. In Figure 25, a 0.1 mPa harmonic load was applied to the $5 \times 2 \times 0.01 \text{ mm}^3$ cantilever design under five different damping conditions from 10% down to 0.1% of the critical damping factor. When 10% of the critical damping factor was used, which roughly represents atmospheric pressure conditions, the amplitude response was weak and occurred over a broad frequency. As the percentage of the critical damping factor used was reduced, the amplitude response of cantilever increased sharply.

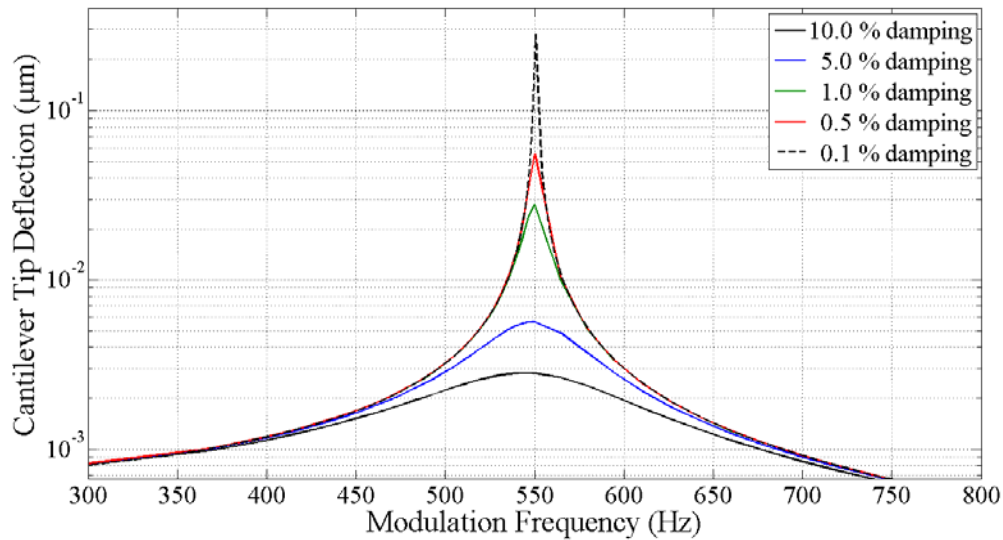


Figure 25. Amplitude displacement frequency response generated in FEM software of a $5 \times 2 \times 0.01 \text{ mm}^3$ cantilever under a 0.1 mPa harmonic load for different damping conditions.

Harmonic modal analysis was then performed on a $7 \times 2 \times 0.01 \text{ mm}^3$ cantilever design. The relative amplitude displacement of the four lowest order modes were looked at for a 0.1 mPa applied harmonic load and using 10% of the critical damping factor. The magnitude of the amplitude response for each of the four modes are shown in Figure 26, and the overall mode shapes are the same as those seen in Figure 24. For modes 1 & 3, the magnitude of the displacement is the same anywhere along the tip of the cantilever. The maximum displacement for modes 2 & 4 occur at the corners of the cantilever tip, due to the torsional motion. The two largest contributing modes to the amplitude deflection are the first and second modes, while the amplitude generated in the third and fourth modes were extremely small.

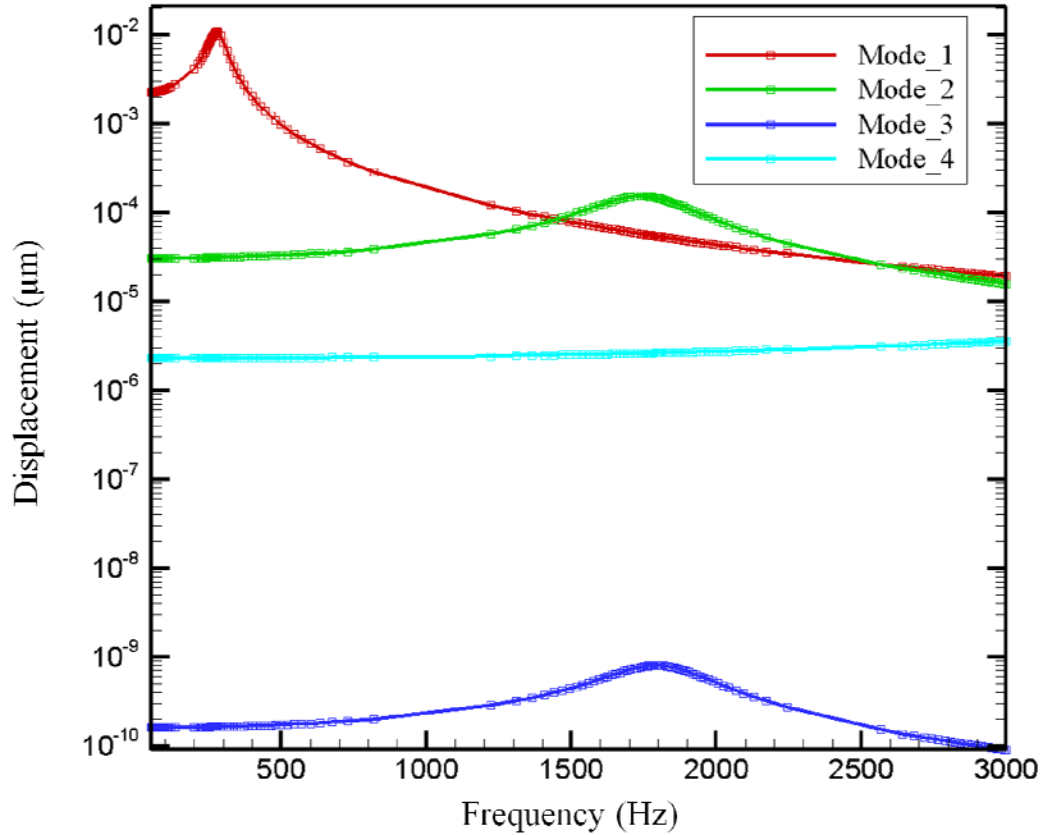


Figure 26. Amplitude displacement response shown for the first four lowest resonant modes of the $7 \times 2 \times 0.01 \text{ mm}^3$ cantilever under a 0.1 mPa harmonic load and 10% of the critical damping coefficient.

To further compare the damping effects, Figure 27 illustrates the resulting tip deflections for three cantilever beam designs under the 0.1 mPa sinusoidal load utilizing 10% and 0.5% of the critical damping coefficients. It is clear that the tip deflection of the 0.5% damped cases greatly exceeded that of the 10% damped cases which have over an order of magnitude less deflection. The $3 \times 1 \times 0.01 \text{ mm}^3$ cantilever beam illustrated by the dashed blue line in Figure 27, had a maximum of 7 nm tip displacement at the first resonant frequency of 1,517 Hz with the 0.5% damping coefficient. The $5 \times 2 \times 0.01 \text{ mm}^3$ cantilever illustrated with the black dashed line in Figure 27 had a maximum tip displacement of 56 nm at 550 Hz, under the 0.5% damping condition. The final beam

illustrated by the red lines in Figure 27 is a $7 \times 2 \times 0.01 \text{ mm}^3$ cantilever. Under the same 0.5% damping condition, it had a maximum tip displacement of 280 nm at 280 Hz modulation frequency. The second resonance mode peak is observed with the $7 \times 2 \times 0.01 \text{ mm}^3$ cantilever which is the lowest peak on the graph with a 3 nm tip torsional displacement at 1,759 Hz.

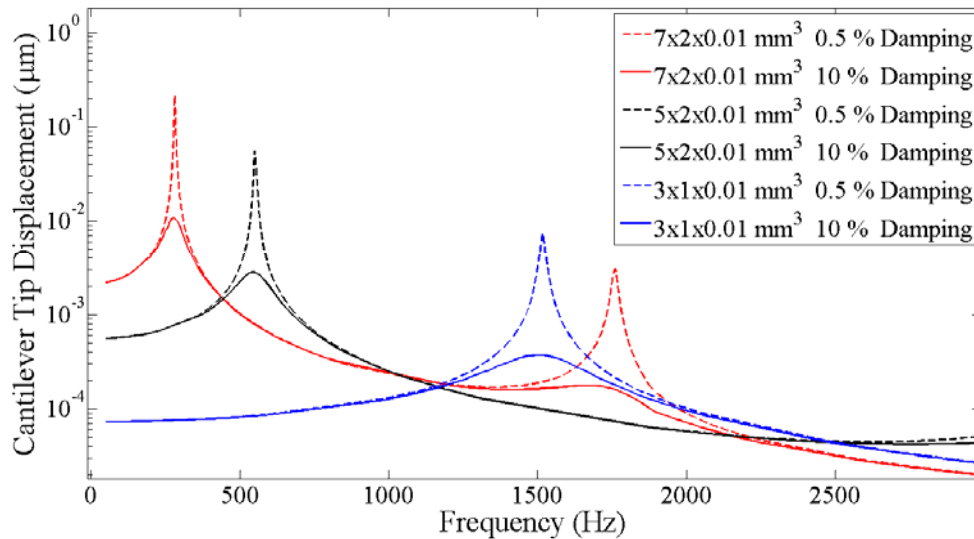


Figure 27. Three cantilever designs, using a $10 \mu\text{m}$ thick device layer, under a 0.1 mPa harmonic load with 0.5% damping illustrated by the dashed lines while a 10% damping factor results in significantly less deflection shown by the solid lines.

Due to the small displacement of the $3 \times 1 \times 0.01 \text{ mm}^3$ cantilever, they were not considered as candidates for fabrication. Another series of simulations was performed using four different cantilever designs shown in Figure 28, which compares the performance of designs with $5 \mu\text{m}$ or $10 \mu\text{m}$ thick device layers. In Figure 28, the $5 \mu\text{m}$ device layers are represented by a dashed line and the $10 \mu\text{m}$ thick device designs are shown with a solid line. The simulation again used a 0.1 mPa sinusoidal load with 0.5% of the critical damping factor. The more flexible $7 \times 2 \times 0.005 \text{ mm}^3$ design showed

significantly more deflection than the other designs. The next most sensitive design was the $5 \times 2 \times 0.005 \text{ mm}^3$ cantilever, deflecting ~ 2 times more than the $7 \times 2 \times 0.01 \text{ mm}^3$ design.

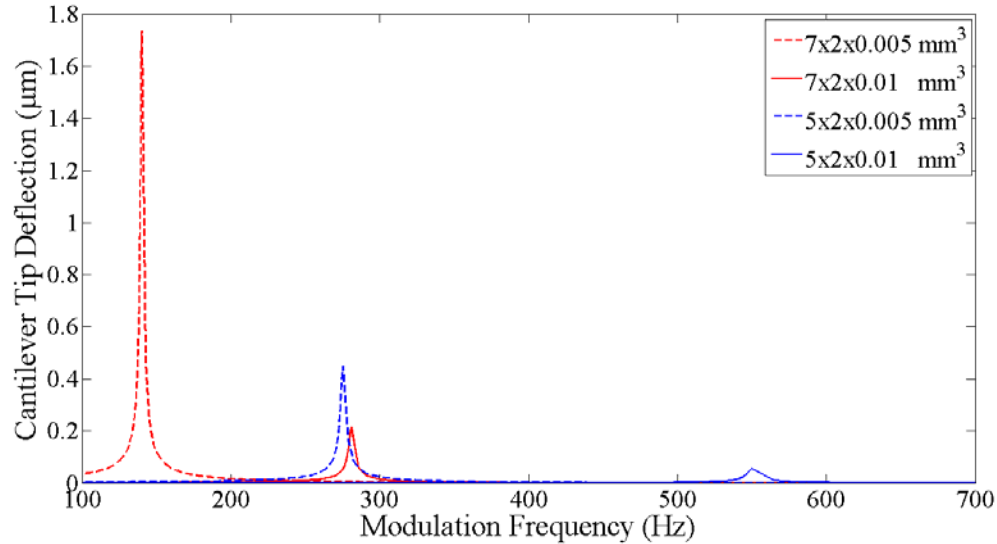


Figure 28. Tip displacement results for four different cantilever designs under 0.1 mPa harmonic load, 0.5% of the critical damping coefficient, the more flexible $7 \times 2 \times 0.005 \text{ mm}^3$ design showed significantly more deflection.

Additional simulations reduced the damping conditions for the analysis to 0.1% of the critical damping coefficient to simulate a lower pressure environment. Shown in Figure 29 is the tip displacement amplitude response of a $5 \times 2 \times 0.01 \text{ mm}^3$ silicon cantilever under four sinusoidal load conditions. Simulated sinusoidal load pressures of 0.03-7.5 μTorr (0.05-1 mPa) resulted in amplitude displacements of 0.14- 2.8 μm respectively. The modeled results predict cantilever deflections which could easily be measured optically with a laser interferometer setup and provided a reasonable estimate of PA performance of the cantilever design.

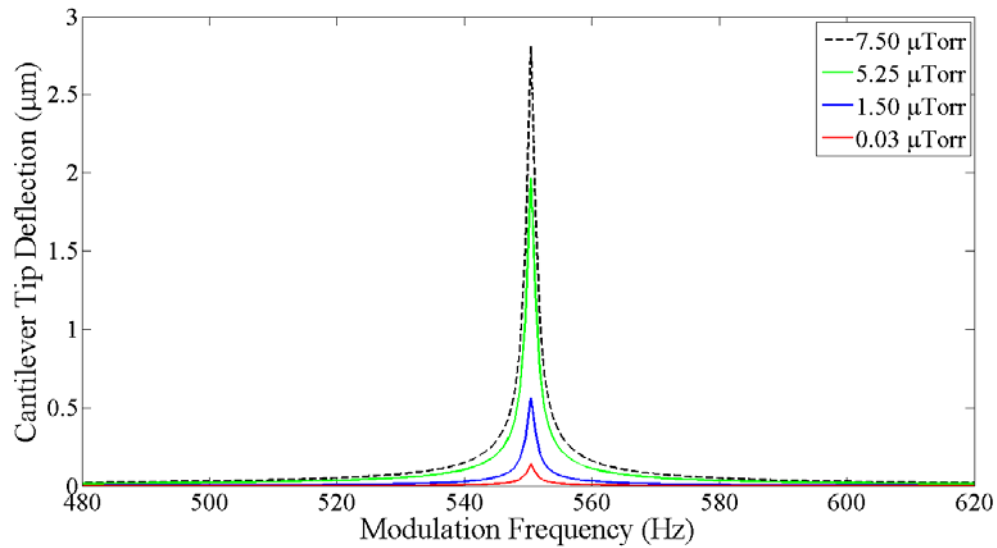


Figure 29. Resultant tip deflections from modal harmonic analysis of a plain silicon $5 \times 2 \times 0.01 \text{ mm}^3$ cantilever design under four periodic load conditions using 0.1% of the critical damping coefficient.

The predicted resonant frequency from the analytical and FEM models of the $5 \times 2 \times 0.01 \text{ mm}^3$ and $5 \times 2 \times 0.005 \text{ mm}^3$ cantilever designs are summarized in Table 4. Using the equations for the effective mass in Equation (3.17) to calculate the cantilever resonant frequency with Equation (3.16), the results produce higher resonant frequencies than the FEM simulation predict. The actual resonant frequency of the cantilever devices is expected to fall between the two frequency predictions, with some deviation expected due to variations in the fabrication process and the final dimensions of the cantilevers.

Table 4. Analytical and FEM resonant frequency calculations for two cantilever designs.

Cantilever Design (mm^3)	Resonant Frequency (Hz)	
	Analytical (Hz)	FEM (Hz)
$5 \times 2 \times 0.01$	766	550
$5 \times 2 \times 0.005$	383	275

There are several advantages to developing an accurate FEM simulation to evaluate cantilever performance in the PA chamber. With a well established framework in place, both traditional rectangular and non-traditional racket and dual anchored cantilever designs could rapidly be evaluated in order to optimize the next generation THz PA sensor. For a fixed device layer thickness, racket and dual anchor designs may present an advantageous means of modifying the spring constant of the beams by changing the anchor width while maintaining a larger tip area to capture the PA pressure.

Analysis of the analytical equations and FEM results highlights the two factors that were considered in selection of a beam design for fabrication, the magnitude of the tip displacement and the cantilever's resonant frequency. If the PA system is modulated at the resonant frequency of the cantilever, this results in the maximum deflection for the device design. Selection of a reduced resonant frequency design due to Equation (3.5) showed the anticipated change in chamber pressure per cycle is inversely proportional to the modulation frequency, and a lower resonant frequency means a lower spring constant and therefore greater deflection of the cantilever.

3.4. Summary

In this chapter, the anticipated pressure changes in the PA chamber were considered through the use of the ideal gas law and the kinetic theory of gasses. Factors used to determine the anticipated change in pressure were based on the chamber dimensions, the THz radiation source power, modulation frequency, and the absorption coefficient of the gas under investigation. The HITRAN and JPL databases were used to

find the molecular absorption coefficients for CH_3CN and the absorption coefficients were used to calculate the anticipated pressure changes in the PA chamber.

Several factors were considered in selection of a cantilever beam designs for fabrication. Cantilever length, width, and thickness parameters affected the resultant tip displacement under static and dynamic load conditions, as well as the cantilever resonant frequencies. The other factor that significantly affected the cantilever displacement was the amount of damping; reduced damping conditions lead to a sharp amplitude response when the applied pressure was modulated at the natural resonant frequency of the cantilever. The anticipated change in chamber pressure per cycle is inversely proportional to the modulation frequency, so the selection of a reduced resonant frequency design would allow for more deflection. From the modeled beam designs, the $5 \times 2 \times 0.01 \text{ mm}^3$ beam was selected first for fabrication. This design was selected due to the moderately high resonant frequency and predicted tip deflections were adequate for low pressure loads. To increase sensitivity, a $5 \times 2 \times 0.005 \text{ mm}^3$ cantilever was selected for fabrication next due to the predicted increase in tip deflection and lower resonant frequency.

IV. Fabrication

Based on the harmonic load deflection results from the FEM models and analytical predictions, several cantilever beam designs were fabricated using the device layer of Ultrasil SOI (100) wafers. SOI technology offers several advantages for PA cantilever sensor fabrication. Crystalline silicon as the device layer offered good uniformity, repeatability, and low residual stress that resulted in excellent PA cantilever designs. SOI wafers with device layer thicknesses ranging from 5-20 μm were used to create cantilever sensors. Conventional micro-fabrication systems were used at the AFIT class 1,000 and Air Force Research Laboratory (AFRL) class 100 cleanrooms to complete the necessary device fabrication steps. Process development and proper execution of the fabrication techniques were critical to successfully making these sensitive devices. The following sections will discuss in detail the Photolithography Mask Fabrication and Cantilever Device Fabrication processes that were developed and used to create the PA sensors in this effort.

4.1. Photolithography Mask Fabrication

The photolithography mask design and fabrication process began with the drawing layouts created in the L-Edit software. Layouts consisted of multiple layers, and each layer represented a step in the fabrication sequence. All the photolithography mask design layouts and mask fabrication processes were conducted in-house using a Heidelberg μPG 101 direct write system, which allowed for rapid design concept to a completed photolithography mask that was used in a traditional contact mask aligner

system. The μ PG 101 system can read three data file format types: DXF, CIF, and BMP. DXF is the standard AutoCAD file format, CIF is the Caltech Intermediate Form format, and BMP is the MS-Windows[®] Bitmap format. DXF and CIF file formats can be used to expose standard 2-D designs while the BMP format can be used to perform grayscale lithography to create 3-D structures in photoresist. In the L-Edit software, mask designs are created as Tanner Database (TDB) file, then all the layers are changed to a single layer type, and the file is exported to a CIF file format prior to transferring the design to the Heidelberg direct write system.

Heidelberg direct write systems with 3 μ m or 1 μ m minimum feature sizes were available in the cleanroom, and each system offered unique capabilities. The Heidelberg 3 μ m mode μ PG 101 machine can write to a maximum area of 100 \times 100 mm², using a 405 nm wavelength diode laser, and yields a write speed of 30 mm²/min. While the 1 μ m mode μ PG 101 machine has a maximum write area of 30 \times 30 mm², using a 375 nm wavelength laser, and yields a write speed of 3 mm²/min. Actual write times for a mask was typically 4-7 hrs depending on the final dimensions of the design.

Nanofilm photomasks, 4 \times 4 in² blank plates made of soda lime were used in the Heidelberg system to produce the photolithography masks. The Heidelberg units could accept mask sizes up to 5 \times 5 in². Mask blanks are available in a number of configurations, a low reflective chrome coating and AZ1518 photoresist options were used. The chrome metallization layer was 100 nm and the photoresist layer was 530 nm thick.

To determine the laser power settings for the μ PG 101 systems with the Nanofilm photomasks, a series of power exposure tests were performed. In the course power series

exposure, the laser power was held fixed and laser pulse duration on time was varied from 100% down to 10%, in 10% increments. After exposure, the photomasks were developed for 30 s in a (3:1) solution of de-ionized (DI) water and 351 developer with slight agitation to refresh the developer at the surface of the mask. Vernier marks from an exposure series test are shown in Figure 30 which illustrates the three conditions of exposure: under, correct, and over exposure. Under exposure, shown in Figure 30 (a), left a thin layer of PR in the exposed areas which are the dark shaded regions in the optical microscope image. Results of a correct level of exposure are displayed in Figure 30 (b), which left all the verniers intact and the exposed PR was developed away down to the low reflective chrome. Over exposure in Figure 30(c), shows that the narrow line segment of the verniers in the upper left corner developed away due to the high exposure dosage. It was determined that 8 mw at 90% on the 3 μm machine produced very consistent results at desired minimum feature size with the Nanofilm masks.

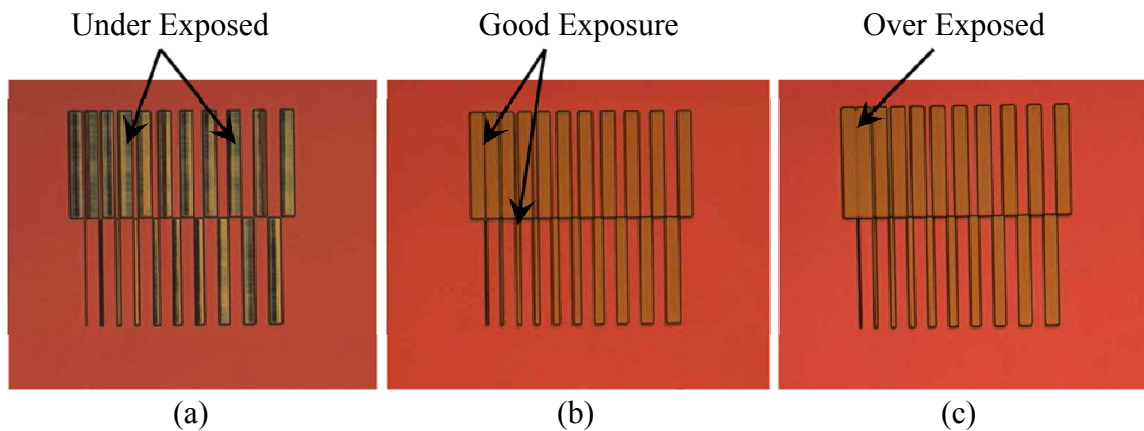


Figure 30. Verniers from the power exposure series result shown in (a) were under exposed, a good exposure level in (b), and over exposure dose in (c) where the narrow line of resist was removed during the develop process.

After the photomasks were developed, the exposed chrome layer was removed using Cyantek CR-4 etchant. CR-4 is a versatile, nitric acid etchant that can be used to

remove Cr, Cu, Ni, and NiCr metals. The photomasks were etched in the CR-4 liquid with slight agitation for 60-90 seconds, with some small variation depending on the feature sizes and the amount of exposed chrome. The masks were then rinsed with DI water, dried, and inspected under the microscope. When the etch process was complete, the PR was removed from the mask through a standard acetone, methanol, isopropyl alcohol, and DI cleaning process. Any remaining trace amounts of PR was then removed in an oxygen plasma asher for 4 minutes, leaving the mask surface extremely clean and ready for use.

4.2. Cantilever Device Fabrication

The fabrication process begin with the device layer side of the 150 mm diameter SOI wafer being coated with 1818 photoresist and baked at 110 °C for 5 minutes. The photoresist layer protected the silicon device layer during the dicing process as the wafer was cut into $1 \times 1 \text{ in}^2$ squares designed to fit into the PA chamber. Based on the 1 inch square samples, a maximum of 21 samples could be made out of each 150 mm diameter SOI wafer. The PR layer was then removed and the diced sample was cleaned in a buffered oxide etch (BOE) solution to etch away the native oxide on the device layer surface. The BOE solution used was a 7:1 volume ratio of 40% NH_4F in water to 49% HF in water and yielded a 78 nm/min etch rate of SiO_2 at room temperature. After approximately 30 s in the BOE solution, the device layer surface was completely hydrophobic during the subsequent DI water rinse, which was a good indicator that the native oxide layer was completely removed.

Beginning from a clean device layer surface, the remaining fabrication sequences used to create the cantilever sensors is summarized in Figure 31. A reflective metal layer of Ti/Au (200/1,000 Å) was deposited via electron beam evaporation at the tip of the cantilever in Figure 31 (A). In Figure 31 (B), a patterned photoresist layer was then used to define the cantilever shape for the subsequent deep reactive ion etch (DRIE) through the device layer. Shown in Figure 31 (C) is a two step DRIE and then a reactive ion etch (RIE) through the backside of the handle wafer. The final etch step in the fabrication process was the removal of the BOX layer with HF vapor, as illustrated in Figure 31 (D). A completed $5 \times 2 \times 0.01 \text{ mm}^3$ silicon device is shown in Figure 31 (E) which had a $6 \text{ }\mu\text{m}$ gap etch through the device layer that defined this particular cantilever's dimensions. A more detailed discussion of the fabrication processes is divided into the following Metal Deposition, Device Layer Etch, and Backside Etch sections.

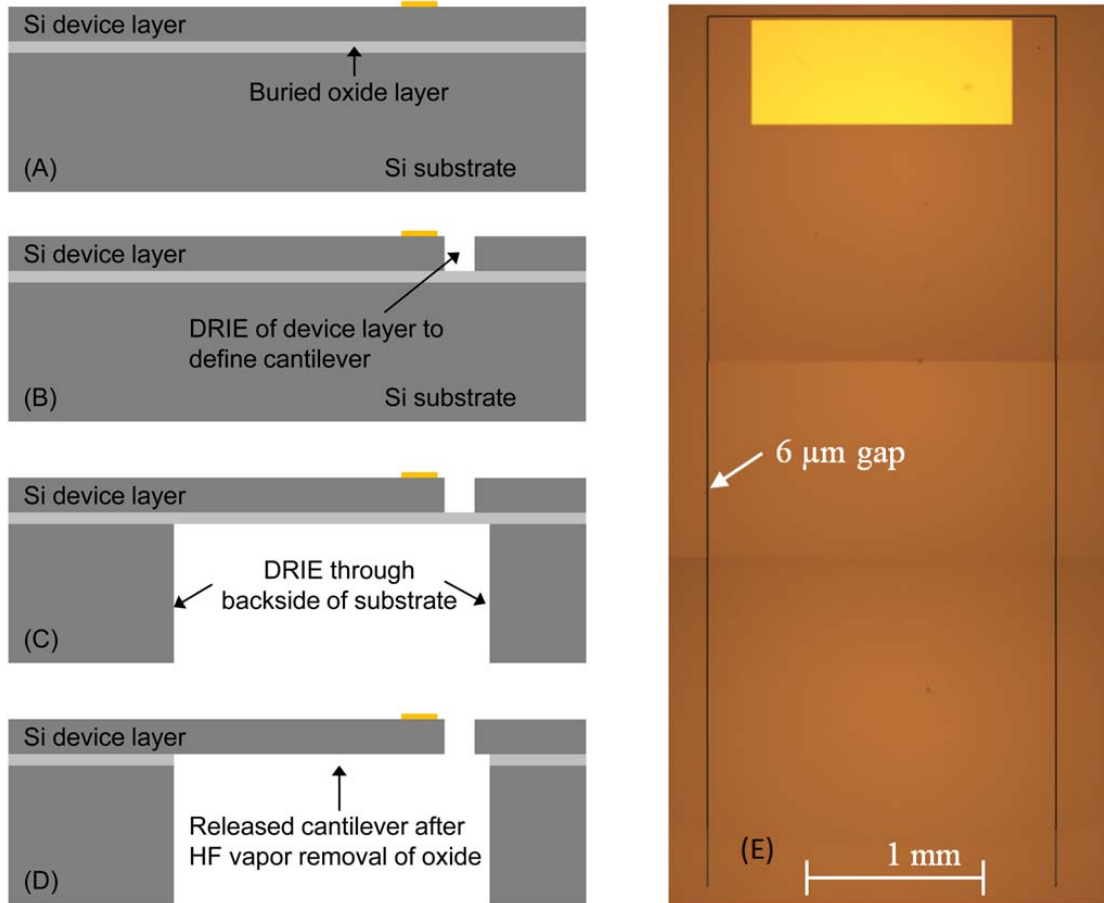


Figure 31. Cantilever fabrication process began with the (A) deposit Ti/Au for reflective surface, (B) etch device layer to define cantilever, (C) backside etch through handle wafer, and (D) the removal of the exposed BOX with HF vapor. An optical image (E) of a fabricated $5 \times 2 \times 0.01 \text{ mm}^3$ silicon cantilever with a $6 \text{ }\mu\text{m}$ gap etched through the device layer to define the cantilever beam.

4.2.1. Metal Deposition

To provide the necessary reflective surface for the laser and photodiode optical measurement technique in the PA chamber, a small reflective area near the tip of the cantilever was needed. A bi-layer photoresist method was used to pattern the sample before metal deposition. After the sample went through a dehydration bake, a coating of MicroChem PMGI SF-11 was spun on at 4,500 RPM and subsequently soft baked for 5 minutes at $170 \text{ }^\circ\text{C}$. SF-11 is a specific make of the polydimethylglutarimide (PMGI)

series of resists, where the “11” represents an average coating thickness of 1.1 μm , depending on the application spin speed. Then an imaging resist layer of 1805 was applied at 3,500 RPM and then soft baked at 110 $^{\circ}\text{C}$ for 90 s. The 1805 PR layer was then exposed in a Karl Suss MJB3 mask aligner using vacuum contact mode and the metal deposition photomask pattern. The exposed 1805 resist was developed away with a (5:1) solution of DI water and 351 developer for 30 s. With the desired pattern defined in the 1805 PR layer, the sample was placed in an OAI deep UV (DUV) flood exposure system for 200 s. The shorter 240-290 nm wavelengths of light emitted in the DUV system are absorbed by the 1800 series patterned resist protecting the PMGI layer below from exposure and exposes the uncapped SF-11 layer. The sample was then soaked in 101A developer for 60 s, which ensured remaining SF-11 was undercutting the 1805 photoresist cap. After a thorough rinse in DI water, the samples were dried off with the N_2 gun and the sample was baked on the hotplate at 100 $^{\circ}\text{C}$ for 5 min. Samples were then placed in the oxygen plasma asher for 3 min at 75 W to remove any organic residue on the exposed silicon surface and to promote better adhesion for the subsequently deposited metal layers. The photoresist patterned samples were finally ready for metal deposition

Both a Torr International electron beam (e-beam) evaporation and a Denton plasma magnetron sputter deposition systems were available to deposit the desired thin film metal reflective layer. Due to the more directional deposition of films, the e-beam evaporation system was selected to perform the metal deposition. The evaporation system had four available pockets; Fabmate[®] crucibles were used to contain the Ti and Au evaporation materials.

Once the samples were loaded into the chamber, the evaporator system achieved a typical base pressure better than 7×10^{-7} Torr. An adhesion layer of 200 Å of Ti was first deposited using an automated ramp, soak, and deposition sequence which yielded a stable deposition rate of 1 Å/s. The material thickness and deposition rate was monitored by a quartz crystal thickness sensor, which provided status to the deposition controller to adjust the e-beam source power to maintain the desired deposition rate. When the desired thickness was reached, the system automatically turned off the e-beam and closed the shutter. After the crucible cooled for approximately 3 min, the pockets were rotated to the crucible containing the Au target material. The quartz thickness monitor and deposition controller programs were then modified to perform the Au deposition; adjusting the appropriate Z-factor, tooling factor, material density, and desired deposition rate. Then in a another automated sequence, 1,000 Å of Au was deposited at rate of 2 Å/s. The automated deposition sequences were developed to remove the manual monitoring and adjustments necessary to maintain the desired deposition rates. The automated sequences also ensured consistent soak and power ramp rates to maintain repeatability from run to run.

Metal lift-off was then performed in three steps: tape lift-off, acetone bath, and then two, 30 min soaks in a heated PG-Remover solution. The tape lift-off process typically removed ~90% or more of the unwanted metal from the surface of the photoresist layer. Deposited gold features on the samples were very sparse, tape lift-off significantly reduced the amount of time required in the solvent and stripper solutions to remove the PR coatings. Additionally, with the majority of the unwanted metal removed from the samples, less debris was in the solutions that could potentially be redeposited

back onto the surface of the devices. After a standard cleaning process, the samples went through a dehydration bake again and were ready for the device layer etch.

4.2.2. Device Layer Etch

To pattern the cantilever shape into the silicon device layer, a thin layer of S1818 photoresist was used. The Microposit S1818 was spun on at 3,000 RPM, then baked at 110 °C for 90 s, creating a 2.2 μm thick layer. The sample was then exposed on the MJB3 mask aligner with the device layer etch mask using vacuum contact mode to achieve the best resolution. Samples were then spray developed with the same (5:1) solution of 351 developer for 30 s. The S1818 is a solvent based positive series photoresist. To make the PR layer more robust, an additional dehydration bake was performed at 110 °C for 20 min to drive out the solvents.

Using a single device layer etch mask designed with a 3 μm gap, multiple gap widths were achievable on different samples through varying the device layer etch conditions. A deep reactive ion etch (DRIE) plasma tool was used to create narrow 3 μm gaps that were etched through the device layer surface of the SOI samples to define the cantilever shape. The majority of the cantilever designs fabricated in this effort were $5 \times 2 \times 0.01 \text{ mm}^3$ and $5 \times 2 \times 0.005 \text{ mm}^3$. A DRIE only etch of the 3 μm patterned slit produced the smallest gap, while a subsequent isotropic RIE etch on other samples allowed gaps up to 8 μm wide in this work. The advantage of using the DRIE is that it's an anisotropic etch process, which results in a near vertical sidewall profile and virtually no mask under cut to create gap widths the same resolution as the photoresist mask pattern. Shown in Figure 32 (a), a schematic layout of the cantilever devices created and

Figure 32 (b) an optical image of a device with a small 3 μm gap achieved with the DRIE process.

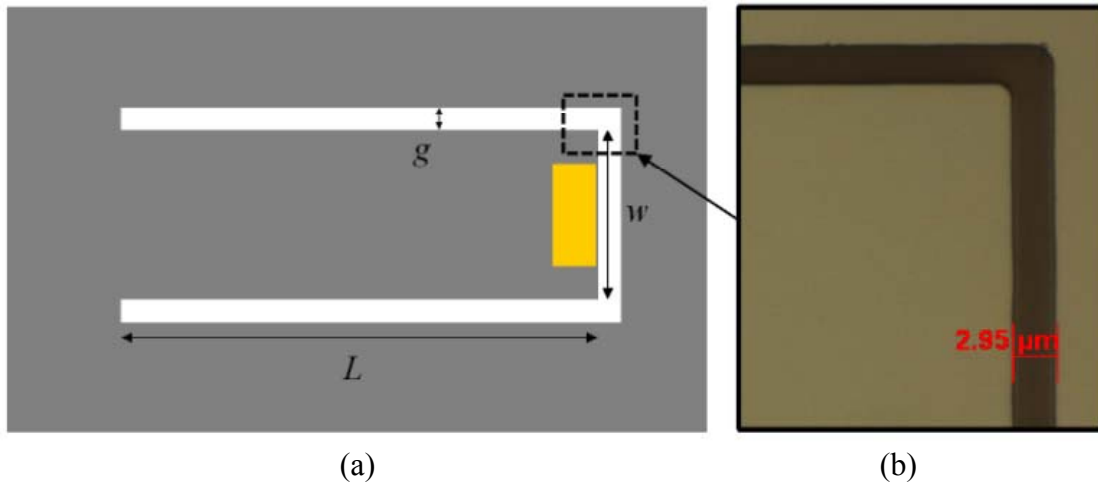


Figure 32. (a) Layout of cantilever design and in (b) an optical image of the 3 μm gap etched through the device layer with the Plasma-Therm DRIE system.

To perform the DRIE, a Plasma-Therm Versaline DSE system was used; where DSE stands for Deep Silicon Etch technology. The system can handle up to 4 in diameter wafers and the etch recipe used produced an overall average etch rate of 7.5 $\mu\text{m}/\text{min}$. The system utilizes a three-step sequence over a 5 s period, performing passivation and etch steps removing 625 nm of silicon per period. The DRIE system utilizes rapid changes in chamber pressure, inductively coupled plasma (ICP) RF power, platen RF power, and platen DC bias to control the etch chemistry at the surface of the wafer.

The Versaline etcher utilizes a load lock and smaller samples must be loaded into the system on a 4 in carrier wafer. The carrier wafers were coated with a $\sim 20 \mu\text{m}$ layer of SU-8 2025 which was hard baked for 30 min at 200 $^{\circ}\text{C}$. A small amount of Fomblin oil was used under the samples to hold the samples in place and provide thermal conductivity from the sample to the carrier wafer.

Cantilever designs were defined in the device layer of the SOI by etching a small gap around three sides of the cantilever beam. The 3 μm wide patterned gap formed a continuous 12 mm long trench around the cantilever edge. To ensure the trench was formed completely through the silicon device layer, a 20% over etch was performed in the DRIE based on the 7.5 $\mu\text{m}/\text{min}$ etch rate. An advantage to using SOI wafers is that the buried oxide (BOX) layer acts as an excellent etch stop in the DRIE system.

Some samples went through an additional isotropic RIE etch to increase the gap width; gaps up to about 8 μm wide were made. A Trion Phantom RIE system was used to perform the isotropic etch. Process conditions utilized 30 sccm SF_6 , 3 sccm O_2 , at a chamber pressure of 150 mTorr, and 150 W of RIE power. The relatively high chamber pressure and low RIE power etched the silicon back under cutting the PR mask material. In Figure 33, the sample was etched under the above listed RIE conditions for 240 s and the image is shown with the PR mask layer still in place. The etch undercut the PR mask layer 2.55 μm on both sides of the trench creating an 8.4 μm wide gap around the cantilever. The RIE etch conditions caused a 638 nm/min undercut etch rate of the silicon device layer.

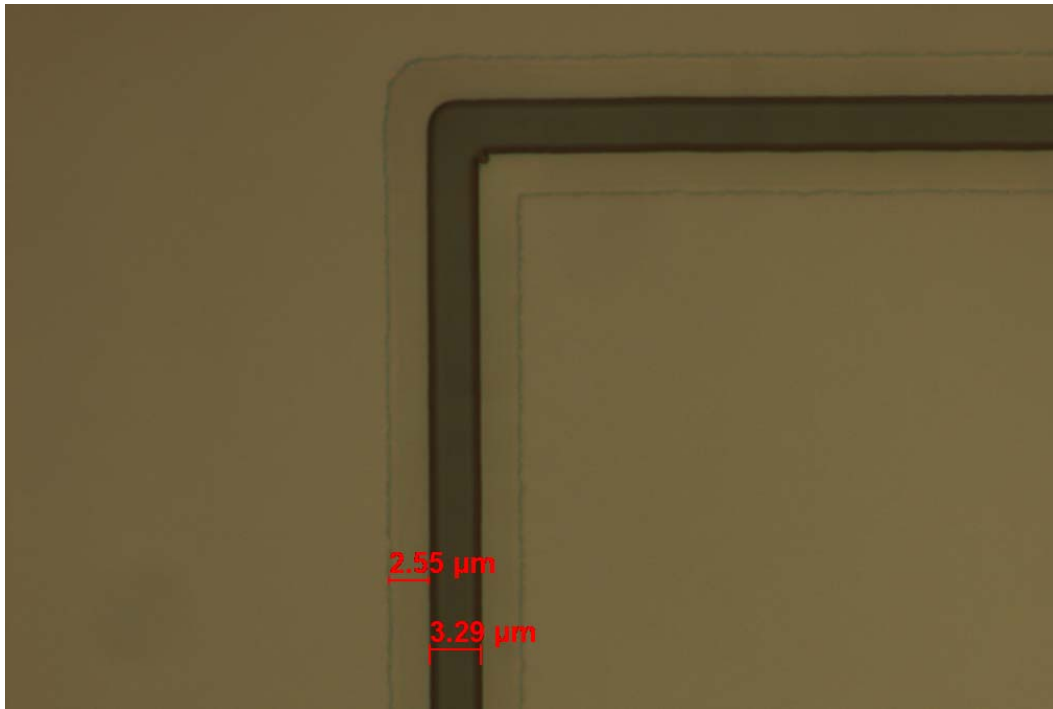


Figure 33. Larger 8.4 μm gap shown with photoresist mask still in place after additional isotropic etch.

4.2.3. Backside Etch

To complete the sensors, the backside of the carrier wafer and buried oxide below the cantilever had to be removed to completely release the cantilever beam. With the cantilever pattern etched in the device layer, the sample was then coated with a layer of SF-11 to protect the silicon and gold surfaces during subsequent processing steps. The protective SF-11 layer was baked at 200 °C for 5 min, creating a robust film that could later be heated directly on a hotplate surface. To pattern the portion of the handle wafer below the cantilever for removal, the backside of the wafer was coated with a 20 μm layer SU-8 25. The backside of the sample was then exposed on a Suss MAB-6 backside mask aligner using the backside etch mask. SU-8 is a negative tone epoxy based photoresist. When the resist is exposed to UV radiation, a strong acid is formed in the

film. During a post exposure bake (PEB) step, the newly formed acid and thermal heating causes the epoxy to cross-link and harden. Samples were then immersed in a SU-8 Developer solution for 4 min to remove any unexposed SU-8, creating a hole patterned below the cantilever. After the develop steps, the sample was hard baked on a covered hotplate at 110 °C for 1 hour to further harden the SU-8. The SU-8 was then permanently attached to the back side of the wafer after the hard bake step.

The exposed silicon area of the handle wafer below the cantilever was then removed in the Plasma-Therm DRIE using the same etch recipe listed above, achieving a bulk etch rate of 8 $\mu\text{m}/\text{min}$. Initially, the DRIE etch process was used to completely etch through the 450-525 μm thick handle wafers down to the BOX etch stop layer. While that DRIE only bulk etch process worked, sample yield was extremely low, and some cantilevers broke off the samples in the DRIE. Heat generated during the DRIE process combined with the Fomblin oil caused portions of the PMGI protective layer to crack and resulted in non-uniform stresses between the device layer and the PMGI. The power and pressure variations utilized in the DRIE process proved to be too strong for the sensitive devices. Therefore it was necessary to stop the DRIE process 20-30 μm away from the BOX layer, leaving a silicon support membrane in place. The remaining silicon membrane of the handle wafer material was then removed in the RIE. Process conditions used 30 sccm SF_6 , 3 sccm O_2 , 100 W RIE power, and a process pressure of 150 mTorr. This mild etch condition for the final etch allowed for a slow, uniform removal of the remaining Si that covered the BOX layer.

The cantilever beams were extremely fragile during the fabrication process due to their large length to thickness ratio (L/h). The device created here had ratios of 500/1

for the 10 μm device layers and 1,000/1 for the 5 μm thick device layers. Without the thin Si support layer, the residual stress between the device layer, BOX, and SF-11 often caused fractures through the cantilever structure, ruining the device. Figure 34 (a) shows one of the sample surfaces where the SF-11 protective layer experienced some cracking near the anchor point of the cantilever, the darker region of the image is the cantilever curving out of plane. Figure 34 (b) is another sample viewed from the backside, shows the resultant stress in the device and BOX layer due to the SF-11 cracking after the DRIE and RIE processes. A small fracture in the device layer started under a crack in the SF-11 on the left side of the cantilever near the base, propagated across the cantilever beam and caused the device to fail. While a few cantilevers were successfully created using the SF-11 protective layer exclusively, improvements were needed in the fabrication processing methods and techniques to increase the device yield.

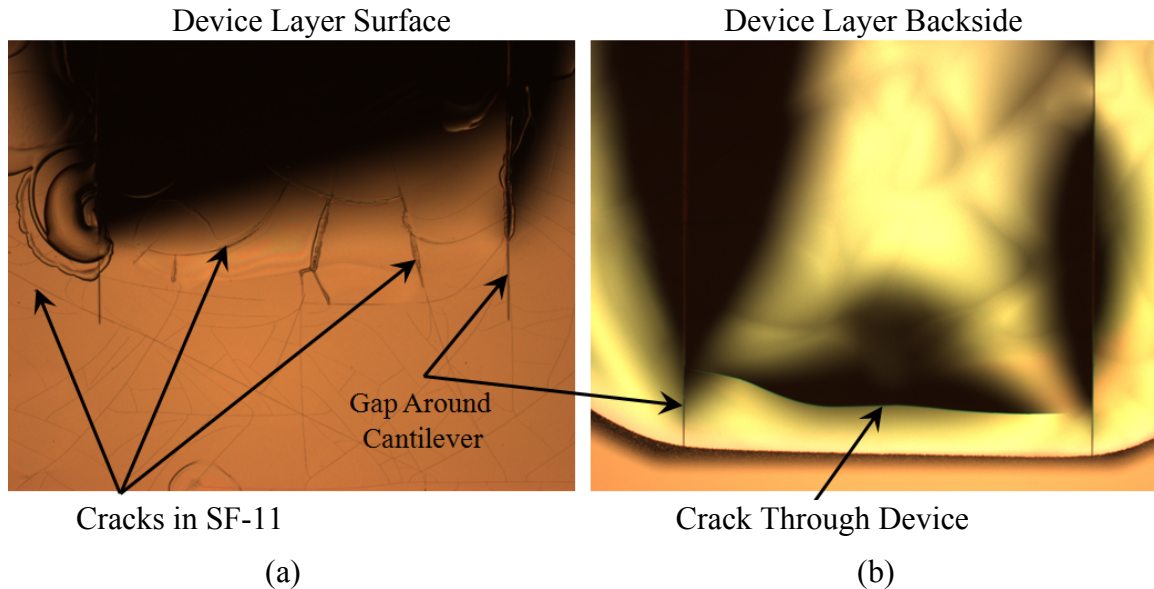


Figure 34. Device surface in (a) with cracks in protective SF-11 photoresist after backside DRIE. Another sample viewed from the backside in (b) after DRIE and RIE, stress between the cracks in the SF-11, BOX, and device layer caused the cantilever to crack near the anchor.

A successful processing method was developed where the backside DRIE was stopped leaving the thin silicon membrane in the handle wafer intact as described earlier, but the PMGI layer was stripped off and replaced by a layer of 1818 which was applied at a low spin speed. The thicker resist layer was then baked for 5 min on a 100 °C hotplate. With a new PR coating to protect the device layer and provide some physical support for the device layer, the remaining thin Si membrane on the backside was again removed in the RIE tool. This new PR protective layer proved essential in the fabrication process and greatly improved the sample yield. The protective PR layer didn't experience any undesirable heating effects such as cracking, which were observed on samples if they were completely etched in the DRIE and then in the RIE. Results of the improved processing method is shown in Figure 35 where the images were taken from the backside of the devices. The images show the tips of the cantilevers with the BOX and device

layers; where the samples still had the protective 1818 layer in place and the surfaces appeared very uniform, unlike the images in Figure 34. Figure 35 (a) was a 5 μm device layer and Figure 35 (b) was a 10 μm device layer. The dark shaded regions around the cantilever edges again indicates the curvature in the devices due to the residual stresses between the BOX and device layers with the greater deflection occurring in the a 5 μm device layer sample in Figure 35 (a).

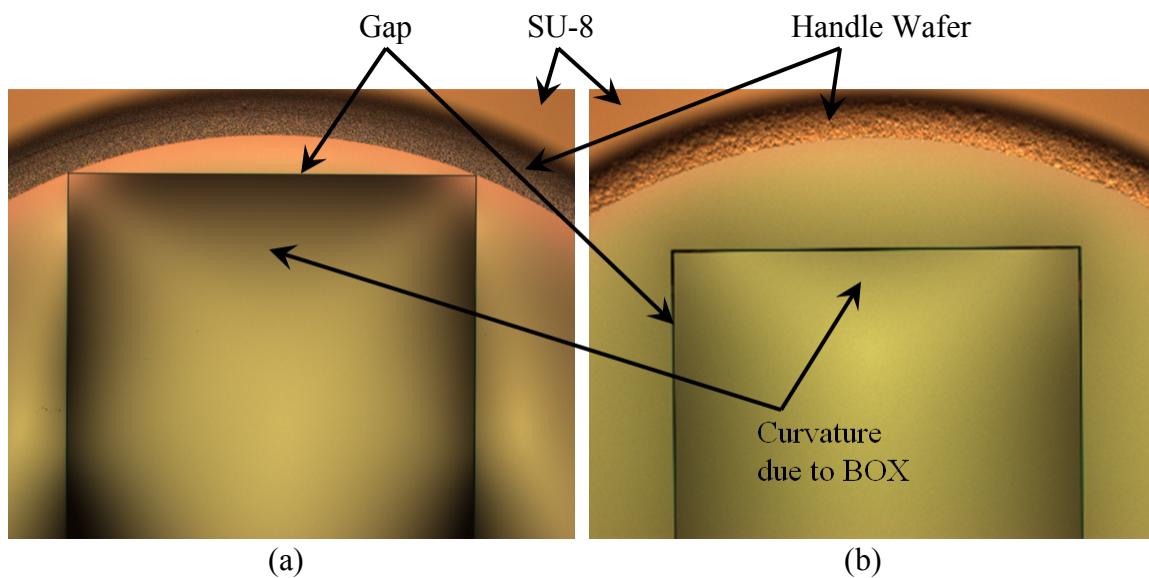


Figure 35. Darker areas on cantilever are due curvature in device layer and BOX, viewed from backside, of 5 μm device layer in (a) and a 10 μm device layer in (b) with 1818 PR used as protective/support layer on device surface.

The next fabrication step was to remove the BOX layer and completely release the cantilevers. Three methods to remove the oxide layer were considered, 49% HF, BOE, or a HF vapor etch. Plasma etching of the oxide layer was not considered feasible due to the slow etch rate and low selectivity between Si and SiO₂ when etching with a CF₄ etch chemistry. The 49% HF solution produces an extremely aggressive oxide etch and would present challenges in handling; transferring the sensitive samples from the etch solution into the DI water rinse in a timely manner would be difficult. A BOE etch

would also work, but it takes approximately 13 minutes to etch through a 1 μm thick oxide layer at room temperature. Also, moving the sample in liquid solution could cause the cantilever to move, break the PR support layer, and potentially break the cantilevers. The best solution to removing the oxide layer was to use a HF vapor etch. Samples were suspended over the 49% hydrofluoric acid solution where the HF vapor then etched away the exposed BOX layer over a period of approximately 4 min. The protective 1818 PR layer on the device surface was able to sufficiently protect the Ti/Au reflective layer during the HF vapor etch. The protective photoresist layer was removed from the samples through a series of acetone soaks, a final rinse in isopropyl alcohol, and the samples were allowed to air dry. Figure 36 (a) shows a residual PR film that tended to linger around the cantilever gap after the acetone cleaning process on the fully released cantilevers. To remove any lingering PR from the cantilever surface and the narrow cantilever gap region, an O_2 plasma ash was performed for several minutes to ensure the cantilever could oscillate unimpeded. After a total of 15 min in a 125 W O_2 plasma ash, the sample shown in Figure 36 (b) came out very clean, and all the residual PR residue was removed from the surface and the gap region.

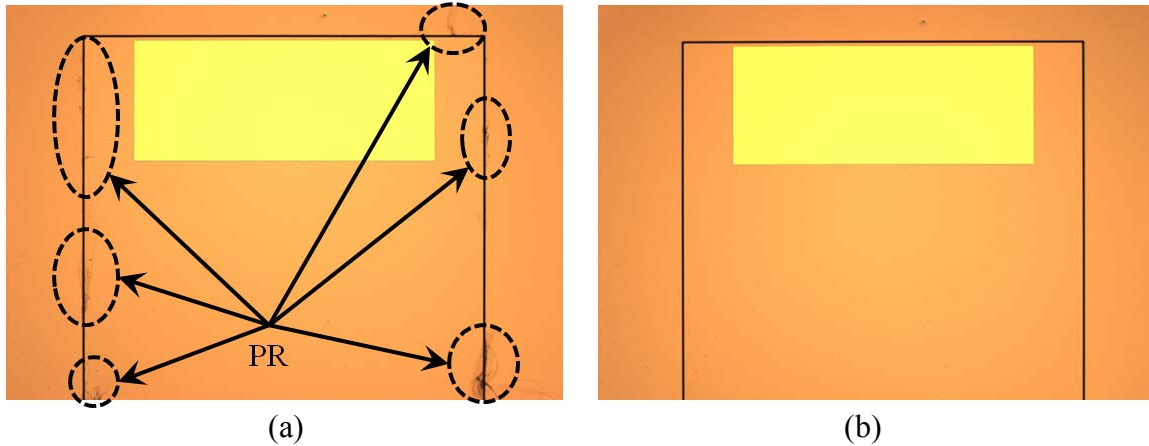


Figure 36. Residual PR in the highlighted areas remained around gap after acetone clean of released cantilever shown in (a) and same cantilever shown in (b) after 15 min O₂ plasma ash at 125 W had no remaining PR.

The cantilever tip displacement of several completed devices were then measured on a Zygo white light interferometer. A 3-D surface profile of a $5 \times 2 \times 0.01 \text{ mm}^3$ cantilever device is shown in Figure 37, the out of plane displacement at the tip of the cantilever was $15 \text{ }\mu\text{m}$. The $5 \times 2 \times 0.005 \text{ mm}^3$ devices measured had an average out of plane tip displacement of $12 \text{ }\mu\text{m}$. For both the $10 \text{ }\mu\text{m}$ and $5 \text{ }\mu\text{m}$ thick device layer designs, the effective gap near the cantilever tips was increased to approximately $5\text{-}7 \text{ }\mu\text{m}$ due to the small out of plane tip displacement. The small curvature in the cantilever designs was acceptable, achieving a radius of curvature of roughly $0.83\text{-}1.04 \text{ m}$, and the devices were ready for testing in the THz PA chamber.

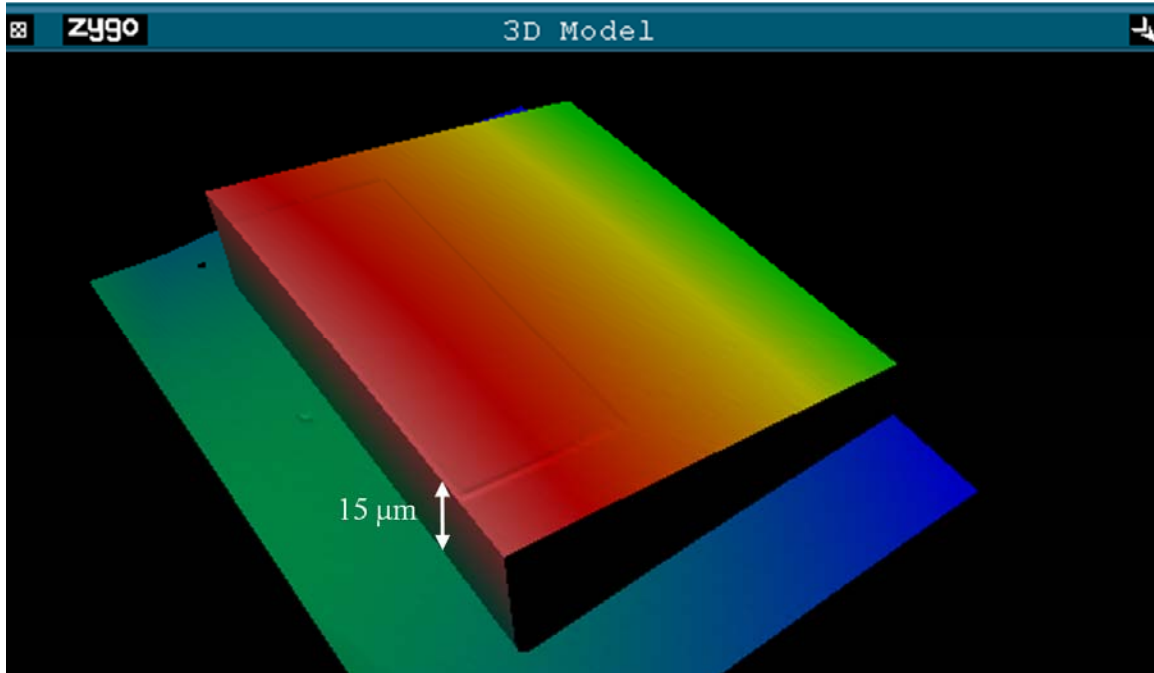


Figure 37. Zygo 3D model of a $5 \times 2 \times 0.01 \text{ mm}^3$ cantilever design showed a $15 \text{ }\mu\text{m}$ out of plane tip displacement.

4.3. Summary

The entire process from initial sensor device concept design, mask fabrication, through completed fabrication of the cantilever sensors was performed in this work. The cantilever beam designs were constructed using the device layer of Ultrasil SOI (100) wafers. Selection of the SOI device layer and buried oxide layer thicknesses were important parameters that affect both the cantilever performance characteristics and manufacturability of the devices. The BOX layer was used as an etch stop material for both the front and backside plasma etches used to define the cantilever device designs. Use of a $1 \text{ }\mu\text{m}$ BOX layer yielded good manufacturability of the high aspect ratio cantilever devices, but selection of a thinner BOX layer should improve results even further.

The displacement sensitivity of the cantilever sensor design was a function of the cantilever length over thickness ratio as described in Equation (3.11), and the sensitivity improves as the length over thickness ratio is increased. Large length over thickness ratios meant that the cantilever designs were sensitive, but they could also be very fragile. The brittle nature of macro scale silicon was observed when residual stress between the photoresist protective layer, device, and BOX layers caused highly localized stress points which cracked the earlier fabricated cantilever samples. Challenges in the device fabrication process were overcome through extensive fabrication process development and utilization of photoresist support layers at different points along the fabrication process. Length to thickness ratios of 500-1,000 were achieved in this work and the sensitive MEMS cantilevers were the key technology that enabled this very compact THz PA spectroscopy technique. The high length/thickness ratios were necessary in order to be sensitive to the low pressure pulses generated in the THz photoacoustic chamber.

As a sensor platform, the silicon cantilevers should perform well, elastically deforming for small cantilever tip deflections. The successful fabrication of an extremely sensitive MEMS cantilever PA sensor was a challenging task. Completed devices were then tested in the custom THz photoacoustic chamber described next in the Experimental Results section.

V. Experimental Results

The experimental results are discussed in four distinct topic areas: the experimental setup, cantilever dynamic behavior, PA spectral data collection, and the sensitivity of the system. The first important aspect to discuss is the cantilever sensor dynamic behavior in response to the PA effect in the test chamber. Relevant information about the behavior of the cantilever sensor includes determining the resonant frequency, quality factor, time constants, and PA signal vs. cantilever deflection for the system over a range of tested pressures. Based on the identified cantilever sensor traits, data collection rates, techniques, and PA spectral collection results are then discussed. Finally, the sensitivity and detection limits of this unique THz photoacoustic spectroscopy system developed in this work are evaluated.

5.1. Experimental Setup

The compact custom fabricated THz photoacoustic chamber had overall dimensions of approximately $2 \times 2 \times 2$ in³ and was constructed out of stainless steel. The test chamber consisted of two segments; a front and back half with the cantilever sensor mounted in between them. The back portion of the chamber contained the absorption cell section while the front half had a small balance volume. The absorption region portion has a cylindrical shape with dimensions 2 inches long and a diameter of 10 mm. A schematic diagram of the back portion of the PA cell and cantilever position is shown in Figure 38.

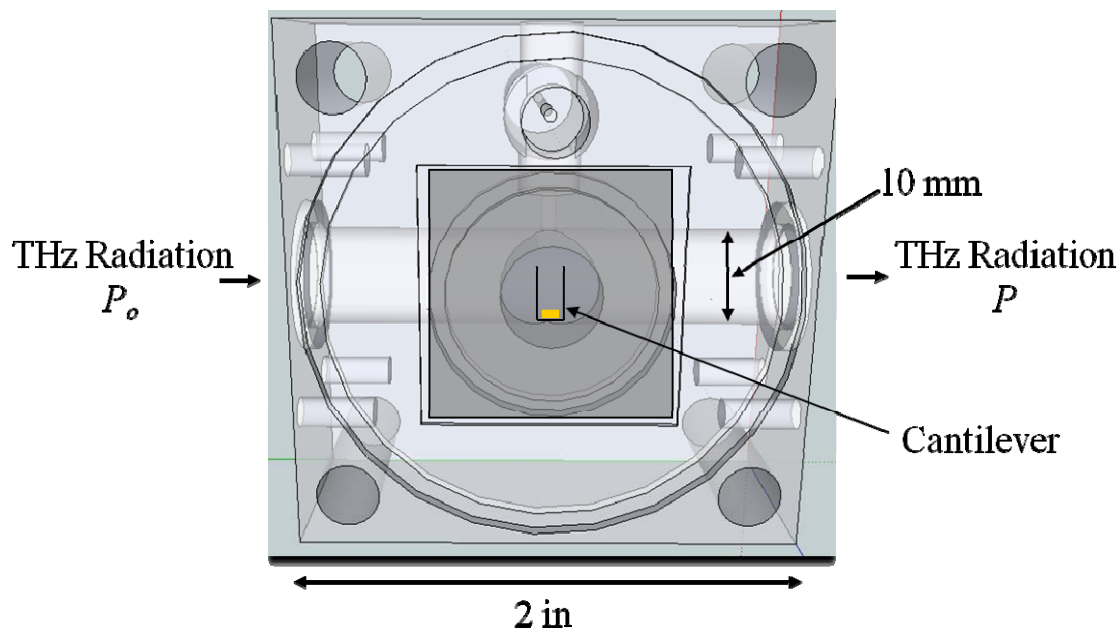


Figure 38. Schematic diagram of photoacoustic cell shown with the front portion of the chamber removed; highlights the chamber dimensions and cantilever position in relation to the absorption cell volume.

To seal the chamber for low vacuum conditions, Teflon windows were used to enclose the ends of the absorption cell and an antireflective (AR) coated glass window sealed the balance volume so optical measurements of the cantilever deflection could be made with a HeNe laser. A Pfeiffer HiCube™ turbo pumping station was used to evacuate the chamber and achieve a low base pressure vacuum level. Methyl cyanide, also called Acetonitrile, was the first gas used to characterize the cantilever sensor. Liquid methyl cyanide was exposed to the low vacuum environment and allowed to vaporize. Through a series of valves, the CH₃CN vapor was allowed into the acoustic cell in a highly controlled manner and the absolute chamber pressure was continuously monitored with a MKS Baratron® capacitance monometer vacuum gauge.

Photoacoustic data collection was controlled through a series of LabVIEW VI's and the signals were collected with a National Instruments (NI) USB-6221 multifunction

data acquisition (DAQ) card. To generate the THz radiation and cause the photoacoustic effect, a Virginia Diodes Inc. (VDI) Amplifier Multiplier Chains were used. The signal to the VDI THz radiation diode was provided by an Agilent E8254A PSG-A signal generator. Controlled through the LabVIEW interface, the output of the signal generator was set to a specified THz radiation frequency which was then amplitude modulated on and off with a 50% duty cycle square wave at the desired modulation frequency. Emitted power by the THz VDI source ranged from 0.6–1.4 mW and is frequency dependent. At low chamber pressures, the output power of the THz source was too high and therefore had to be attenuated at low pressures to prevent molecular saturation. On the opposite side of the chamber from the THz source, there's a VDI detector positioned to monitor the transmitted power that exits the chamber and simultaneously measure the absorption spectra with traditional techniques. For this experiment, the amplifier chain used radiation generated over the 0.250-0.375 THz frequency range. An advantage to the test setup is that additional amplifier multiplier chains can be adapted to the system to reach higher frequencies, up to 1.5 THz if required.

The PA chamber and optics for the experimental setup were mounted on an optical bench. Two optical measurement techniques were employed to examine the photoacoustic effect; a diagram of the test setup is shown in Figure 39. A HeNe ($\lambda=633$ nm) laser beam, guided through a series of mirrors, beam splitter, irises, and focusing lens, was reflected off the tip of the cantilever, back to a photodiode where the laser beam power was measured. An iris beam clipping method or optical beam deflection method, similar to Garcia-Valenzuela *et al.* [108] was used to collect PA spectral data in the THz test chamber when the reference mirror was blocked.

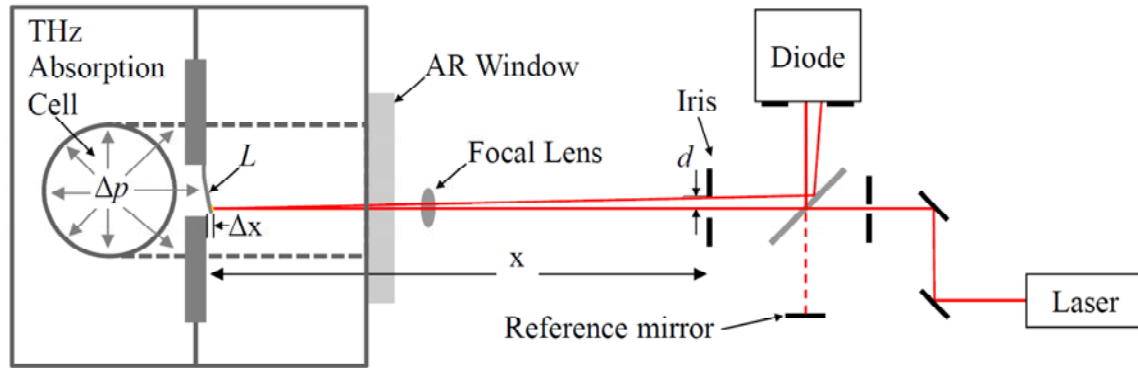


Figure 39. Diagram (not to scale) shows both the PA optical measurement techniques used; beam clipped by the iris when the reference mirror is blocked and a Michelson interferometer displacement measurement when the reference arm was used.

To quantify the sinusoidal changes in power observed at the photodiode, a Michelson interferometer measurement was also incorporated into the experiment. Switching to the interferometer measurement was accomplished by unblocking the reference mirror, modifying the filter settings of the photodiode amplifier, and removing the iris closest to the PA chamber. Accurate cantilever tip deflections measurements were made through the generated constructive and destructive interference signal measured at the diode detector. For large cantilever deflections, the photodiode signal goes through maxima to minima interference patterns as the cantilever deflects a distance of $\lambda/4$.

In both measurement techniques, the photodiode signal was sent to a Stanford Research Systems SR560 preamplifier, setup in a band pass filter configuration. The photodiode signal was also sent to a Stanford Research Systems SR530 lock-in amplifier. The amplitude modulated frequency from the Agilent E8254A signal generator is used as the reference signal for the SR530 lock-in amplifier. The two channel output of the lock-in amplifier reported the magnitude and phase components of the amplified photodiode signal compared to the reference.

For the iris beam clipping method, the measured photoacoustic signal at the diode was greatly affected by the iris placement at distance x , in front of the cantilever and the positioning of the focal lens. The focal lens was positioned such that the beam formed a tight spot at the tip of the cantilever and beam spot at the detector was smaller than the detector opening. Iris placement in front of the cantilever served two purposes. The first function was to reduce the diameter of the incoming beam before the laser light impinged the cantilever. The second purpose was to act again as an aperture; light reflected off the deflected cantilever was then clipped by the iris before it reached the photodiode. The diameter of the iris closest to the chamber was set to ~ 0.8 mm. The final spot size of the HeNe laser beam at the photodiode was ~ 1.0 mm in diameter. The beam displacement, d , from steady state shown in Figure 39, is expressed by

$$d = x \tan\left(\sin^{-1} \frac{\Delta x}{L}\right) \quad (5.1)$$

where, x is the distance from the cantilever steady state position to the iris, Δx is the cantilever deflection distance, and L is the cantilever length. In order to obtain the optimal signal, the THz source was modulated at the resonant frequency of the cantilever and the chamber, mounted on a three axis stage, was adjusted until the photodiode signal produced a symmetric amplitude sine wave. The HeNe laser beam at the photodiode is assumed to have a Gaussian profile which was passed through an aperture iris with a 0.8 mm diameter, as shown in Figure 40. The iris closest to the PA chamber allowed different amounts of HeNe laser light through depending on the positioning of the beam through the aperture.

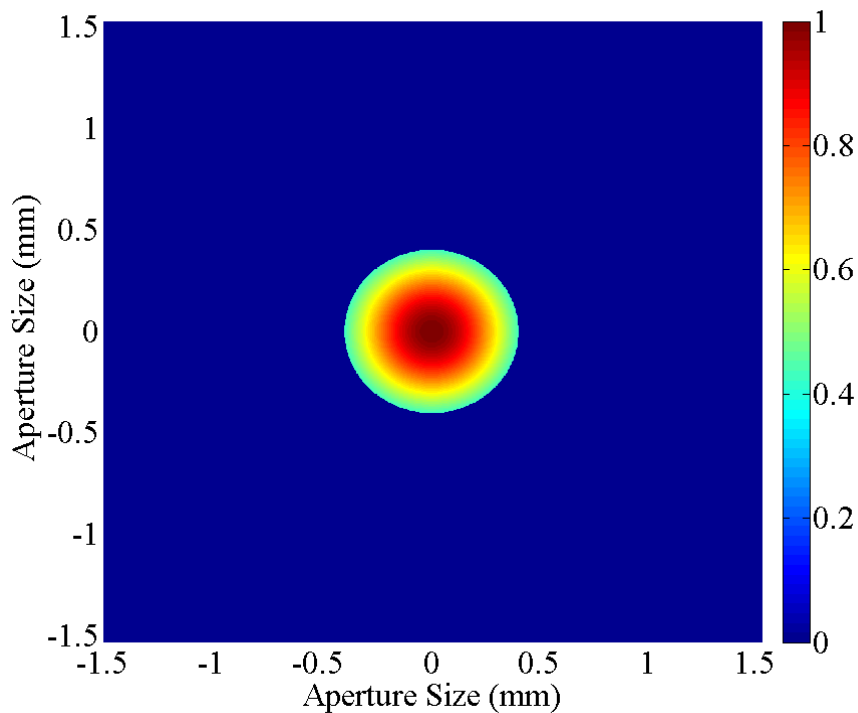


Figure 40. Assumed Gaussian profile of the HeNe laser beam, passed through a 0.8 mm diameter iris, with normalized intensity color bar on right.

The system was also equipped with an attenuator to control the intensity of the HeNe laser beam that was sent to through the optical setup. The wheeled attenuator was placed ~6 inches away from the laser, and positioned at an angle a few degrees greater than perpendicular to the beam as to not reflect light back into the laser cavity. A model of the signal at the photodiode was performed in MATLAB[®], creating a 1,000×1,000 mesh grid of the intensity element to represent the beam and aperture. The sum of the intensities of the elements in the aperture represented the energy in beam. Since the aperture size was considered fixed, the intensity of the light can be varied by modifying the attenuation level of the beam. In Figure 41, five beam attenuation levels were swept across the entire aperture opening, centered along an axis, the intensities were summed up for each location of the beam.

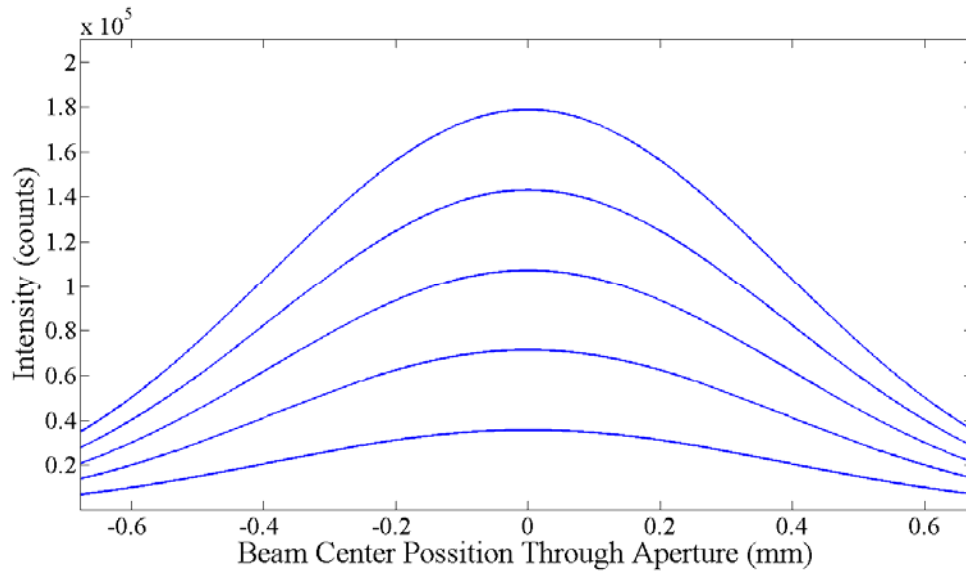


Figure 41. Signal intensity strengths for five different attenuation levels of the HeNe laser beam centered on one axis and swept across the aperture along the other axis. The strongly attenuated signal is the bottom curve and the above curves are due to decreasing the amounts of beam attenuation.

If the center of the Gaussian beam is positioned approximately 0.33 mm off center on one axis, small displacements of the cantilever cause a linear change in the intensity. The peak-to-peak voltage signal created at the photodiode is due to the linear regions of the beam intensity profile caused by the clipping iris when the center of the beam was shifted by a total distance of $2d$. The sinusoidal peak-to-peak voltage signal from the photodiode and the magnitude of the lock-in amplifier signal were used to collect the photoacoustic spectral data from the sample gas. The higher the intensity of the HeNe beam, the stronger the amplitude response of the PA signal. The PA signal and interferometer measurements are discussed further in the results section.

The photoacoustic test chamber, fabricated by the AFIT model shop team, shown in Figure 42, was setup in the THz Spectroscopy Research Laboratory at the Wright State University campus in Fairborn, Ohio.

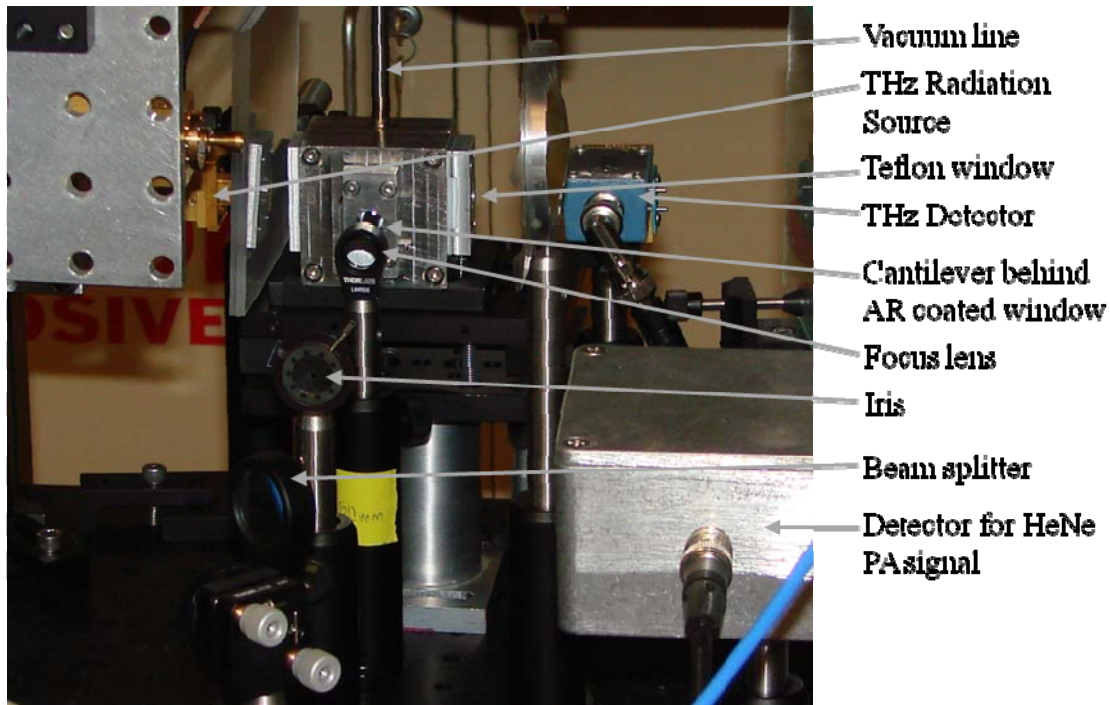


Figure 42. Photograph of experimental setup highlights the PA chamber, optics, iris, detector for HeNe PA signal, THz radiation source, and THz detector.

There is a welded feed through for an electrical signal line that can be used with a piezoelectric cantilever design. A single $\frac{1}{4}$ in stainless steel vacuum line connection is also welded to the PA chamber. The front surface of the chamber was modified to mount two gold coated pushpins which can provide an electrical connection to a top and bottom metal electrode for future cantilever designs. The ends of the cylindrical absorption chamber are sealed with o-rings and ~ 1 mm thick Teflon windows which are pressed in place with a face plate and screws. Teflon material is optically transparent over the wavelength spectrum we are investigating with the radiation source. When the cantilever sample is mounted inside the chamber, it is centered behind a quartz or anti-reflective (AR) coated window that is connected to the chamber with o-rings and face plate in the same fashion as the Teflon windows.

Identified in Figure 42 is the THz radiation source and THz detector to capture the transmitted THz output signal. In front of the chamber is a small lens with a 5 cm focal length to focus the laser on the tip of the cantilever. The reflected signal off of the cantilever then goes back through the iris, off the beam splitter, and the final PA signal is measured at the silicon photo detector. The HeNe photo detector outputs a voltage signal caused by either the iris clipped beam or the interferometer signal when the reference arm is used. A metal housing around the detector successfully reduced some of noise in the detector output signal.

5.2. Cantilever Dynamics

To investigate the cantilever and photoacoustic chamber performance, methyl cyanide was selected because it has documented absorption lines over a large spectrum (0.018 – 1.8065 THz), making it an ideal gas since the radiation source can span a large portion of that spectrum. Also, methyl cyanide has both strong and weak absorption line strengths within that frequency range, which would demonstrate the large dynamic range capability of the cantilever PA system. Initial photoacoustic data was taken using an absorption line frequency of 312.633 GHz, identified as Freq 1 from here forward. Then, to acquire the optimal PA signal from the cantilever, a modulation frequency scan was performed using the THz Freq 1 absorption line. Modulation frequency scans from 1-700 Hz found that the maximum PA signal was achieved when the system was modulated at the resonant frequency ($\omega \cong \omega_o$) of the cantilever. Figure 43 shows the PA signal from the lock-in amplifier as a function of modulation frequency over the 3-400 mTorr pressure ranges tested using the $5 \times 2 \times 0.01 \text{ mm}^3$ cantilever design.

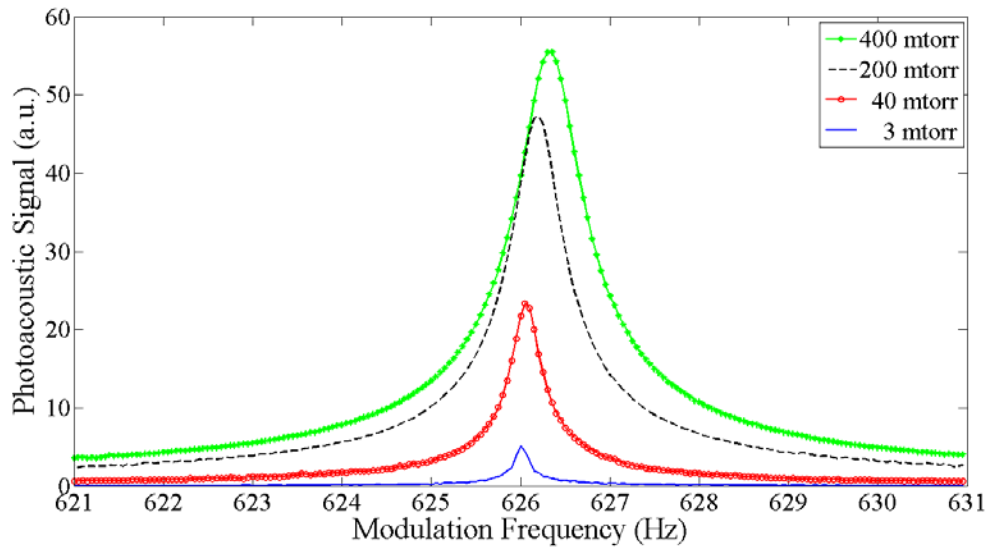


Figure 43. PA response of the $5 \times 2 \times 0.01 \text{ mm}^3$ cantilever as a function of modulation frequency for four different pressures tested revealed the maximum PA signal was achieved at slightly higher modulation frequencies with increased chamber pressure.

A plot of the modulation frequencies that achieved the maximum amplitude displacement are shown versus the chamber pressure in Figure 44. The required modulation frequency to achieve the maximum PA signal increased with a slight non-linearity with increasing chamber pressure; approximately $8.8 \times 10^{-4} \text{ Hz/mTorr}$ for the $5 \times 2 \times 0.01 \text{ mm}^3$ cantilever over the pressures tested.

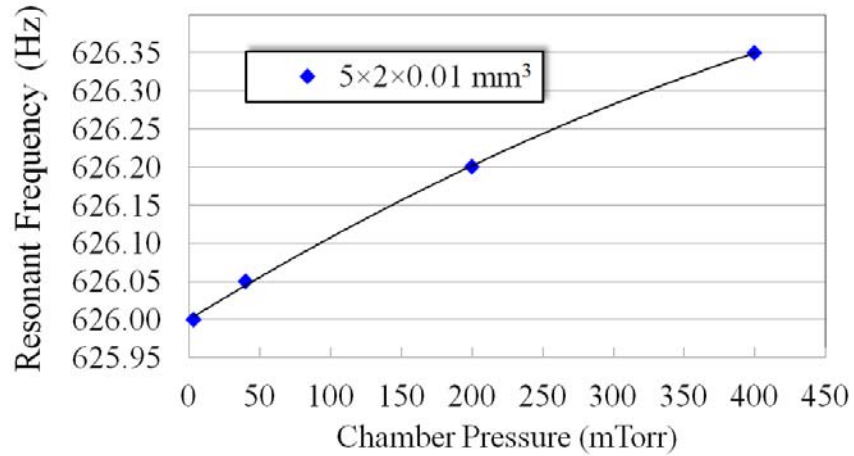


Figure 44. Resonant frequency of the $5 \times 2 \times 0.01 \text{ mm}^3$ cantilever taken over a range of pressures shown with a second degree polynomial curve fit.

The modulation frequency response of the $5 \times 2 \times 0.005 \text{ mm}^3$ cantilever is shown in Figure 45. The maximum chamber pressure tested for the $5 \text{ }\mu\text{m}$ thick cantilever was lower due to the increased amplitude response of the more sensitive cantilever design. The frequency response of the $5 \times 2 \times 0.005 \text{ mm}^3$ cantilever design increased at a very linear $4.3 \times 10^{-3} \text{ Hz/mTorr}$, over the smaller pressure range tested. The chamber pressure played a more significant role in the resonant frequency of the $5 \text{ }\mu\text{m}$ thick cantilever. The resonant frequency shift, with increasing chamber pressure was 4.86 times faster with the $5 \text{ }\mu\text{m}$ thick device compared to the $10 \text{ }\mu\text{m}$ thick cantilever design.

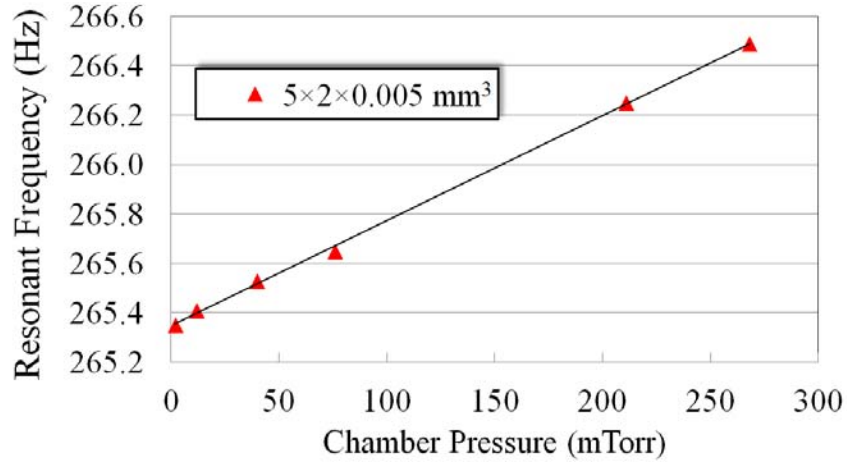


Figure 45. Resonant frequency response for the $5 \times 2 \times 0.005 \text{ mm}^3$ cantilever was taken over a smaller pressure range and had a linear increase with chamber pressure.

The small observed shifts in the resonant frequencies of the cantilevers was attributed to an increase in the effective spring constant of the system due to the gas interactions with the cantilever, which increased the spring constants as a function of chamber pressure. Several groups have reported similar shifts in resonant frequency with changes in pressure and for different gas compositions [87, 109, 110]. More importantly, from the modulation frequency scans, the quality factor of the cantilever in the low vacuum conditions was assessed. Quality factor of a cantilever can be expressed as

$$Q = \frac{\omega_o}{\Delta\omega} = \frac{f_o}{\Delta f} \quad (5.2)$$

where f_o is the resonant frequency of the cantilever and Δf is the full width at half the maximum of the PA signal. Due to the low damping conditions of the rarified gas in the PA chamber, the cantilevers had a sharp resonance response to the modulation frequency scan and small Δf values of 0.15-2.08 Hz were measured. At the low vacuum pressures tested, the $5 \times 2 \times 0.01 \text{ mm}^3$ and $5 \times 2 \times 0.005 \text{ mm}^3$ cantilever design had very high quality

factors which are shown in Figure 46. A high quality factor here is desirable because the cantilever amplitude displacement is increased for small applied pressure loads.

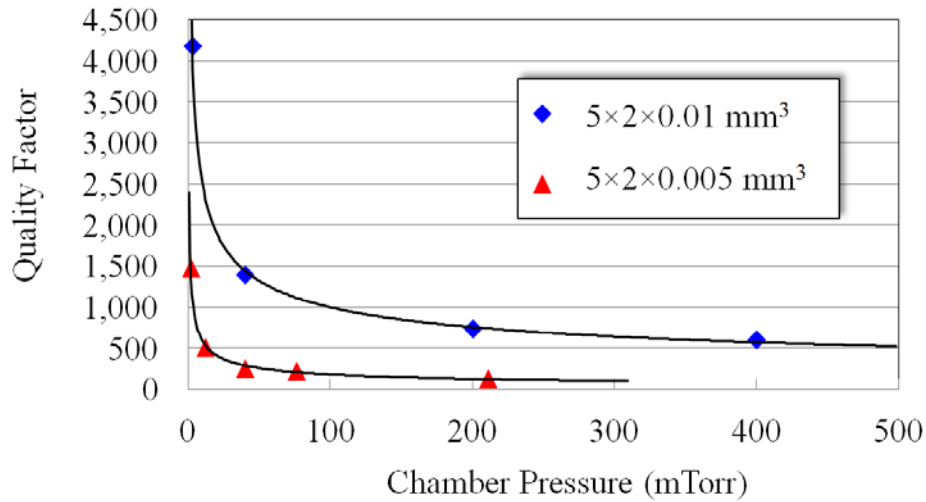


Figure 46. Based on Equation (5.2), the quality factor for the $5 \times 2 \times 0.01 \text{ mm}^3$ and $5 \times 2 \times 0.005 \text{ mm}^3$ cantilever designs were evaluated over a segment of low chamber pressures.

Modulating the THz radiation at the resonant frequency of the cantilever found at each pressure, the dynamics of cantilever excitation and relaxation were investigated. Shown in Figure 47 is a sample of PA data collected from the system at a chamber pressure of 3 mTorr using THz Freq 1. The duration of the modulated THz excitation was 8 s, and it can be seen in the graph that the lock-in PA signal was just approaching a steady state before the radiation was turned off. The long required excitation time at lower chamber pressures is expected due to the extremely low pressure change generated per modulation pulse.

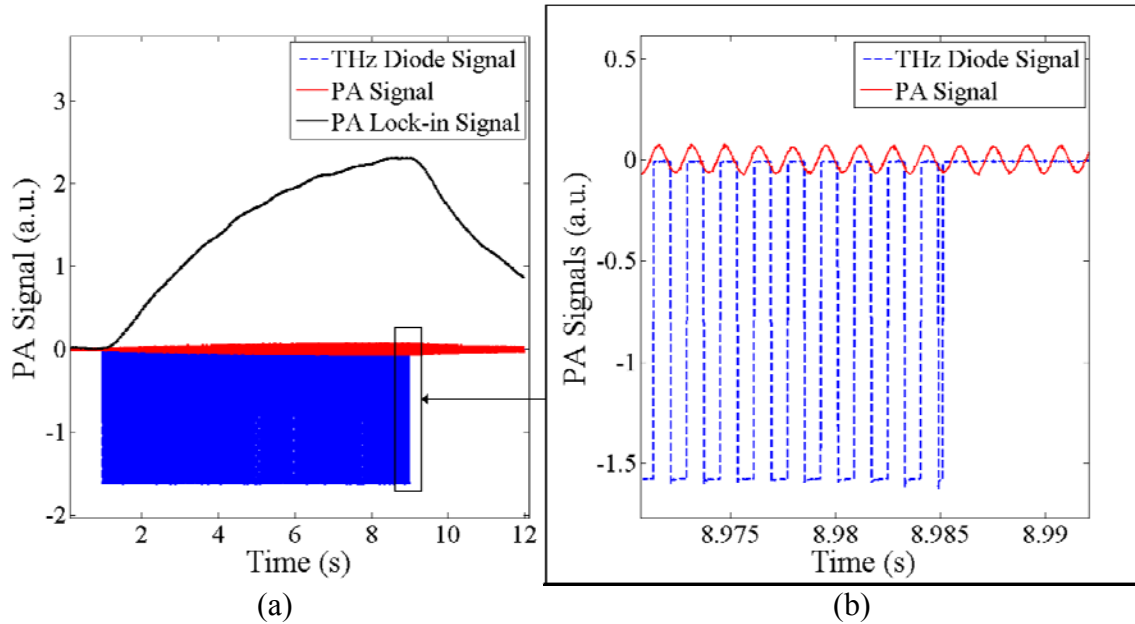


Figure 47. PA data recorded at 3 mTorr in plot (a) shows the slow response of the lock-in amplifier and raw PA signals at the low chamber pressure and a quality factor of 4,085. Plot (b) is a zoomed in view of the raw PA signal from the diode and modulated THz signal as the radiation turned off.

As the chamber pressures increased, the PA signal response time for the cantilever to reach a stable amplitude periodic deflection decreased. Shown in Figure 48, PA data collected at a chamber pressure of 80 mTorr. The higher chamber pressures showed a more rapid approach to periodic steady state conditions, generated a stronger PA signal, and the output of the lock-in amplifier signal reached a steady state value in approximately 4 s.

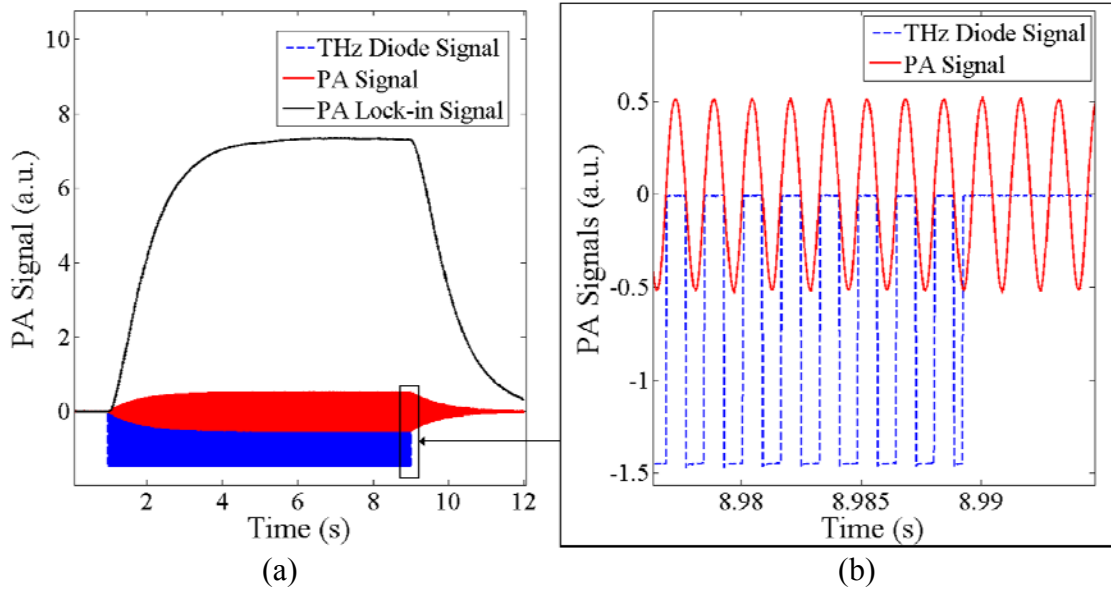


Figure 48. PA data in plot (a), taken at 80 mTorr had a quality factor of 1,091 illustrates the quicker response time of the lock-in PA signal and raw PA signal from the THz excitation radiation at higher chamber pressure. Plot (b) is a zoomed in view of the raw PA signal from the diode and modulated THz signal.

For a range of pressures, the cantilever was brought up to an excited periodic amplitude deflection, the THz radiation was turned off, and the exponential decay of the PA signal was recorded. An exponential curve fit was then performed on the PA data to extract the time constant, τ . The resulting time constant versus pressure plot for the $5 \times 2 \times 0.01 \text{ mm}^3$ cantilever design is shown in Figure 49. Time constants dramatically decreases as the chamber pressure gets lower and moves from the molecular to intrinsic damping pressure regime. For the investigated pressures, an equation for the time constant as a function of pressure was found to be

$$\tau(p_c) = 0.2162 p_c^{0.3304} \quad (5.3)$$

where the chamber pressure p_c is given in mTorr. The resultant function shown in Equation (5.3) had a strong correlation to the experimental measurements and had an R-squared value of 0.9994.

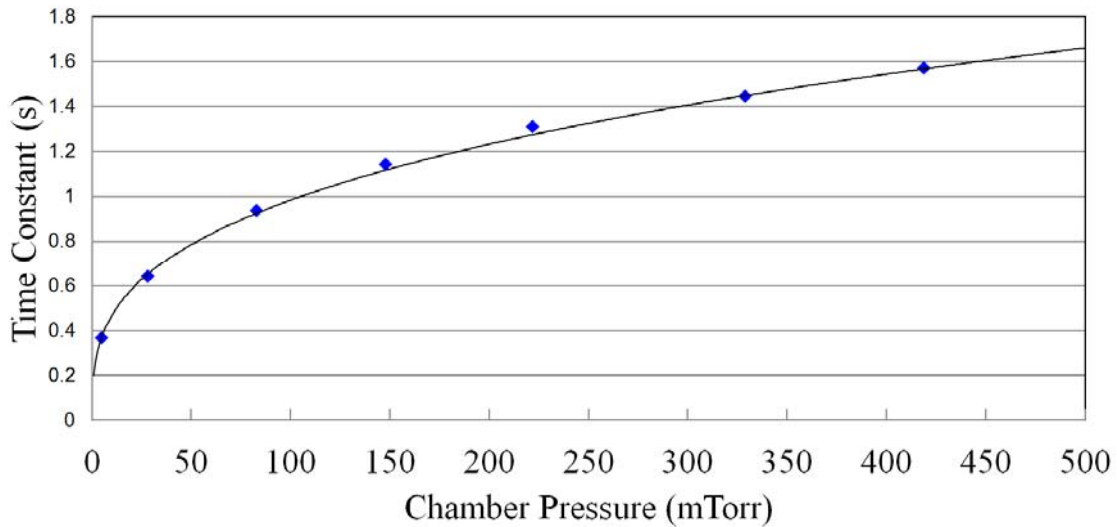


Figure 49. Time constants found through exponential curve fit to the decay of PA signals over the range of pressures shown for $5 \times 2 \times 0.01 \text{ mm}^3$ cantilever.

Equation (3.5) described the photoacoustic change in pressure as a linear function of the THz radiation source output power. To investigate the linearity of the PA signal measurement, multiple power levels were evaluated by reducing the THz radiation power prior to insertion in the PA chamber. In the THz region of the electromagnetic spectrum, a piece of thin plexiglass reduces the amount of transmitted power by $\sim 50\%$ through absorption and reflection mechanisms. To establish a baseline, PA data was first collected with the THz radiation source unattenuated. For this discussion, the unattenuated radiation power is referred to P_0 , meaning no plexiglass was used. When one plexiglass plate is used between the THz source and the PA chamber, the condition is referred to as P_1 , two pieces as P_2 , and so on. As the number of plexiglass plates increased, the PA signals decreased. Figure 50 shows a zoomed in view of the four power conditions tested; the THz diode signals are the dashed lines and the PA signals are the corresponding solid lines of the same color.

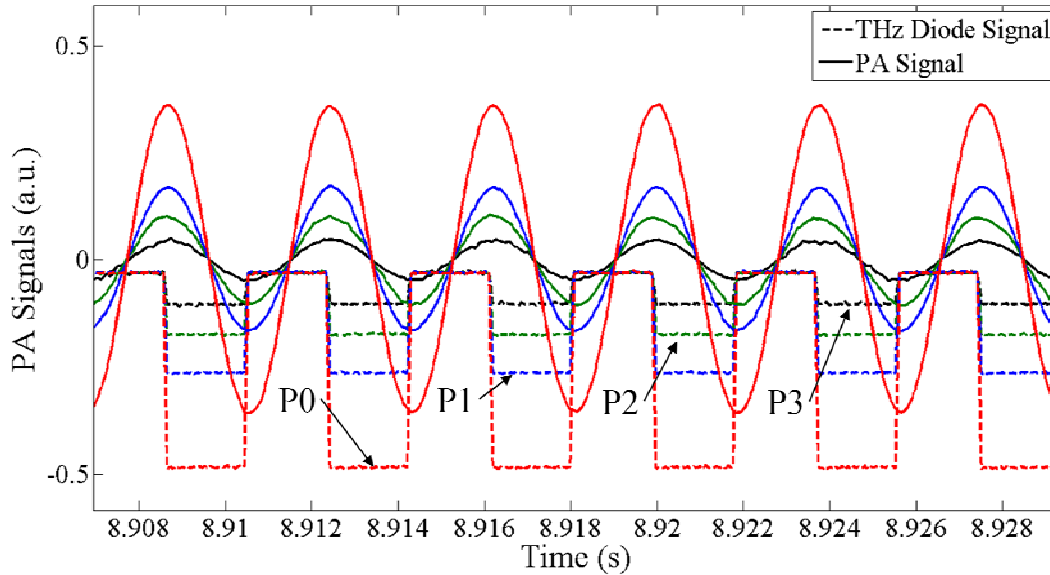


Figure 50. Measured THz diode signal and corresponding PA signals for four different THz source powers P0-P3 inserted into the PA chamber.

The data set collected above in Figure 50 is shown in its entirety below in Figure 51 and includes the PA signals from the lock-in amplifier. Due to the high frequency of the signals, the PA signals shown in red and the THz diode signals in blue are not individually resolvable in the figure. The lock-in PA signals labeled P0-P3 in Figure 51 grew uniformly under the excitation pressures at the four THz input powers. The amplitude of the PA signal labeled P0 grew much more rapidly due to the higher THz radiation power. The signals reached a stable excited state condition by time ≈ 6 s, then the THz radiation was turned off at time = 9 s and the PA signals decayed down to a near motionless state of rest.

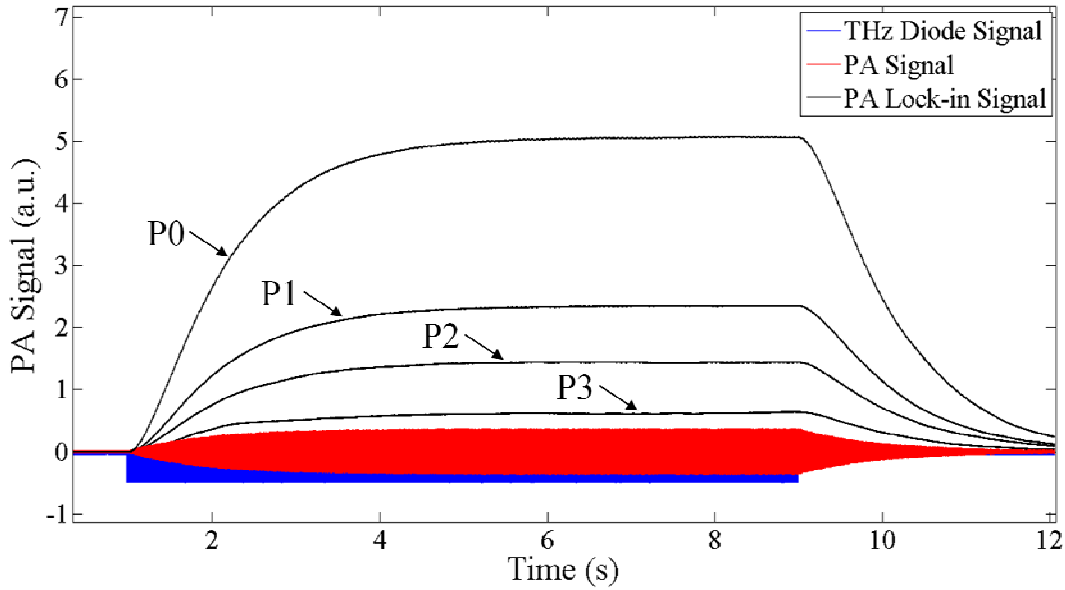


Figure 51. PA Lock-in Signals generated due to the P0-P3 power levels of the THz radiation source.

As the THz radiation power was attenuated with plexiglass, the relative changes in the THz diode signal and PA signals are compared in Table 5. When the system was transitioned from no attenuation to one piece of plexiglass (P0→P1), there was a 48.33% reduction in the THz diode signal strength, 53.01% reduction in the PA signal, and a 53.55% reduction in the PA lock-in signal. The transitions from P1→P2 showed a 38.27% reduction and P2→P3 had a 49.59% reduction in THz diode signal. Differences in the amount of THz diode signal reduction was due to the small variation in thicknesses of the plexiglass sheets which were approximately 1/16th of an inch thick. For all cases, the change in the lock-in PA signal was greater than the change in the raw PA signal.

Table 5. Relative change in PA signals as power inserted into the chamber is reduced.

	Δ THz Diode Signal (%)	Δ PA (%)	Δ Lock-in PA signal (%)
P0→P1	48.33	53.01	53.55
P1→P2	38.27	38.39	38.80
P2→P3	49.59	55.56	56.06

The mean of the PA signals over ten modulation periods taken after 8.9 s in the data set and was plotted versus the mean THz diode signal in Figure 52. PA signal data in red and the lock-in PA signal in black showed linear responses to the changes in THz radiation input power. The lock-in PA signal used a time constant of 300 ms, measuring the PA signal amplitude at the modulation frequency over a larger time interval. The PA signal, measured over a smaller time scale contained the entire diode signal frequency spectrum in the real time measurements. Both PA signals cross below the zero value on the Y-axis because the output of the THz diode voltage signal is non-zero even when the THz radiation source was off.

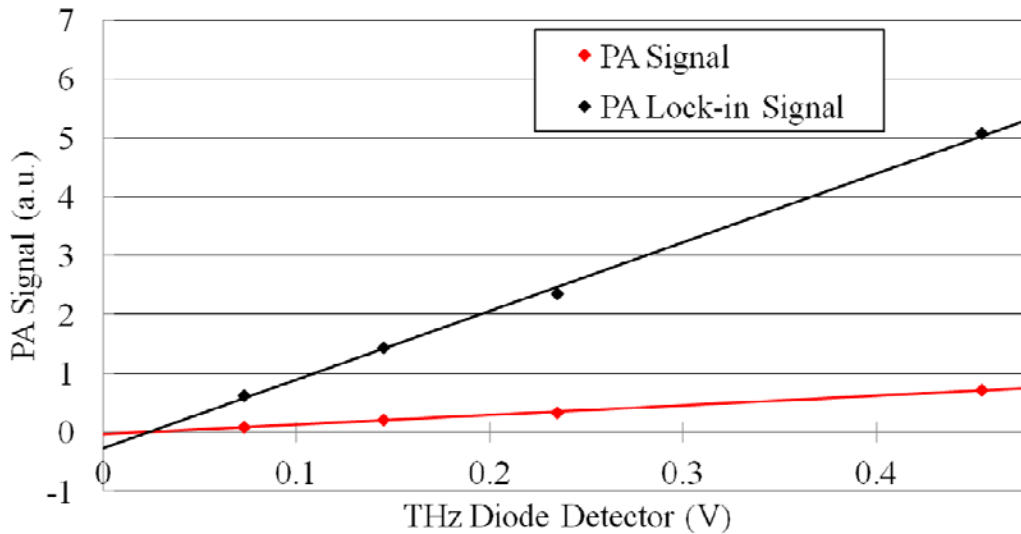


Figure 52. Linear response of the PA Signal and PA Lock-in Signals produced versus the absolute value of the THz detector voltage.

To quantify the PA signal generated by the diode voltage measurements, cantilever displacement measurements with a Michelson interferometer configuration were performed. Peak-to-peak PA signal and cantilever tip displacement measurements shown in Figure 53 were taken across a small range of pressures. The diamond shaped markers represent the peak-to-peak PA signal, corresponding to the axis scale on the left side of the graph. Circular data points on the graph with error bars correspond to the axis on the right which shows the amplitude of cantilever deflection from center position given in microns. When the chamber was pumped down to a high vacuum condition, no THz PA signal could be measured. It can be seen in the graph that as the pressure increased with the addition of methyl cyanide, the measured PA signal and cantilever deflection continued to increase with pressure. Above $\sim 7 \mu\text{m}$ deflection, the PA signal increased only slightly due to the positioning of the laser beam through the iris. This strong correlation between the PA signal and deflection measurements provide good justification for using the iris clipped PA method for the range of deflections encountered. An additional advantage of the of the iris clipped PA method is the modest required sampling rate; four channels of data can be digitized at 60k samples per second, allowing for multiple channels of data to be collected simultaneously.

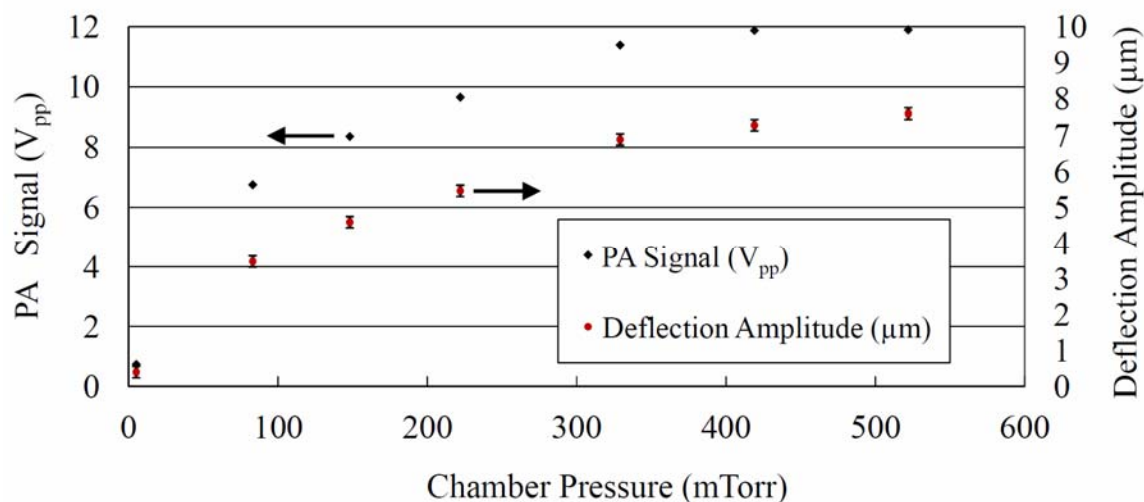


Figure 53. Graph of measurements taken on $5 \times 2 \times 0.01 \text{ mm}^3$ cantilever at different chamber pressures show PA peak-to-peak signals represented by a diamond shape corresponded to the scale on left while the interferometrically measured cantilever amplitude deflections, shown with a circle and error bars correspond to the deflection scale on the right.

5.3. THz Photoacoustic Spectra

Based on the pressure dependent dynamic cantilever behavior in the PA system, a few techniques were developed to accurately collect PA molecular spectra. Photoacoustic spectral data collection was also performed across a range of pressures. As discussed earlier in the cantilever sensor analysis, chamber pressure greatly affected PA signal strength and response time. Therefore, two data collection techniques were investigated; fast scan methods to coarsely cover a broader frequency spectrum and a slow scan method to achieve a stronger and more accurate PA signal. Spectral data collection measurements were performed in two steps, excitation and signal averaging segments. The amplitude modulated THz radiation at the specified THz frequency was turned on for a period of time, which was defined as the excitation time. This excitation time or period allowed the cantilever to attain a stable periodic level of amplitude

displacement from the generated PA pressure pulses. After the excitation time, the PA signal was averaged over the second specified interval, referred to as the signal averaging period. The PA signal measured during the signal averaging period was recorded as the PA signal for that specific THz frequency. The THz frequency was then increased by a small amount, referred to as the frequency step size, and the measurement sequence was repeated.

To show the effects of excitation time and resulting PA signal, multiple excitation times were investigated. The signal averaging period was held constant for each of the trials and was set to a 0.1 s duration. Shown in Figure 54 are the results of three excitation times, recorded at a chamber pressure of 59 mTorr with a frequency step size of 0.05 MHz, and compared to the simulated absorption spectra. The 2 s excitation PA spectral collection took 9.7 min, the 0.5 s excitation set took 2.8 min, and the 0.1 s excitation data set took 0.9 min to collect. The PA response shows a pronounced frequency shift at the rapid 0.1 s excitation time and a reduction in PA signal strength. This observed frequency shift highlights three regions of particular interest in the PA signal. First is the frequency location of the maximum PA signal, it should ideally occur at line center frequency where the maximum absorption occurs. The other two important regions are the rising and the falling edge of the absorption curve about the maximum PA signal which are due to the line broadening mechanisms mentioned earlier.

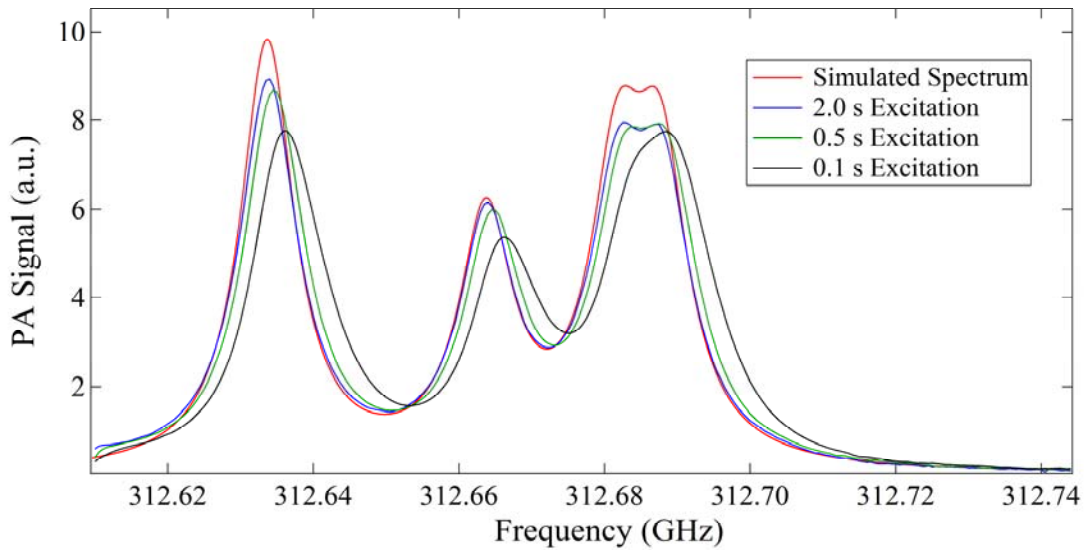


Figure 54. Spectral PA signals taken at 59 mTorr with 2, 0.5, and 0.1 s excitation times using a 0.05 MHz step size, moving from low to high frequency; the PA peak response shifted to higher frequencies and reduced amplitudes as the excitation time was decreased.

PA spectral data collection at low chamber pressures (2-60 mTorr) can take longer due to the slower cantilever amplitude displacement response times. On the rising edge of the PA signal, photoacoustic excitation to full periodic amplitude deflection under low pressure conditions can take more than 4-12 s due to the low excitation pressure generated in the chamber and the high quality factor of the cantilever resonator. Likewise on the falling edge of the PA signal, once the cantilever reaches a periodic excited state, the small damping coefficient at the lower chamber pressures and continued excitation at a lower absorption strength, causes the amplitude deflection to reduce slowly. The brief excitation time results in an overall frequency shift in the line shape of the PA signal, which could potentially be accounted for in post data processing. Radiation excitation frequency and the corresponding PA response are the crucial

parameters which would be used for chemical identification applications, so they must be accurately identified.

That being said, the fast scan technique tested above is extremely useful and could be used to quickly evaluate small spectral regions for absorption lines if an unknown chemical were evaluated with the system. Then a slower more accurate scan could be performed to identify the line center absorption frequency and the relative PA amplitudes for each absorption line. To achieve an accurate line center absorption frequency during a spectral scan, the excitation time had to be increased as the chamber pressure decreased. At the lower 2-5 mTorr pressures tested, spectral line broadening appeared to be dominated by Doppler broadening effects, and formed the narrowest spectral line widths. As line broadening increased with pressure, the frequency step size could be increased and the excitation time could be decreased. In Figure 55 a small portion of spectra was recorded for three low pressure cases. Each collection took 10-12 hours due the small 0.05 MHz step size utilized and the 12-15 s excitation time before the subsequent 0.5 s average PA signal were recorded. The PA spectra presented in Figure 55 is of interest for two reasons. This spectral region contains strong absorption lines and it also contains two peaks in close proximity, separated by only 6 MHz. The data in Figure 55 also shows the effects of pressure broadening in the PA signal as the two closely spaced absorption lines merge into one PA peak at higher chamber pressures.

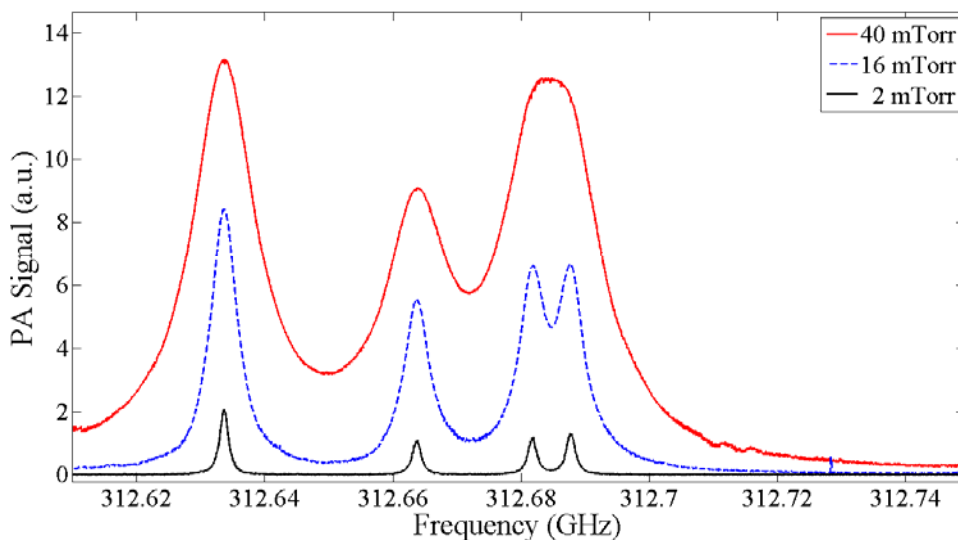


Figure 55. PA spectral data plots of CH_3CN collected with the $5 \times 2 \times 0.01 \text{ mm}^3$ cantilever at three pressures utilized a 0.05 MHz step size and recorded the 0.5 s average PA signal for each frequency step.

During the long data collection runs, the PA measurement scheme employed for the experiment using the iris clipped laser beam diode signal and lock-in amplifier signals proved to be extremely stable. The PA chamber maintained low vacuum levels well, and over the course of long data collections, the chamber pressure increased very slowly with an average system leak rate of 0.5-1 mTorr/hr.

A similar data spectral scan is shown in Figure 56, with the $5 \times 2 \times 0.005 \text{ mm}^3$ cantilever, which compares the difference between PA spectra when the THz source power was attenuated and unattenuated. The two data collections utilized a 0.05 MHz frequency step size, which produced a high-resolution PA spectra. Due to the difference in the exposed THz radiation power and corresponding PA responses, the collection parameters required modification. Since the un-attenuated THz signal caused a higher amplitude of deflection in the cantilever, the excitation time was increased to 15 s, 5 s longer than the attenuated THz data collection. The longer excitation time of the

unattenuated THz collection allowed the PA signal to reach a more stable steady state, achieve a higher signal to noise ratio, and somewhat decreased the variation in the PA signal around the 312.685 GHz frequency compared to the attenuated collection. It is clear in Figure 56 that the un-attenuated radiation source causes an increase in PA signal as well as increased broadening of the absorption line profile.

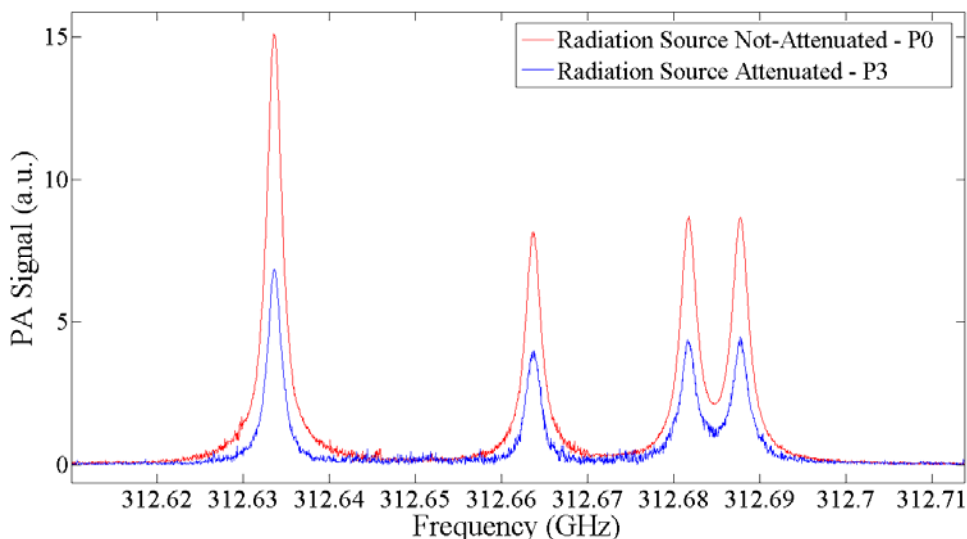


Figure 56. PA spectra with the $5 \times 2 \times 0.005 \text{ mm}^3$ cantilever recorded at 4 mTorr with the THz radiation source not-attenuated and attenuated by plexiglass.

To demonstrate the broader spectral performance of the THz photoacoustic system, a 0.72 GHz frequency scan was performed spanning 312.07-312.79 GHz. This low pressure PA signal taken at 13 mTorr successfully captured the 13 rotational absorption lines in the methyl cyanide spectral region scanned. The data collection method utilized 0.2 MHz step size, 12 s excitation, and then the 0.5 s average signal from the lock-in amplifier was recorded. This larger PA scan of methyl cyanide shown in Figure 57 took 12.5 hrs to collect and also compares the simultaneously recorded THz diode signal to the modeled absorption coefficient profile. The scaled simulated spectra

very closely matched the measured PA signature of the gas with a small deviation at higher absorption strengths. The PA signal also decreases somewhat over time, due to the chamber pressure leak rate; which discussed more later in this section.

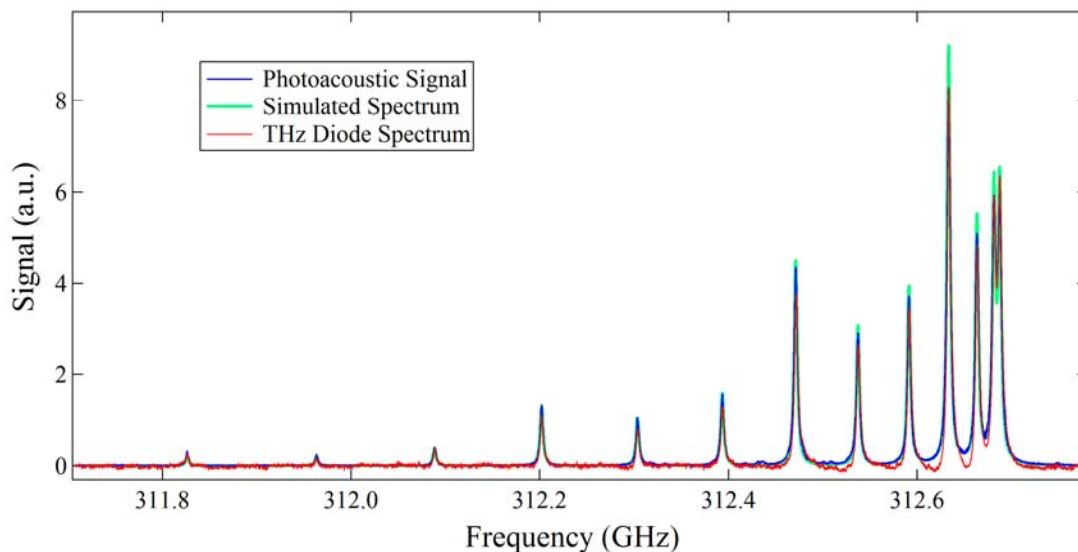


Figure 57. Photoacoustic data and the simultaneously recorded THz diode signal are compared to the simulated absorption spectra of methyl cyanide recorded at 13 mTorr with the $5 \times 2 \times 0.01 \text{ mm}^3$ cantilever.

Shown in Figure 58 are the THz diode signal in (a) and the PA signal in (b) of the rotational absorptions lines of CH_3CN recorded over the 476.7-478.15 GHz range with a $5 \times 2 \times 0.005 \text{ mm}^3$ cantilever. For the data collection, the system utilized a 0.2 MHz step size with an excitation period of 4 s, followed by a signal averaging time of 0.5 s. This spectrum took approximately 9.1 hrs to collect, over which time the chamber pressure rose from 15 to 21 mTorr. The recorded THz diode signal in Figure 58 (a) shows the signal strength after transmission through the PA chamber. The voltage signal from the THz diode fluctuated from -0.6 to -1.08 V over the frequency range scanned, which illustrates the THz diode's output strength and frequency dependence. The strong

absorption lines are visible in the diode signal while weaker lines below 476.8 GHz, are masked by the fluctuations in the diode signal and the short absorption length.

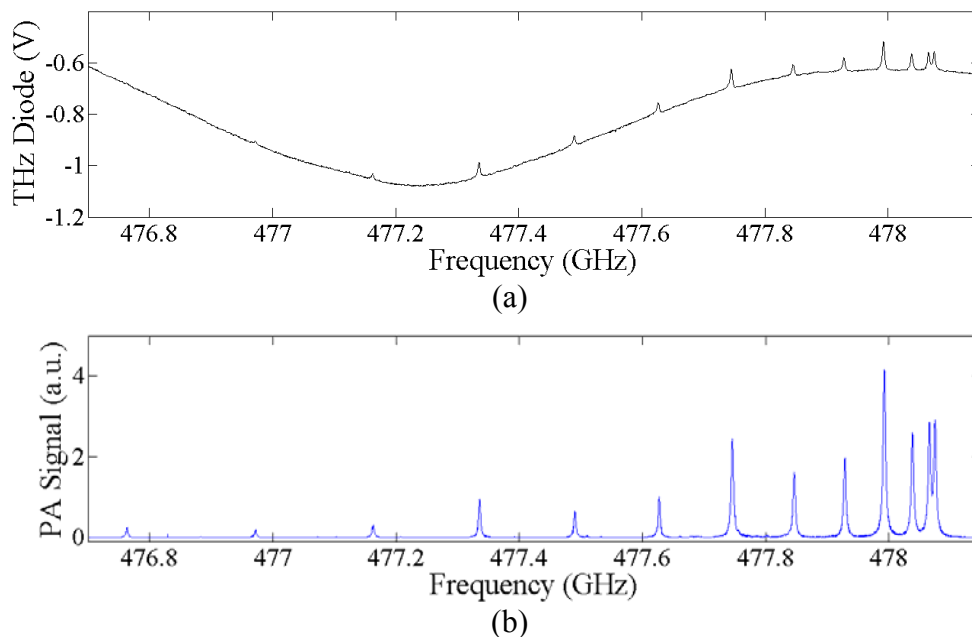


Figure 58. CH_3CN spectra collected at 15 mTorr; THz diode measured transmittance shown in (a) and simultaneous recorded PA signal in (b) from the $5 \times 2 \times 0.005 \text{ mm}^3$ cantilever sensor.

Another segment of spectra of CH_3CN is shown in Figure 59 using the $5 \times 2 \times 0.005 \text{ mm}^3$ cantilever, which was recorded at 38 mTorr. The THz diode transmittance in Figure 59 (a) showed a large power increase in the 460-461 GHz range. In Figure 59 (b), the strong PA signals below 459.7 GHz are primarily due the ground state rotational absorption lines. The spectral collection used a THz frequency step size of 0.5 MHz, an excitation time of 4 s, and then recorded the 1 s averaged PA signal from the lock-in amplifier.

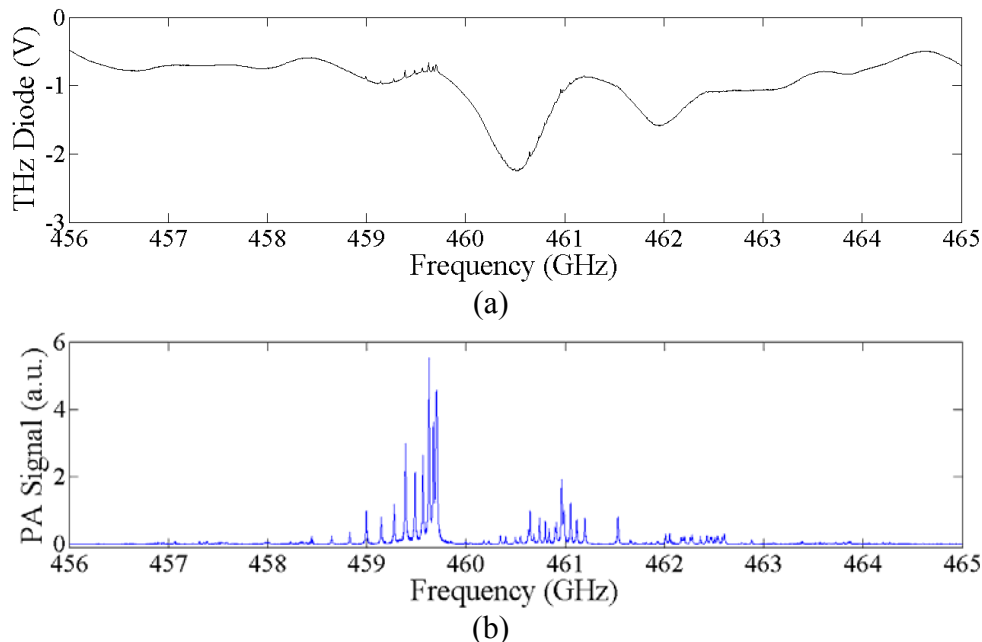


Figure 59. CH_3CN spectra collected at 38 mTorr used the $5 \times 2 \times 0.005 \text{ mm}^3$ cantilever sensor; THz diode transmittance shown in (a) had a large power increase between 460-461 GHz and the simultaneously recorded PA signal shown in plot (b).

A zoomed in view of the PA signals from the above plot in the 459.79-461.6 GHz range is shown in Figure 60 and the signals are due to the first excited state rotational absorption lines. The overlaid simulated absorption spectra almost perfectly matched the PA data in Figure 60 that was created using a chamber pressure of 41 mTorr and a broadening conditions of 105 MHz/Torr. The increased measured THz diode transmitted power around the 460.5 GHz frequency had a small effect on the PA signal, making the PA signal slightly stronger than the simulated spectra in that region.

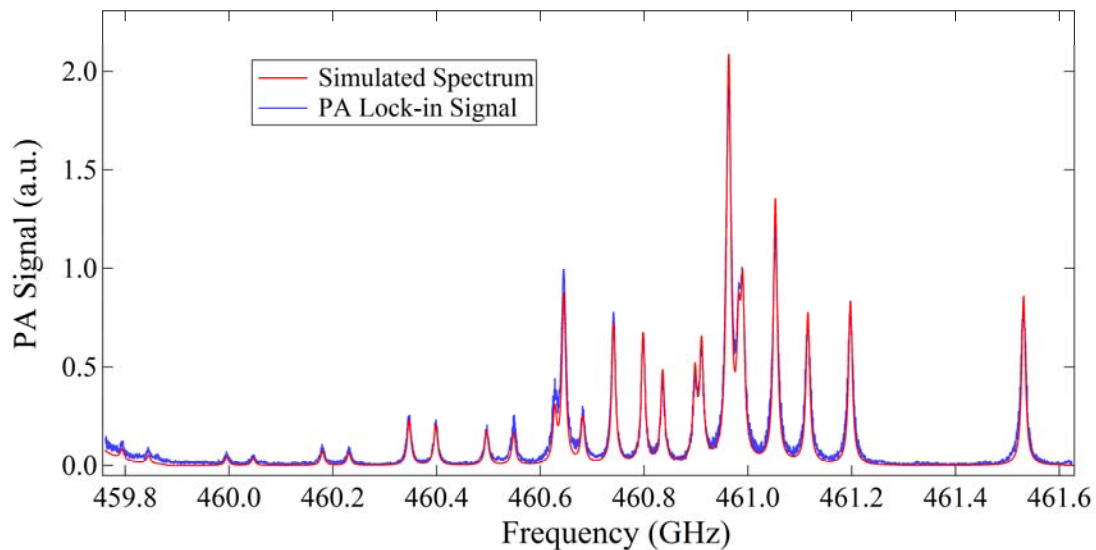


Figure 60. Simulated spectrum of CH_3CN matched very well to the PA spectral data of the first excited state rotational absorption lines in the 459.79-461.6 GHz range.

Another zoomed in view of the PA data from Figure 59 highlights the signals in the 457.1-458.7 GHz range, which is shown in Figure 61. The simulated absorption profile is due to the first excited state rotational absorption lines. In this region of the spectrum, there are other stronger absorption lines; perhaps from an excited state that are masking the weaker, ground state absorption lines.

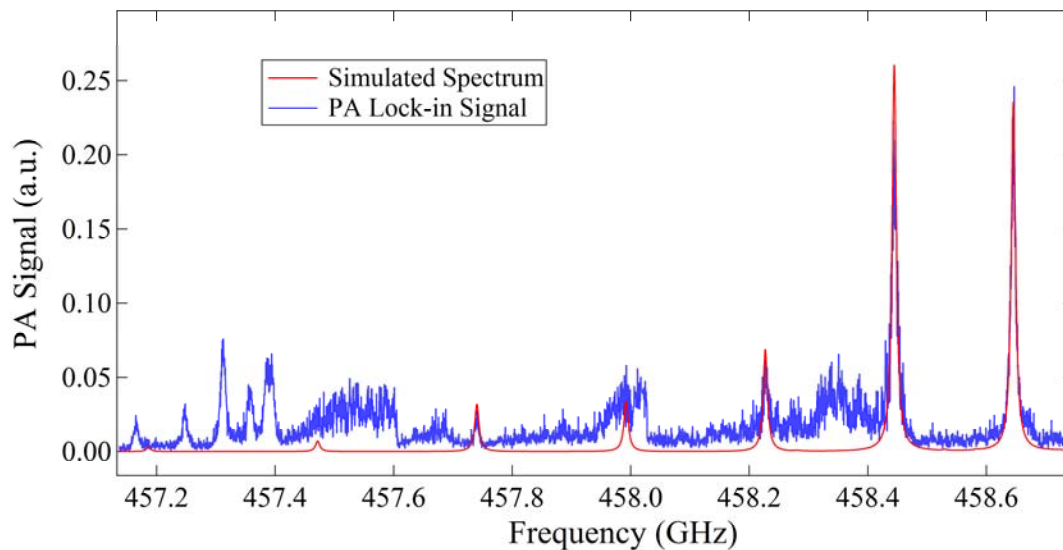


Figure 61. Stronger excited state absorption lines masked the weaker ground state absorption lines of the simulated spectrum at 457.186 GHz, 457.471 GHz, and 457.992 GHz.

A final zoomed in view of the PA data from Figure 59 highlights the signals in the 461.6-462.6 GHz range, shown in Figure 62. Several excited state rotational absorption are observed over the 461.6-462.6 GHz interval, which are not accounted for in the simulations from the database.

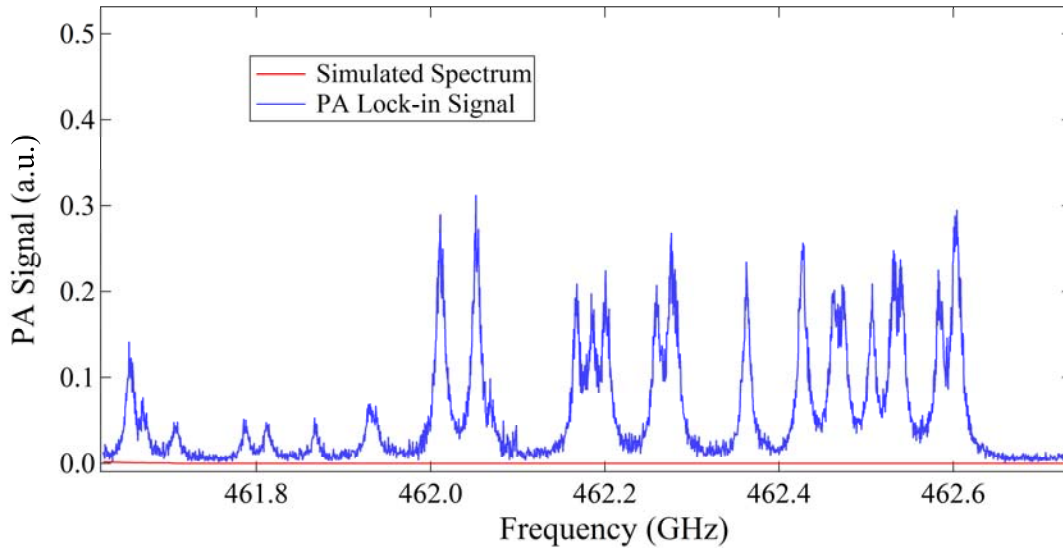


Figure 62. PA spectra of higher excited state absorption lines not accounted for in the simulated spectrum are shown from 461.6-462.6 GHz.

The highest chamber pressure used to collect PA spectra with the $5 \times 2 \times 0.005 \text{ mm}^3$ cantilever was 268 mTorr. Simultaneously recorded THz diode signal from the spectral collection is shown in Figure 63, with the corresponding PA data shown in Figure 64 and Figure 65. The spectra was collected using a 3 s excitation, 1 s signal averaging time, and 1 MHz frequency step size. In the frequency range shown, the THz source data sheet listed an output power of $\sim 50 \text{ } \mu\text{W}$. At this low radiation power, fluctuations in the THz diode signal measurements were more apparent as the frequency was increased in the 1 MHz steps. The THz diode signal mean fluctuation was $2 \times 10^{-4} \text{ V}$ between each frequency step increment. These fluctuations could be due to noise in the detector signal or due to fluctuation in the output power of the amplitude modulated radiation source. If a small portion of the fluctuations are due changes in the output power, that would translate to some variation in the PA signal as well. Other than the strong absorption

lines around 588 GHz, there are no obviously distinguishable absorption peak in the THz diode signal.

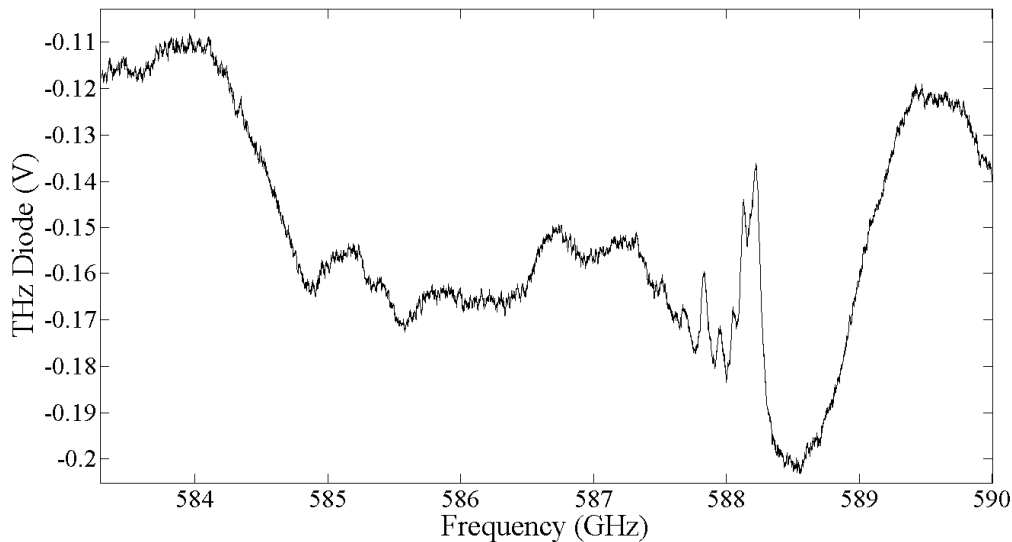


Figure 63. CH₃CN THz diode transmittance spectra collected at 268 mTorr showed a 2×10^{-4} V mean fluctuation in the signal magnitude between frequency steps.

The relatively high chamber pressure of 268 mTorr caused the absorption lines to broaden and generate the large PA signal shown in Figure 64. A zoomed in view of the data set shown in Figure 65 highlights the large number of weak absorption lines below 586 GHz that became more prominent due to the elevated chamber pressure. Another effect of the higher chamber pressure is that the broadening of the absorption lines elevates the effective noise floor of the measurements, reducing the SNR. More analysis on the SNR value of the measurements is discussed later in this section.

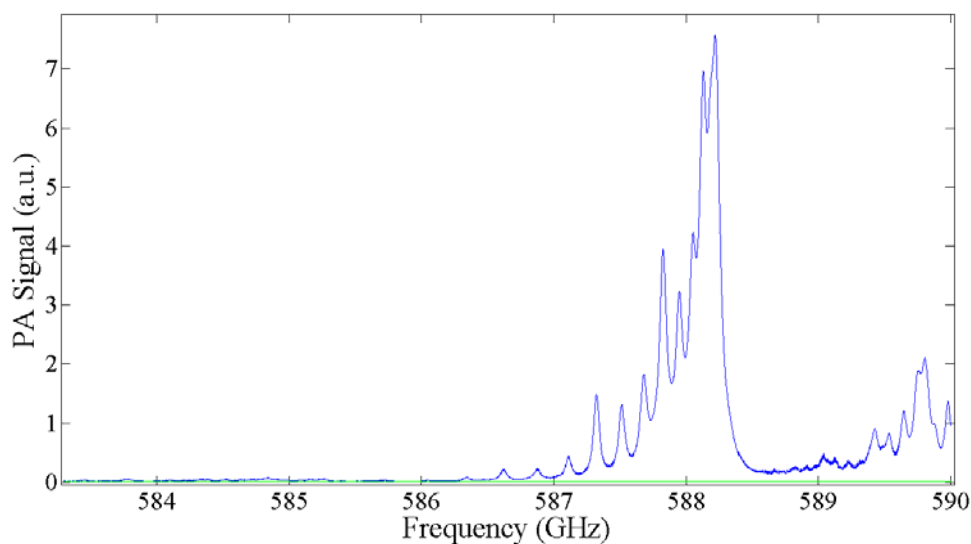


Figure 64. PA spectra of CH_3CN collected at 268 mTorr with the $5 \times 2 \times 0.005 \text{ mm}^3$ cantilever sensor showed significant line broadening due to the high chamber pressure.

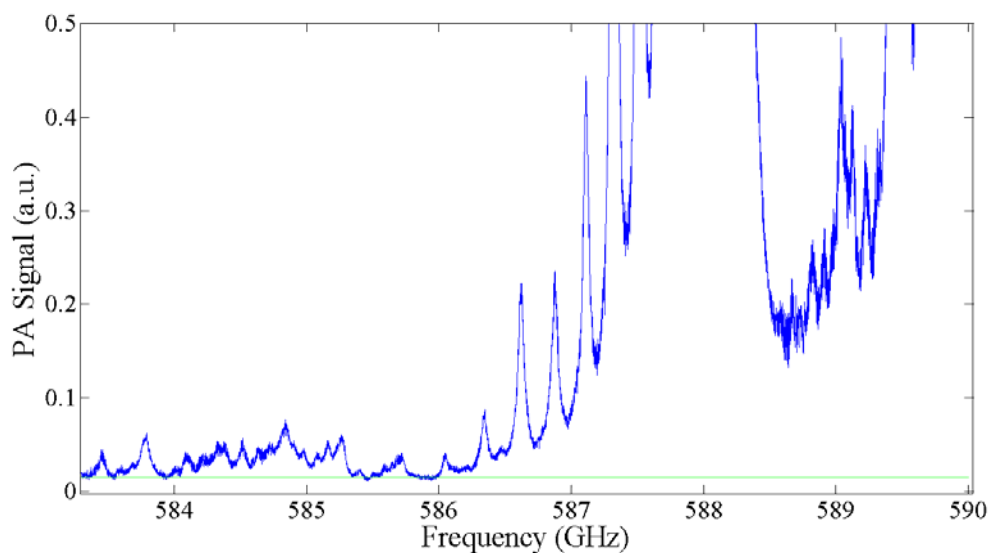


Figure 65. Zoomed in view of the same PA spectra shown in Figure 64 has a large number of weak spectral absorption lines below 586 GHz that are visible due to the high chamber pressure.

The PA system setup had a low leak rate of 0.5-1 mTorr per hour, depending on the chamber pressure. To evaluate the leak rate effect on the PA signal, a modulation frequency scan was performed over a 23 hour period, every hour, a modulation scan was

performed which took 15 min. Over the course of the data collection, the chamber pressure rose from 10 mTorr to 22 mTorr in 23 hours. The result of the modulation scans are shown in the two plots in Figure 66 and Figure 67. The modulation scans were performed on the $5 \times 2 \times 0.005$ mm³ cantilever, over the 260-270 Hz frequency range at 0.05 Hz increments. In Figure 66, the peak amplitude of the PA signal dropped a small percentage every hour and the amplitude of the PA signal was reduced by a total of 66.9% over the 23 hour period. In Figure 67, all 23 of the data sets are overlaid in the plot; the PA signal reduced in amplitude and increased in resonant frequency by 0.1 Hz due to the increase in chamber pressure. The arrow in Figure 67 indicates the direction of the maximum PA signal strength over time. As the chamber pressure rose, the partial pressure of the CH₃CN gas in the chamber was reduced, which resulted in the corresponding reduction in PA signal strength. The partial pressure factor was discussed in Equation (3.5) and it clearly affects the generated PA changes in pressure over long data collections. The change in PA signal strength with respect to chamber pressure increases quickly at lower pressures because the quality factor of the cantilevers rapidly decreases with increased pressure below 50 mTorr (see Figure 46 for quality factors).

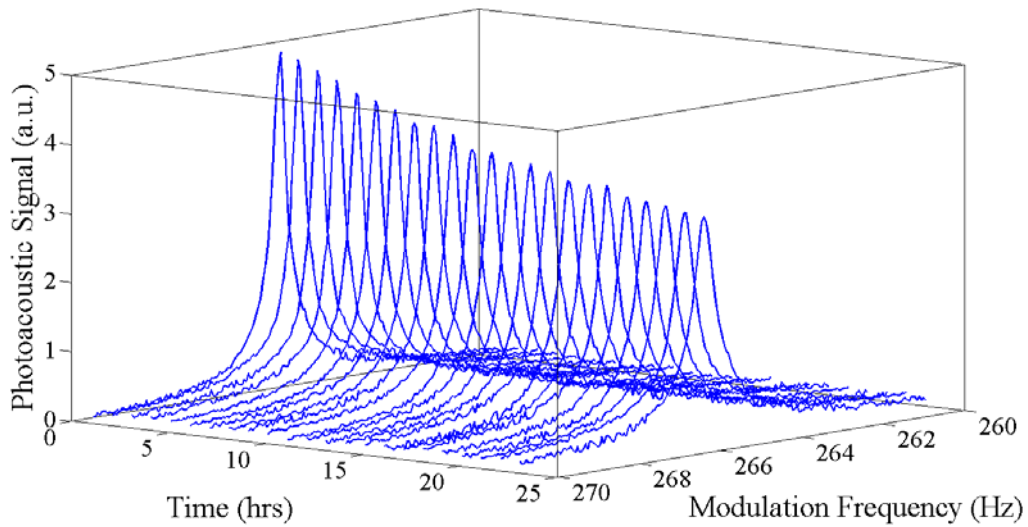


Figure 66. 3-D view of PA modulation frequency scan data collected over a 15 min period every hour for a 23 hr period showed a 66.9% reduction in PA signal amplitude over the test period.

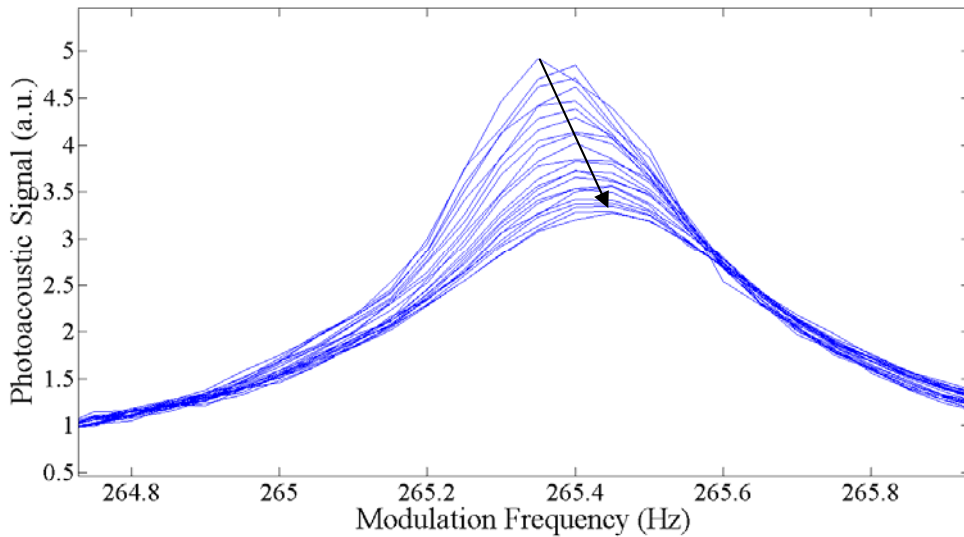


Figure 67. 2-D view of data scan showed a 0.1 Hz increase in the modulation frequency required to achieve maximum PA signal as the chamber pressure rose from 10 mTorr to 22 mTorr over the 23 hour period.

Based on the PA spectra, the performance of the system was systematically evaluated for each data collection set. The SNR, given in Equation (2.6), was first

evaluated by determining the maximum and minimum signals found in the spectra. Locating the maximum value was done through MATLAB[®] scripts, where the maximum PA signal value and the location in the array of data was found. To determine the noise floor of the PA signals, several methods were considered. The noise level of the PA measurement was assessed from the PA data with the THz source on. For an optimal low noise signal, the noise measurements must be performed away from strong rotational absorption lines and away from any weak excited state ro-vibrational absorption lines. Strong absorption lines experience more line broadening with increasing chamber pressure. Therefore, there can be significant PA signal in the tail of the absorption profile even at relatively low pressures.

To locate the noise floor of the PA signal, the root-mean-squared (RMS) value of the signal was calculated for different interval sample sizes. The $Signal_{RMS}$ value for the selected intervals were calculated by

$$Signal_{RMS} = \sqrt{\frac{(s_1^2 + s_2^2 + \dots + s_n^2)}{n}} \quad (5.4)$$

where n is the number of samples in the interval, and s is the PA signal value measured at each frequency step. From the first data point in the array to include the number of subsequent samples in the defined sample size, the RMS value of sample set size was calculated over the entire data set. The calculated SNR for the different interval sample sizes is shown in Table 6.

Table 6. SNR results for multiple sample size intervals for data set in Figure 58 (b).

Sample Size	Max Signal (V)	RMS Noise	Frequency (GHz)	SNR
10	4.1814	0.0006	476.911	6,696.9
25	4.1814	0.0010	476.941	4,156.1
50	4.1814	0.0014	476.941	2,953.5
100	4.1814	0.0017	476.911	2,479.0
200	4.1814	0.0022	476.910	1,932.3
500	4.1814	0.0025	476.854	1,668.3

A sample size $n=100$ consecutive samples provided a conservative RMS noise floor for the PA spectral data, and was used for the remainder of the analysis. Over the noise floor samples, the frequency must be away from any absorption lines and the external noise contributions during the sample set interval must also be small in order to obtain a low noise signal. The molecular spectral collection shown in Figure 58, had a maximum PA signal of 4.1814, an RMS noise signal of 1.73×10^{-3} V measured with $n=100$ over the frequency interval 476.911 GHz, and established a SNR = 2,479 for that data set.

Utilizing the sampling method described above, with $n=100$, the SNR for several of the collected data sets are shown in Figure 68. Many factors affected the SNR for each data set. Spectrums were collected over a large frequency ranges and utilized three different THz diode sources. Settings on the photodiode and lock-in amplifiers required adjustment for large versus small cantilever deflections since large cantilever displacements caused PA signals greater than 10 V, which would over load the DAQ card ± 10 V limit. The largest limitation appears to be the overall noise in PA system and in the PA measurements, which are discussed in the next section.

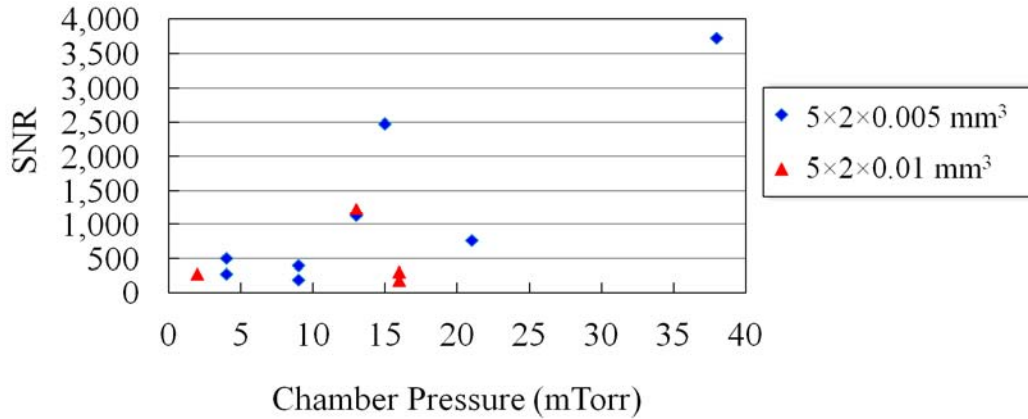


Figure 68. Calculated SNR using $n=100$ for the PA spectral data collections shown over the lower portion of the pressure range tested.

With the method for evaluating the PA signal-to-noise ratio for each data set, the important factors of sensitivity and NNEA coefficients are evaluated. Using Equation (2.7), the sensitivity (α_{\min}) of the PA measurement determines what the smallest absorption coefficient the system could detect based on the absorption strength and SNR for the measurement. The best sensitivity results for the two cantilever designs are shown in Table 7. The $5 \times 2 \times 0.005 \text{ mm}^3$ cantilever design was found to be 57.4% more sensitive than the $5 \times 2 \times 0.01 \text{ mm}^3$ design.

Table 7. Best sensitivity results for the two cantilever sensors.

Cantilever Design (mm ³)	Chamber Pressure (mTorr)	Radiation Frequency (GHz)	α_{peak} (cm ⁻¹)	SNR	α_{\min} (cm ⁻¹)
5×2×0.01	13	312.633	0.02400	1,221	1.97×10^{-5}
5×2×0.005	38	459.627	0.05387	3,719	1.13×10^{-5}

Equation (2.8) defined the NNEA as a function of the radiation source output power P_o , minimum detectable absorption coefficient α_{\min} , and the sampling time T . Although the two data collections compared in Table 8 were performed at different

regions of the frequency spectrum, they were the best performers for their respective sensor designs. The PA data set represented for the $5 \times 2 \times 0.01 \text{ mm}^3$ cantilever design is shown in Figure 57, and PA results for the $5 \times 2 \times 0.005 \text{ mm}^3$ design are displayed in Figure 59 (b).

Table 8. Best NNEA's achieved by the system for each sensor design.

Cantilever Design (mm^3)	Chamber Pressure (mTorr)	P_o (μW)	T (s)	NNEA ($\text{cm}^{-1} \text{ W Hz}^{-1/2}$)
$5 \times 2 \times 0.01$	13	~ 100	0.5	1.39×10^{-9}
$5 \times 2 \times 0.005$	38	~ 25	1	2.83×10^{-10}

There are two factors used in the sensitivity and NNEA calculations which have some margin of error associated with them. The first potential source of error is the peak absorption coefficient (α_{peak}) extracted from the simulation software which was used to calculate the sensitivity. In order to make the simulations match the recorded PA spectral data, higher than expected line broadening coefficients were used. Use of an increased broadening term also causes the peak absorption coefficient to increase, which in turn reduces the effective sensitivity. The other factor that was estimated to a close degree as possible was the power output of the THz radiation source. There are insertion losses in power as the radiation entered the PA chamber, depending how close the source was to the Teflon window, and if the power was attenuated by plexiglass prior to entering the chamber. Fluctuations in the THz diode output power are frequency dependent, which also contributes to the uncertainty of the power used to calculate the NNEA.

5.4. Performance Analysis and Limitations

The ultimate performance of the PA system can be limited by several factors, which include noise in the PA signal measurement, fluctuations in gas pressure, fluctuations in radiation output power, acceleration noise, and electrical noise. The frequency spectrum of the PA system noise and active PA signals were investigated while the chamber was at 200 mTorr. In Figure 69, a 1 s duration of PA data from the iris clipped PA signal was evaluated using Fourier analysis of the PA signal to look at the noise contributions in the frequency domain. In the inset image of Figure 69, is the single-sided amplitude of the FFT when the THz source was off. With the THz source operated at Freq 1 at a modulation frequency of 626.02 Hz, the PA signal was well over a thousand times greater than the noise. For this data collection, the PA system had a reasonably low level of spectral noise in the PA signal measurement. Two portions of the spectrum that stood out slightly were the noise signals occurring below 200 Hz and region around the resonant frequency of the cantilever. The beam block used in the data sample collection to prevent the reference arm from creating an interference signal generated diffuse reflections back to the photodiode. The reflections off the diffuse surface, unknowingly at the time, also contributed to the noise in the signal. The amplitude of the signal around the resonant frequency of the cantilever beam was attributed to the pickup of vibrations in the experimental setup due to noise and vibrations in the room.

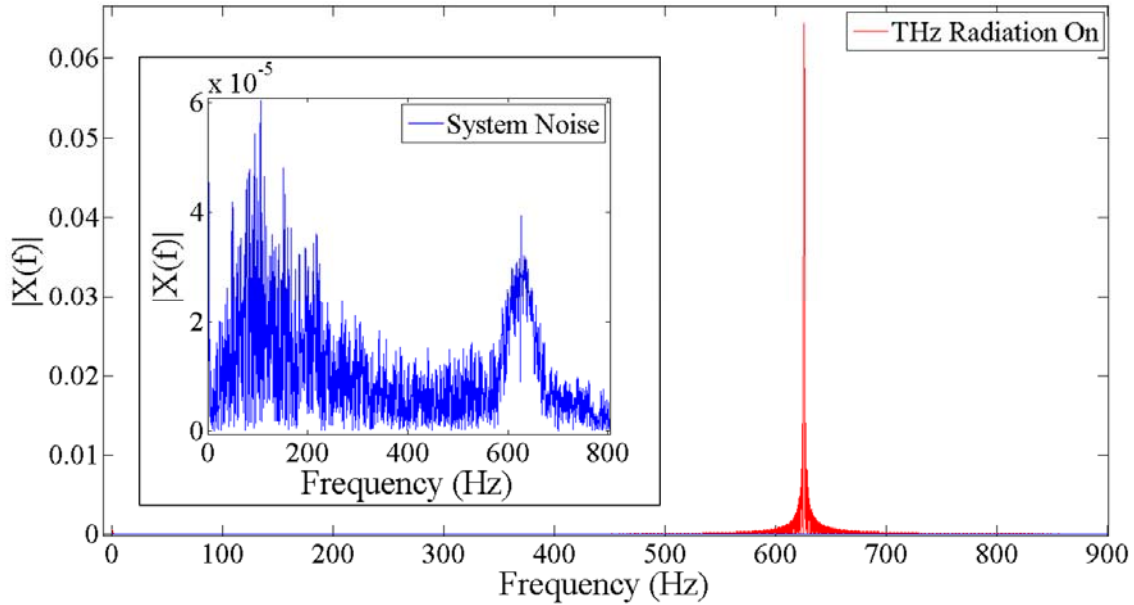


Figure 69. Fourier analysis of a 1 s photoacoustic signal, collected at 200 mTorr taken at Freq 1, showed very low noise in the system with no single dominant noise frequency in the iris clipped PA measurement method with the $5 \times 2 \times 0.01 \text{ mm}^3$ cantilever.

The noise in the PA signal of the $5 \times 2 \times 0.005 \text{ mm}^3$ cantilever design was also measured, at 268 mTorr and the results of the lower portion of the frequency spectrum are shown in Figure 70. For the measurement, the THz source was powered on, but no radiation output was being generated. The reference arm to the interferometer for this data set was blocked with a metallic surface, which reflected the laser beam down away from the photodiode detector, and further reduced the amount of noise in the signal spectrum. In this configuration, the primary sources of noise not due to the cantilever occurred at intervals of the electrical noise sources: 60, 120, 180, 240, and 300 Hz. The signal strength at the resonant frequency of the cantilever due to the small fluctuations in the cantilever position is approximately 3.5 times the strength of the electrical noise occurring at 120 Hz.

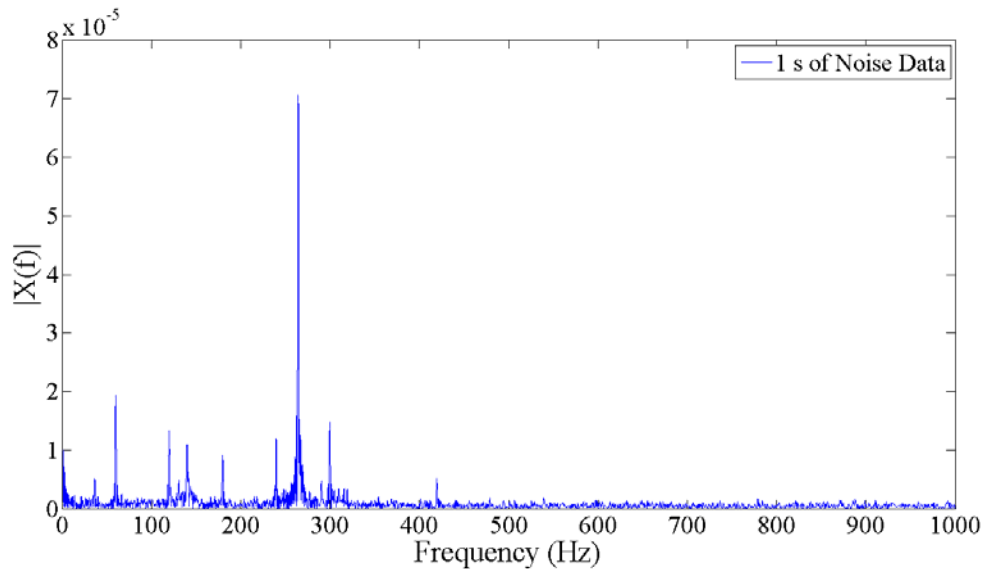


Figure 70. Lower portion of the frequency spectrum for the $5 \times 2 \times 0.005 \text{ mm}^3$ cantilever in the larger PA cell at 268 mTorr, showed significant signal at the resonant frequency of the cantilever and at 60 Hz intervals from electrical noise.

Comparing the amplitudes of the noise signals in Figure 69 and Figure 70, shows that the signal strength for the more flexible $5 \times 2 \times 0.005 \text{ mm}^3$ cantilever at the resonant frequency is approximately 2 times the amplitude of the thicker $5 \times 2 \times 0.01 \text{ mm}^3$ cantilever. Assuming the cantilevers were exposed to similar external vibrational noise sources, the more flexible cantilever design would be expected to exhibit higher deflection. An expanded view of the frequency spectrum data in Figure 70, is shown in its entirety out to 30 kHz in Figure 71. The high frequency noise in the signal is largely attributed to noise from the HeNe laser.

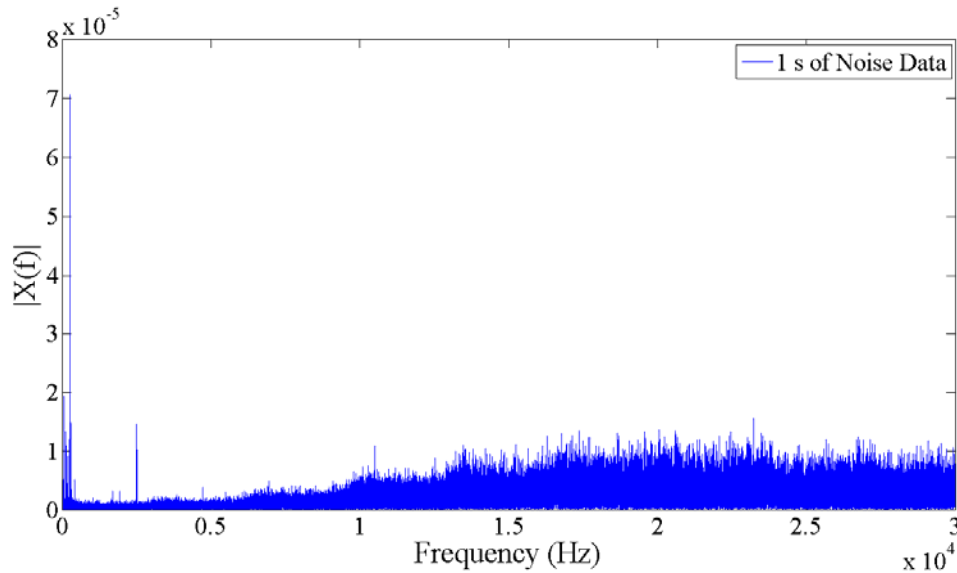


Figure 71. Complete frequency spectrum from data in Figure 70 out to 30 kHz, highlights the high frequency noise attributed to the HeNe laser source for the PA measurements.

The total noise in the measured HeNe laser PA signal is the sum of the fluctuations in the laser intensity, the photodiode, and electronic band pass amplifier noise. The RMS noise fluctuations in the output amplitude of the HeNe laser is specified at $<0.5\%$ over a 30 Hz to 10 MHz frequency range. Over long operating conditions, the laser output was rated to drift $\pm 2\%$ per hour. Since the PA data collection method relied on the relative changes in the photodiode signal over a short period of time, the maximum noise contribution from the laser output can be considered limited to $<0.5\%$ of the laser output, which equates to a maximum fluctuations of $5\ \mu\text{W}$ of output power over the 30 Hz to 10 MHz frequency range. The Stanford Research Systems SR560 preamplifier was operated in a band pass, AC amplification mode, which still amplified the both the desired PA signal and a small portion of the laser power fluctuations. The output noise on the SR560 is rated at $<4\ \text{nV}/\text{Hz}^{1/2}$ at 1 kHz; while the PA signal noise averaged around the 1 mV to -1 mV interval range. The noise specification for the amplifier is at least two

orders of magnitude less than the measured PA signal average and was therefore minimally contributed to the overall HeNe laser measurement noise. For the PA measurement configuration utilized in this experiment, the largest contributor to the noise in the PA signal was attributed to the fluctuation in the HeNe laser power.

Thermal fluctuations of the gas pressure in PA chamber is another potentially limiting factor to the sensitivity of the PA measurement and is discussed in [111]. For random thermal motion of the gas, it was assumed that the number of atoms and the volume of the PA chamber are both fixed. Also, it must be assumed that the sum of the translational energies of the atoms are the only energies that contribute to the chamber pressure in the PA cell. The translational energy of atoms E_A changes with the volume as $V^{2/3}$. It then follows that pressure P , is related to the mean energy of the atoms through

$$P \equiv \bar{P} = -\frac{\overline{\partial E_A}}{\partial V} = \frac{2}{3V} \overline{E_A} = \frac{2}{3V} U = \frac{Nk_B T}{V} \quad (5.5)$$

where U is the potential energy of a monatomic gas, which is

$$U = \frac{3}{2} Nk_B T. \quad (5.6)$$

In measuring the potential energy, the standard deviation δU , is related to the heat capacity C_V of the gas as

$$(\delta U)^2 = \overline{E_A^2} - \overline{E_A}^2 = k_B T^2 \frac{\partial U}{\partial T} = k_B T^2 C_V. \quad (5.7)$$

Then the fluctuation in pressure δP , can be calculated using $\overline{P^2}$ and \bar{P}^2 , where

$$\overline{P^2} = \overline{\left(\frac{\partial E_A}{\partial V} \right)^2} = \frac{4}{9V^2} \overline{E_A^2} \quad (5.8)$$

and $\overline{P^2}$ is used from Equation (5.5) to produce

$$(\delta P)^2 = \overline{P^2} - \overline{P}^2 = \frac{4}{9V^2} (\overline{E_A^2} - \overline{E_A}^2) = \frac{4}{9V^2} (\delta U)^2 = \frac{4}{9V^2} k_B T^2 C_V. \quad (5.9)$$

From Equations (5.5) and (5.9), the relative fluctuations in pressure due to the thermal motion of the atoms is

$$\frac{\delta P}{P} = \frac{2T}{3V} (k_B C_V)^{\frac{1}{2}} \frac{V}{N k_B T} = \left(\frac{2}{3N} \right)^{\frac{1}{2}}. \quad (5.10)$$

The results of Equation (5.10) show the relationship of the relative fluctuations in pressure is related to the total number of particles in the enclosed system and that it is approximately $N^{-1/2}$. Therefore, this defines the smallest pressure load the cantilever sensor could be exposed to due to the relative thermal fluctuations of the gas in the chamber.

Based on a PA chamber volume of 3.99 cm³, Table 9 shows several pressure changes due to thermal fluctuations over a range of operating condition pressures. In this low pressure regime, the fluctuations in pressure are very small. The number of molecules at 400 mTorr in the volume increased by factor of 200 times the 2 mTorr pressure condition and the fluctuation in pressure only increased by an order of magnitude.

Table 9. Pressure changes due to thermal fluctuations of the gas in a 3.99 cm³ PA chamber.

Chamber Pressure (Torr)	Number of Molecules	$\delta P \approx PN^{-\frac{1}{2}}$ (Torr)
0.002	2.61×10^{14}	1.24×10^{-10}
0.05	6.53×10^{15}	6.19×10^{-10}
0.4	5.22×10^{16}	1.75×10^{-9}

To determine an estimate of the cantilever deflection caused by the thermal fluctuations, it was assumed that the fluctuations occur at random intervals and at no specific frequency. The quality factors of the cantilevers were high in the low pressure environment, and the PA signals had full width half-max values were typically less than 1 Hz. Due to the very narrow resonance excitation frequency window; it is reasonable to use the steady state displacement equations for cantilever deflection due to a static load pressure. Using Equation (3.11) and the fluctuation pressures δP from Table 9, estimated cantilever displacements due to the small fluctuations are shown for two different cantilever designs. For the two cantilever designs, the estimated tip displacements due to the fluctuations in pressure ranged from 1.19×10^{-8} - 1.35×10^{-5} μm , which is extremely small.

Table 10. Estimated cantilever deflections due to fluctuations in PA chamber pressure.

Chamber Pressure (Torr)	$\delta P \approx PN^{-\frac{1}{2}}$ (Torr)	Cantilever Design	
		$5 \times 2 \times 0.01 \text{ mm}^3$ Deflection (μm)	$5 \times 2 \times 0.005 \text{ mm}^3$ Deflection (μm)
0.002	1.24×10^{-10}	1.19×10^{-8}	9.54×10^{-8}
0.05	6.19×10^{-10}	5.95×10^{-8}	4.76×10^{-7}
0.4	1.75×10^{-9}	1.68×10^{-7}	1.35×10^{-5}

Now consider what would be the minimum detectable absorption coefficient, α_{min} based on the fluctuation pressures listed in Table 10. Rewriting Equation (3.5) allows α_{min} to be represented by the source power P_o , modulation frequency f_m , chamber pressure P_c , and cylindrical chamber dimensions of length L and radius r .

$$\alpha_{min} = \Delta p \frac{f_m 3\pi r^2}{P_o} = \delta P \frac{f_m 3\pi r^2}{P_o} = \frac{P_c}{\sqrt{N}} \frac{f_m 3\pi r^2}{P_o} = \sqrt{\frac{P_c k_B T \pi}{L}} \frac{f_m 3r}{P_o} \quad (5.11)$$

Notice that the minimum absorption coefficient based on the thermal fluctuation limited case is a function of the PA chamber dimensions. The α_{min} function varies as r/\sqrt{L} , so a PA chamber design that is longer and has a smaller radius should produce a slightly smaller absorption limit. Increasing the radiation source output power should also improve the detection limit, as long as the source power is below the saturation limit of the gas under investigation. The minimum absorption coefficient based on the thermal fluctuation levels at the resonant frequency of each of the cantilevers is shown in Table 11. The calculations assumed a radiation power level of 0.1 mW, a 3.99 cm³ PA cell, and used the measured resonant frequency of each cantilever design. If the PA system was limited by the thermal fluctuations of the gas in the chamber, the minimum detectable absorption coefficient would be approximately 1.46×10^{-6} - 1.03×10^{-7} cm⁻¹. The minimum detectable absorption coefficients for the two cantilever designs shown in Table 7 suggest the measurable value by the system is an order of magnitude higher than the gas fluctuation limits shown in Table 11.

Table 11. Minimum absorption coefficient at the gas thermal fluctuation limit for the 3.99 cm³ PA cell.

Chamber Pressure (Torr)	$\Delta p = \delta P$ (Torr)	Cantilever Design	
		$5 \times 2 \times 0.01$ mm ³ α_{min} (cm ⁻¹)	$5 \times 2 \times 0.005$ mm ³ α_{min} (cm ⁻¹)
0.002	1.24×10^{-10}	2.44×10^{-7}	1.03×10^{-7}
0.05	6.19×10^{-10}	1.22×10^{-6}	5.15×10^{-7}
0.4	1.75×10^{-9}	3.44×10^{-6}	1.46×10^{-6}

Now the extent of cantilever motion due to thermal vibrations in the cantilever device is considered. Garcia-Valenzuela *et al.* investigated several limiting conditions of

optical measurements of cantilever deflections [108]. If the thermal noise in the cantilever was the limiting factor for measuring the minimum detectable displacement (*MDD*), they developed an equation that was applicable for the first resonance and below the resonant frequency conditions

$$MDD = \sqrt{\frac{4k_B T \Delta \nu Q / k \omega_o}{Q^2 (1 - \omega^2 / \omega_o^2) + \omega^2 / \omega_o^2}} \quad (5.12)$$

where Q is the quality factor, and $\Delta \nu$ is the bandwidth of the detector and electronics. For the case when thermal fluctuations occur at the cantilever resonant frequency, the equation simplified to

$$MDD(\omega = \omega_o) = \sqrt{\frac{4k_B T \Delta \nu Q}{k \omega_o}} \quad (5.13)$$

Similarly, when the thermal changes occur much lower than resonance, the equation becomes

$$MDD(\omega \ll \omega_o) = \sqrt{\frac{4k_B T \Delta \nu}{k \omega_o Q}} \quad (5.14)$$

Equation (5.14) is valid when the PA chamber is not subjected to external excitation radiation sources. The temperature fluctuations of the cantilever in the chamber should be extremely slow due the large thermal mass of the stainless steel chamber and low pressure environment. Minimum cantilever displacements from thermal fluctuations occurring when $\omega \ll \omega_o$ is shown in Table 12 for a range of quality factors. The quality factor of the cantilevers varied a great deal due to the 2-400 mTorr pressure conditions tested.

Table 12. Minimum detectable cantilever displacement due to thermal fluctuations when $\omega \ll \omega_0$.

Quality Factor	Cantilever Design	
	$5 \times 2 \times 0.01 \text{ mm}^3$ <i>MDD</i> (μm)	$5 \times 2 \times 0.005 \text{ mm}^3$ <i>MDD</i> (μm)
4,000	2.73×10^{-8}	
1,400	4.62×10^{-8}	2.06×10^{-7}
500	7.73×10^{-8}	3.36×10^{-7}
100		7.51×10^{-7}

The amplitude of the minimum detectable displacement due to thermal fluctuations in the cantilever varies significantly depending on the quality factor and the frequency of the thermal fluctuations. The case when $\omega = \omega_0$ results in minimum displacement values 2-4 orders of magnitude greater than the $\omega \ll \omega_0$ cases. In Table 13 when $\omega = \omega_0$, the MDD has a maximum value of 1.09-2.81 Å for the highest quality factors listed for each cantilever design. Displacement measurements using different optical detection methods have reported the ability to sense vertical cantilever displacements of less than 0.1 nm [112]. With such small thermal fluctuations generated by the cantilever in Table 12 and Table 13, the thermal fluctuations of the cantilever is most likely not the limiting factor.

Table 13. Minimum detectable cantilever displacement due to thermal fluctuations for the case when $\omega = \omega_0$.

Quality Factor	Cantilever Design	
	$5 \times 2 \times 0.01 \text{ mm}^3$ <i>MDD</i> (μm)	$5 \times 2 \times 0.005 \text{ mm}^3$ <i>MDD</i> (μm)
4,000	1.09×10^{-4}	
1,400	6.47×10^{-5}	2.81×10^{-4}
500	3.87×10^{-5}	1.68×10^{-4}
100		7.51×10^{-5}

Acceleration noise is due to external applied forces that induce cantilever motion. Sources of the acceleration noise can be coupled into the system through vibrations in the PA chamber, vacuum connections, and table. Only the forces acting normal to the cantilever surface are coupled into the amplitude of the cantilever motion. During long PA spectral collections, the excitation times between measurements was 4-12 s, depending on the pressure. Strong spikes in the PA signal due to external acceleration noise typically showed up as isolated increases in the PA signal, and neighboring sample data points were measured at lower levels. An extreme example of acceleration noise coupled into the cantilever PA signal is shown in Figure 72 where ~22 strong PA spikes were found over the 1.4 GHz frequency scan. The PA spectra shown in Figure 72 contained abnormally high amounts of noise spikes in the measurement, which was uncommon. While the occasional strong noise peak is not a problem, reoccurring weak disturbances are and they can significantly raise the noise floor of the measurements. Therefore, coupling of acoustic noise and vibrations from the room into the cantilever motion was determined to be the strongest contributors to fluctuations in the PA measurements.

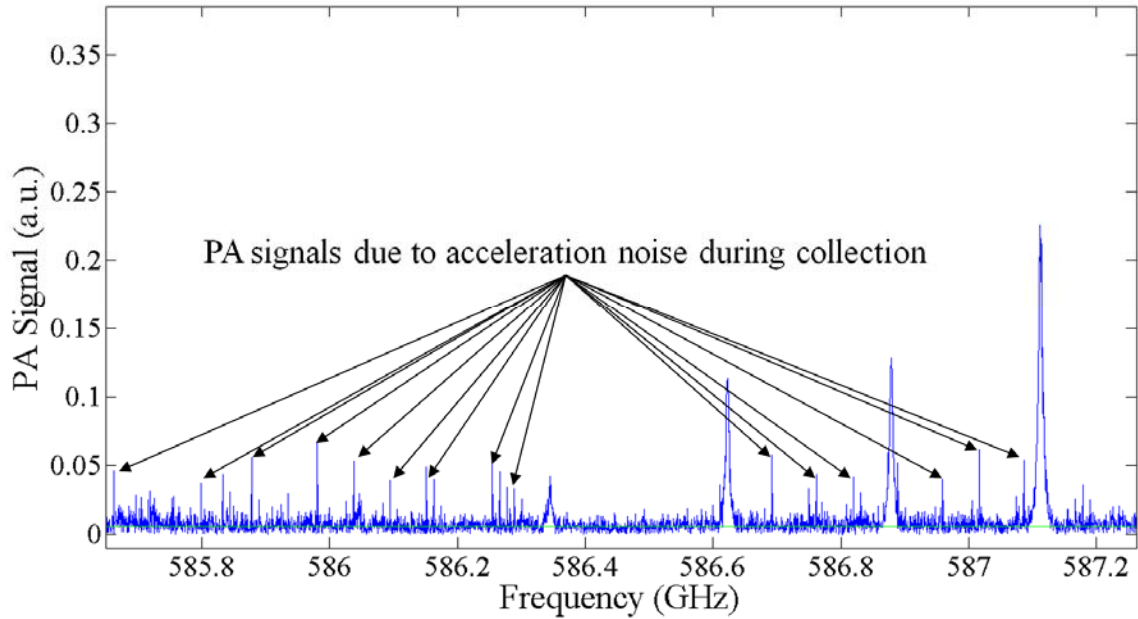


Figure 72. Example of PA signal spikes, which occurred due to acceleration noise coupled into the cantilever through the PA chamber and experimental setup.

5.5. Summary

In this section, the experimental setup and PA data collection techniques were discussed. Cantilever response to the photoacoustic effect was evaluated using two optical measurement methods, a laser beam iris clipped method and a Michelson interferometer configuration. The laser beam clipped method was advantageous due to the large dynamic range of the cantilever deflections and the modest required data sampling rate which allowed the simultaneous collection of multiple data signals.

Cantilever dynamic behavior was then investigated in the PA chamber and found that the strongest PA response occurred when the THz radiation source was amplitude modulated at the resonant frequency of the cantilever. The cantilever response time to reach a steady state amplitude deflection was significant at low pressures and the response time decreased with increasing chamber pressure. The quality factor of the

cantilevers was high due to the low pressure environments, causing the PA signal to decay very slowly from an excited periodic amplitude deflection.

Response and decay times of the PA signal determined how quickly PA spectral data could be collected since the excitation time and frequency step size affected the results. Therefore there are competing elements to spectral collections, an increased chamber pressure reduces the needed excitation time but also causes significant absorption line broadening. If higher spectral line resolution is desired, the chamber must be at lower pressures, at the cost of a longer time required to collect the spectral signature.

Short and long THz frequency scans of the rotational absorption lines of CH_3CN were performed over a range of pressures. The best sensitivity of $1.13 \times 10^{-5} \text{ cm}^{-1}$ and a NNEA of $2.83 \times 10^{-10} \text{ cm}^{-1} \text{ W Hz}^{-1/2}$ was achieved using the $5 \times 2 \times 0.005 \text{ mm}^3$ cantilever design, with the spectra recorded at 38 mTorr. Spectra recorded at 4 mTorr still produced a strong PA response, achieving a SNR=504. The compact PA absorption cell was only 2 inches long, which is orders of magnitude smaller than traditional long path absorption systems. The spectroscopy system developed here performed exceptionally well at low chamber pressures compared to the other PA trace detection and spectroscopy systems shown in Table 1.

VI. Conclusions

PA spectroscopy and chemical sensing is an exciting area of research that has many industrial and commercial applications. Creating the sensitive MEMS cantilever sensors and analyzer was a multidisciplinary effort, which requires incorporation of chemistry, physics, and engineering principles. In this research effort, sensitive PA cantilever sensors were successfully designed, modeled, fabricated, and tested under very low chamber pressures for THz molecular spectroscopy. Design parameters of length, width, and thickness of the cantilever structures were analyzed and used to create cantilever designs that were sensitive to the low pressures generated in the PA chamber. Along the path to creating these sensitive devices, several fabrication processes and techniques were developed to make this effort successful. The compact PA THz spectroscopy system developed in this work is significantly smaller than traditional long path gas phase molecular spectroscopy systems which creates a real possibility for a portable spectroscopy system.

6.1. Contributions

Several contributions to the field of MEMS and THz PA spectroscopy were accomplished in this work. Summaries of each contribution area are discussed in the two following sections which cover the development of the sensitive cantilever fabrication processes and the collection of THz PA molecular spectroscopy using the sensitive cantilever devices at low chamber pressures.

6.1.1. Fabrication

Through the development of the fabrication processes, very sensitive MEMS cantilever PA sensors with length over thickness ratios of 500 and 1,000 were created. The $5 \times 2 \times 0.005 \text{ mm}^3$ cantilever design created here was more sensitive than cantilever devices used in [6, 79-82, 84-86, 102, 109, 113] and similar to designs in [87]. The fabrication method developed here allowed the patterned deposition of the Ti/Au reflective layer at the tip of the cantilever to be performed as the first step in the fabrication sequence. Alignment marks created during the Ti/Au deposition made the later mask alignment steps extremely accurate. The DRIE etch used to create the narrow gap through the device layer to define the cantilever shape was able to identically match the PR pattern. A benefit of the DRIE process is that the etch is not affected by mask to wafer orientation or the crystal plane orientation of the silicon wafer. DRIE of the device layer surface performed here eliminates large gaps in the corners of the cantilever designs seen in [87] due to their wet etch of silicon device layer.

6.1.2. PA Spectroscopy and Sensitivity Results

With this novel system, the first-ever cantilever based THz photoacoustic spectrum was collected and analyzed at low chamber pressures in the 2-60 mTorr range. The pressure regimes tested here were several orders of magnitude lower than the trace gas detection cantilever PA systems discussed earlier [5, 6, 80-82, 84, 85, 102]. Significant PA signals were achieved at chamber pressures as low as 2 mTorr. For THz spectroscopy applications, the sensor size and chamber pressures tested were also an

order of magnitude smaller than the membrane sensor system used by Krupnov *et al.* [88]. By collecting PA spectra in the 2 mTorr pressure regime, it allowed for a primarily Doppler limited line broadening of the methyl cyanide, making strong closely spaced absorption lines highly resolvable.

In this research effort, the custom fabricated THz photoacoustic spectroscopy system achieved a sensitivity of $1.97 \times 10^{-5} \text{ cm}^{-1}$ and a NNEA of $1.39 \times 10^{-9} \text{ cm}^{-1} \text{ W Hz}^{-1/2}$ with the $5 \times 2 \times 0.01 \text{ mm}^3$ cantilever design. The more sensitive $5 \times 2 \times 0.005 \text{ mm}^3$ cantilever sensor design achieved a sensitivity of $1.13 \times 10^{-5} \text{ cm}^{-1}$ and a NNEA of $2.83 \times 10^{-10} \text{ cm}^{-1} \text{ W Hz}^{-1/2}$. The NNEA results shown in Table 8 for this work compare very well to previously reported, short path PA systems listed in Table 1. The NNEA of our system was 4.72 times higher than the membrane system in [88], while the dimensions of their absorption chamber and sensor were 2.6 times longer and 10 times larger respectively. Compared to the best reported trace detection cantilever sensor system [83], our system NNEA was 1.66 times higher and their absorption chamber dimensions were 2.3 times longer. Finally, the NNEA of our system was 1.42 times higher than the tuning fork detector system [91], their chamber was 2.8 times longer and their sensor was 6.6 times larger than the cantilever designs.

The PA system operated at significantly lower chamber pressures, taking advantage of the high quality factors. Over the range of low vacuum environments tested, the experimental data collected provided valuable insight into the range of damping conditions in the PA chamber. The quality factor of the $5 \times 2 \times 0.01 \text{ mm}^3$ cantilever designs ranged from 4,173-596 over the 3-400 mTorr chamber pressures. The

more sensitive $5 \times 2 \times 0.005 \text{ mm}^3$ cantilever design had quality factors of 1,474-128 over a smaller pressure range of 2-211 mTorr.

Additionally, due to its compact size and with a few modifications, the PA system can be used as a portable chemical sensing and spectroscopy platform. This is a great advantage in comparison to a large traditional absorption cells for spectroscopy applications, leading to a hand held THz chemical sensor or MEMS detector arrays for THz imaging applications.

6.2. Future Research

The sensitive MEMS sensors created here enabled the THz PA molecular spectroscopy system dimensions to be made significantly smaller than traditional long path absorption designs. Recommendations for future research are discussed regarding improvements to the cantilever design and manufacturing, as well as modifications to the PA experimental setup. The overall footprint of the PA test setup could be further reduced if a piezoelectric layer was incorporated on the cantilever designs. A piezoelectric sensor configuration would provide a compact way of evaluating the cantilever response to the PA pressures and the optical measurement method could be used in tandem with or potentially be eliminated entirely, depending on the piezoelectric performance. The cantilever fabrication process was developed to ensure the device layer surface was protected during every step of the fabrication sequence. PZT or ZnO are promising piezoelectric layers that could be implemented into the designs. The protective photoresist layer used during the cantilever release process would completely protect the piezoelectric materials from the strong HF vapors. Miniaturized arrays of

piezoelectric cantilevers could be used for PA imaging applications where individual read outs from each cantilever would represent a pixel of the image.

Promising improvements in cantilever fabrication include modifications to the selection of SOI material layer construction and to the cantilever designs. Reduction in the BOX layer thickness to $\sim 0.2 \mu\text{m}$ on the SOI wafers would significantly reduce the residual stress between the device layer and oxide layers during the release process. A $\sim 0.2 \mu\text{m}$ BOX layer would still provide an adequate etch stop layer for the DRIE and RIE etch processes. The final stages to release the cantilever device was the removal of the BOX layer over HF vapor. Any defects in the protective PR coating leaves the potential of etching any deposited films on the device layer surface. Removal of a thinner, $\sim 0.2 \mu\text{m}$ BOX would require 80% less time over the HF vapor compared to a $1 \mu\text{m}$ thick oxide, reducing the amount of time and risk to damaging deposited films on the device layer surface.

The minimum detectable absorption coefficient for the system could further be reduced by creating a more sensitive cantilever design, with a lower resonant frequency. Analysis of the noise in the frequency spectrum of the PA signal for the cantilevers was performed in section 5.4 Performance Analysis and Limitations. The dominant noise signals were electrical at intervals of 60 Hz and at the resonant frequencies of the cantilevers. Creation of cantilever designs with length over thickness ratios $>1,000$ at resonant frequencies that fall between the electrical noise peaks would make for a device with an increased sensitivity. Several SOI manufactures sell thinner device and BOX layer materials, which increases the number of potential designs. Additional sensitive cantilever designs and fabrication modifications like filleting of the cantilever corners

would improve the integrity of the membrane surrounding the cantilever were discussed in Appendix A.

With a few modifications, the experimental setup could be refined to increase the performance of this novel THz PA spectroscopy system. The PA system had a very slow leak rate but the high quality factor of the cantilevers at the low chamber pressures tested meant the system performance was sensitive to changes in pressure. To achieve the optimal amplitude deflection performance of the cantilever, the modulation frequency must be very accurate, within a few (1-3) hundredths of a Hertz. Incorporation of the chamber pressure reading into the LabView control system would be beneficial; the modulation frequency could then be scaled based on the pressure readings during PA spectral collections. Another option to increase the performance would be to periodically perform resonant frequency modulation scans during long spectra data collections, ensuring an optimal excitation. Although, the additional frequency scan option would slightly increase the overall data collection time, it would provide a PA amplitude scaling measure that could be used in post data processing to correct for the changes in pressure.

The second improvement would be the use of a lower noise laser source for the cantilever displacement measurements. The HeNe laser used had some high frequency components that contributed a large portion of the additional noise in the raw PA signal measurements.

The PA beam clipping measurement technique allowed for an accurate deflection measurement, which utilized low data sampling rates. A data acquisition card with a higher sampling rate (1 MS/s or more) would allow for better resolution of a Michelson interferometer configuration where high frequencies would be encountered due to large

amplitude deflections of the cantilever. Converting the experimental setup and data collection to a Michelson configuration would allow the optical layout to be further reduced in size by eliminating the beam clipping iris, making the system even more compact.

Appendix A. Additional Cantilever Design Models

Additional cantilever shapes and piezoelectric cantilever designs were evaluated for their potential applications in the PA system. Some dual anchored cantilever and rackets were the first non-traditional shapes considered. A dual anchored $5 \times 3 \times 0.01 \text{ mm}^3$ design used two small anchor segments that were 1 mm long and 0.5 mm wide each and is shown in Figure 73. The proposed cantilever design in Figure 73 offers a large surface area to capture the changes in pressure while creating a lower spring constant due to the small anchoring arms.

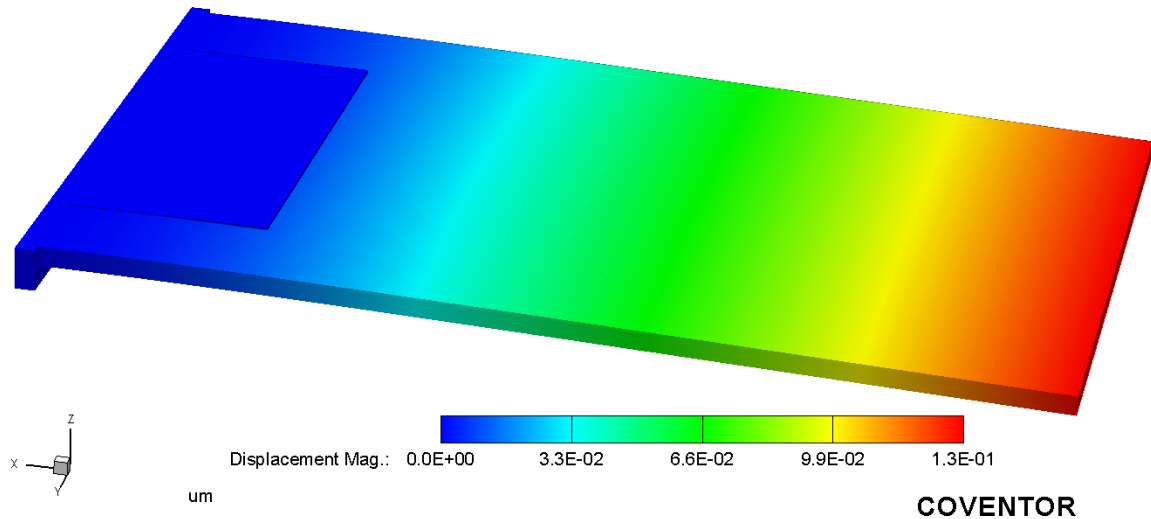


Figure 73. Dual anchored cantilever design had total over all dimensions of $5 \times 3 \times 0.01 \text{ mm}^3$; the two anchor segments were 1 mm long and 0.5 mm wide. Deflection was due to a 10 mPa static load condition.

An image of the mises stress in the above design is shown in Figure 74, where a high concentration of stress is found where the small anchor arms attach to the plate. Highly localized stress points can be a failure point for MEMS devices and can be reduced through filleting the corners in the design. Fillets reduce the amount of stress by

creating a radius of curvature in the design, which distributes the stress over a larger region, thereby reducing the peak value of the stress.

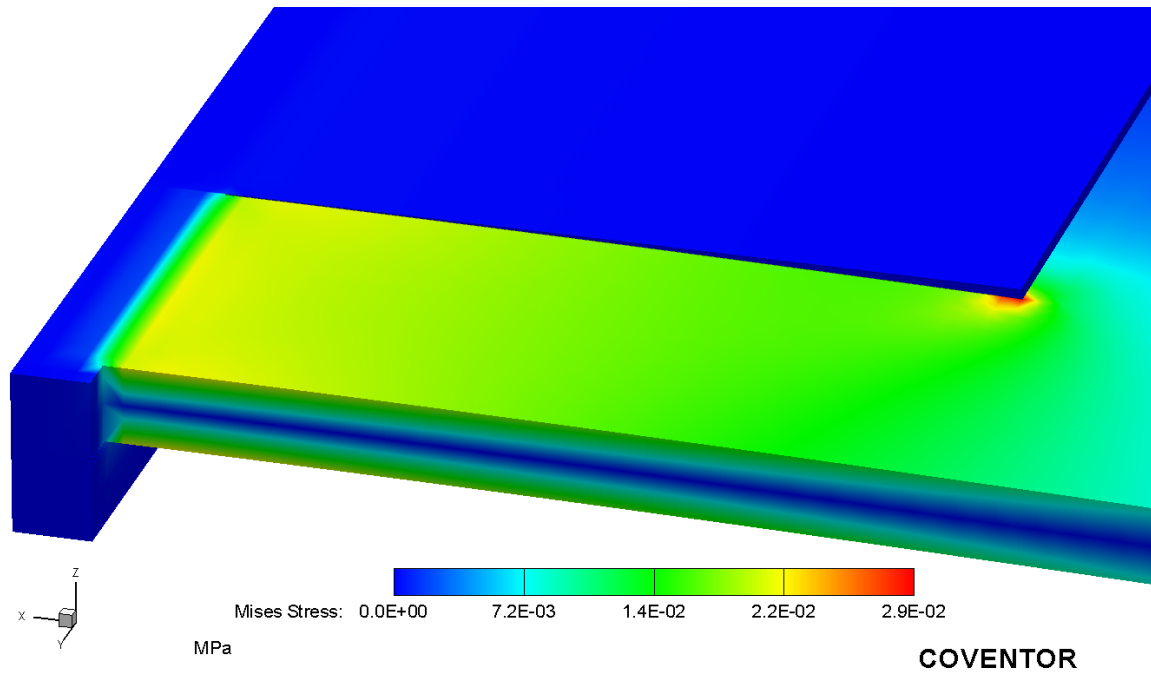


Figure 74. Mises stress map showed a high concentration of stress in the corner where the anchor arm attachment to the plate.

An improved version, is a dual anchored $5 \times 3 \times 0.005 \text{ mm}^3$ design that used the same anchor segments of 1 mm long and 0.5 mm wide but the corners of the anchor points were filleted using a 300 μm radius. A map of the mises stress distribution is shown in Figure 75, where the location of the highest stresses have moved away from the corners of the device to the surface area at the anchor location of the device.

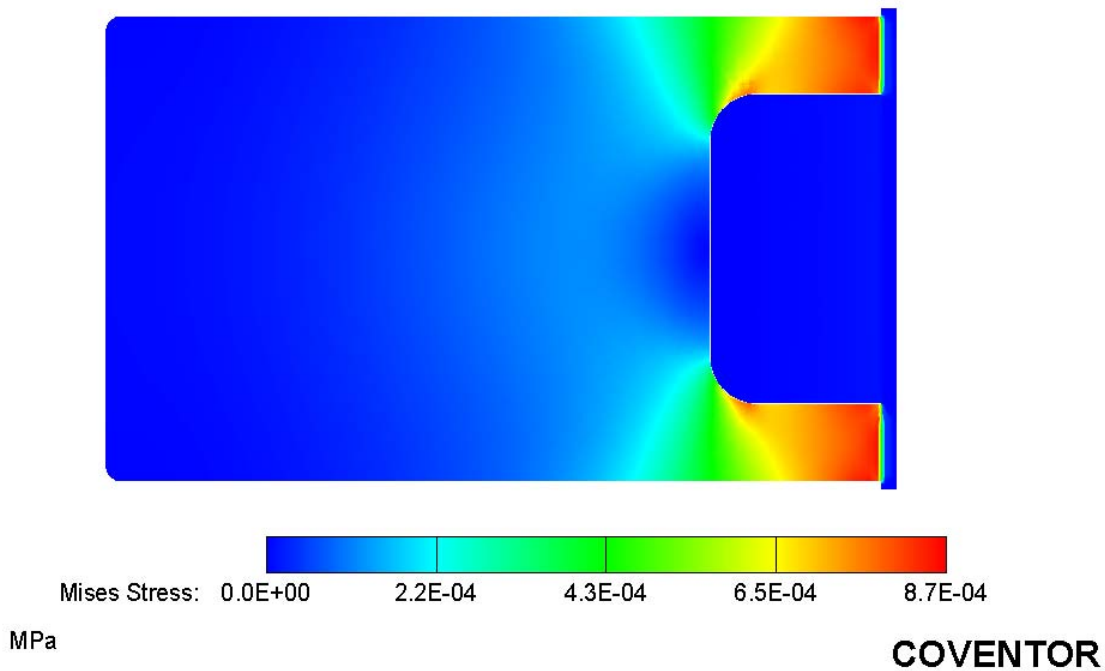


Figure 75. Corners filleted using a 300 μm radius reduced the peak level of stress in the corners, and the stress is now at a maximum at the surface of the device at the anchor points.

Another dual anchored $5 \times 3 \times 0.01 \text{ mm}^3$ design used two larger anchor segments that were 1 mm long and 1 mm wide each, which increased the stiffness of the structures. The dual anchor designs with the two different anchor arm widths were all simulated using a 5 & 10 μm thick device layers. A performance comparison between the traditional and dual anchored cantilever designs is presented in Figure 76. The designs were subjected to a 0.1 mPa harmonic load and a damping condition of 0.5% times the critical damping coefficient. The thinner 5 μm device layer designs shown with the dashed lines in the graph, experience much more deflection than their 10 μm device layer counter parts. The resonant frequency of the designs also shifted lower as the spring stiffness was reduced. Further modifications could be made to the dual anchor designs by adjusting the arm widths and lengths. In modifying the designs, it would be important

to avoid resonant frequencies near the electrical noise sources observed in the PA measurements shown in Figure 70.

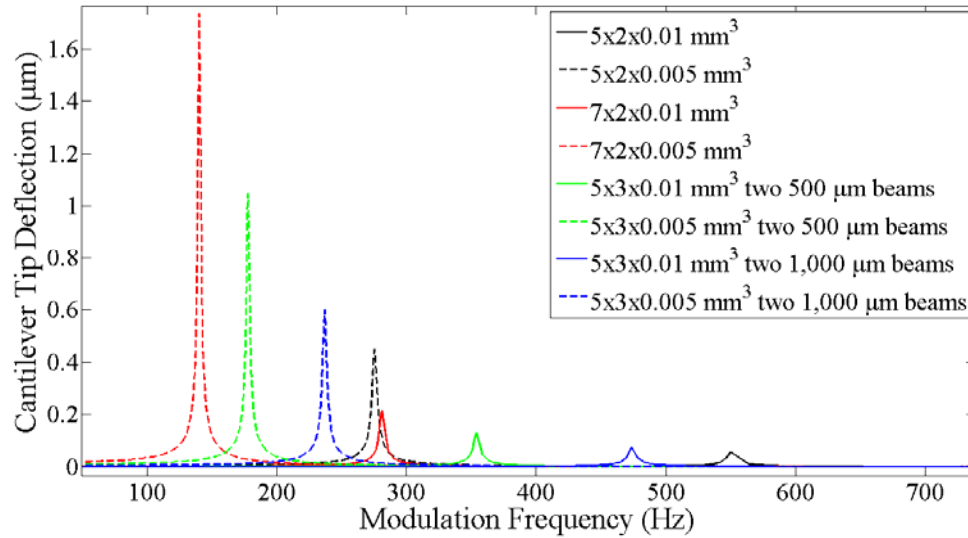


Figure 76. Amplitude displacement comparison between traditional and dual anchored cantilever designs under 0.1 mPa harmonic load using 0.5% of the critical damping factor.

In CoventorWare[®], performance of piezoelectric cantilever devices was also performed. In the software, the *MemMech* solver with the *Piezoelectric* option selected for the device physics to model the performance of the piezoelectric cantilever devices. Through the fabrication process file, the device, oxide, electrode, and PZT layer thicknesses were established. The respective layer thicknesses built upon the 5 µm thick silicon device layer were a 0.25 µm oxide, 120 nm Ti/Pt, 1 µm PZT, and a 120 nm Ti/Pt top electrode. Shown in Figure 77 is the mises stress distribution on a 5×2×0.005 mm³ cantilever design with the PZT layer covering 1/16th the length of the cantilever from the base of the anchor point under 1 Pa static load.

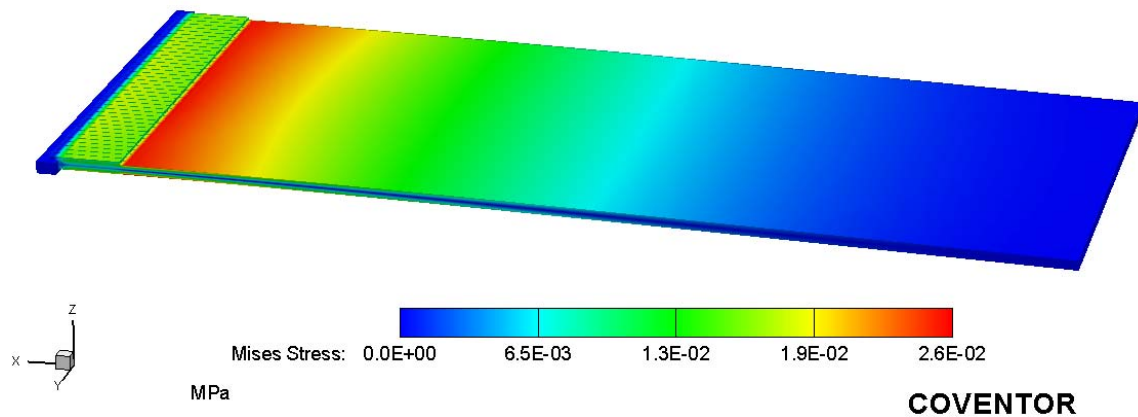


Figure 77. Mises stress distribution on a $5 \times 2 \times 0.005 \text{ mm}^3$ cantilever design with Pt electrodes and a piezoelectric layer of PZT covering $1/16^{\text{th}}$ the length of the cantilever under a 1 Pa static load.

A series of simulations were performed which investigated the generated output voltage from the piezoelectric layer for different PZT coverage lengths along the cantilever beam. The fractional portion of the cantilever length covered by PZT was evaluated at ratios of 1, 1/2, 1/4, 1/16, 1/32, and zero. A static 1 Pa pressure load was applied to the bottom side of the silicon device layer, causing the cantilever designs to deflect. The resulting generated voltages are shown in Figure 78. The highest voltage was generated by the design that had PZT on $1/16^{\text{th}}$ the length of the beam. The cantilever with PZT coverage along the entire length of the beam produced the lowest voltage and also experienced the least amount of deflection do to the applied pressure load. The additional layers required to incorporate a piezoelectric material into the cantilever design increased the thickness of the cantilever by nearly 30%. The cantilever designs with a large fraction of PZT coverage were less flexible, deformed less under the pressure load, and therefore generated less voltage.

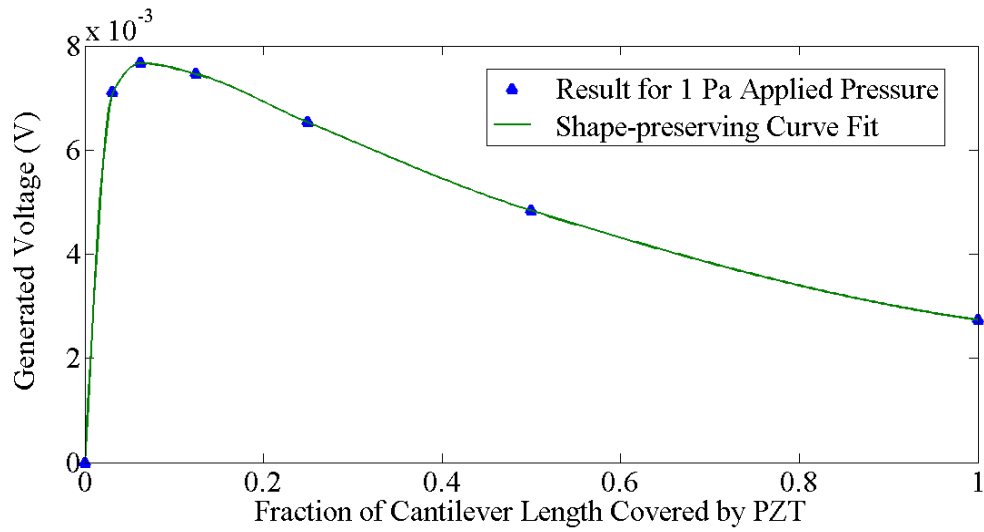


Figure 78. Simulation results of the voltage generated for different fractional coverage lengths of PZT along the length of the cantilever.

A potential advantage of the dual anchor cantilever designs is that the vast majority of the stress due to bending is focused across the length of the 1 mm long anchor arms. A series connection between piezoelectric layers on the anchor arms in this highly stress region should create a stronger voltage signal, but further simulations were not performed.

Appendix B. PA Chamber Design

The photoacoustic chamber design is a critical part in making a sensitive, compact analyzer for PA chemical sensing and spectroscopy [4, 114]. Three chamber configurations were created over the period of this research effort. Chambers with a 1 cm and 0.5 cm absorption cell diameters were fabricated using the same chamber length of 2 in. Two balance volumes for the chamber designs were also created. Chamber designs relied on compression seals with o-rings and three welds to achieve a high vacuum seal. The figures below provide additional views and dimensions of the PA chamber designs. A computer-aided design (CAD) model of an assembled PA chamber design is shown Figure 79 and an exploded view of the chamber is provided in Figure 80 prior to assembly.

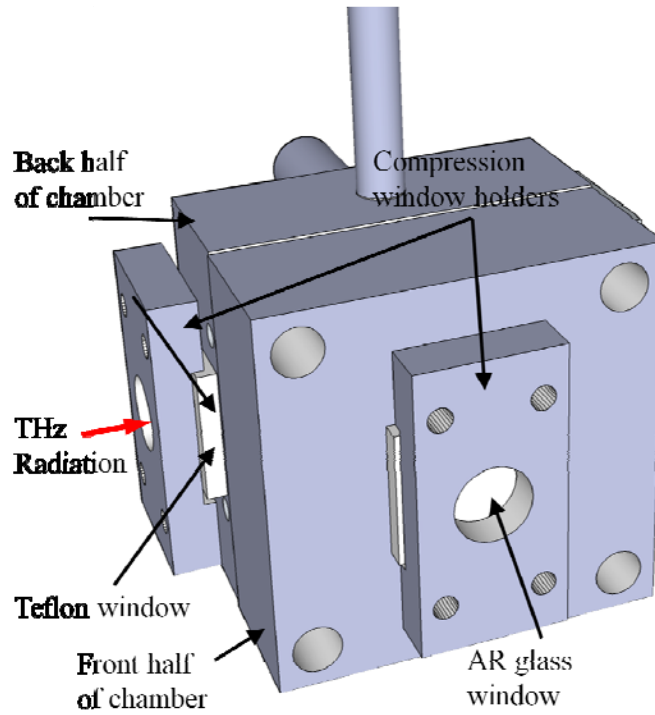


Figure 79. Assembled CAD model of the PA chamber with labels of primary components.

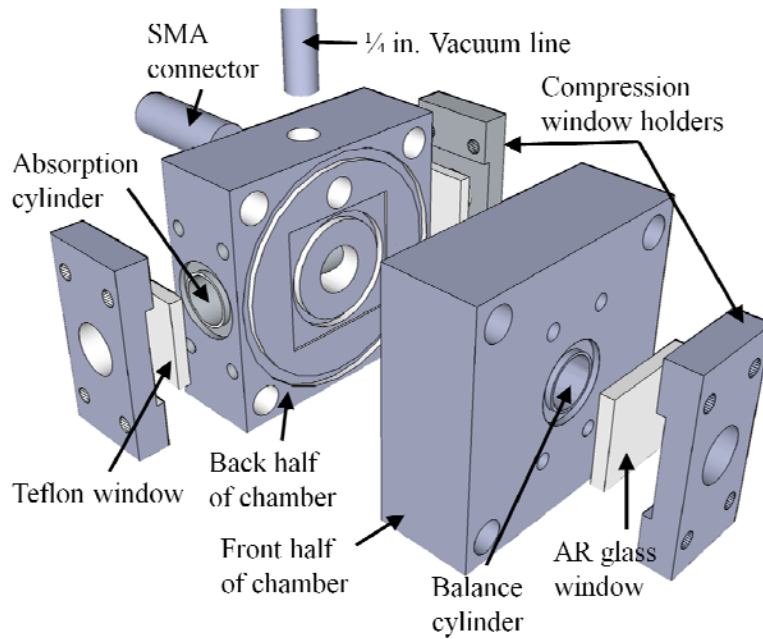


Figure 80. Exploded view of chamber shows the individual pieces prior to assembly.

The back half of the PA chamber with the cylindrical absorption cell area is shown in Figure 81. Inner o-ring in the recessed area for the SOI device provides a stable mounting surface for the sample. The outer o-ring, with a 4.87 cm outer diameter provides the seal for the front and back portions of the PA chamber. The diameter of the cylindrical absorption cell on the left side of the diagram is shown at 1 cm; for the second chamber design, the diameter was reduced to a 0.5 cm diameter. The same 1.56 cm outer diameter o-ring was used to seal the Teflon windows in place for both chamber diameters.

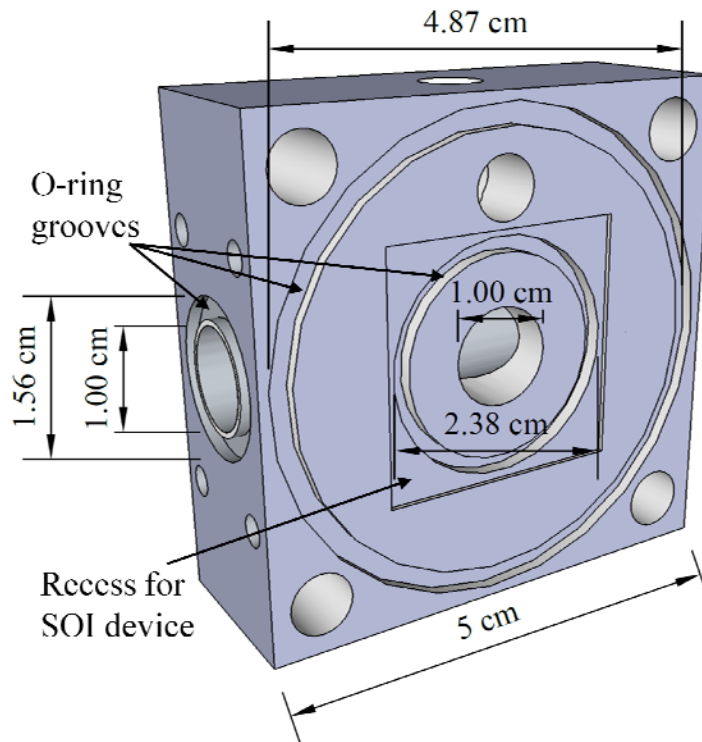


Figure 81. Back half of the PA chamber which contains the absorption cell shows the area for the SOI device placement and location of o-rings to seal the chamber.

A semi-transparent view of the PA chamber is shown from the side in Figure 82 (a) and a frontal view in Figure 82 (b) highlights the internal configuration of the system. The balance volume shown in the right side of Figure 82 (a) was increased to a radius of 1.5

cm for the third chamber design, but not enough data was collected fully determine the effects of the larger balance region volume.

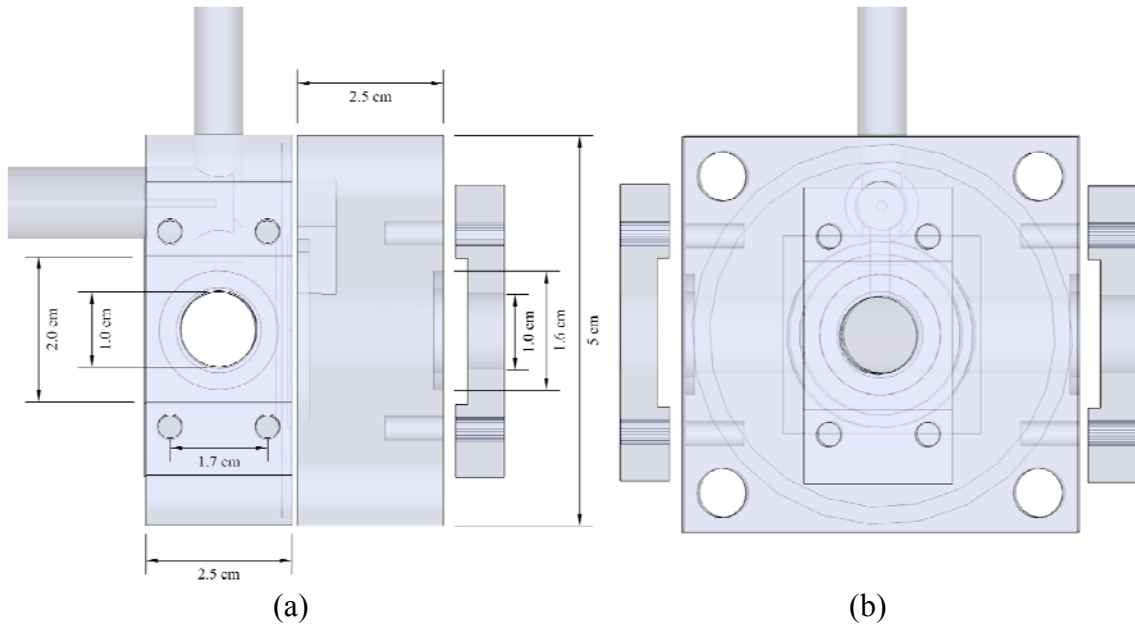


Figure 82. Side view in (a) and frontal view in (b) of PA chamber shown in semi-transparency to highlight internal construction of the system.

Appendix C. Additional PA Spectral Data

Numerous data collections were performed on CH_3CN . This appendix contains supplemental PA data and brief discussions of the results. Due to the chamber vacuum leak rate, the strength of the PA signal decreases over time. PA data in Figure 83 shows the raw recorded PA data, PA scaled for pressure increase effects, and the simulated absorption spectra for 38 mTorr of CH_3CN . The PA data was scaled such that the peak absorption line ratios were matched to the absorption ratios from the simulations.

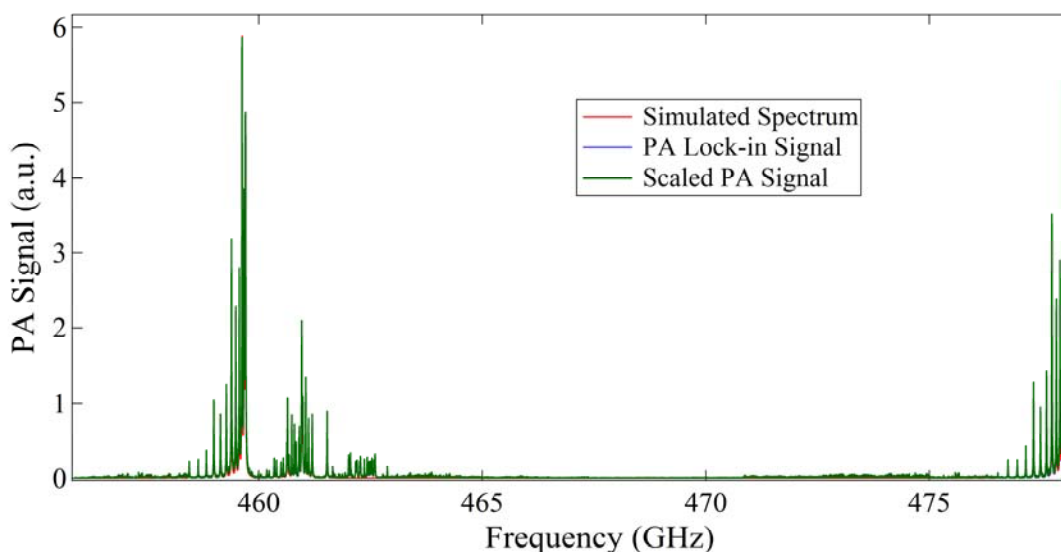


Figure 83. Full display of PA spectral snippet shown in Figure 59 (38 mTorr) with addition of scaled PA signal data due to the chamber pressure changes due to the vacuum leak rate.

Figure 84 compares the raw PA signal, scaled Pa signal, and simulated absorption spectra for the strong ground state absorption lines early in the spectral recording. The scaled strong absorption lines and simulated absorption lines matched very well. Now compared to the later recorded data in Figure 85, the raw PA signal data has fallen due to the partial pressure of the CH_3CN gas in the chamber. The scaled PA data matches

simulated spectrum better for long data collections, although this particular scaled data slightly over predict the PA signal response. Additional research into improved data collection techniques and data analysis could still improve the overall system performance.

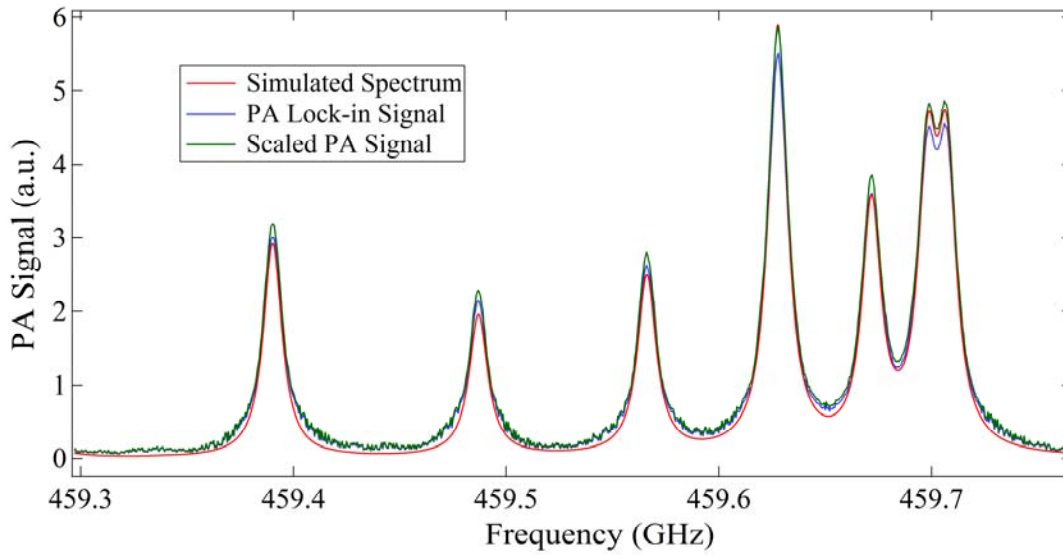


Figure 84. Zoomed in view of Figure 83 ground state absorption lines scaled PA signal matched up to the simulated spectrum.

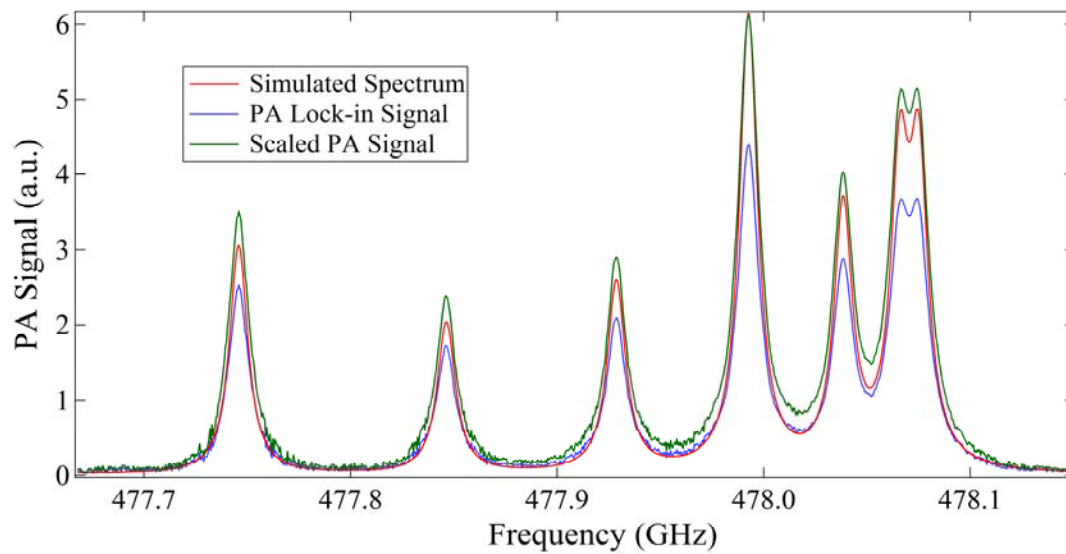


Figure 85. Zoomed in view of ground state absorption scaled PA signal matched up to the simulated spectrum.

Appendix D. MATLAB® Code for PA Data Analysis

The PA data collected in the LabVIEW software was analyzed using MATLAB® scripts written to read in and manipulate column data from a text file. Below is the MATLAB® script used to analyze and plot the PA spectral data collected.

```
%% Analysis PA Spectral Data
% reads data from *.txt file
clear all; close all; clc;

%% Enter radiation source power
power = 0.000025 % Power in watts

%% Enter absorption strength at for the strongest line
% Absorption coefficient in cm^-1 for
absorption_max = 0.053871

%% Enter the signal averaging time (sec)
averaging_time = 1;
%% Window sample size
window_size = 100

%% Description of Data file content
% Column 1 is not used
% Column 2 is the THz Diode excitation frequency, Loaded in THz from the file
% Column 3 is the Oscilloscope signal from the HeNe diode
% Column 4 is the THz Diode average voltage
% Column 5 is the lock-in Amplifier signal (R)

[filename, pathname, filterindex] = uigetfile({ '*.*', 'All Files (*.*)'}, ...
    'Select THz data files to process...', 'MultiSelect', 'on');

%% Loop over selected files, reading each into a data matrix
% Read in base pressure file first
B = [];
if ~iscell(filename) % handle single file selection
    nFiles = 1;
    filename = {filename};
else
    nFiles = size(filename,2);
end
for i = 1:nFiles
```

```

    fid = fopen(fullfile(pathname,char(filename(i))));
    B = [B; textscan(fid, '%[^...] %f %f %f %f', 'delimiter', ' ', 'MultipleDelimsAsOne', 1)];
    fclose(fid);
end

%% Plots the Oscilloscope signal
figure;
axes2 = axes('Parent',gcf,'FontSize',24,'FontName','Times New Roman');
box(axes2,'on');
hold(axes2,'all');
hold on;
for i = 1:nFiles
    hold on;
    plot(1000*B{i,2},B{i,3}/1000,'g');
end
ylabel('PA Signal (a.u.)','FontSize',30,'FontName','Times New Roman')
xlabel('Frequency (GHz)','FontSize',30,'FontName','Times New Roman');
pf(1) = 4.5;
pf(2) = 14.5;
width = 40; % [cm]
height = 10; % [cm]
set(gcf,'Units','centimeters','Position',[pf(1) pf(2) width height]);
hold off;

%% Finds the variance over a window_size interval
dimension=size(B{1,5});
for i=1:dimension(1,1)-window_size
    var1(i,1) = var(B{1,5}(i:i+window_size,1));
end
[o,p] = min(var1); % locates the index of minimum variance

for i=1:dimension(1,1)-window_size
    var_THz(i,1) = var(B{1,4}(i:i+window_size,1));
end

figure;
axes2 = axes('Parent',gcf,'FontSize',24,'FontName','Times New Roman');
box(axes2,'on');
hold(axes2,'all');
plot(1000*B{1,2}(1:dimension(1,1)-window_size,1),var1);
hold on;
plot(1000*B{1,2}(1:dimension(1,1)-window_size,1),var_THz,'r');
ylabel('Variance','FontSize',30,'FontName','Times New Roman');
xlabel('Frequency (GHz)','FontSize',30,'FontName','Times New Roman');
pf(1) = 4.5;

```

```

pf(2) = 1.5;
width = 40; % [cm]
height = 10; % [cm]
set(gcf,'Units','centimeters','Position',[pf(1) pf(2) width height]);
hold off

%% Fluctuations in THz signal
for i=1:dimension(1,1)-1
    THz_diode_fluctuations(i,1) = B{1,4}(i,1) - B{1,4}(i+1,1);
end

Sig_fluct=abs(THz_diode_fluctuations);
THz_Fluctuation_mean=mean(sqrt(THz_diode_fluctuations.^2))

figure;
axes2 = axes('Parent',gcf,'FontSize',24,'FontName','Times New Roman');
box(axes2,'on');
hold(axes2,'all');
plot(1000*B{1,2}(1:dimension(1,1)-1,1),Sig_fluct);
hold on;
plot(1000*B{1,2}(1:dimension(1,1)-1,1),THz_Fluctuation_mean,'g','LineWidth',2.5);
ylabel('Mean Fluctuations in THz Diode Signal (V)','FontSize',30,'FontName','Times
New Roman');
xlabel('Frequency (GHz)','FontSize',30,'FontName','Times New Roman');

pf(1) = 4.5;
pf(2) = 1.5;
width = 40; % [cm]
height = 25; % [cm]
set(gcf,'Units','centimeters','Position',[pf(1) pf(2) width height]);
hold off

%% Fluctuations in R-lock-in signal
for i=1:dimension(1,1)-1
    R_signal_fluctuations(i,1) = B{1,5}(i,1) - B{1,5}(i+1,1);
end

R_Sig_fluct=abs(R_signal_fluctuations);
R_Fluctuation_mean=mean(sqrt(R_signal_fluctuations.^2))

figure;
axes2 = axes('Parent',gcf,'FontSize',24,'FontName','Times New Roman');
box(axes2,'on');
hold(axes2,'all');
plot(1000*B{1,2}(1:dimension(1,1)-1,1),R_Sig_fluct);

```

```

hold on;
plot(1000*B{1,2}(1:dimension(1,1)-1,1),R_Fluctuation_mean,'g','LineWidth',2.5);
ylabel('Mean Fluctuations in PA Signal (a.u.)','FontSize',30,'FontName','Times New Roman');
xlabel('Frequency (GHz)','FontSize',30,'FontName','Times New Roman');

pf(1) = 4.5;
pf(2) = 1.5;
width = 40; % [cm]
height = 25; % [cm]
set(gcf,'Units','centimeters','Position',[pf(1) pf(2) width height]);
hold off

%% find RMS noise floor of R-signal for window size interval
dimension=size(B{1,5});
for i=1:dimension(1,1)-window_size
    RMS1(i,1) = sqrt(mean((B{1,5}(i:i+window_size,1)).^2));
end
[o1,p1] = min(RMS1); % locates the index of minimum RMS noise
disp('Index start and frequency of lowest noise');
disp(p1)
disp(1000*B{1,2}(p1,1));

figure;
semilogy(1000*B{1,2}(1:dimension(1,1)-window_size,1),RMS1);
hold on;
semilogy(1000*B{1,2}(1:dimension(1,1)-window_size,1),var1,'r');
hold off;

RMS_noise = sqrt(mean((B{1,5}(p1:p1+window_size,1)).^2));
disp('RMS Noise Floor');
disp(RMS_noise);

Frequency1_of_noise_measured = 1000*B{1,2}(p1,1)
Frequency2_of_noise_measured = 1000*B{1,2}(p1+window_size,1)

Max_PA_signal = max(B{1,5});

disp('Max_PA_signal');
disp(Max_PA_signal);

SNR = Max_PA_signal / RMS_noise;
disp('SNR RMS_noise');
disp(SNR);

```

```

%% Sensitivity absorption_min
alfa_min = absorption_max / SNR;

disp('Sensitivity, alfa_min in cm^-1');
disp(alfa_min);

%% NNEA
NNEA = alfa_min * power * sqrt(averaging_time);
disp('NNEA, in cm^-1 W Hz^(-1/2)');
disp(NNEA);

%% Plots the "R" lock in signal

figure;
axes2 = axes('Parent',gcf,'FontSize',24,'FontName','Times New Roman');
box(axes2,'on');
hold(axes2,'all');
hold on;
for i = 1:nFiles
    hold on;
    array_size = ones(size(B{i,2}));
    plot(1000*B{i,2},B{i,5},'b');
    plot(1000*B{i,2},RMS_noise*array_size,'g')
end
ylabel('PA Signal (a.u.)','FontSize',30,'FontName','Times New Roman');
xlabel('Frequency (GHz)','FontSize',30,'FontName','Times New Roman');
pf(1) = 5;
pf(2) = 2;
width = 40; % [cm]
height = 20; % [cm]
set(gcf,'Units','centimeters','Position',[pf(1) pf(2) width height]);
hold off;

%% Plots the THz detector average voltage

figure;
axes2 = axes('Parent',gcf,'FontSize',24,'FontName','Times New Roman');
box(axes2,'on');
hold(axes2,'all');

for i = 1:nFiles
    hold on;
    plot(1000*B{i,2},2*B{i,4},'k')
end
ylabel('THz Diode (V)','FontSize',30,'FontName','Times New Roman');
xlabel('Frequency (GHz)','FontSize',30,'FontName','Times New Roman');

```

```
pf(1) = 5;  
pf(2) = 15;  
width = 40; % [cm]  
height = 10; % [cm]  
set(gcf,'Units','centimeters','Position',[pf(1) pf(2) width height]);  
hold off;
```

Appendix E. Visual Bibliography

A visual bibliography provides insight into the research topic areas, what groups are pursuing research on those topics and how they are interrelated. Visual bibliographies can be organized by topic area, funding sources, research groups, or other relevant relationships. Figure 86 is a visual bibliography showing how PA detect articles are related through direct references.

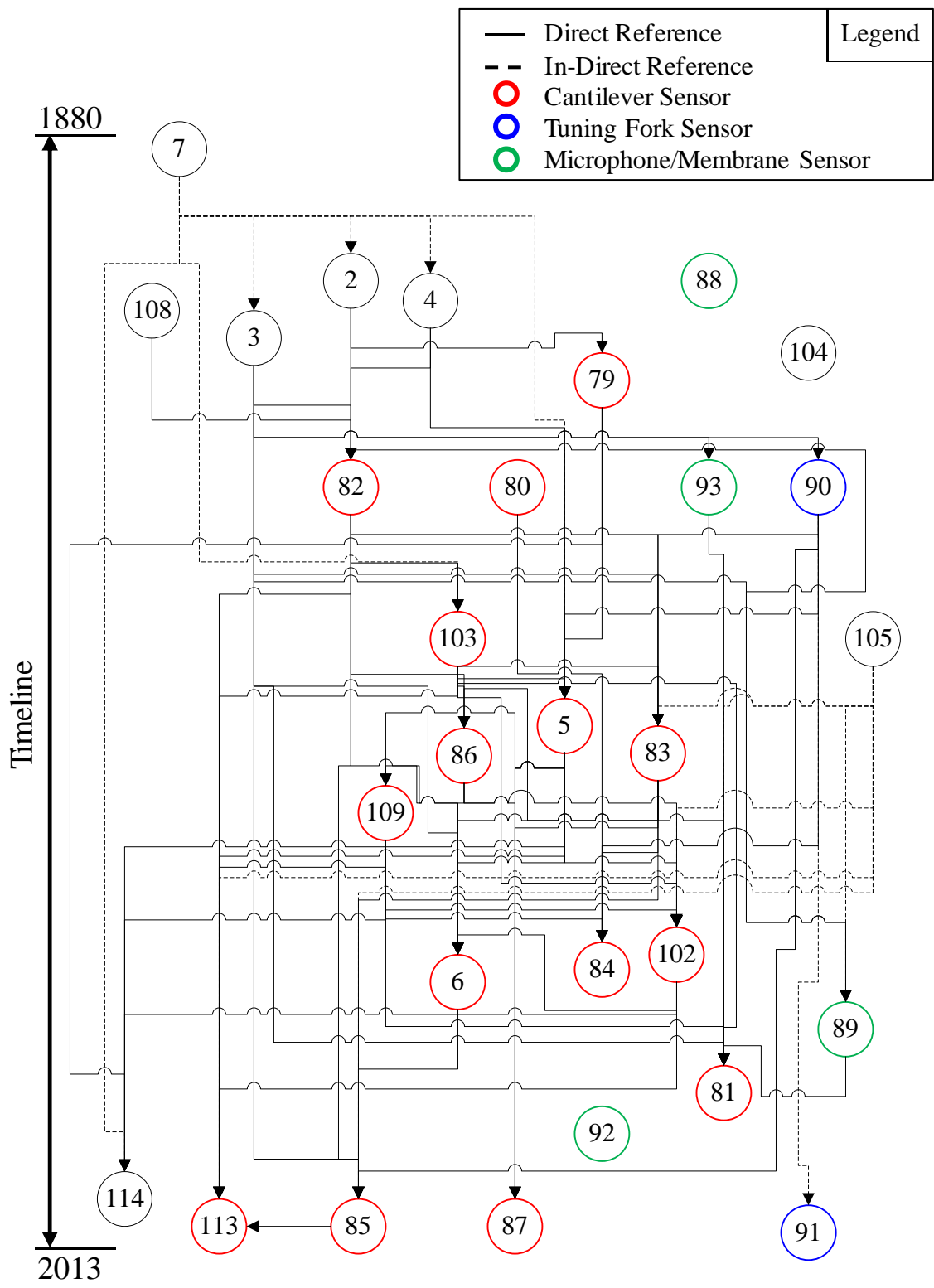


Figure 86. Visual bibliography connects related works, arranged by direct references.

Vita

Nathan E. Glauvitz began his professional career in 2000, graduating from the University of Wisconsin-Madison with a BS in Electrical Engineering. His first tour in the United States Air Force was as a missileer at Minot Air Force Base, ND in the 740th Missile Squadron. In 2007, he earned his master's degree from AFIT in Microelectronics and MEMS. The follow on assignment was at the Air Force Research Laboratory, Directed Energy Directorate, Kirtland AFB, New Mexico, where he worked as a developmental engineer. Major Glauvitz began the PhD program at AFIT in the Fall of 2010, worked on his PhD in Electrical Engineering at the Air Force Institute of Technology, Wright-Patterson Air Force Base, Ohio; completing the program in the Fall of 2013.

Bibliography

- [1] R. Herrmann and C. Onkelinx. "Quantities and Units in Clinical Chemistry Nebulizer and Flame Properties in Flame Emission and Absorption Spectrometry," *Pure & Appl. Chem.*, vol. 58, pp. 1737-1742, 1986.
- [2] A. Rosencwaig. *Photoacoustics and Photoacoustic Spectroscopy*. New York: John Wiley & Sons Inc, 1980.
- [3] A. Miklos, P. Hess and Z. Bozoki. "Application of acoustic resonators in photoacoustic trace gas analysis and metrology," *Rev. Sci. Instrum.* 72(4), pp. 1937-1955, 2001.
- [4] G. A. West, J. J. Barrett, D. R. Siebert and K. V. Reddy. "Photoacoustic spectroscopy," *Rev. Sci. Instrum.* 54(7), pp. 797-817, 1983.
- [5] T. Kuusela and J. Kauppinen. "Photoacoustic gas analysis using interferometric cantilever microphone," *Applied Spectroscopy Reviews* 42(5), pp. 443-474, 2007.
- [6] T. Kuusela, J. Peura, B. A. Matveev, M. A. Remenny and N. M. Stus'. "Photoacoustic gas detection using a cantilever microphone and III–V mid-IR LEDs," *Vibrational Spectroscopy* 51(2), pp. 289-293, 2009.
- [7] A. G. Bell. *Upon the Production of Sound by Radiant Energy*. Washington, D.C.: Gibson Brothers, Printers, 1881.
- [8] S. Ariyoshi, C. Otani, A. Dobroiu, H. Matsuo, H. Sato, T. Taino, K. Kawase and H. M. Shimizu. "Superconducting Detector Array for Terahertz Imaging Applications," *Japanese Journal of Applied Physics*, vol. 45, pp. L1004-L1006, 2006.
- [9] H. Tao, E. A. Kadlec, A. C. Strikwerda, K. Fan, W. J. Padilla, R. D. Averitt, E. A. Shaner and X. Zhang. "Microwave and terahertz wave sensing with metamaterials," *Opt. Express* 19(22), pp. 21620-21626, 2011.
- [10] S. Chen, Y. Choe, L. Baumgartel, A. Lin and E. S. Kim. "Edge-released, piezoelectric MEMS acoustic transducers in array configuration," *Journal of Micromechanics and Microengineering* 22(2), pp. 1-9, 2012.
- [11] A. Hulanicki, S. Glab and F. Ingman, "Chemical Sensors Definitions and Classifications," *Pure & Appl. Chem.*, vol. 63, No. 9, pp. 1247-1250, 1991.
- [12] A. Mandelis. *Principles & Perspectives of Photothermal & Photoacoustic Phenomena*. New York: Elsevier Science Publishing Co. Inc., 1992.

- [13] A. Ellis, M. Feher and T. Wright. *Electronic and Photoelectron Spectroscopy Fundamentals and Case Studies*. United Kingdom: Cambridge University Press, 2005.
- [14] W. Brugel. *An Introduction to Infrared Spectroscopy*. New York: John Wiley & Sons Inc, 1962.
- [15] S. L. Dexheimer. *Terahertz Spectroscopy: Principles and Applications*. Boca Raton: CRC Press, 2008.
- [16] J. U. White, N. L. Alpert, A. G. Debell and R. M. Chapman. "Infrared grating spectrophotometer," *J. Opt. Soc. Am.* 47(5), pp. 358-360, 1957.
- [17] J. U. White and N. L. Alpert. "Wide range infrared absorption cell," *J. Opt. Soc. Am.* 48(7), pp. 460-462, 1958.
- [18] R. G. Pilston and J. U. White. "A long path gas absorption cell," *J. Opt. Soc. Am.* 44(7), pp. 572-572, 1954.
- [19] S. Matsuura, Pin Chen, G. A. Blake, J. C. Pearson and H. M. Pickett. "A tunable cavity-locked diode laser source for terahertz photomixing," *Microwave Theory and Techniques, IEEE Transactions on* 48(3), pp. 380-387, 2000.
- [20] I. R. Medvedev, M. Behnke and F. C. D. Lucia. "Chemical analysis in the submillimetre spectral region with a compact solid state system," *Analyst (12)*, pp. 1299-1307, 2006.
- [21] I. R. Medvedev, C. F. Neese, G. M. Plummer and F. C. De Lucia. "Submillimeter spectroscopy for chemical analysis with absolute specificity." *Opt. Lett.* 35(10), pp. 1533-1535, 2010.
- [22] F. R. Blom, S. Bouwstra, M. Elwenspoek and J. H. J. Fluitman. "Dependence of the quality factor of micromachined silicon beam resonators on pressure and geometry," *J. Vac. Sci. Technol. B* 10(1), pp. 19-26, 1992.
- [23] C. H. Townes and S. Geschwind. "Limiting sensitivity of a microwave spectrometer." *J. Appl. Phys.* 19(8), pp. 795-796, 1948.
- [24] G. T. Kovacs. *Micromachined Transducers Sourcebook*. United States: WCB/McGraw-Hill, 1998.
- [25] M. J. Madou. *Fundamentals of Microfabrication: The Science of Miniaturization*. Boca Raton: CRC Press LLC, 2002.
- [26] S. D. Senturia. *Microsystem Design*. United States: Springer, 2001.

- [27] E. J. Boyd and D. Uttamchandani. "Measurement of the anisotropy of young's modulus in single-crystal silicon," *Microelectromechanical Systems, Journal of* 21(1), pp. 243-249, 2012.
- [28] J. E. E. Baglin. "Ion beam nanoscale fabrication and lithography - A review," *Appl. Surf. Sci.* 258(9), pp. 4103-4111, 2012.
- [29] W. Chen and H. Ahmed. "Fabrication of 5–7 nm wide etched lines in silicon using 100 keV electron-beam lithography and polymethylmethacrylate resist," *Applied Physics Letters* 62(13), pp. 1499-1501, 1993.
- [30] C. Vieu, F. Carcenac, A. Pépin, Y. Chen, M. Mejias, A. Lebib, L. Manin-Ferlazzo, L. Couraud and H. Launois. "Electron beam lithography: Resolution limits and applications," *Appl. Surf. Sci.* 164(1–4), pp. 111-117, 2000.
- [31] T. H. P. Chang, M. Mankos, K. Y. Lee and L. P. Muray. "Multiple electron-beam lithography," *Microelectronic Engineering* 57–58(0), pp. 117-135, 2001.
- [32] R. Chang. *Chemistry*. United States: McGraw-Hill, Inc., 1994.
- [33] K. Biswas and S. Kal. "Etch characteristics of KOH, TMAH and dual doped TMAH for bulk micromachining of silicon," *Microelectron. J.* 37(6), pp. 519-525, 2006.
- [34] P. A. Sturrock. *Plasma Physics: An Introduction to the Theory of Astrophysical, Geophysical & Laboratory Plasmas*. United States: Cambridge University Press, 1994.
- [35] W. H. Juan, S. W. Pang, A. Selvakumar, M. W. Putty and K. Najafi. "Using electron cyclotron resonance (ECR) sources to etch polyimide molds for fabrication of electroplated microstructures," *Digest Solid-State Sensor and Actuator Workshop*, Hilton Head Island, S.C., pp. 82-85, 1994.
- [36] F. Laermer and A. Schilp. "Method of anisotropically etching silicon," Patent Number: 5501893, 1996.
- [37] MEMS & Nanotechnology Exchange: <https://www.mems-exchange.org/MEMS/fabrication.html>.
- [38] M. K. Hooda, M. Wadhwa, S. Verma, M. M. Nayak, P. J. George and A. K. Paul. "A systematic study of DRIE process for high aspect ratio microstructuring," *Vacuum* 84(9), pp. 1142-1148, 2010.

- [39] J. Parasuraman, A. Summanwar, F. Marty, P. Basset, D. E. Angelescu and T. Bourouina. "Deep reactive ion etching of sub-micrometer trenches with ultra high aspect ratio," *Microelectronic Engineering* 113(0), pp. 35-39, 2014.
- [40] D. Xu, B. Xiong, G. Wu, Y. Wang, X. Sun and Y. Wang. "Isotropic silicon etching with gas for wafer-level micromachining applications," *Microelectromechanical Systems, Journal of* 21(6), pp. 1436-1444, 2012.
- [41] V. Craciun, J. Elders, J. G. E. Gardeniers and I. W. Boyd. "Characteristics of high quality ZnO thin films deposited by pulsed laser deposition," *Applied Physics Letters* 65(23), pp. 2963-2965, 1994.
- [42] S. Venkatachalam and Y. Kanno. "Preparation and characterization of nano and microcrystalline ZnO thin films by PLD," *Current Applied Physics* 9(6), pp. 1232-1236, 2009.
- [43] Y. M. Wong, S. Wei, W. P. Kang, J. L. Davidson, W. Hofmeister, J. H. Huang and Y. Cui. "Carbon nanotubes field emission devices grown by thermal CVD with palladium as catalysts," *Diamond and Related Materials* 13(11-12), pp. 2105-2112, 2004.
- [44] C. E. Baddour, F. Fadlallah, D. Nasuhoglu, R. Mitra, L. Vandsburger and J. Meunier. "A simple thermal CVD method for carbon nanotube synthesis on stainless steel 304 without the addition of an external catalyst," *Carbon* 47(1), pp. 313-318, 2009.
- [45] B. L. Crossley, N. E. Glauvitz, B. T. Quinton, R. A. J. Coutu and P. J. Collins, "Characterizing multi-walled carbon nanotube synthesis for field emission applications," *Carbon Nanotubes Applications on Electron Devices*, J. M. Marulanda, Ed. InTech, pp. 105-126, 2011.
- [46] C. Lee and J. Park. "Growth model of bamboo-shaped carbon nanotubes by thermal chemical vapor deposition," *Applied Physics Letters* 77(21), pp. 3397-3399, 2000.
- [47] N. E. Glauvitz, R. A. Coutu Jr., P. J. Collins and L. A. Starman. "Etching silicon dioxide for CNT field emission device," *MEMS and Nanotechnology, Conference Proceedings of the Society for Experimental Mechanics Series* (6). New York: Springer, pp. 93-99, 2013.
- [48] S. Porro, S. Musso, M. Vinante, L. Vanzetti, M. Anderle, F. Trotta and A. Tagliaferro. "Purification of carbon nanotubes grown by thermal CVD," *Physica E: Low-Dimensional Systems and Nanostructures* 37(1-2), pp. 58-61, 2007.

- [49] S. Porro, S. Musso, M. Giorcelli, A. Chiodoni and A. Tagliaferro. "Optimization of a thermal-CVD system for carbon nanotube growth," *Physica E: Low-Dimensional Systems and Nanostructures* 37(1-2), pp. 16-20, 2007.
- [50] C. Wang, S. Cho and N. Kim. "Comparison of SiO₂-based double passivation scheme by e-beam evaporation and PECVD for surface passivation and gate oxide in AlGa_N/Ga_N HEMTs," *Microelectronic Engineering* 109(0), pp. 24-27, 2013.
- [51] B. Olbrechts and J. Raskin. "PECVD oxide as intermediate film for wafer bonding: Impact of residual stress," *Microelectronic Engineering* 87(11), pp. 2178-2186, 2010.
- [52] E. W. Becker, W. Ehrfeld, P. Hagmann, A. Maner and D. Münchmeyer. "Fabrication of microstructures with high aspect ratios and great structural heights by synchrotron radiation lithography, galvanofforming, and plastic moulding (LIGA process)," *Microelectronic Engineering* 4(1), pp. 35-56, 1986.
- [53] M. W. Börner, M. Kohl, F. J. Pantenburg, W. Bacher, H. Hein and W. K. Schomburg. "Sub-micron LIGA process for movable microstructures," *Microelectronic Engineering* 30(1-4), pp. 505-508, 1996.
- [54] C. Burbaum, J. Mohr, P. Bley and W. Ehrfeld. "Fabrication of capacitive acceleration sensors by the LIGA technique," *Sensors and Actuators A: Physical* 27(1-3), pp. 559-563, 1991.
- [55] S. McNamara and Y. B. Gianchandani. "LIGA fabricated 19-element threshold accelerometer array," *Sensors and Actuators A: Physical* 112(1), pp. 175-183, 2004.
- [56] N. Miyano, K. Tagaya, K. Kawase, K. Ameyama and S. Sugiyama. "Fabrication of alloy and ceramic microstructures by LIGA-MA-SPS process," *Sensors and Actuators A: Physical* 108(1-3), pp. 250-257, 2003.
- [57] C. Ho, K. Chin, C. Yang, H. Wu and S. Chen. "Ultrathick SU-8 mold formation and removal, and its application to the fabrication of LIGA-like micromotors with embedded roots," *Sensors and Actuators A: Physical* 102(1-2), pp. 130-138, 2002.
- [58] C. K. Malek and V. Saile. "Applications of LIGA technology to precision manufacturing of high-aspect-ratio micro-components and systems: A review," *Microelectron. J.* 35(2), pp. 131-143, 2004.

- [59] Z. Bi, Z. Zhang and P. Fan. "Characterization of PZT ferroelectric thin films by RF-magnetron sputtering," *International Conference on Nanoscience and Technology, Journal of Physics: Conference Series (61)(2007)*, pp. 120-124, 2006.
- [60] Z. Bi, Z. Zhang and P. Fan. "Effect of sputter deposition parameters on the characteristics of PZT ferroelectric thin films," *International Conference on Nanoscience and Technology, Journal of Physics: Conference Series (61)(2007)*, pp. 115-119, 2006.
- [61] R. Mamazza, N. Y. Mark, R. G. Polcawich, B. H. Piekarski, P. Murali and G. J. Reynolds. "Comparison of ferroelectric and piezoelectric properties of sol-gel grown and sputter deposited Pb(Zr, Ti)O₃ thin films," *Presented at 15th IEEE International Symposium on the Applications of Ferroelectrics, 2006 Isaf '06*, pp. 314-317, 2006.
- [62] T. Haccart, E. Cattan and D. Remiens. "Dielectric, ferroelectric and piezoelectric properties of sputtered PZT thin films on Si substrates: influence of film thickness and orientation," *Semiconductor Physics, Quantum Electronics & Optoelectronics*, vol. Vol 5, pp. 78-88, 2002.
- [63] G. Velu, D. Remiens and B. Thierry. "Ferroelectric properties of PZT thin films prepared by sputtering with stoichiometric single oxide target: Comparison between conventional and rapid thermal annealing," *Journal of the European Ceramic Society 17(14)*, pp. 1749-1755, 1997.
- [64] M. Kratzer, L. Castaldi, B. Heinz, R. Mamazza, D. Kaden, H. Quenzer and B. Wagner. "In-situ large scale deposition of PZT films by RF magnetron sputtering," *Conference proceedings of Applications of Ferroelectrics (ISAF/PFM), 2011 International Symposium on Piezoresponse Force Microscopy and Nanoscale Phenomena in Polar Materials*, pp. 1-4, 2011.
- [65] K. Sreenivas, M. Sayer and P. Garrett. "Properties of D.C. magnetron-sputtered lead zirconate titanate thin films," *Thin Solid Films 172(2)*, pp. 251-267, 1989.
- [66] Z. D. Wang, Z. Q. Lai and Z. G. Hu. "Low-temperature preparation and characterization of the PZT ferroelectric thin films sputtered on FTO glass substrate," *J. Alloys Compounds 583(0)*, pp. 452-454, 2014.
- [67] Y. Lin, C. Andrews and H. A. Sodano. "Enhanced piezoelectric properties of lead zirconate titanate sol-gel derived ceramics using single crystal PbZr_{0.52}Ti_{0.48}O₃ cubes," *Journal of Applied Physics 108(6)*, pp. 064108(1-6), 2010.

- [68] L. M. Sanchez, D. M. Potrepka, G. R. Fox, I. Takeuchi and R. G. Polcawich. "Improving PZT thin film texture through Pt metallization and seed layers," *MRS Proceedings (1299)*, 2011.
- [69] T. Oikawa, M. Aratani, H. Funakubo, K. Saito and M. Mizuhira. "Composition and orientation dependence of electrical properties of epitaxial $\text{Pb}(\text{Zr}_x\text{Ti}_{1-x})\text{O}_3$ thin films grown using metalorganic chemical vapor deposition," *J. Appl. Phys.* 95(6), pp. 3111-3115, 2004.
- [70] S. K. Pandey, A. R. James, C. Prakash, T. C. Goel and K. Zimik. "Electrical properties of PZT thin films grown by sol-gel and PLD using a seed layer," *Materials Science and Engineering: B 112(1)*, pp. 96-100, 2004.
- [71] C. Pandis, N. Brilis, D. Tsamakidis, H. A. Ali, S. Krishnamoorthy and A. A. Iliadis. "Role of low O_2 pressure and growth temperature on electrical transport of PLD grown ZnO thin films on Si substrates," *Solid-State Electronics 50(6)*, pp. 1119-1123, 2006.
- [72] K. Kakimoto, H. Ohsato, H. Kakemoto and Y. Masuda. "Stoichiometry and crystal orientation of YAG-PLD derived ferroelectric PZT thin film," *Journal of the European Ceramic Society 24(6)*, pp. 993-997, 2004.
- [73] Q. Wang, X. Du, B. Xu and L. E. Cross. "Theoretical analysis of the sensor effect of cantilever piezoelectric benders," *J. Appl. Phys.* 85(3), pp. 1702-1712, 1999.
- [74] K. Kanda, I. Kanno, H. Kotera and K. Wasa. "Simple fabrication of metal-based piezoelectric MEMS by direct deposition of thin films on titanium substrates," *Microelectromechanical Systems, Journal of 18(3)*, pp. 610-615, 2009.
- [75] J. Hwang, W. S. Kim, H. Park and T. Kim. "The effect of intermediate anneal on the ferroelectric properties of direct-patternable PZT films," *Sensors and Actuators A: Physical 117(1)*, pp. 137-142, 2005.
- [76] J. F. Shepard Jr., P. J. Moses and S. Trolrier-McKinstry. "The wafer flexure technique for the determination of the transverse piezoelectric coefficient (d_{31}) of PZT thin films," *Sensors and Actuators A: Physical 71(1-2)*, pp. 133-138, 1998.
- [77] C. Lee, T. Itoh and T. Suga. "Self-excited piezoelectric PZT microcantilevers for dynamic SFM-with inherent sensing and actuating capabilities," *Sensors and Actuators A: Physical 72(2)*, pp. 179-188, 1999.
- [78] C. Lee, T. Itoh and T. Suga. "Micromachined piezoelectric force sensors based on PZT thin films," *IEEE Transactions on Ultrasonics, Ferroelectrics, and Frequency Control 43(4)*, pp. 553-559, 1996.

- [79] M. H. de Paula, A. A. de Carvalho, C. A. Vinha, N. Cella and H. Vargas. "Optical microphone for photoacoustic spectroscopy," *J. Appl. Phys.* 64(7), pp. 3722-3724, 1988.
- [80] N. Ledermann, P. Muralt, J. Baborowski, M. Forster and J. Pellaux. "Piezoelectric $\text{Pb}(\text{Zr}_x\text{Ti}_{1-x})\text{O}_3$ thin film cantilever and bridge acoustic sensors for miniaturized photoacoustic gas detectors," *Journal of Micromechanics and Microengineering* 14(12), pp. 1650-1658, 2004.
- [81] E. McNaghten, K. Grant, A. Parkes and P. Martin. "Simultaneous detection of trace gases using multiplexed tunable diode lasers and a photoacoustic cell containing a cantilever microphone," *Applied Physics B: Lasers and Optics* 107(3), pp. 861-871, 2012.
- [82] J. Kauppinen, K. Wilcken, I. Kauppinen and V. Koskinen. "High sensitivity in gas analysis with photoacoustic detection," *Microchemical Journal* 76(1-2), pp. 151-159, 2004.
- [83] V. Koskinen, J. Fonsen, K. Roth and J. Kauppinen. "Cantilever enhanced photoacoustic detection of carbon dioxide using a tunable diode laser source," *Applied Physics B: Lasers and Optics* 86(3), pp. 451-454, 2007.
- [84] B. D. Adamson, J. E. Sader and E. J. Bieske. "Photoacoustic detection of gases using microcantilevers," *J. Appl. Phys.* 106(11), pp. 114510(1-4), 2009.
- [85] J. Peltola, M. Vainio, T. Hieta, J. Uotila, S. Sinisalo, M. Metsälä, M. Siltanen and L. Halonen. "High sensitivity trace gas detection by cantilever-enhanced photoacoustic spectroscopy using a mid-infrared continuous-wave optical parametric oscillator," *Opt. Express* 21(8), pp. 10240-10250, 2013.
- [86] P. Sievilä, V. Rytönen, O. Hahtela, N. Chekurov, J. Kauppinen and I. Tittonen. "Fabrication and characterization of an ultrasensitive acousto-optical cantilever," *J Micromech Microengineering* 17(5), pp. 852-859, 2007.
- [87] P. Sievilä, N. Chekurov, J. Raittila and I. Tittonen. "Sensitivity-improved silicon cantilever microphone for acousto-optical detection," *Sensors and Actuators A: Physical* 190(0), pp. 90-95, 2013.
- [88] A. F. Krupnov and A. V. Burenin. "New methods in submillimeter microwave spectroscopy," in *Molecular Spectroscopy: Modern Research*, K. N. Rao, Ed. New York: Academic Press, Inc., pp. 93-126, 1976.

- [89] M. Hippler, C. Mohr, K. A. Keen and E. D. McNaghten. "Cavity-enhanced resonant photoacoustic spectroscopy with optical feedback cw diode lasers: A novel technique for ultratrace gas analysis and high-resolution spectroscopy," *J. Chem. Phys.* 133(4), pp. 044308(1-8), 2010.
- [90] A. A. Kosterev, Y. A. Bakhrkin, R. F. Curl and F. K. Tittel. "Quartz-enhanced photoacoustic spectroscopy," *Opt. Lett.*, vol. 27, pp. 1902-1904, 2002.
- [91] S. Borri, P. Patimisco, A. Sampaolo, H. E. Beere, D. A. Ritchie, M. S. Vitiello, G. Scamarcio and V. Spagnolo. "Terahertz quartz enhanced photo-acoustic sensor," *Appl. Phys. Lett.* 103(2), pp. 021105(1-4), 2013.
- [92] Q. Wang, Z. Ma and Z. He. "A novel photoacoustic spectroscopy system using diaphragm based fiber fabry-perot sensor," *Procedia Engineering* 15(0), pp. 5395-5399, 2011.
- [93] J. Besson, S. Schilt and L. Thévenaz. "Multi-gas sensing based on photoacoustic spectroscopy using tunable laser diodes," *Spectrochimica Acta Part A: Molecular and Biomolecular Spectroscopy* 60(14), pp. 3449-3456, 2004.
- [94] Y. Wang, C. Lee and C. Chiang. "A MEMS-based air flow sensor with a free-standing micro-cantilever structure," *Sensors* 7(10), pp. 2389-2401, 2007.
- [95] L. Du, Zhan Zhao and Cheng Pang. Design and fabrication MEMS-based micro solid state cantilever wind speed sensor. Presented at Information Acquisition ICIA '07. International Conference. 2007.
- [96] H. J. Kim, Y. B. Kim, J. Park and T. S. Kim. "Biological element detection sensor application of micromachined PZT thick film cantilever," *Proceedings of IEEE Sensors 2003*, pp. 1054-1058, 2003.
- [97] Y. Lee, G. Lim and W. Moon. "A piezoelectric micro-cantilever bio-sensor using the mass-micro-balancing technique with self-excitation," *TRANSDUCERS '05', the 13th International Conference on Solid-State Sensors, Actuators and Microsystems*, pp. 644-647, 2005.
- [98] Y.-S. Kim, H.-J. Nam, S.-M. Cho, D.-C. Kim and J.-U. Bu. "A self-actuating PZT cantilever integrated with piezoresistor sensor for AFM with high speed parallel operation," *Fifteenth IEEE International Conference Micro Electro Mechanical Systems*, pp. 689-692, 2002.
- [99] S. Murakami, K. Inoue, Y. Suzuki, S. Takamatsu, T. Kitano, M. Kinoshita, K. Yamashita and M. Okuyama. "Fabrication of sonic sensors using PZT thin film on Si diaphragm and cantilever," *Applications of Ferroelectrics, Proceedings of the 13th IEEE International Symposium on*. pp. 463-466, 2002.

- [100] H. Sharma and R. Mutharasan. "Adhesion determines resonance response of piezoelectric cantilever sensors," *Appl. Phys. Lett.* 98(11), pp. 114101, 2011.
- [101] D. T. Petkie, T. M. Goyette, R. P. A. Bettens, S. P. Belov, S. Albert, P. Helminger and F. C. De Lucia. "A fast scan submillimeter spectroscopic technique," *Rev. Sci. Instrum.* 68(4), pp. 1675-1683, 1997.
- [102] J. Fonsen, V. Koskinen, K. Roth and J. Kauppinen. "Dual cantilever enhanced photoacoustic detector with pulsed broadband IR-source," *Vibrational Spectroscopy* 50(2), pp. 214-217, 2009.
- [103] V. Koskinen, J. Fonsen, J. Kauppinen and I. Kauppinen. "Extremely sensitive trace gas analysis with modern photoacoustic spectroscopy," *Vibrational Spectroscopy* 42(2), pp. 239-242, 2006.
- [104] "JPL molecular spectroscopy catalog." (2013) <http://spec.jpl.nasa.gov/>.
- [105] L. S. Rothman *et al.* "The HITRAN2012 molecular spectroscopic database," *J Quant Spectrosc Radiat Trans*, 2013.
- [106] R. D. Cook, D. S. Malkus, M. E. Plesha and R. J. Witt. *Concepts and Applications of Finite Element Analysis*. United States: John Wiley & Sons, Inc., 2002.
- [107] *CovnetorWare Analyzer Reference*. Ver. 2010, Coventor Inc., Cary NC, 2010.
- [108] A. Garcia-Valenzuela and J. Villatoro. "Noise in optical measurements of cantilever deflections," *J. Appl. Phys.* 84(1), pp. 58-63, 1998.
- [109] V. Koskinen, J. Fonsen, K. Roth and J. Kauppinen. "Progress in cantilever enhanced photoacoustic spectroscopy," *Vibrational Spectroscopy* 48(1), pp. 16-21, 2008.
- [110] K. Hane, T. Iwatuki, S. Inaba and S. Okuma. "Frequency shift on a micromachined resonator excited photothermally in vacuum," *Review of Scientific Instruments* 63(7), pp. 3781-3782, 1992.
- [111] L. Couture and R. Zitoun. *Statistical Thermodynamics and Properties of Matter*. The Netherlands: Gordon and Breach Science Publishers, 2000.
- [112] S. Alexander, L. Hellemans, O. Marti, J. Schneir, V. Elings, P. K. Hansma, M. Longmire and J. Gurley. "An atomic-resolution atomic-force microscope implemented using an optical lever," *J. Appl. Phys.* 65(1), pp. 164-167, 1989.

- [113] C. B. Hirschmann, S. Sinisalo, J. Uotila, S. Ojala and R. L. Keiski. "Trace gas detection of benzene, toluene, p-, m- and o-xylene with a compact measurement system using cantilever enhanced photoacoustic spectroscopy and optical parametric oscillator," *Vibrational Spectroscopy* 68(0), pp. 170-176, 2013.
- [114] C. Haisch. "Photoacoustic spectroscopy for analytical measurements," *Measurement Science and Technology* 23(1), pp. 012001(1-17), 2012.

REPORT DOCUMENTATION PAGE			<i>Form Approved</i> OMB No. 0704-0188		
The public reporting burden for this collection of information is estimated to average 1 hour per response, including the time for reviewing instructions, searching existing data sources, gathering and maintaining the data needed, and completing and reviewing the collection of information. Send comments regarding this burden estimate or any other aspect of this collection of information, including suggestions for reducing this burden to Department of Defense, Washington Headquarters Services, Directorate for Information Operations and Reports (0704-0188), 1215 Jefferson Davis Highway, Suite 1204, Arlington, VA 22202-4302. Respondents should be aware that notwithstanding any other provision of law, no person shall be subject to any penalty for failing to comply with a collection of information if it does not display a currently valid OMB control number. PLEASE DO NOT RETURN YOUR FORM TO THE ABOVE ADDRESS.					
1. REPORT DATE (DD-MM-YYYY) 26-12-2013		2. REPORT TYPE Dissertation	3. DATES COVERED (From — To) September 2010 - 26 December 2013		
4. TITLE AND SUBTITLE MEMS Cantilever Sensor for THz Photoacoustic Chemical Sensing and Spectroscopy			5a. CONTRACT NUMBER		
			5b. GRANT NUMBER		
			5c. PROGRAM ELEMENT NUMBER		
6. AUTHOR(S) Glauvitz, Nathan E, Maj, USAF			5d. PROJECT NUMBER 14G239N		
			5e. TASK NUMBER		
			5f. WORK UNIT NUMBER		
7. PERFORMING ORGANIZATION NAME(S) AND ADDRESS(ES) Air Force Institute of Technology Graduate School of Engineering and Management (AFIT/EN) 2950 Hobson Way WPAFB OH 45433-7765			8. PERFORMING ORGANIZATION REPORT NUMBER AFIT-ENG-DS-13-D-03		
9. SPONSORING / MONITORING AGENCY NAME(S) AND ADDRESS(ES) Dr. Gernot Pomrenke Air Force Office of Scientific Research 875 N Randolph St, Ste 325 Rm 3112 Arlington AFB, VA 22203			10. SPONSOR/MONITOR'S ACRONYM(S) AFOSR		
			11. SPONSOR/MONITOR'S REPORT NUMBER(S)		
12. DISTRIBUTION / AVAILABILITY STATEMENT Distribution A. Approved for Public Release; Distribution Unlimited					
13. SUPPLEMENTARY NOTES This material is declared a work of the U.S. Government and is not subject to copyright protection in the United States.					
14. ABSTRACT Sensitive Microelectromechanical System (MEMS) cantilever designs were modeled, fabricated, and tested to measure the photoacoustic (PA) response of gasses to terahertz (THz) radiation. Surface and bulk micromachining technologies were employed to create the extremely sensitive devices that could detect very small changes in pressure. Fabricated devices were then tested in a custom made THz PA vacuum test chamber where the cantilever deflections caused by the photoacoustic effect were measured with a laser interferometer and iris beam clipped methods. The sensitive cantilever designs achieved a normalized noise equivalent absorption coefficient of $2.83 \times 10^{-10} \text{ cm}^{-1} \text{ W Hz}^{-1/2}$ using a 25 μW radiation source power and a 1 s sampling time. Traditional gas phase molecular spectroscopy absorption cells are large and bulky. The outcome of this research resulted was a photoacoustic detection method that was virtually independent of the absorption path-length, which allowed the chamber dimensions to be greatly reduced, leading to the possibility of a compact, portable chemical detection and spectroscopy system.					
15. SUBJECT TERMS MEMS, cantilever, terahertz, photoacoustic, spectroscopy, chemical sensor					
16. SECURITY CLASSIFICATION OF:			17. LIMITATION OF ABSTRACT	18. NUMBER OF PAGES	19a. NAME OF RESPONSIBLE PERSON
a. REPORT	b. ABSTRACT	c. THIS PAGE			UU
U	U	U			19b. TELEPHONE NUMBER (Include Area Code) (937)255-3636, ext 7230; Ronald.coutu@afit.edu